Internal Report
DESY F15-80/05
November 1980

JETS OF HADRONS

by

W. Hofmann

JETS OF HADRONS

W. HOFMANN

INSTITUT FÜR PHYSIK
UNIVERSITÄT DORTMUND
DORTMUND, GERMANY

FEBRUARY 1980

Acknowledgements

The author is a member of the CERN-College de France-Heidelberg-Karlsruhe collaboration (CCHK), and of its sucessor, the Annecy-CERN-College de France-Dortmund-Heidelberg-Warsaw group (ACCDHW), both studying rare event types in proton-proton interactions using the Split-Field-Magnet facility at the CERN-ISR.

It is a pleasure for me to thank the participants in these experiments

P. Burlaud, M. Della Negra, D. Drijard, H.G. Fischer, G. Fontaine, H. Frehse, P. Frenkiel, G. Ghesquière, R. Gokieli, P. Hanke, P.G. Innocenti, W. Isenbeck, E.E. Kluge, V. Korbel, D. Linglin, A. Minten, A. Norton, G. Sajot, M. Panter, A. Putzer, K. Rauschnabel, R. Sosnowski, J. Spengler, S. Stein, J. Stiewe, O. Ullaland, H.D. Wahl, D. Wegener.

More recently, the author joined the DASP II collaboration working at the electron-positron storage ring DORIS at DESY. The experience and efforts of all members of the DASP II group

H. Albrecht, P. Böckmann, C.W. Darden, H. Hasemann, L. Jönsson, A. Krolzig, A. Markees, W. Schmidt-Parzefall, H. Schröder, K.R. Schubert, H.D. Schulz, F. Selonke, E. Steinmann, D. Wegener, R. Wurth

made it possible to gain important information on T-production and its decay modes.

I especially want to thank Prof. D. Wegener for innumberable valuable suggestions, many interesting discussions, steady encouragement and last not least for his substantial contributions to the experiments cited above.

I acknowledge interesting and helpful discussions with Prof. E. Reya and Prof. M. Glück concerning applications of QCD.

I thank my coworkers at Dortmund, Dr. A. Markees and J. Spengler for many helpful comments and for their help in technical problems.

Finally, I thank Mrs. C. Strungat for typing this manuscript, and Mrs. H. Bußmann who prepared the illustrations.

This work was supported by the Bundesministerium für Forschung und Technologie.

1. Introduction

The development of high energy physics during the last decade was characterized by the rapidly increasing energies of particle accelerators, thus allowing to study particle interactions at very high center of mass (cms) energies and momentum transfers. The step to four momentum transfers, which are large compared to the masses of the particles involved, lead to a new phenomenological model, the parton picture.[1-4] This model was strongly supported by the observation of the "jet" phenomenon in deep inelastic interactions.[5-7]

At high momentum transfers one observes that the emitted secondaries form bunches with a preferred axis, the jet axis (it is however difficult to give a general, model independent definition of a "jet", we shall postpone this to a later chapter). The first experimental evidence for the existence of jets, originated from fragmenting partons, came independently from two reactions: in electron-positron annihilations at $\sqrt{s} > 5$ GeV the emitted particles tend to occupy a cylindrical volume of phase space, the longitudinal extension of which is large compared to its diameter.[5] The orientation of the cylinder, or jet axis, changes randomly from event to event. Secondly, jets have been observed in proton-proton interactions at ISR energies [6,7]. In a rare type of events, a particle of large transverse momentum with respect to the beam axis is produced.[8-10] Such events had been predicted as a consequence of a large-angle elastic scattering of partons.[11] A detailed analysis of the event structure revealed that these events contain two bunches of particles emitted at large angles, one of them includes the high $p_\perp$ particle, while the second jet opposite in azimuth compensates the transverse momentum of the first one.[6,7] The properties of jets seen in these two types of reactions turned out to be quite similar[7].

It seems astonishing that the concept of jets has been introduced so late, in spite of the fact that already in normal proton-proton interactions the produced secondaries are preferentially emitted along the direction of the incoming protons, thus forming two jets, in today's language.

There is, however, an essential difference: the jets seen in e^+e^- collisions and in high $p_\perp$ events are, at least on an event to event basis, not correlated with any obvious symmetry axis of the process, like the direction of the primary particles. Since they are produced by large momentum transfers, which probe distances small compared to the typical hadron radii, these jets are intimatly related to the parton structure of hadrons.

The jet structure visible in normal hadron-hadron collisions does not exhibit these particular features. It could be explained eg. in terms of multiperipheral models [12] and in fact did not yield too much insight into the dynamics and systematics of strong interactions. Only recently, and using the parton picture as a guide line, physicists started to see these phenomena as a manifestation of the parton structure of matter, and attempts to describe the observed particle spectra in terms of parton densities as measured in deep inelastic lepton-hadron interactions were made.[13,14] Meanwhile, the production of jets resulting from the fragmentation of colored parton systems seems to be a common link between the various hadronic final states in normal hadron-hadron interactions, in lepton induced reactions, and in annihilation reactions.[15]

The aim of this work is to summarize our present knowledge on jets as a universal phenomenon in high energy physics, and to investigate the dynamics of jet production and fragmentation.

The paper is subdivided as follows. In chapter 2 the experimental information on jets from e^+e^- annihilations is discussed. This type of jets is rather well known from both the experimental and the theoretical side, and is used as a reference for further discussions. In chapter 3 we try to describe the structure of jets by simple longitudinal phase space models, and the implications imposed by four-momentum conservation are studied. Chapter 4 presents models for jet development in terms of the quark-parton language; the QCD corrections to the naive quark model are discussed in chapter 5. In chapter 6 we leave

the "safe" ground of e^+e^- annihilations, and investigate the structure of the jets observed in lepton-hadron reactions and in decays of bound states of heavy quarks. Hadron-hadron interactions at large momentum transfers are considered in chapter 7. Phenomenological models for the fragmentation of the multiquark systems involved will be compared to recent data. In chapter 8 extensions of the quark-parton jet concept to hadronic interactions at low momentum transfers are studied. Finally a brief summary is given.

This work is intended to give an introductory review to the phenomenon of jets in hadronic final states, it contains therefore quite a lot of "old" physics, which seems to be relevant for the understanding of jets. Since the major aim is to discuss physical concepts and models, it has not been tried to give an exhaustive compilation of data and references, only those actually used in the discussion are quoted. We take this opportunity to apologize to all those authors, whose important contributions to the field are not quoted because of ignorance or lack of space.

2. Jets in e^+e^- annihilations

When the first electron-positron storage rings in the GeV range came into operation, one of the surprising results was that over a wide range of energies the ratio R of the hadronic cross section to the total cross section for muon pair production is approximately constant. This implies a pointlike coupling of the virtual photon to the hadronic final state. A natural explanation of this phenomenon is given by the quark-parton model[1-4]: the virtual photon creates a quark-antiquark pair. According to the postulates of the quark model, these quarks fragment into observable hadrons with unit probability. Quark creations and decays are governed by violently different time scales and thus may be treated independently. As the photon-quark coupling is determined by the square of the quark charge, one obtains in the naive quark model

$$R = \frac{\sigma(e^+e^- \to \text{hadrons})}{\sigma(e^+e^- \to \mu^+\mu^-)} = \sum_{\substack{\text{quarks} \\ \text{above threshold}}} q_i^2 \qquad (2.1)$$

The sum is extended over all quark species above threshold. In the standard model with quarks carrying a SU(3) color charge,[16,17] eqn.(2.1) reads

$$R = (\text{number of colors}) \cdot \sum_{\substack{\text{quark} \\ \text{flavors}}} q_i^2 = 3 \sum_{\substack{\text{quark} \\ \text{flavors}}} q_i^2 \qquad (2.2)$$

Higher order calculations using the formalism of Quantum Chromo Dynamics[18] to describe the interaction between quarks strongly support these results: corrections in the first order of the strong coupling constant α_S are small[19] (O (20%)), higher order terms[20] are negligible compared to the experimental accuracy. Within the first order approximation, we get[19]

$$R(S) = 3 \sum_{\substack{\text{light} \\ \text{quark flavors}}} q_i^2 \left(1 + \frac{\alpha_S}{\pi} + \cdots\right)$$

$$+ 3 \sum_{\substack{\text{heavy} \\ \text{quark flavors}}} q_i^2 \left(1 + \frac{4}{3}\alpha_S f(v) + \cdots\right) \quad v \frac{3-v^2}{2} \; \upsilon \; (s-4m_i^2) \qquad (2.3)$$

with

$$v = (1-4m_q^2/s)^{1/2} \qquad (2.4)$$

and

$$f(v) = \frac{\pi}{2v} - \frac{3+v}{4}\left(\frac{\pi}{2} - \frac{3}{4\pi}\right) \qquad (2.5)$$

s is the square of the center of mass energy. Since the four momentum of the virtual photon is timelike there are steps in R at $s = 4\,m_i^2$ due to the production of new heavy quark flavors. Close to these thresholds the relative velocity of the quarks is small, and nonperturbative effects like resonance formation dominate. Therefore eqn (2.1) does not hold in the vicinity of thresholds. In fig. 2.1 the measured values of R are compared with eqn (2.2), including the known thresholds for charmed, and bottom quarks. As in all following figures, contributions from heavy lepton decays have been subtracted, resp. are irrelevant. The approximate agreement of experimental data and theory supports the assumptions that quarks dress into hadrons with unit probability, and that this mechanism is sufficiently soft not to interfere with the hard production process.

In a soft fragmentation process, the final state hadrons are expected to have small transverse momenta with respect to the quark axis of flight. Noting further that the mean hadron multiplicity in e^+e^- annihilations (fig. 2.2) rises slower than the cms energy

$$\langle n_{\text{charged}} \rangle = 2 + 0.2 \ln s + 0.18 (\ln s)^2 \qquad (2.6)$$

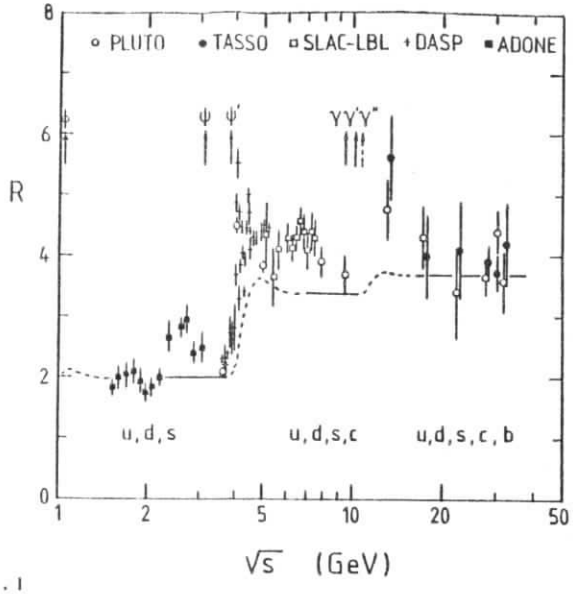

Fig. 2.1

The ratio R of hadronic to μμ cross sections as measured by the ϒϒ group at ADONE[21], SLAC-LBL[22], PLUTO[23], DASP [59] and TASSO [24]. Contributions from heavy lepton decays subtracted.

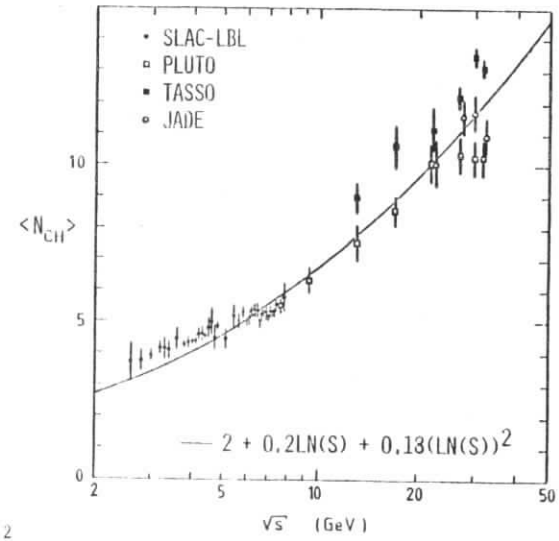

Fig. 2.2

Mean charged multiplicity in e^+e^- annihilations vs. √s. Data from SLAC-LBL[25], PLUTO[26,34], JADE[220], and TASSO[24]. Contributions from heavy lepton decays are subtracted, resp. are irrelevant. The errors shown for the high energy data refer to statistical errors only, systematical errors are typically ± 1 unit.

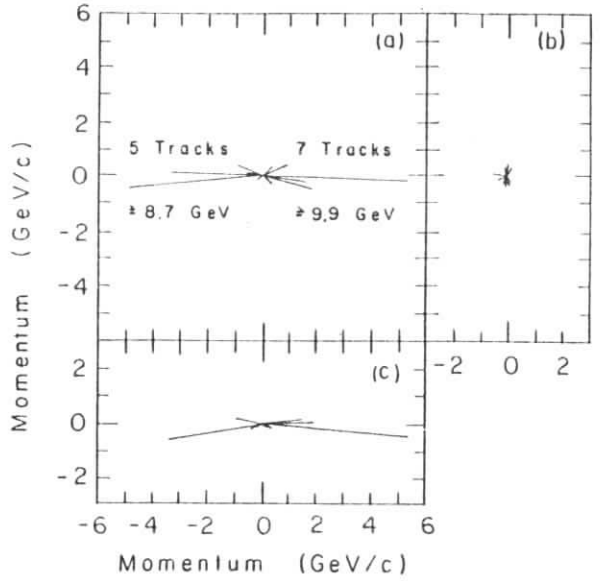

Fig. 2.3

Momentum space representation of a typical two jet event[27], shown in three orthogonal projections.

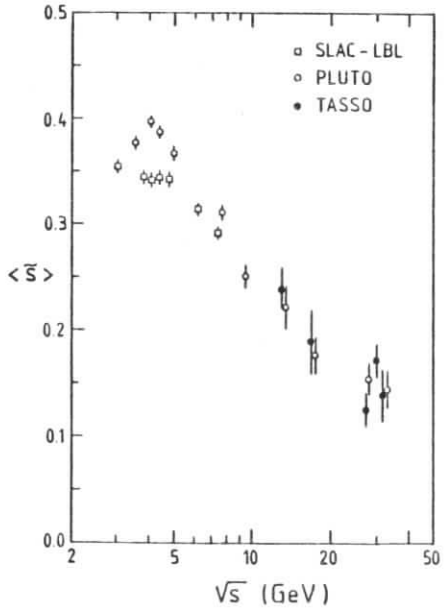

Fig. 2.4

Mean sphericity as a function of √s. Data from refs. 33,24,34.

which is equivalent to an increase of the mean hadron momenta with s, one expects that the final state particles form to jets around the directions of the two quarks.

2.1 Evidence for jets

Various approaches are possible to prove the two jet structure of the hadronic final state. At very high energies, the mean momentum parallel to the jet axis should be large compared to the transverse momentum for typical fragments, and one may hope to "see" a jet structure simply by inspection of the events. This is in fact true at PETRA energies, as can be seen from fig. 2.3.

However, for further investigations it is necessary to have a quantitative measure for the jet-ness of hadronic final states. This can be achieved by two different methods. First, a number measuring the jet-ness can be compiled using the four momenta of all produced (or, as a first approximation, of all detected) particles[28-31]. Secondly, one can study inclusive multiparticle correlations. One of the most commonly used, and experimentally convenient quantities of the first type is the sphericity $\tilde{S}$[32]

$$\tilde{S} = \frac{3}{2} \min \frac{\Sigma p_{\perp i}^2}{\Sigma \bar{p}_i^2} \qquad (2.7)$$

$p_{\perp i}$ is the transverse momentum of the i-th particle with respect to an axis choosen to minimize $\tilde{S}$.

The expected behaviour of $\tilde{S}$ is as follows: at low energies and multiplicities, momentum conservation enforces the produced particles to move back to back, and $\tilde{S}$ will be small. At higher energies, phase space models predict the particle distribution to be more and more spherical, and $\tilde{S}$ rises with energy to the asymptotic value 1. In contrast, jet models with limited transverse momentum with respect to the jet- or sphericity axis predict asymptotically

$$\tilde{S} = \frac{3}{2} \frac{\langle p_\perp^2 \rangle}{\langle \bar{p}^2 \rangle} \sim \left(\frac{\langle n \rangle}{\sqrt{s}}\right)^2 \langle p_\perp^2 \rangle \qquad (2.8)$$

With increasing energy, $\tilde{S}$ increases until $\langle \bar{p}^2 \rangle \gg \langle p_\perp^2 \rangle$, and than decreases according to eqn (2.8). First evidence for a jet structure, seen as a decrease of $\tilde{S}$ as the energy increases, came from the SLAC-LBL magnetic detector at SPEAR, at cms energies above 5 GeV.[5] Today's knowledge on $\tilde{S}$ is summarized in fig. (2.4). Data clearly favors the jet like production of particles. The decrease of $\tilde{S}$ is less rapid than predicted by eqn. (2.8). There are two reasons for this behaviour: first eqn. (2.8) is only valid if the cms energy is well above all thresholds. At present energies, this is clearly not füllfilled (fig. 2.1). Second, at high energies radiative corrections tend to broaden the jets. This last topic will be discussed later in this chapter, and in chapter 5.

More recently, other test quantities besides sphericity have been proposed[29-31], with the aim to study properties of the parton state immediately after the hard production process, and to integrate over those details of the final state, which are specific for the last fragmentation steps at low momentum transfers. These quantities try to overcome one of the great problems of sphericity: due to the quadratic terms in $p_\perp$ and $\bar{p}$ $\tilde{S}$ is not clustering invariant[31], or, in the language of QCD, it is not infrared save. This means that $\tilde{S}$ takes different values, when evaluated using the final state π^0's of an event, resp. using the γ rays after the decay of the π's.

Various quantities have been proposed which do not suffer from this drawback, like thrust [30]

$$T = 2 \max \frac{\tilde{\Sigma} p_{\parallel i}}{\Sigma |\bar{p}_i|} \qquad (2.9)$$

($\tilde{\Sigma}$ means that the summation is extended over particles having $p_\parallel = \bar{p} \cdot \bar{e} > 0$; $\bar{e}$ is a unit vector choosen to maximize thrust), spherocity[29]

$$\hat{S} = \left(\frac{4}{\pi}\right)^2 \min \left(\frac{\Sigma p_{\perp i}}{\Sigma |\bar{p}_i|}\right)^2 \qquad (2.10)$$

or generalisations of sphericity[35]

$$\hat{S}_h = \left(\frac{4}{\pi}\right)^h \min \left(\frac{\Sigma p_{\perp i}}{\Sigma |\bar{p}_i|}\right)^h \qquad (2.11)$$

The basic philosophy of this quantities is to use linear sums of momenta. As in the high energy limit the decay products of resonances tend to have parallel momenta, quantities based on linear sums are rather insensitive to resonance decays resp. to infrared divergencies due to bremsstrahlung effects. Modifications like eqn (2.11) give different weight to tails of the $p_\perp$ distribution.

Further clustering invariant quantities are based on the energy flow per solid angle,[36] like

$$\varepsilon = \frac{2}{\sqrt{s}} \max \int_{\cos\theta_0}^{1} \frac{d\varepsilon}{d\cos\theta} d\cos\theta \qquad (2.12)$$

with $\cos\theta = \bar{p}_i \cdot \bar{e} / |\bar{p}_i|$. The axis $\bar{e}$ is chosen to maximize the energy ε. Quantities similar to (2.12) had already been introduced in studies of jets produced in normal hadron-hadron interactions [37,38]. At present energies, however, even these infrared safe quantities are considerably influenced by hadronisation effects [31]. Therefore, and to avoid confusion, we will try to stick to the 'standard' jet measures sphericity and thrust. A rough idea of the quality of reconstructing the jet axis is given by fig. 2.5; at $\sqrt{s}$ =10 GeV the mean angle between the axis found by minimizing sphericity resp. maximizing thrust is of the order of 15^o.

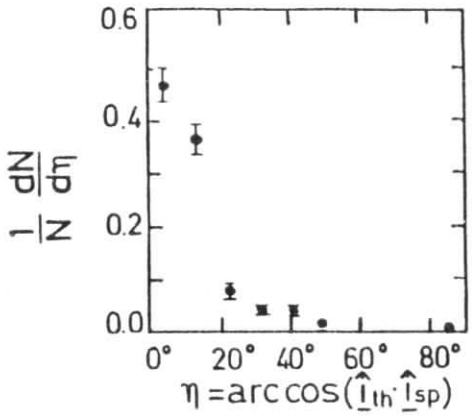

Fig. 2.5
Distribution of the angle η between the thrust and the sphericity axes at 9.4 GeV from PLUTO[40].

Finally, another test quantity proposed recently [39] is worth to be mentioned: since there is no natural axis defined for final states in e^+e^- annihilations, it seems necessary to have a set of observables characterizing the shape of the event without refering to a specific axis to be optimized. Such a quantity is e.g. given by

$$H_l = \frac{(4\pi)}{2l+1} \sum_{m=-1}^{+1} \left| \sum_i Y_l^m(\Omega_i) \frac{|\bar{p}_i|}{\sqrt{s}} \right|^2 \qquad (2.13)$$

where the inner sum runs over all final state particles and Y_l^m are the usual spherical harmonics. A coordinate system has to be choosen to evaluate H_l, but the values of H_l are independent of this choise. Energy-momentum conservation requires

$$H_o = 1 \; ; \quad H_1 = 0 \qquad (2.14)$$

H_2, H_3 ... describe the event configuration.

Besides these exclusive jet measures, information on a jet like structure of the final state can be obtained from inclusive spectra resp. correlations.

Fig. 2.6 shows the mean momentum parallel ($p_\parallel$) and transverse ($p_\perp$) with respect to the jet axis found by maximizing thrust. As expected for jets, the mean transverse momentum is roughly independent of the jet energy, and of the same order of magnitude as observed in hadron-hadron interactions. The numerical values should be taken with same care, however, since they depend on the method used to define the jet axis. In contrast to the mean transverse momentum, the mean longitidinal momentum increases continously with energy. Of course due to the selection of the jet axis, $\langle p_\parallel \rangle$ will always be slightly larger than $\langle p_\perp \rangle$. This selection bias should be strongest at low energies, or multiplicities. The difference between $\langle p_\parallel \rangle$ and $\langle p_\perp \rangle$, which increases with energy, is a clear signature for jets. The predominance of jet like final states even at moderate energies ($\sqrt{s}$ = 9.4 GeV) is most drastically demonstrated in fig. 2.7, where the distribution of $x_\parallel = 2\ p_\parallel/\sqrt{s}$ and of $x_\perp = 2\ p_\perp/\sqrt{s}$ is shown.

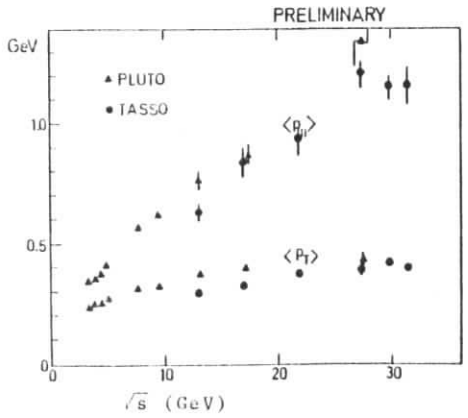

Fig. 2.6
Mean momentum components parallel and perpendicular to the jet axis defined by thrust[24,34].

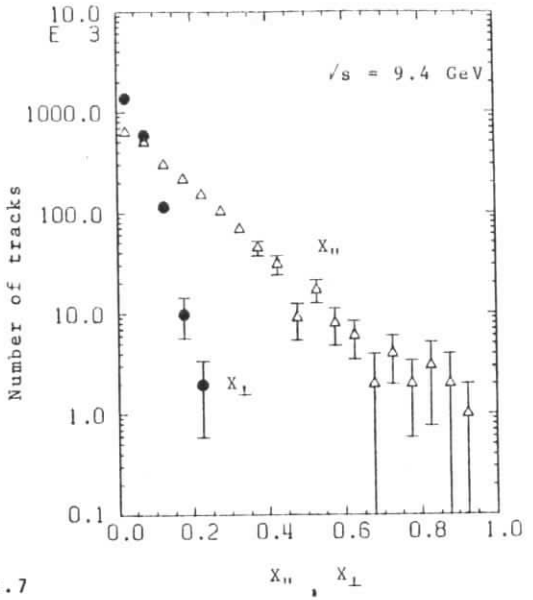

Fig. 2.7
Comparison of the $x_\parallel$ and $x_\perp$ distributions for charged tracks (PLUTO data at $\sqrt{s}$ = 9.4 GeV)[41]

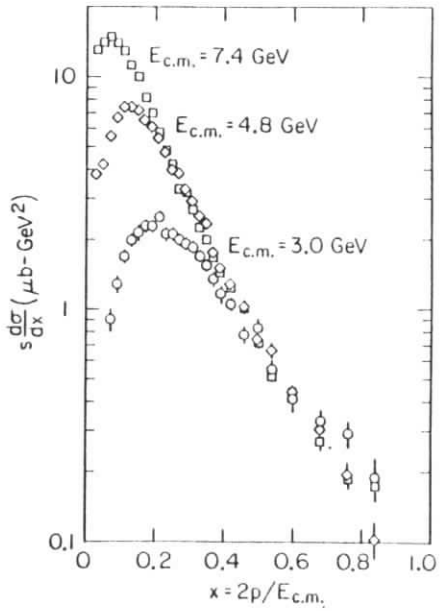

Fig. 2.8
Inclusive cross section sdσ/dx vs.s. Data from the SLAC-LBL detector[44]

2.2 Inclusive distributions

We start with a brief description of the formalism for inclusive production [42,43]

$$e^+e^- \to h + x \quad .$$

The hadron h is characterized by its mass m and its four momentum $p = (E,\vec{p})$.

The virtual photon, as seen in the rest system of h, has transverse and longitudinal polarization components. As a consequence the cross section for h production is described by two independent structure functions when summing over the polarisation states of h, e^+ and e^-. Defining these structure functions in close analogy to those used in deep inelastic scattering one obtains (in the nomenclature used in ref. 42, F_1 and F_2 are negative for $0 \le x \le 1$)

$$\frac{d^2\sigma}{dx_R d\Omega} = \frac{\alpha^2}{s} x_R \left(-F_1^h + \frac{1}{4} x_R F_2^h \sin^2\theta\right) \qquad (2.15)$$

with $x_R = 2E/\sqrt{s}$. The structure functions F_1^h and F_2^h depend on E, s, and on the type of h. At high energies, where m is negligible, the dimensionless structure functions must depend only on a dimensionless combination of E and s, since the theory contains no further mass scale. F_1 and F_2 should therefore scale in x_R. Integrated over Ω, one gets

$$s \frac{d\sigma}{dx_R} \underset{E,\, s \gg m}{=} 4\pi\alpha^2 x_R \left(-F_1^h(x_R) + \frac{1}{6} x_R F_2^h(x_R)\right) \qquad (2.16)$$

In the limit $E \gg m$, x_R can be replaced by $x = 2|\vec{p}|/\sqrt{s}$ in eqn (2.16).

Experimental results for $d\sigma/dx$ are shown in figs. 2.8 and 2.9 for the energy range $3.0 \le \sqrt{s} \le 7.4$ and $5.0 \le \sqrt{s} \le 31.6$ GeV respectivly; in the low energy region data from the SLAC-LBL [44] detector has been chosen as a representative sample, the high energy results come from the TASSO detector at PETRA [24]. Except the threshold region $x = O(m/\sqrt{s})$, and eventually except the very lowest energy, all spectra scale in x within the accuracy of the measurements.

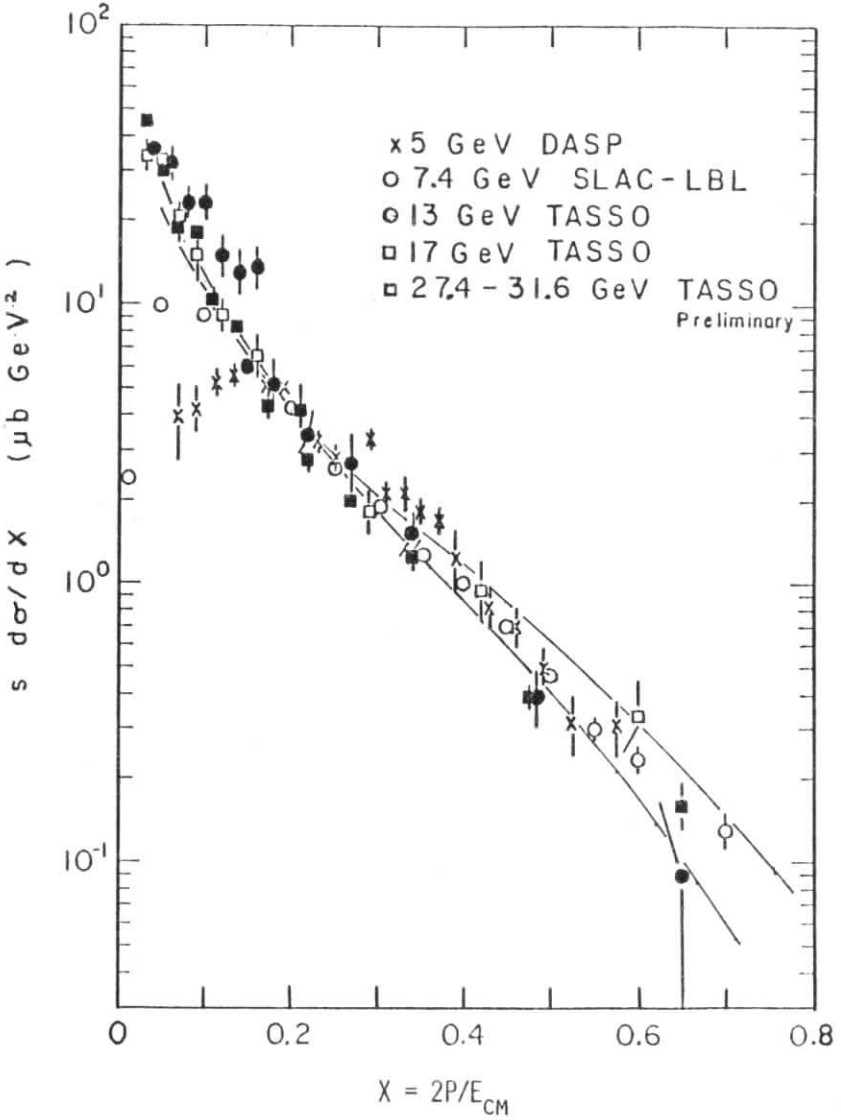

Fig. 2.9
Inclusive cross section $s d\sigma/dx$ from DASP [45], SLAC-LBL [44], and TASSO [24]. The curves $\frac{1}{x}(1-x)^2$ and $\frac{1}{x}(1-x)^3$ shown for comparison are normalized at x = 0.2.

The formalism of deep inelastic processes suggests further, that for particle production via spin 1/2 partons F_1 and F_2 are related

$$F_1^h(x) = \frac{1}{2} \times F_2^h(x) \qquad (2.17)$$

and predicts their shape in the limit of very high energies and for x close to 1

$$|F_2(x)| \underset{x \to 1}{=} (1-x)^n \qquad (2.18)$$

Fig. 2.9 shows that eqn. (2.18) gives a reasonable description of the high energy data for $0.2 \leq x \leq 0.7$ with n between 2 and 3. Actually, to account for the roughly logarithmic rise of the mean multiplicity with $\sqrt{s}$, eqn. (2.18) has been completed to give

$$s \frac{d\sigma}{dx} \sim \frac{1}{x}(1-x)^n \qquad (2.19)$$

Eqn. (2.15) furthermore makes definite predictions for the dependence of $d^2\sigma/dx d\Omega$ on the polar angle θ. In the scaling limit $x >> m_h/\sqrt{s}$, one gets for hadron production via spin 1/2 quarks, using eqn (2.17)

$$\frac{d\sigma}{d\Omega} \sim 1 + \cos^2\theta \qquad (2.20)$$

whereas for spin o quarks

$$F_1(E,s) = 0 \qquad (2.21)$$

and

$$\frac{d\sigma}{d\Omega} \sim \sin^2\theta$$

The usual way to present experimental results on angular distributions is to fit the data by

$$\frac{d\sigma}{d\Omega} \sim 1 + a \cos^2\theta \qquad (2.22)$$

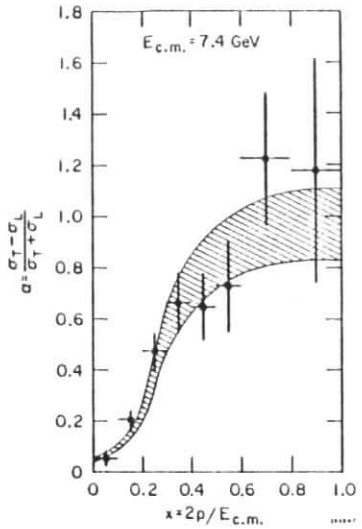

Fig. 2.10
Observed inclusive a vs. x of the particles in hadronic events at $\sqrt{s} = 7.4$ GeV.[33] The prediction of a jet model using $a_{quark} = 1$ is represented by the shaded band.

Fig. 2.10 shows a as a function of x measured at $\sqrt{s} = 7.4$ GeV by the SLAC-LBL collaboration. As expected, a is compatible with 1 for fast ($|\vec{p}| >> m$) particles. At low x, a drops to 0 because those particles carry a small fraction of the initial quarks momentum; their momenta are determined by the final stage of hadronisation and therefore are distributed isotropically. Alternativly, the direction of the primary source of a jet can be reconstructed e.g. by the thrust axis. Fig. 2.11 shows the distribution of the thrust axis as measured at $\sqrt{s} = 7.7$, 9.4, and 30 GeV. All are in good agreement with $1+\cos^2\theta$, although the statistics is too low to enable a determination of a. Figs. 2.10 and 2.11 support the picture of hadron production by quark fragmentation. They show, that the virtual photon does not couple directly to mesons of integer spin, which dominate the final state. Instead there must be an intermediate spin 1/2 particle!

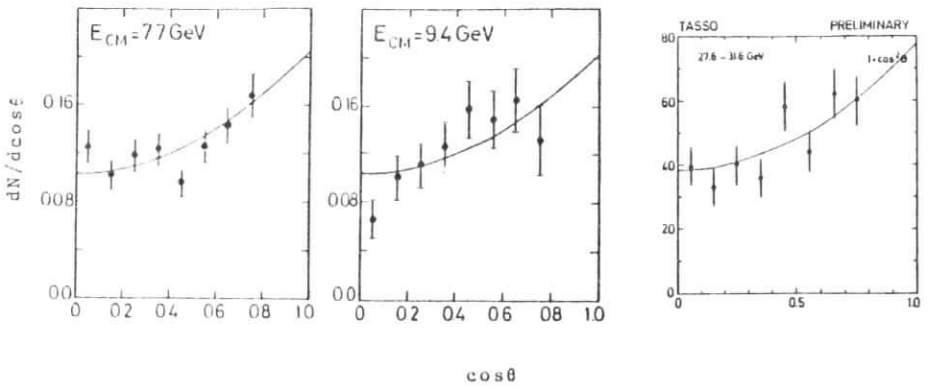

Fig. 2.11
Angular distribution of the jet axis at $\sqrt{s}$ = 7.7, 9.4 [40] and 30 GeV.[24] The curves represent the function $1+\cos^2\theta$ normalized to the data.

For further studies, and to enable a comparison with the jets observed in hadron-hadron collisions, it is convenient to use quantities referring to the jet axis, like the rapidity $y = 1/2 * \ln((E+p_\parallel)/(E-p_\parallel))$, or the transverse momentum $p_\perp$. These quantities are, of course, somewhat sensitive to the way the jet axis is defined, the influence being strongest for very slow ($|\vec{p}|$ = 0 (300 MeV)) and very fast ($x \to 1$) particles.

Fig. 2.12 shows the rapidity distribution per event, $(1/\sigma)(d\sigma/dy)$, as measured by the SLAC-LBL[22] and TASSO[24] detectors, with respect to the sphericity (SLAC-LBL) and thrust axis (TASSO). For the SLAC-LBL data, a fast particle ($x > .3$) in one of the jets is requested in order to allow a reliable determination of a jet axis already at energies as low as 5 GeV. The density shown is twice the density observed in the hemisphere opposite to the fast particle. As shown in ref. 22, this method introduces nearly no bias.

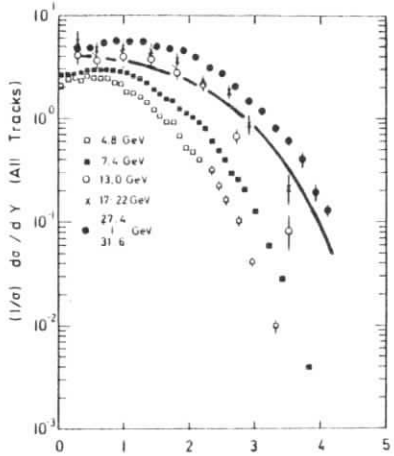

Fig. 2.12
Rapidity distributions for charged particles assuming $m = m_\pi$, measured at $\sqrt{s}$ = 4.8, 7.4[22] and at 13, 17, 27.6-31.6 GeV[24]. The full line shows the distribution of secondaries in inelastic pp interactions at $\sqrt{s}$ = 31 GeV[46].

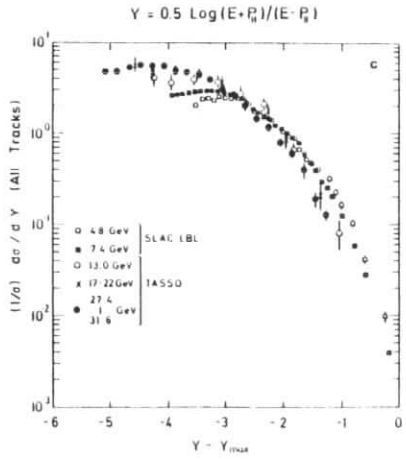

Fig. 2.13
Rapidity distributions (same as in fig. 2.12) plotted vs $y-y_{max} = y-\frac{1}{2}\ln(s/m_\pi^2)$.

The rapidity distributions show the following features

- the length of the rapidity interval populated increases with ln s
- at high energies, the rapidity distribution develops a plateau around y = 0
- the height of the plateau seems to increase slightly with increasing cms energy.

For comparison, the rapidity distribution observed for mesons produced in proton-proton interactions at $\sqrt{s}$ = 31 GeV[46] is included in fig. 2.12, it is in surprisingly good agreement with the high energy TASSO data, taking into account that in proton-proton interactions a sizeable fraction of energy is carried off by leading nucleons so that as far as meson production is concerned, the proton-proton data at $\sqrt{s}$ = 31 GeV should be compared with e^+e^- annihilations at $\sqrt{s}$= 15···20 GeV. There are indications that the height of the plateau is slightly larger for the e^+e^- -data, furthermore the distributions seem to develop a hole at y = 0. At least the second effect is probably due to biases introduced by the definition of the jet axis.

To handle the rapidity distribution at high rapidities, the principle of limiting fragmentation [2,47] has proven to be a useful concept in hadron-hadron interactions. It states that the rapidity distribution is composed of a projectile resp. target fragmentation region of a length of 2···3 units, and of a plateau region joining the two fragmentation regions. As the energy increases, the fragmentation region is boosted to higher rapidities without changing its shape, and the length of the plateau increases; the properties of the plateau region are independent of the projectile resp. target particle.

Fig.2.13 demonstrates that these ideas seem to work as well for quark jets: the rapidity distributions at various cms energies roughly coincide when plotted as a function of $y-y_{max}$.

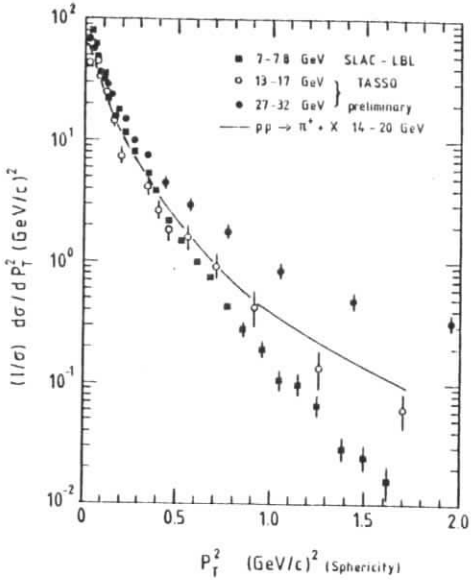

Fig. 2.14
Distribution of transverse momenta with respect to the sphericity axis.[22,24] The SLAC-LBL and the proton-proton data are normalized arbitrarily.

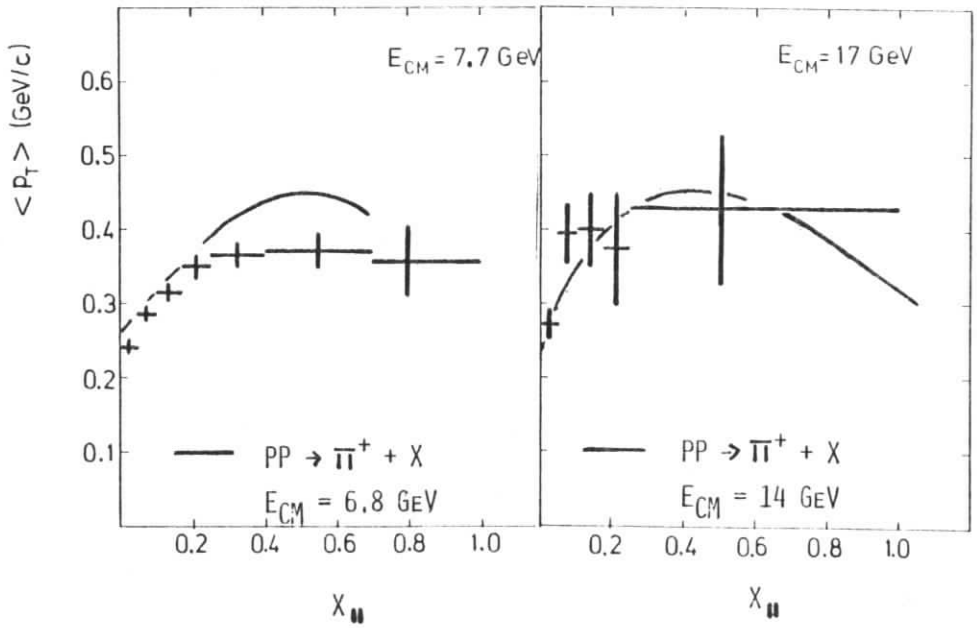

Fig. 2.15
Seagull plot $\langle p_\perp \rangle$ vs x_{II} from charged tracks,[41] compared to data from proton-proton interactions at $\sqrt{s}$ = 6.8 and 14 GeV.[49,50]

Fig. 2.14 shows the distribution of transverse momenta at $\sqrt{s} = 7$[22], $\sqrt{s} = 13$-17 and $\sqrt{s} = 30$ GeV.[24] As a reference, the $p_\perp$ distribution of pions produced in proton-proton collisions at $\sqrt{s} = 14$-20 GeV is shown.[48] Taking into account that, at the lowest energy, transverse momenta above 1 GeV/c are damped due to energy and momentum conservation, all data in the range $\sqrt{s} = 7$ GeV to $\sqrt{s} = 20$ GeV agree. Again there is no severe difference between hadrons produced in proton-proton and in electron-positron collisions, respectivly. However, the $p_\perp$ distribution at $\sqrt{s} = 30$ GeV develops a strong tail towards higher $p_\perp$'s, starting at $p_\perp^2 = 0.5$ GeV^2. There is no correspondent feature observed in proton-proton interactions; in the $p_\perp$ range studied here the slope of the $p_\perp$ distribution is nearly independent of $\sqrt{s}$ for $\sqrt{s} > 15$ GeV. We shall return to this phenomena in section 2.4.

The dependence of the mean transverse momentum on $x_\parallel$ is shown in fig. 2.15 for two energies. Note that the shape of these curve is sensitive to the way the jet axis is defined, systematic changes at low and high $x_\parallel$ may be as large as 20···30%. Like the corresponding proton-proton data, the distributions show a pronouced seagull effect at $x_\parallel = 0$.

2.3 Flavor composition of the final state

In the preceeding sections we have shown that the hadronic final states in e^+e^- annihilations are dominated by two jet systems, which are in many respects similar to the jets observed in inelastic hadron-hadron interactions. Let us now turn to the flavor composition of these jets. Unfortunately, the bulk of data on particle ratios in e^+e^- annihilations is concentrated at $\sqrt{s}$ from 3 to 6 GeV, where effects due to the charm threshold dominate, and where heavy particle cross sections will be far from their scaling limit.
The main questions to be investigated are
- which particles dominate the final state, and how is the cms energy distributed among the various species

- do particle ratios conserve isospin symmetry
- as the photon couples proportional to the quark charge squared, SU(n) flavor symmetry should be violated as far as the absolute magnitude of cross sections is concerned. However based on SU (n) one expects the slope of ($d\sigma/dx$) at large x to be similar for all flavors.

Fig. 2.16 shows $d\sigma/d|\vec{p}|$ at $\sqrt{s}$ from 4 to 5.2 GeV for pions, kaons, and protons[45]. Contributions from τ decays are not subtracted, but they are small. Obviously, pion production dominates.

Because of charge conjugation, particles and their antiparticles are produced at identical rates. Isospin symmetry predicts further

$$\sigma_{\pi^0} = \frac{1}{2}(\sigma_{\pi^+} + \sigma_{\pi^-}) \qquad (2.23)$$

$$\sigma_{K^+,K^-} = \sigma_{K^0,\bar{K}^0} \qquad (2.24)$$

etc. In fig. 2.17 the inclusive π^0 cross section is compared to the $\pi^\pm$ cross sections, at $4.9 \leq \sqrt{s} \leq 7.4$ GeV.[53]

Within the error limits, data agree with eqn (2.23).

Fig. 2.18 shows the ratio of the neutral and charged kaon cross sections as a function of $\sqrt{s}$. Again the result is in good agreement with eqn (2.24).

This holds as well for the inclusive production of neutral and charged D mesons, respectivly (fig. 2.19).

To study the flavor dependence of structure functions, $d\sigma/d|\vec{p}|$ (fig. 2.16) is not well suited because obviously phase space effects dominate. Expressed in terms of Lorentz invariant cross sections $Ed^3\sigma/dp^3$, the pion, kaon and proton yields are nearly identical (fig. 2.20)[45]. The interpretation of this observation is ambigious: the conclusion that the structure functions F^π, F^k, and F^p are identical seems to conflict with the naive quark model with

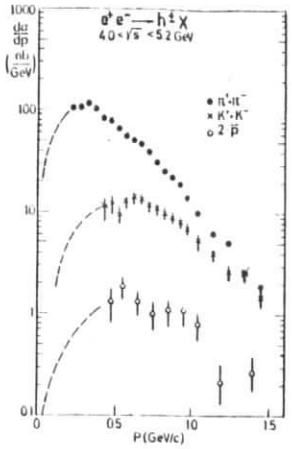

Fig. 2.16
Differential cross sections $d\sigma/d|\bar{p}|$ for $\pi^\pm$, $K^\pm$, and $\bar{p}$ production, averaged over cms energies from 4 to 5.2 GeV.[45]

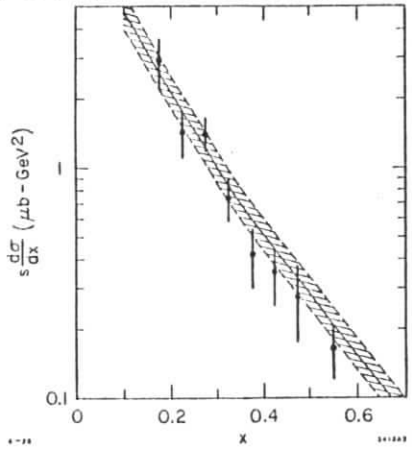

Fig. 2.17
Inclusive π^0 cross section $s \cdot d\sigma/dx$ from the LGW experiment.[53] The dashed band shows 1/2 of the sum of π^+ and π^- cross sections from MARK I (at E_{CM} = 5 GeV).

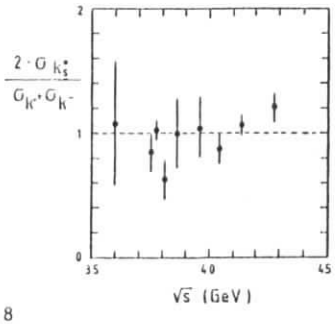

Fig. 2.18
Ratio of neutral to charged kaon production vs $\sqrt{s}$ [54]

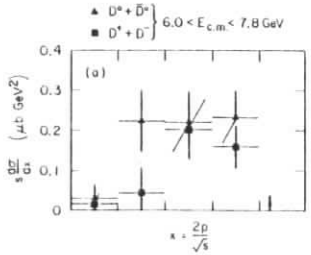

Fig. 2.19
Cross section for inclusive production of charged and neutral D mesons as a function of x.[55]

charge +2/3 u quarks and charge -1/3 d quarks. It is further hard to imagine that asymptotically mesons and baryons are produced at the same rates. It seems more natural to assume that at these energies the particle emission is governed by statistical or thermodynamical laws[51] rather than by parton dynamics. In fact the observed spectra correspond to the thermal emission of a source having a temperature close to the pion mass[51]. Furthermore, the kaon rate in fig. 2.20 is slightly enhanced due to decay of charm-anticharm resonant structures. These arguments are supported by fig. 2.21: at $\sqrt{s}$ from 6 to 8 GeV the inclusive K^0 cross section lies well below the pion cross section[55,56] (for z > 0.2, we use

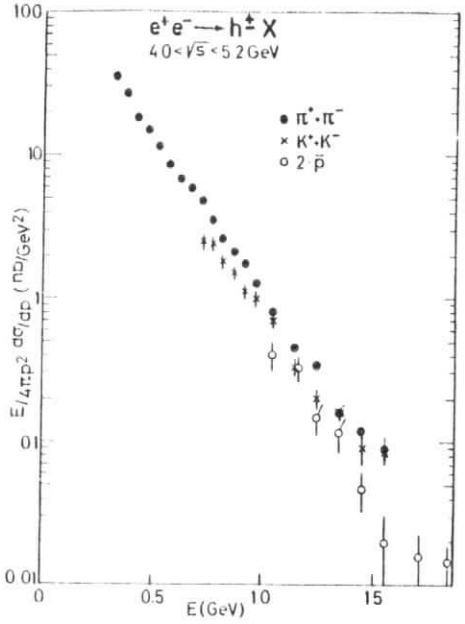

Fig. 2.20
Invariant cross section $Ed^3\sigma/dp^3$ as a function of particle energy. Same data as in fig. 2.16.

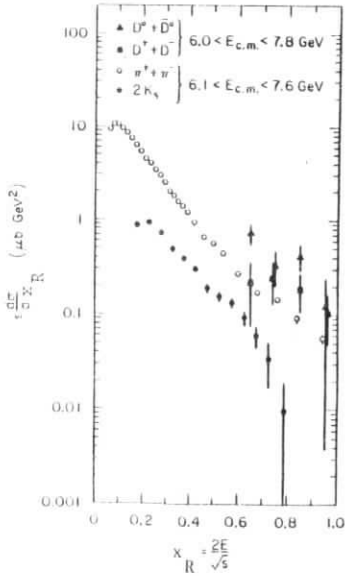

Fig. 2.21
Inclusive spectra for charged and neutral D-mesons and for charged π-mesons and K^0_s.[55,56]

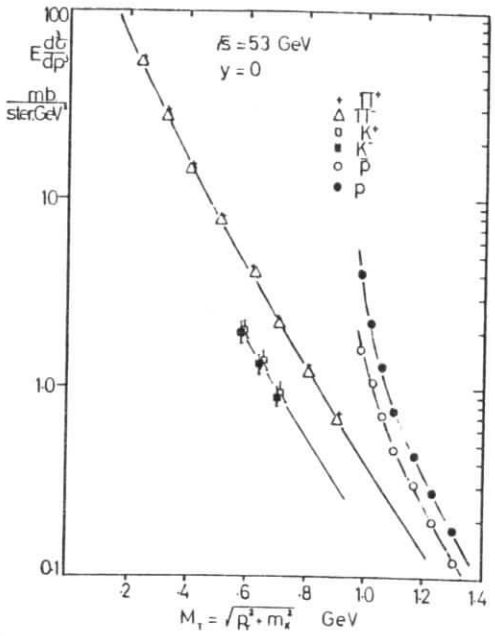

Fig. 2.22
Invariant cross section $Ed^3\sigma/dp^3$ at $y_{cms} = 0$ as a function of transverse energy for proton-proton interactions at $\sqrt{s} = 53$ GeV.[52]

$$\left(\frac{d\sigma}{dx_R}\right)_\pi \Big/ \left(\frac{d\sigma}{dx_R}\right)_k \approx \left(E\frac{d^3\sigma}{dp^3}\right)_\pi \Big/ \left(E\frac{d^3\sigma}{dp^3}\right)_k \quad).$$

Taking into account that the pion data in fig. 2.21 is slightly smeared out at x ≈ 1 due to the finite momentum resolution, the shape of the pion and kaon cross sections roughly agree.

Again it is interesting to note the similarity between fig. 2.20 and its correspondence obtained in proton-proton interactions: in fig. 2.22 the particle yields observed at the ISR at $\sqrt{s} = 52$ GeV are shown as a function of the transverse energy $m_\perp = \sqrt{p_\perp^2 + m^2}$ (in hadron-hadron interactions longitudinal momenta are not damped exponentially, therefore $m_\perp$ is the quantity relevant for comparison[51]). Within factors of 2, the various cross sections coincide here as well!

Fig. 2.21 further contains the cross section for D meson production [55]. At high x_R, the D cross section is larger than the pion yield. However, this is a pure threshold effect; the D threshold at these energies is $x_R = 0.5$. Since about 25% of all quark-antiquark events contain a pair of D mesons, the cross section at large x_R is strongly enhanced. For the same reason, no serious statements on the shape of the D spectra are possible, except perhaps that they fall with increasing x_R. A fit in terms of eqn (2.19) gives

$$\left(\frac{d\sigma}{dx_R}\right)_D = \frac{1}{x_R}(1-x_R)^{0.42\ ^{+0.28}_{-0.23}}$$

To conclude : the particle ratios observed in e^+e^- annihilations are in good agreement with isospin symmetry. The assumption of a flavor independent shape of the structure functions is at least not contradicted by present data.

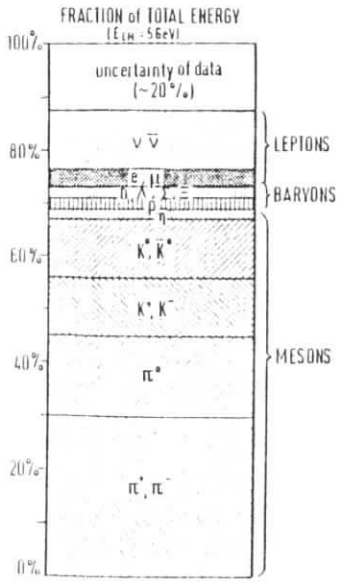

Fig. 2.23 Fraction of total energy carried away by different particle species (at E_{CM}= 5 GeV). (from ref. 41)

Finally, fig. 2.23 summarizes how the total energy is shared among particles at $\sqrt{s}$ = 5 GeV, including τ decays. Fig. 2.23 has been taken from ref. 41, in addition to the data discussed above information on K^o [57], η [58], lepton [59-62] and baryon [63,64] production has been used in the compilation.

2.4 Scaling violations at high energies

In section 2.2 we found that in the energy range $5 \lesssim \sqrt{s} \lesssim 17$ GeV the inclusive particle distributions in jets scale in x_R and have a fixed, limited $p_\perp$ with respect to the jet axis, the deviations from universal distributions at low x_R and at large $p_\perp$ being induced by phase space effects. At $\sqrt{s}$ = 30 GeV, however, the $p_\perp$ distribution changes qualitativly, it develops a tail towards larger $p_\perp$, which must have a dynamical origin (fig. 2.14). In the following we shall investigate this effect more in detail. For the discussion, we will mainly use results from TASSO [24]; similar results have been reported from the PLUTO [65] and MARK-J [66] collaborations. The widening of the $p_\perp$ distribution can have its origin in

- the production of a new quark flavor
- the $p_\perp$ distribution for quark fragmentation is energy dependent, the average $p_\perp$ grows as s increases
- as in hadron-hadron interactions [6-11], single hard scattering processes dominate the cross section at large $p_\perp$ and s. Candidates for such processes are e.g. the emission of hard gluon bremsstrahlung under large angles by the primary quark [69,70] or the production of meson resonances with large transverse momenta by constituent interchange mechanisms [71].

The first possibility can be immediately ruled out by other data [24]. The other two possibilities can be discriminated by examining the phase space structure of the events: an increase of the fragmentation-$p_\perp$ with energy still yields particle distributions which are symmetric in azimuth with respect to the

jet axis. Hard parton processes produce a third jet, either by gluon fragmentation in quark-gluon models or by the decay of the excited meson in the CIM model[71]. In most cases this jet will be more or less aligned with one of the initial jets, and the cross section of the cylinder will be deformed into an ellipsoid; sometimes, a planar three jet structure will be recognizable.

In search for planar events, the TASSO Collaboration assigned an event plane in such a way as to minimize the sum of the momentum components squared out of this plane[67]. Obviously, the jet axis as defined via the minimum sphericity is contained in that plane. Fig. 2.24 shows the mean transverse momentum squared in the event plane, $\langle p_\perp^2 \rangle_{IN}$, and normal to the event plane $\langle p_\perp^2 \rangle_{OUT}$ per event at $\sqrt{s}$ from 13 to 17 and at $\sqrt{s}$ around 30 GeV.[24] By definition of the event plane, $\langle p_\perp^2 \rangle_{IN}$ is larger than $\langle p_\perp^2 \rangle_{OUT}$. The comparison of the low- and high energy data proves that this effect is not able to explain the tail at $\langle p_\perp^2 \rangle_{IN}$ in the 30 GeV data. In fact, models with a fragmentation symmetrically in azimuth are not able to describe this tail consistenly. This observation is very much in favor of the last hypothesis. In fact, events sitting in the tail of the $\langle p_\perp^2 \rangle_{IN}$ distribution show a three jet signature; fig. 2.25 gives a "typical" example.

The planar events were analyzed as three jet events and the average $p_\perp$ per jet was measured. Fig. 2.26 shows the observed $\langle p_\perp \rangle$ distribution. The average $p_\perp$ value is 0.3 GeV. Hence the planar events which lead to large $\langle p_\perp \rangle$values when treated as two jet events, have the canonical $\langle p_\perp \rangle$value of ~ 0.3 GeV when analyzed as three jet events.

Does the hypothesis of a hard bremsstrahlung process explain the sudden onset of the effect when going from s = 17 to s = 30? The probability for emission of a hard field quantum is given by[68]

$$w = \text{const.} \frac{\alpha_S}{\pi} \ln\left(\frac{s}{\mu^2}\right) \qquad (2.24)$$

where α_S is the strong coupling constant and μ is a cut off

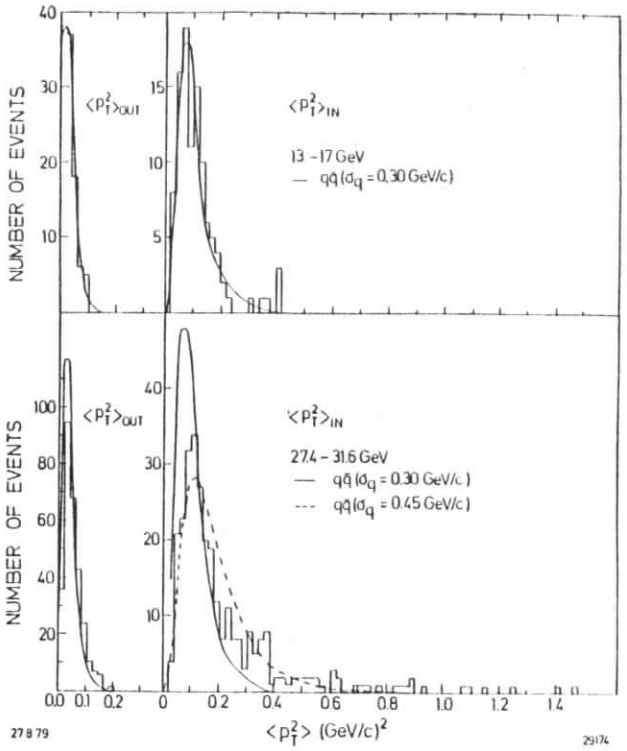

Fig. 2.24

Mean transverse momentum squared in and perpendicular to the event plane per event. The full and dotted lines are predictions of jet models using particle distributions symmetrically in azimuth.[24]

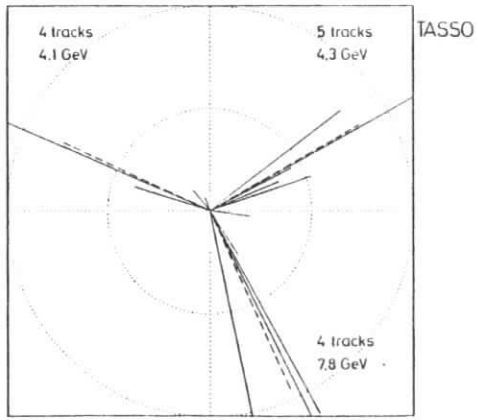

Fig. 2.25

A 3-jet event projected into the event plane.[24]

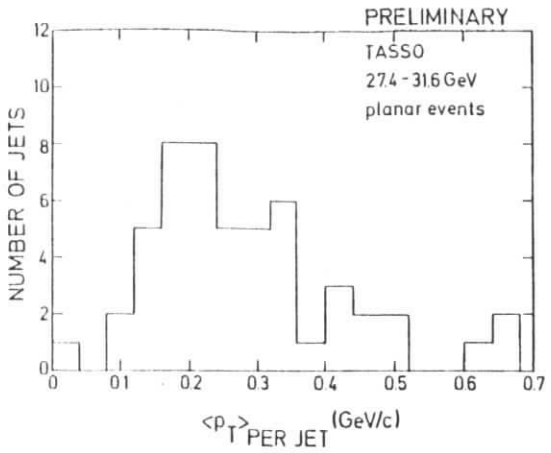

Fig. 2.26
Distribution of the average p_T per jet for noncollinear planar events analysed as three jet events.[24)]

parameter of the order 1 GeV. w varies rather slowly with energy. Two further circumstances are relevant, however: first, a third jet can be recognized as soon as the mean longitudinal momentum of fragments is larger than $\langle p_\perp \rangle$. Since $\langle p_n \rangle$ is roughly proportional to the jet energy, this criterion introduces a much faster variation in the fraction of events which can be identified as multijet events. Secondly, there are two competing mechanisms governing the energy loss of a fast quark: hard bremsstrahlung and soft hadronisation (although we shall see in chapter 5 that a strict distinction of the two mechanisms is not justified). Their relative importance depends on the ratio of the corresponding time scales. As we shall note in chapter 4, the fragmentation time of a jet is of the order

$$\tau_{\text{frag.}} \sim \frac{\sqrt{s}}{m_o^2} \qquad (2.25)$$

with m_o being a typical hadronic mass scale. On the other hand, the partial lifetime for emission of a quantum carrying a fraction z of the quarks momentum at an angle θ is given by[68)]

$$\tau_{\text{brems.}} \approx \frac{1}{\sqrt{s}\, z(1-z)\sin^2\theta/2} \qquad (2.26)$$

From eqn (2.25) and (2.26) follows, that the relative importance of hard processes increases proportional to s. This explains the fast transition from the hadronisation dominated regime to the region where hard interactions are obvious.

A unique identification of the hard process as gluon bremsstrahlung is not possible at the present quality of data; however the main features of data are consistent with this interpretation[72,73)].

A more detailed discussion on hard processes in jet fragmentation will follow in chapter 5.

3 Jets in longitudinal phase space models

As we have seen in the last chapter, the physics of jets at small energies, up to $\sqrt{s} \approx 10-20$ GeV, is dominated by phase space effects due to the nonzero transverse momenta and particle masses. To arrive at a quantitative description of the limitations imposed by pure four momentum conservation, and to separate jet dynamics from kinematics, it is useful first to study a simple phase space model for jet production.

This section is organized as follows. We shall present the uncorrelated jet model for e^+e^- annihilations, discuss the physical meaning of the parameters involved, and give the asymptotic behaviour of the model. Next scaling variables and the approach to the scaling limit will be discussed. In the remainder of the chapter, possible generalizations of the model are presented, as the inclusion of resonance production and the use of more sophisticated matrix elements. Finally, a model considering exact quantum statistics will be mentioned.

3.1 The uncorrelated jet model (UJM)

The fully exclusive decay probability of a virtual photon of the four momentum $Q = (\sqrt{s}, \bar{p})$ into N identical particles is in the UJM given by [75,76]

$$\Gamma_N \sim \prod_{i=1}^{N} \left(\frac{d^3 p_i}{E_i} f\,(p_{\parallel}^i, p_{\perp}^i) \right) \delta^4(\Sigma p_i - Q) \qquad (3.1)$$

, neglecting spins and photon polarization. $p_i = (E_i, \bar{p}_i)$ is the four momentum of the i-th secondary, which for simplicity will be assumed to be a chargeless pion. To get final state jets, the invariant momentum space element $d^3\bar{p}_i/E_i$ [77] is weighted with a matrix element depending on the longitudinal and transverse momenta with respect to the jet axis defined by a unit vector $\bar{e}$

$$p_{\parallel} = \bar{p} \cdot \bar{e} \; ; \quad p_{\perp} = |\bar{p} \times \bar{e}| \qquad (3.2)$$

As the n-particle matrix element factorizes into n independent probabilities, the model contains no dynamical correlations. In the following we shall adopt the simplest choice for f generating a transverse momentum cut off

$$f\,(p_{\parallel}, p_{\perp}) \sim \exp(-\lambda p_{\perp}) \qquad (3.3)$$

Such models have been discussed by many authors; we shall follow the presentation of ref. 78.

In terms of the transversely cut off momentum space volume (the grand partition function)

$$\Omega(\bar{e}, Q) = \sum_{N=2}^{\infty} \frac{\kappa^N}{N!}\, \Gamma_N \qquad (3.4)$$

the inclusive single particle spectrum in the photon rest frame, normalized to the total cross section σ, is given by

$$(E/\sigma)(d^3\sigma/dp^3) = \kappa \exp(-\lambda p_{\perp})\,\Omega(\bar{e}, Q-p)/\Omega(\bar{e}, Q) \qquad (3.5)$$

with the trival sum rules ($x_R = 2E/\sqrt{s}$)

$$\frac{1}{\sigma} \int dx_R dp_{\perp}^2 \frac{d^3\sigma}{dx_R dp_{\perp}^2} = \langle N \rangle \; ;$$

$$\frac{1}{\sigma} \int dx_R dp_{\perp}^2 \, x_R \frac{d^3\sigma}{dx_R dp_{\perp}^2} = 2 \qquad (3.6)$$

The physical significance of the parameters κ and λ is evident: λ^{-1} determines the transverse jet width and κ characterizes the multiplicity distribution, an increase in κ giving a higher weight to larger particle numbers.

Asymptotically, one has

$$\frac{E}{\sigma} \frac{d^3\sigma}{dp^3} = \frac{1}{\sigma} \frac{1}{\pi} \frac{d^2\sigma}{dy dp_{\perp}^2}$$

$$= \kappa \exp(-\lambda p_{\perp}) \qquad (3.7)$$

$S \to \infty$, y fixed

Consequently, the particle density per unit of rapidity is

$$\frac{1}{\sigma}\frac{d\sigma}{dy} \underset{\substack{S\to\infty \\ y \text{ fixed}}}{=} \frac{\kappa\pi}{\lambda^2} = \tilde{\kappa} \qquad (3.8)$$

leading to a mean multiplicity

$$\langle N\rangle \underset{S\to\infty}{=} \tilde{\kappa} \ln S \qquad (3.9)$$

Let us assume, for the moment being, that this asymptotic rapidity plateau is identical to the plateau observed in e^+e^- annihilations at the highest energies, resp. in pp interactions at ISR energies. The characteristic values of $\tilde{\kappa}$ and λ [79] may then be fixed to

$$\lambda = 6.2\ \text{GeV}^{-1}; \qquad \tilde{\kappa} = \frac{\kappa\pi}{\lambda^2} = \frac{3}{2}\frac{1}{\sigma}\left(\frac{d\sigma}{dy}\right)_{\text{charged}} = 3$$

The asymptotic behaviour of the inclusive x_R - distribution is given by eqs. (3.1) and (3.5) if we note that $\Omega(\bar{e},Q-p)$ is a function of the particles transverse mass $m_\perp$ and of the longitudinal missing mass M_L

$$M_L = \{(\sqrt{s} - E)^2 - (\bar{e}\bar{p})^2\}^{1/2}$$

$$= \sqrt{s}\ (1-x_R + \frac{m_\perp^2}{S})^{1/2} \qquad (3.10)$$

with the asymptotic limit

$$\Omega(\bar{e},Q-p) = \frac{M_L^{2\tilde{\kappa}-2}}{\ln(M_L/m_\perp)}(1+O(\ln^{-1}(M_L/m_\perp))) \qquad (3.11)$$

$$m_\perp << M_L, \sqrt{s}$$

For $1-x \gg m_\perp^2/s$ and large s, this amounts to scaling of

$$\frac{E}{\sigma}\frac{d^3\sigma}{dp^3} = \kappa e^{-\lambda p_\perp}(1-x_R)^{\tilde{\kappa}-1} \qquad (3.12)$$

in the photon rest system.

For $x_R^2 \gg m_\perp^2/s$, we have

$$\frac{1}{\sigma}\frac{d\sigma}{dx_R} = \frac{2\tilde{\kappa}}{x_R}(1-x_R)^{\tilde{\kappa}-1} = \frac{6}{x_R}(1-x_R)^2 \qquad (3.13)$$

To summarize, within the UJM we expect scaling in x_R at infinite energies, the cross section being power behaved in $(1-x_R)$.

3.2 The approach to scaling

The typical SPEAR- or DORIS-energies, where the bulk of e^+e^- data was produced, masses and transverse momenta are not a priori negligible. The approach to scaling will therefore be discussed in more detail again following ref. 78.

Obviously, the scaling limit of $d\sigma/dx_R$ is reached latest for x_R close to 0 and 1. At $x_R = 0$ scaling is violated because of threshold effects, in the vicinity of $x_R = 1$ the unobserved system has a low missing mass and hence $\Omega(\bar{e},Q-p)$ is not asymptotic. Consequently, scaling in $d\sigma/dx_R$ will be approached from below at low x_R and from above at high x_R. Besides the trivial scaling violation near the threshold

$$\frac{1}{\sigma}\frac{d\sigma}{dx_R} = \frac{\tilde{\kappa}}{2}\lambda^2 S\,(x_R^2 + \frac{4m^2}{S})^{1/2}(1+\cdots) \qquad (3.14)$$

the cross section can be estimated using a twofold asymptotic

expansion of $\Omega(\tilde{e},Q)$

$$\frac{1}{\sigma}\frac{d\sigma}{dx_R} = 2\tilde{\kappa}\,\frac{(1-x_R)^{\tilde{\kappa}-1}}{x_R}\,\frac{\ln(S/4m^2)}{\ln((S/4m^2)(1-x_R))}$$

$$*(1+O(\ln^{-1}(\frac{S}{4m^2}(1-x_R)))(1+O(\frac{1}{\lambda^2 x_R^2 S})) \qquad (3.15)$$

Scaling is thus expected to hold for

$$(\lambda^2 x_R^2 S)^{-1}\ ,\ \ln^{-1}((S/4m^2)\ (1-x_R)) << 1 \qquad (3.16)$$

Due to the slow convergence of the series, the "<<" should be taken seriously.

To study the approach to scaling quantitativly, it is more convenient to calculate $\Omega(\tilde{e},Q)$ by numerical integration.[78,80,81] The results for $(1/\sigma)\ (x_R d\sigma/dx_R)$ are compared in fig. 3.1 for $\sqrt{s}$ = 3.0, 3.8, 4.8 and 20 GeV with the asymptotic limit. Although there seems to be an early scaling already at $\sqrt{s}$ = 3$\cdots$ 5 GeV for x_R >0.2, the calculation shows that one is still far from the scaling limit, which is reached within O (10%) at $\sqrt{s}$ = 20 GeV for 0.05< x_R< 0.8.

Fig. 3.2 shows the height of the rapidity plateau at y = 0 as a function of $\sqrt{s}$. [82] At energies of $\sqrt{s}$ = 3$\cdots$10 GeV, the particle density is ~30% below the asymptotic value of eqn. 3.8; even at the highest energies available at present accelerators (ISR) the UJM predicts the plateau height not to be constant.

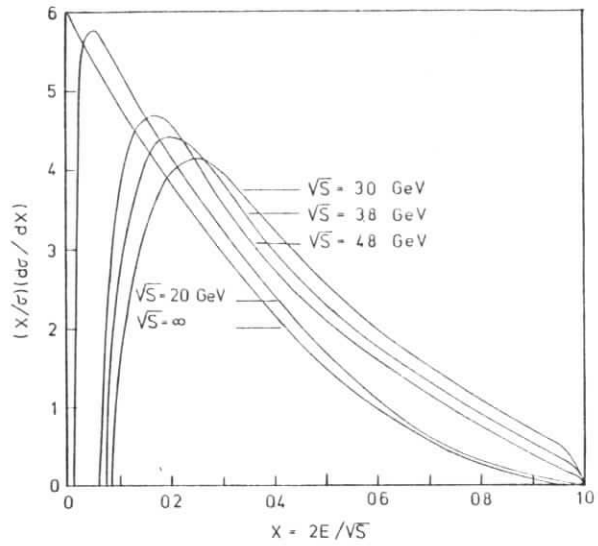

Fig. 3.1
The inclusive single particle spectra in the UJM for λ = 6.2 GeV^{-1}, $\tilde{\kappa}$ = 3. [78]

One further feature of inclusive spectra in the UJM is worth to be noted. Eqn. 3.7 suggests a factorisation of $E\,d^3\sigma/dp^3$ in terms of y and $p_\perp$. Due to the factor E in the invariant momentum space volume, this does not hold if one replaces y by other longitudinal variables as x or $m_{\prime\prime} = (m^2 + p_{\prime\prime}^2)^{1/2}$. This is clearly demonstrated in Fig. 3.3, where $\langle p_\perp \rangle$ is plotted versus $m_{\prime\prime}$.

The "seagull effect" is observed in e^+e^- annihilations [24] as well as in hadron-hadron interactions [50] and is often interpreted as a direct evidence for a parton structure of the produced particles [83-85], one should however be aware that part of the effect may be simple jet kinematics.

Besides these inclusive cross sections, some exclusive quantities like the total jet momentum or the invariant mass of a jet can be estimated in the UJM. Define one jet (in the sense of the parton model) as the collection of all those particles of an e^+e^- event, which have $p_{\prime\prime} > 0$ resp. $p_{\prime\prime} < 0$; the event is then composed of two opposite jets. The total longitudinal momentum carried by one jet is

$$P_{\parallel} = \sum_{i=1}^{N} p_{\parallel i} = \sum_{i=1}^{N} E_i - \frac{m_{\perp i}^2}{2E_i} = \frac{\sqrt{s}}{2} - \sum_{i=1}^{N} \frac{m_{\perp i}^2}{2E_i} \qquad (3.17)$$

or, averaged over many jets

$$\langle P_{\parallel} \rangle = \frac{\sqrt{s}}{2} - \langle m_{\perp}^2 \rangle \int_{\langle m_{\perp} \rangle}^{\sqrt{s}/2} \frac{1}{2E} \frac{1}{\sigma} \frac{d\sigma}{dE} \, dE$$

$$= \frac{\sqrt{s}}{2} - \frac{\langle m_{\perp}^2 \rangle}{\langle m_{\perp} \rangle} \cdot \frac{\tilde{\kappa}}{2} = \frac{\sqrt{s}}{2} - \tilde{\kappa} \langle m_{\perp} \rangle$$

$$= \frac{\sqrt{s}}{2} - 0 \ (1\,\mathrm{GeV}) \qquad (3.18)$$

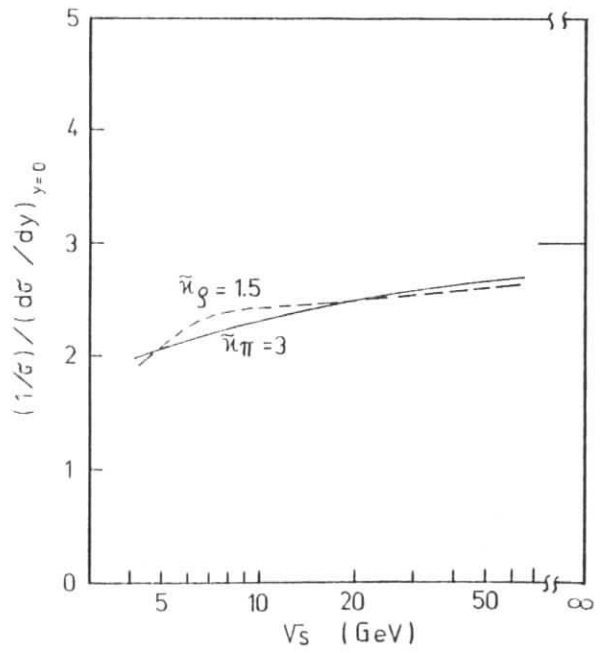

Fig. 3.2
Normalized particle densities at y = 0 in the UJM. Full line: direct production of $\pi, \kappa_\pi = 3$. Dotted line: production via ρ decay, $\kappa_\rho = 1.5$.[82]

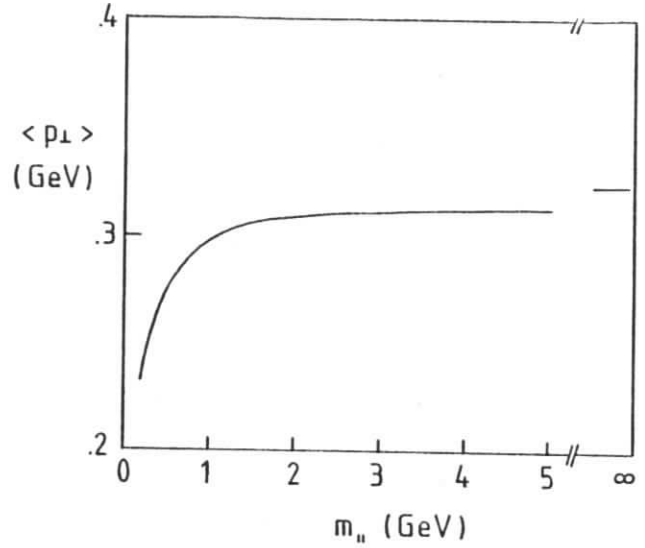

Fig. 3.3
Mean transverse momentum of secondaries as a function of the longitudinal mass for $\lambda = 6.2\ \mathrm{GeV}^{-1}$ in the UJM.

Eqn. 3.18 implies an invariant jet mass growing as $s^{1/4}$

$$\langle M \rangle = \langle (\frac{s}{4} - P_{\parallel}^2)^{1/2} \rangle$$
$$= (\tilde{\kappa} \langle m_{\perp} \rangle \sqrt{s})^{1/2}$$
$$= O(s^{1/4}) \ ; \ \langle M \rangle, s \text{ in GeV} \qquad (3.19)$$

Fig. 3.4 shows that eqn. (3.19) is in very good agreement with the results of the more complicated jet models discussed in the following chapter.

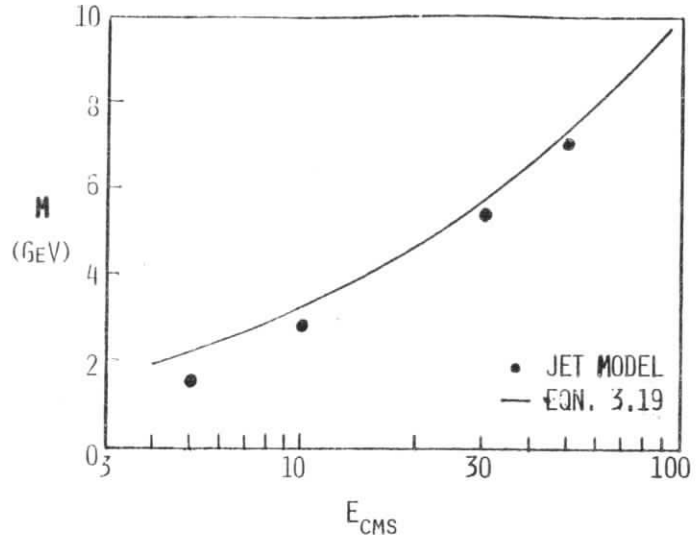

Fig. 3.4
Comparison of the jet mass predicted by eqn (3.19) for $\tilde{\kappa}$ = 3 and $\langle m_\perp \rangle$ = 0.35 with Monte Carlo calculations using the algorithm of Feynman and Field (discussed in chapter 4).

3.3 Comparison with data

Of course the UJM is not able to give a realistic description of the charge, spin or isospin structure of e^+e^- final states. However, with appropriate constants κ and λ it should describe the gross features of inclusive spectra averaged over particle types, quantum numbers etc. In fig. 3.5 a, the UJM prediction with $\tilde{\kappa}$ and λ matched to their ISR values 3 resp. 6.2 GeV^{-1}, is shown together with inclusive $\pi^\pm$ spectra $(s/\beta)(d\sigma/dx_R)$ in e^+e^- annihilations at $\sqrt{s}$ = 4.46-4.90 GeV [45,86]. The UJM values have been evaluated for $\sqrt{s}$ = 4.8 GeV using numerical technics. There is a strong disagreement between the predicted and the measured x_R - slope; furthermore, as we have seen in chapter 2, the high x_R pion cross sections scale over the whole DORIS/SPEAR and PETRA energy range, in contrast to the model.

In principle, the first point could be cured simply by increasing $\tilde{\kappa}$ (eqn. 3.13). This however leads to multiplicities incompatible with experiments (eqn. 3.9).

There is a more natural explanation possible: first, at $\sqrt{s}$ = 4.8 GeV charm production contributes a sizeable fraction to the pion cross section below x ≈ 0.2, [45] which has to be subtracted. Second, in the UJM all particles were assumed to be pions, whereas in practice, also kaons and protons are produced. At moderate $\sqrt{s}$, the rest masses of these particles eat up a good fraction of the available energy, resulting in a steeper decrease of pion spectra at high x. A better (however not fully legetimate) way of comparison is to add up the pion (fig 3.5a), kaon (fig 3.5b) and proton spectra (fig. 3.5c). If one further notes that systematic uncertainites between different experiments [44, 45, 86] are of the order 2 at high x_R, the agreement is quite impressive.

The early scaling of the experimental pion x_R spectra can thus be interpreted as a cancellation of two nonscaling effects: the production of "heavy" particles and the nonasymptotic $\Omega(\bar{e},Q)$.

At higher energies, $\sqrt{s} \geq 17$ GeV, the UJM is in rather good agreement with data from e^+e^- annihilations (fig. 3.6).

3.4 Influence of the UJM - matrix element

Up to now, we used the simplest matrix element which is able to describe the transverse momentum cut-off, $f(p_{\perp\perp}, p_\perp, S) \sim \exp(-\lambda p_\perp)$. More sophisticated UJM-matrix elements have been analyzed in ref.88), with a rather astonishing result.

In the high energy scaling limit the most general form of f is

$$f(p_{\perp\perp}, p_\perp, S) \underset{S\to\infty}{=} f(x, p_\perp) \qquad (3.20)$$

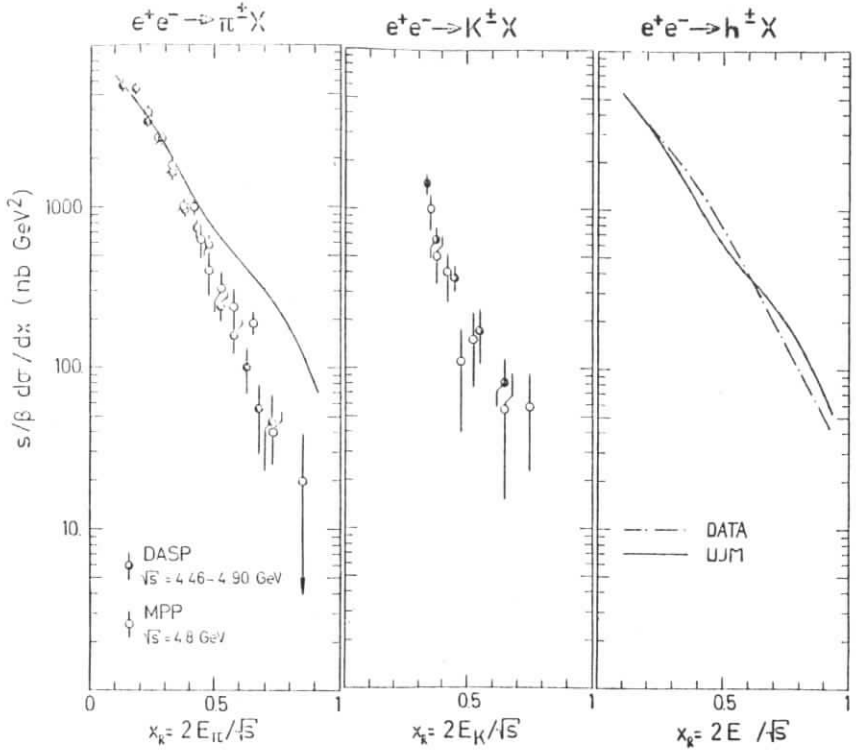

Fig. 3.5

Comparison of UJM predictions (full line) with data from e^+e^- storage rings.[45,86]

a) inclusive $\pi^{\pm}$ spectrum

b) inclusive $K^{\pm}$ spectrum

c) UJM compared to the sum (dashed-dotted line) of the $\pi^{\pm}$ (a), $K^{\pm}$ (b) and $p,\bar{p}$ spectra, after subtraction of charm contributions. The normalisation is arbitrary.

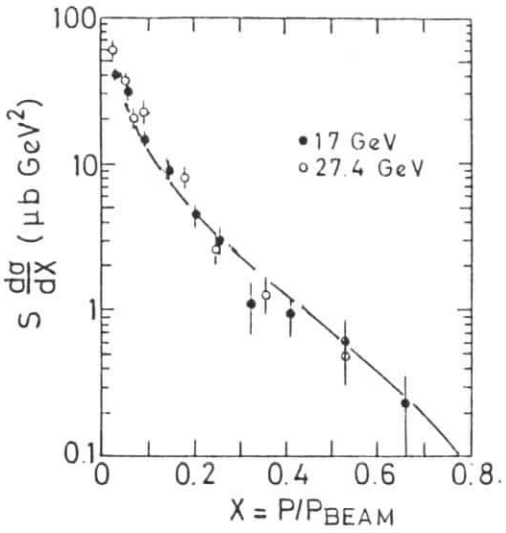

Fig. 3.6

Comparison of the asymptotic limit of the UJM with data from e^+e^- annihilations at $\sqrt{s} \geq 17$ [24]. The UJM parameters are $\tilde{\kappa} = 3$, $\lambda = 6.2\ \mathrm{GeV}^{-1}$, as in fig. 3.5. The normalization is arbitrary.

Let the normalization be such, that

$$f_{,,}(o) = 1 \tag{3.21}$$

with

$$f_{,,}(x) = \int_o^{\infty} dp_\perp^2 \quad f\ (x, p_\perp) \tag{3.22}$$

The inclusive cross section is then given by

$$\frac{1}{\sigma} x_R \frac{d\sigma}{dx_R} \underset{S\to\infty}{=} \frac{1}{\sigma} x \frac{d\sigma}{dx}$$

$$= \tilde{\kappa}\, g(x)(1-x)^{\tilde{\kappa}-1} \qquad (3.23)$$

where $g(x)$ is defined by

$$g(x) = f_{,,}(x) \frac{F(1-x)}{F(1)} \qquad (3.24)$$

$F(x)$ is the "shadow transform" of $f_{,,}(x)$, its definition is given in ref's 88,89). In general, $g(x)$ is a rather flat function of x, even if $f_{,,}(x)$ has a large variation in x. Physically this is due to the fact that, if we try to change the inclusive distribution by changing $f_{,,}(x)$, let's say give it a sharper decrease in x, we give less freedom to the longitudinal momentum of the measured particle, but large momenta of the other particles are suppressed as well so that the damping due to the four momentum conservation (embodied in $F(1-x)$) will be less and so will compensate for the change in $f_{,,}(x)$. This is most drastically shown by noting that $g(x)$ is invariant under the transformation

$$f_{,,}(x) \to \exp(-\alpha x)\, f_{,,}(x);$$

especially we have

$$g(x) = 1 \text{ if } f_{,,}(x) = e^{-\alpha x} \qquad (3.25)$$

So one sees that independent of $f(x, p_\perp)$, $(1/x)\,(d\sigma/dx)$ will always be a function very similar to $\kappa(1-x)^{\kappa-1}$. Accordingly, the two particle distributions turn out to be

$$\frac{1}{\sigma} x_1 x_2 \frac{d^2\sigma}{dx_1 dx_2} \underset{S\to\infty}{=} \begin{cases} \tilde{\kappa}^2 (1-x_1-x_2)^{\tilde{\kappa}-1}\theta(1-x_1-x_2) \\ \text{if 1,2 are in the same hemisphere} \\ \tilde{\kappa}^2 (1-x_1)^{\tilde{\kappa}-1}(1-x_2)^{\tilde{\kappa}-1} \\ \text{if 1,2 are in opposite hemisphere} \end{cases} \qquad (3.26)$$

As expected, the asymptotic UJM has no long range correlations between opposite rapidity hemispheres. Furthermore, for any scaling matrix element, the inclusive rapidity distribution is essentially given by

$$\frac{1}{\sigma}\frac{d\sigma}{dy} = \tilde{\kappa}\ \left(1 - \frac{2\langle m_\perp\rangle}{\sqrt{s}}\cosh y\right)^{\tilde{\kappa}-1} \qquad (3.27)$$

resulting in a rapidity plateau of length $O(\ln S)$ with a shoulder width of roughly 2-3 units in y (fig. 3.7).

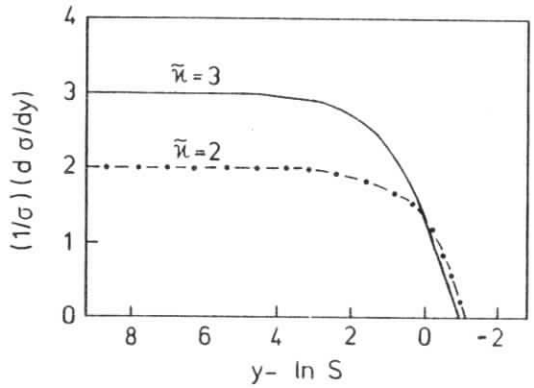

Fig. 3.7
Asymptotic rapidity distributions in the UJM ($\langle m_\perp\rangle = 0.35$)

3.5 The UJM and resonance production

The UJM discussed in the previous chapters describes the production of identical particles without any short range correlation. There is, however, strong evidence from experiments studying particle production in hadronic interactions[79])

that the factorization property of the transition matrix

$$f_N(\bar{p}_1, \bar{p}_2, \cdots, \bar{p}_N, S) = \prod_{i=1}^{N} f(\bar{p}_i, S) \qquad (3.28)$$

holds only in the limit of large invariant masses

$$(p_i + p_j)^2 \gg 1 \text{ GeV}^2$$

whereas low mass particle systems show strong correlations. The most sucessfull interpretation of this phenomena is given in the cluster model,[90] which states that the primarily produced entities are not the final state particles, but instead are excited states which in turn decay isotropically into stable particles.

The most natural way to enclose short range correlations in the UJM is to assume that the intermediate states, called clusters, are emitted independently. In a second step, charge-, energy- and momentum conservation in the cluster decay provide low mass correlations.

In the asymptotic limit of the UJM, for the emission of clusters with a mean decay multiplicity N_c, one has

$$\frac{1}{\sigma}\frac{d\sigma_{hadron}}{dy} \underset{\substack{S\to\infty \\ y \text{ fixed}}}{=} N_c \frac{1}{\sigma}\frac{d\sigma_c}{dy} = N_c \tilde{\kappa}_c \qquad (3.29)$$

where the index c refers to cluster quantities.
The final state hadron distribution is given by the convolution

$$\frac{E}{\sigma}\frac{d^3\sigma}{dp^3} = \int \frac{d^3p_c}{E_c} \left(\frac{E_c}{\sigma}\frac{d^3\sigma_c}{dp_c^3}\right) \left(\frac{E_h'}{\sigma_c}\frac{d^3\sigma_h'}{dp_h'^3}\right) \qquad (3.30)$$

E_h', p_h' and σ_h' characterize the hadronic decay products in the cluster rest frame.

Experiments suggest that the bulk of pions is produced via intermediate vector mesons [91]. As an example, let us take the ρ meson as a representative "cluster". Fig. 3.8 shows UJM results for emission of ρ mesons decaying into two pions compared to direct production in the scaling limit $S\to\infty$. The ρ meson density is chosen such as to give the same plateau height as for direct emission (eqn. 3.29). As expected from momentum conservation, the pion density stays nearly unchanged up to x ~0.8. The mean x of the pions is slightly higher, leading to a reduced multiplicity. It has been shown [82,92] that this effect, although beeing completely irrelevant at asymptotic energies, has severe consequences up to ISR energies, where it improves the approach to scaling at high x, on the other hand however enforces a much slower approach at y = 0.

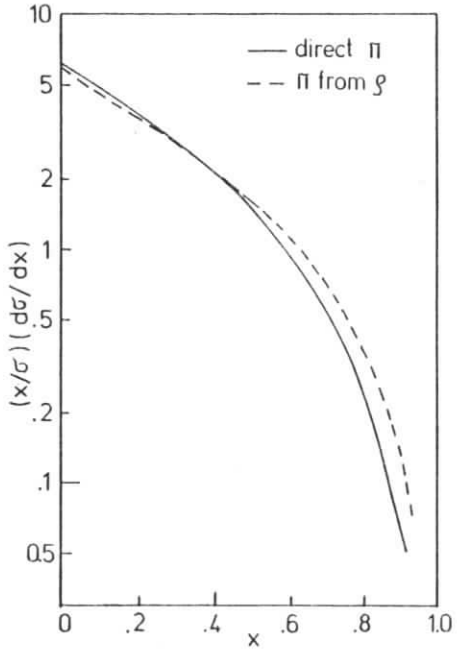

Fig. 3.8
x distributions in the UJM for direct resp. resonance production of pions.

3.6 Quantum statistics

The uncorrelated jet model as discussed above provides a transparent statistical description of the most salient features of jet like multiparticle production. In the formulation of eqn. 3.1, the final state is treated as a free gas in longitudinal momentum space, obeying Boltzmann statistics. Correlation experiments [93] indicate however that hadronic pion production is, at least partially, influenced by Bose-Einstein (BE) statistics, leading to an "attraction" of like sign pions. We shall briefly discuss some of the striking results of models including full BE statistics, following ref. 94 .

As it has been pointed out by Jabs [95], the invariant momentum space representation of the transition probability is not adequate for this purpose. Instead, Γ is given by a non-invariant momentum space volume

$$\Gamma_N \sim \sum_{\{n_r\}} \delta^4 \left(Q - \sum_{r=1}^{\infty} n_r p_r\right) \delta \left(N - \sum_{r=1}^{\infty} n_r\right) \prod_{r=1}^{\infty} f^{n_r}(\bar{p}_r, S) \qquad (3.31)$$

p_r describes the possible momentum states, n_r is the accupation number, which can take the values $n_r = 0, 1, \cdots \infty$ for BE statistics. For simplicity, we choose $f(\bar{p}_r, s) = f(p_{\perp r})$, with the normalization $f(0) = 1$. Eqs 3.4 and 3.31 yield for the asymptotic single particle distribution

$$\frac{1}{\sigma}\frac{d^2\sigma}{dy dp_\perp^2} \underset{\substack{s\to\infty \\ y \text{ fixed}}}{\to} \begin{cases} \frac{\kappa}{2}\,\frac{f(p_\perp)}{1-f(p_\perp)} & \text{for } p_\perp \neq 0 \\ \frac{\kappa}{2}\sqrt{s}\; e^{-|y|} & \text{for } p_\perp = 0 \end{cases} \qquad (3.32)$$

At any fixed $p_\perp \neq 0$ a rapidity plateau is reached as $s\to\infty$ like in models with Boltzmann statistics. At $p_\perp = 0$, however, we have a soft pion divergence resulting in an overall non-scaling behaviour. The mechanism of this enhancement is easily

visualized, if we consider two-particle correlations. Define a correlation function by

$$c(p_1, p_2) = \sigma \frac{d^6\sigma/dp_1^3 dp_2^3}{(d^3\sigma/dp_1^3)(d^3\sigma/dp_2^3)} - 1 \qquad (3.33)$$

In terms of the occupation numbers n_1, n_2 of the states p_1, p_2, c is given by

$$c_{12} = \begin{cases} \dfrac{\langle n_1 n_2\rangle}{\langle n_1\rangle\langle n_2\rangle} - 1 & \text{if 1 and 2 are different states} \\ \dfrac{\langle n_1 (n_2 - 1)\rangle}{\langle n_1\rangle\langle n_2\rangle} & \text{if 1 and 2 label the same state} \end{cases} \qquad (3.34)$$

The term - 1 in the last expression is necessary because the correlation of a particle with itself must not be counted.

Neglecting effects due to cluster decays and phase space limitations, and assuming that the particles underly BE statistics, one gets [97]

$$\langle n_1 n_2\rangle = \begin{cases} \langle n_1\rangle\langle n_2\rangle \text{ if } p_1 \neq p_2 \\ \langle n_1\rangle(1+\langle n_1\rangle) \text{ if } p_1 = p_2 \end{cases} \qquad (3.35)$$

which gives

$$c(p_1, p_2) = \begin{cases} 0 \text{ if } p_1 \neq p_2 \\ 1 \text{ if } p_1 = p_2 \end{cases} \qquad (3.36)$$

Since p_1, p_2 are quantum states, they are identical if

$$|(\bar{p}_1 - \bar{p}_2)| R \lesssim \hbar \equiv 1 \qquad (3.37)$$

R is the uncertainity of the point of emission, or in other words, the radius of the particle source, which is expected to be of the order 1 fm $\equiv$ (200 MeV)$^{-1}$.

An alternative derivation of eqn. (3.36) has been given by Cocconi [98] and by Kopylev and Podgoretzki [99] using higher order interference effects in analogy to optics.

A correlation like in eqn. (3.36) modifies the usual phase space weights in such a way as to favour events which have high particle numbers in identical states. At large rapidities or transverse momenta, this tendency is balanced by the finite amount of energy available; therefore the enhancement of inclusive densities is strongest at low $p_\perp$ and y.

Models of this type have been used to explain the slight rise in $d\sigma/dy$ at y=0 in the ISR energy range [96]. Nevertheless one should keep in mind that conventional phase space models as well predict a non asymptotic behaviour at those energies.

Anyhow these results should be taken rather qualitativly than quantitativly. In reality, a lot of physically different particles are produced, which of course show no BE attraction. Furthermore, the model assumes that all particles are produced in the same volume R^4 in space-time because otherwise the particles could be labeled by their production coordinates (within the limits opposed by the uncertainity relation) and hence were not identical. We shall see later (chapters 4,5), that in quark jets e.g. a BE interference is nearly impossible because of this last argument.

3.7 Summary

The uncorrelated jet model for independent emission of particles enables us to study the main implications of four momentum conservation in jet production. The explicit addition of short range correlations is possible via resonance or cluster production, respectively. Irrespectively of details of the model, and nearly independent of the matrix elements involved, the asymptotic scaling limit is fairly well described by

$$\frac{x_R}{\sigma}\,\frac{d\sigma}{dx_R} = 2\,\tilde{\kappa}\,(1-x_R)^{\tilde{\kappa}-1}$$

(except for possible complications at $p_\perp = 0$ due to BE statistics). The approach to scaling is rather slow, even at PETRA or ISR energies the scaling limit is not fully reached.

4 Jets in parton models

In the last decade, the quark parton model [1-4, 100] has proven to be one of the most useful and intuitive concepts in high energy physics. In the quark parton model, hadrons are composed of partons. The interactions of partons are governed by time scales of the order $\tau = 1/m$ with m being a typical mass of a few hundred MeV. In a moving hadron, the time scale is dilated by the Lorentz factor γ. Then we have two main classes of hadron interactions in the quark parton model: if the interaction time τ_I of hadrons is large compared to $\gamma\tau$, all partons participate coherently in the interaction. If τ_I is small compared to $\gamma\tau$, individual partons may interact. In the asymptotic limit $\tau_I \to 0$ the hadron seems to be composed of free, on-shell quarks. The consistency of the model requires the partons to carry fractional charges, and a new quantum number, color [18,101,102]. Since no fractional charged objects have been observed up to now, there must be a non-asymptotic mechanism confining partons to integer charged states with the observed hadron quantum numbers. This states turn out to be color singlets. Meanwhile, it became customary to turn these arguments upside down and to consider color confinement as the primary mechanism, and the nonexistence of fractionally charged particles as a secondary consequence.

Consider now a process where a large four momentum is transfered to one parton out of a color singlet system. Obviously, due to the large invariant mass of the parton final state, color cannot be confined to a single stable hadron any more. One of the basic assumptions of the quark parton model is that in such a case the confinement of color leads to a bunch of particles moving essentially along the direction of the scattered parton, and that this process happens with the probability 1.

In this chapter, we shall discuss the dynamics of jet formation in more detail, starting with the simplest type of jets: quark jets produced in e^+e^- annihilations.

4.1 Jets from quark confinement

Confinement is most easily visualized in terms of a QCD-supported bag model [104]. QCD -Quantum Chromodynamics- [18] is the most promising candidate for a theory of strong interactions. It is a nonabelian gauge theory in which the interactions between colored quarks are mediated by 8 colored gauge bosons, the gluons. The 3 color charges are generators of an unbroken $SU(3)_c$ symmetry. QCD is an asymptotically free theory, its dimensionless coupling constant α_s/π tends to zero as the energy increases, allowing a perturbative expansion. At low energies, $Q^2 = 0$ (1 GeV^2), the coupling constant diverges. This low energy behaviour of QCD is hoped (but not jet proven) to explain confinement: recent field theoretical investigations indicate that the QCD ground state is a nontrivial two phase vacuum. [105] In the normal phase, outside hadrons, color fields cannot propagate - this effect is known as "chromodynamic Meissner effect" in analogy to the propagation of magnetic fields in a superconductor. There is further an abnormal phase which may contain quarks and gluons as quasifree particles. Since surface- and volume energy is required to create the abnormal phase, the abnormal regions form little bubbles, or "bags" within the normal phase. The dynamics of quark and gluon fields inside a bag is governed locally by the field equations of QCD. It can be shown that such a bag, embedded in the physical vacuum, is stable in its time evolution; the volume energy B (or vacuum pressure) and surface energy S are balanced by the pressure exerted by the gluon fields which are reflected at the phase boundary. [104] B and S can be arranged to give typical bag sizes of 1 cubic fermi. Such a bag containing a quark and a antiquark or three quarks can be identified as a meson or as a baryon, respectively. Actually the spectrum of bag excitation modes reproduces the observed hadronic mass spectrum fairly well. [104] What happens, if a large amount of momentum is transferred to a quark inside a bag? As the quark moves away, the bag changes its shape from a sphere to a cylinder (fig. 4.1), and the kinetic energy of the quark is converted into surface and volume energy of the bag. When the

bag reaches a critical length, it is energetically more favorable to create a new quark - antiquark pair in between the initial quarks. These new quarks screen the initial color fields and the bag breaks up into two new, spherical bags, each containing one initial and one new quark. One of this bags is a slowly moving ground state bag, whilst the other, which contains the fast quark, starts to become cylindrical and so on, until the whole initial energy is converted into a series of bags moving along the direction of the initial momentum transfer. The transverse momentum with respect to the jet axis of these bags is determined by the transverse bag size

$$\langle p_\perp \rangle \approx 0 \ (1 \text{ fermi}^{-1}) \approx 0 \ (200 \text{ MeV})$$

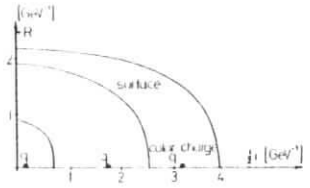

Fig. 4.1
The shape of one quadrant of a typical bag [104] for different quark-antiquark separations. The arrow indicates the radius of an ideal cylindrical vortex tube.

4.2 Space-time development of quark jets

The confinement mechanism proposed above, via successive polarization and deexitation of the vacuum has been investigated already in 1962 by Schwinger [106]. He showed that in certain gauge theories of charged fermion fields, the only asymptotically stable particles are massive neutral bosons. In such theories, electric charge is a confined quantum number, in analogy to the (yet unproven) color confinement in QCD. This phenomenon occurs e.g. in two dimensional (space-time) QED, it may also happen in four dimensional gauge theories if the coupling constant exceeds a certain critical value [106].

Examples of field theories exhibiting the Schwinger phenomenon have been discussed by Casher, Kogut and Susskind [107]. In the following, we shall use 2 dimensional QED [106,107] to give a quantitative description of the process of jet formation. Of cause we are aware of the two essential limitations of this picture: the use of only one space dimension and the absence of photon self couplings in QED. On the other hand, if we keep the attitude of the QCD bag model discussed in the previous section, the nonabelian nature of QCD is mainly responsible for the chromodynamic Meissner effect which in turn reduces the problem to a one dimensional one - the dynamics of a color string.

We shall proceed as follows: first, jet development is discussed using the formalism of two dimensional QED. Next, we try to transform these results into an intuitive physical picture. Finally, a simple graph technic is presented, which further illustrates the mechanisms of jet development, and enables quantitative predictions.

1 + 1 dimensional (space-time) QED is defined by the Lagrangian density

$$L = \bar{\Psi} i\gamma^\mu \partial_\mu \Psi - \frac{1}{4} F_{\mu\nu} F^{\mu\nu} (-g\bar{\Psi}\gamma^\mu \Psi A_\mu) \qquad (4.1)$$

This model is exactly solvable. It has already been mentioned that in this model there are no asymptotic fermion states; the only stable particle is a boson of mass m

$$m = g/\sqrt{\pi} \tag{4.2}$$

The equation of motion in the presence of external current sources is given by

$$(\Box + m^2)\, j^\mu(x) = - m^2 j^\mu_{ext}(x) \tag{4.3}$$

Let us consider the simplest case; the production of a $q\text{-}\bar{q}$ pair by a virtual photon. The external currents in the photon rest system (which correspond to color currents in QCD) are defined by

$$\begin{aligned} j_{0\,ext} &= g\,\delta(z-t) + g\,\delta(z+t) \\ j_{1\,ext} &= -g\,\delta(z-t) + g\,\delta(z+t) \end{aligned} \tag{4.4}$$

(In our notation, x is a two-vector with the components $x_0 = z$, $x_1 = t$).

It is now convenient to express the current in terms of a dipole density ϕ

$$j^\mu = \varepsilon^{\mu\nu}\,\partial_\nu \phi \tag{4.5}$$

in analogy to the well known equations

$$\rho = \frac{\partial \phi}{\partial z}\,, \quad j = - \frac{\partial \phi}{\partial t} \tag{4.6}$$

The external dipole density is then

$$\phi_{ext} = -g\theta(t+z)\theta(t-z) \tag{4.7}$$

and the induced polarization density satisfies

$$(\Box + m^2)\,\phi = g\, m^2\, \theta(t+z)\theta(t-z) \tag{4.8}$$

The resulting dipole density is constant on hyperbolas in space-time, vanishing near the light cone and approaching a constant for distances $|x| > m^{-1}$ from the origin. As the hyperbolas approach the light cone, the regions containing the polarization charge are confined to a length of the order $(tm^2)^{-1}$. The polarization charge combines with the outgoing charge to form a neutral boson as soon as their distance becomes of the order m^{-1} in their common rest frame. In the cms frame this happens after a time t_c

$$t_c \approx \sqrt{Q^2}/m^2 \tag{4.9}$$

The existence of an induced dipole density is equivalent to the creation of charge - anticharge bound states. The momentum distribution of these bosons can be calculated from the field ϕ. One obtains finally

$$\begin{aligned} \frac{1}{\sigma}\; E\,\frac{d\sigma}{dp} &= \frac{1}{\sigma}\;\frac{d\sigma}{dy} \\ &= \frac{1}{(2\pi)^2}\;\left|\; \int d^2x e^{ipx} g\phi_{ext}\right|^2 = \frac{g^2}{\pi\, m} = 1 \end{aligned} \tag{4.10}$$

The time evolution of the main quantities ϕ, $d\sigma/dy$ and ρ is summarized in fig. 4.2.

How can we interprete this results? Particle production happens in the cloud of polarization charge, which is induced by the primary charge-, resp. color sources. Particle creation starts at low rapidities. As time goes on, the initial quark feeds energy into accelerating the polarization cloud until the cloud overtakes the leading quark and neutralizes its charge. One should note that the motion of the polarization cloud proceeds through the creation of new quark pairs in front of the cloud and through the recombination of quark pairs into neutral bosons at their end; it need not be a unique quark in the cloud which is accelerated.

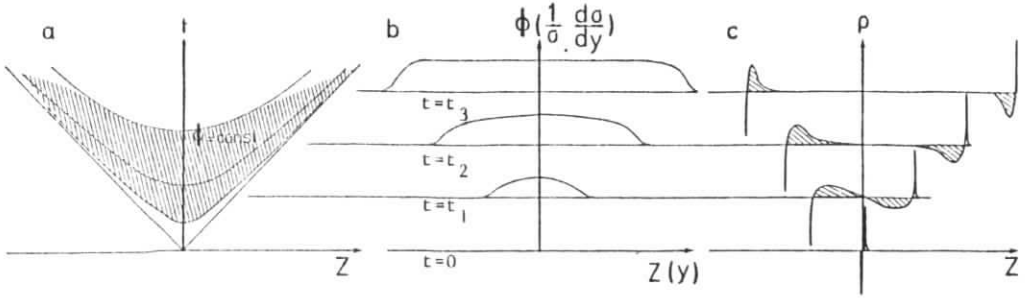

Fig. 4.2
Development of charge confinement in the Schwinger model
a) Lines of constant polarization density in space-time. Particles are produced in the shaded regions.
b) Spatial distribution of the polarization density at different times ($0 < t_1 < t_2 < t_3$). This is equivalent to the rapidity distribution of the emitted particles.
c) Density of charge at different times. (The initial quarks are represented by delta functions).

The process of charge confinement (or "quark fragmentation") turns out to be characterized by a rather long time scale (eqn. 4.9). Furthermore, the cascade extends over large distances in space, as compared to typical particle sizes (fig. 4.2); the extension of the cascade is proportional to the quark energy. The maximum distance between the quark charge and the screening polarization charge, however, stays finite at all times (fig. 4.2c).

There is one difference between QCD and the QED model worth to be noted: in QED, the charge of the leading quark is constant during the whole process. In the nonabelian QCD, the colors of quark and polarisation cloud change due to gluon exchange, the quark color being opposite to the cloud color in the

average. The whole system - quark, cloud, and gluons between them - is a color singlet.

The proportionality between quark momentum and confinement time is important since it ensures that at high energies the outgoing fermions remain free sufficiently long to justify calculations based on the naive parton model.

This model has first been advocated by Bjorken [108]. Since the slowest hadrons are produced first in time, it is known as an "inside-outside" cascade.

Of course it is questionable to which extend details of the model should be taken seriously, and wether it can be generalized to four dimensions (it has been shown that, if the Schwinger phenomenon occurs in a fourdimensional field theory, the model gives a rapidity plateau and an appropriate $p_\perp$ cut off [107]; the problem is, however, to prove that the Schwinger mechanism works e.g. in QCD). Casher, Kogut and Susskind[107] nevertheless succeeded to prove that the inside-outside evolution of the cascade is a feature common to all fragmentation models describing color confinement. Their argument is quite simple: imagine a model where the cascades start at the two initial quarks (e.g. via a multiperipheral chain of low momentum transfers). To neutralize their residual charges, the two cascades have to join somewhere in the middle. Since the fragmentation chain represents a random walk in transverse momentum space, and due to the long time scales involved, the probability that the ends of the two cascades overlap in space time goes to zero as Q^2 goes to infinity. Quarks of energies >> 1 GeV would not be confined in such a model.

Recently, Andersson, Gustafson and Peterson have presented a semiclassical model for quark jet fragmentation[109], which incorporates all features of the Schwinger model, and which gives a reasonable description of the jets observed in deep inelastic lepton scattering.[111] In their model, quarks are

treated as classical particles, which move on well defined trajectories in two dimensional space time. Since there is only one space dimension, the force acting between two charged (or colored) partons is independent of their distance (in a real world, the chromodynamic Meissner effect may simulate such a behaviour). Furthermore it is assumed that the force between quarks and antiquarks is attractive.

In the zero quark mass limit, the world lines of the two valence quarks inside a meson are described by fig. 4.3a): the quarks start to separate, losing momentum at a rate

$$dp/dt = \pm g^2/4\pi .$$

After a certain time, the motion is reversed, the quarks move together, start to separate again and so on. The meson mass is, as in the Schwinger model

$$m \sim \frac{g}{\sqrt{\pi}} = 0.75 \text{ GeV}$$

using g from linear potential charmonium models[110].

In a moving meson, the period of oszillation becomes time-dilated (fig. 4.3b).

In this model, jet formation is visualized in diagrams like fig. 4.4: Two initial quarks move in opposite directions. As soon as a certain energy is stored in the color field (shaded area), the field breaks up somewhere and produces a quark pair.

As soon as kinematically allowed, new pairs are produced in the region between the initial quark and a quark of the first pair, etc.. The quark pairs are assumed to be generated at rest with a negligible pair mass, according to the momentum space element dp/E. Quarks and antiquarks produced at different points C and D in space time will join to form a meson E. This is possible, if at the time

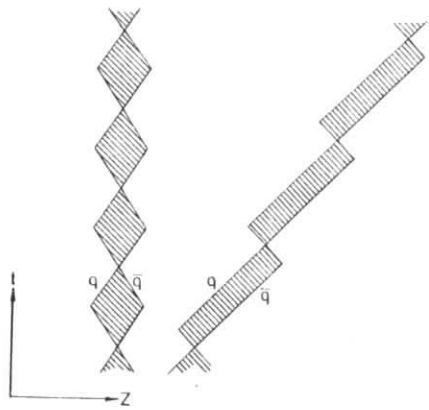

Fig. 4.3
World lines of quarks inside a meson
a) meson at rest
b) moving meson

where quark and antiquark meet in space, the $q\bar{q}$ invariant mass equals the meson mass, or equivalently

$$(Z_C - Z_D)^2 - (t_C - t_D)^2 = m^2 (\frac{4\pi}{g^2})^2 \qquad (4.11)$$

Eqn. 4.11 determines the minimum space-time distance of the production points of quarks appearing in final state mesons.

Quark loops of finite space-time extension (B) are of cause not subjected to this limitation.

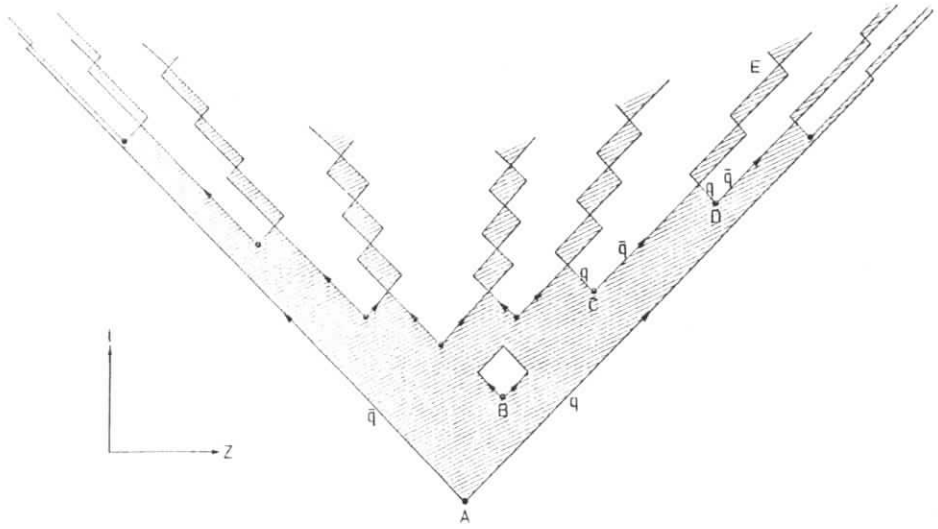

Fig. 4.4
Space-time development of a quark-antiquark cascade.

As a consequence of eqn 4.11, particles are emitted from a hyperbola-like space-time region as in the Schwinger model. Two remarks for the sake of completeness:

- In principle it is possible that a quark pair has a large invariant mass $m >> 1$ GeV. This would split the event into four separate jets. This processes will be rare; if the coupling constant is large enough, quark pairs are created

and recombined as soon as possible.

- Fig. 4.4 is slighly oversimplified. Actually quarks are not only produced as q and $\bar{q}$, but they come in three different colors.
  Considering the full diagrams, however, one finds that the color labels will always be arranged such that each of the jets is a separate color singlet.

In the average, the slowest particles are produced first. There is however no strict mapping between the rapidity and the time of emission of a particle, only the average production time increases with rapidity.

Such statements on rapidities and times of course are not lorentz invariant, usually they will be invalidated by a change of the reference frame. The authors of ref.[109] have investigated this point in detail, their conclusion is that these statements are true in any reference frame, proving the self consistency of the model.

Define now $D_a^{bc}(z)$ as the density of mesons with the valence quark flavour $b\bar{c}$ in the fragmentation region of quark a. z is the fractional momentum of the meson. Masses and transverse momenta are neglected for the moment being.

Averaging over all possible diagrams like fig. 4.4, the model yields a set of coupled integral equations for the D's

$$D_a^{bc}(z) = \delta_{ab} f_c + \sum_d \int_z^1 \frac{dz'}{z'} f_d D_d^{bc}\left(\frac{z}{z'}\right) \qquad (4.12)$$

f_c denotes the probability for a color field to create a pair of quark flavours $c\bar{c}$. The break up is assumed to happen with equal probability anywhere between the quarks generating the field, otherwise f depends on z resp. z'. Color and spin degrees of freedom are implicitely summed over, with the restriction that $b\bar{c}$ is a color singlet . Simplyfied to the case of one flavour, eqn 4.12 reads

$$D(z) = 1 + \int_z^1 \frac{dz'}{z'} D\left(\frac{z}{z'}\right) \qquad (4.13)$$

Eqn 4.13 is easily solved to give

$$D(z) = \frac{1}{z} \quad \text{or} \quad \frac{1}{\sigma} \frac{d\sigma}{dy} = 1 \qquad (4.14)$$

In seemingly contradiction to the data, the model predicts a flat rapidity distribution with a sharp edge at $Y_{MAX} = \ln (\sqrt{s}/m_\perp)$. One has to keep in mind that the mesons described by eqs 4.12 and 4.13 are not the observed stable hadrons. According to the spin weights, 3/4 of them are vector mesons decaying into a number of pions. This results in a smearing of the rapidity distribution, it further increases the height of the plateau.

With the standard choice

$$f_{up} = f_{down} = 0.4$$

$$f_{strange} = 0.2$$

$$f_{charm} = f_{bottom} = \cdots = 0 \qquad (4.15)$$

eqn 4.12 can be solved numerically. The results are in rough agreement with the data (see e.g. fig 4.5).

4.3 An algorithm for simulation of quark jets

To provide a standard jet model representing the state of the art, Feynman and Field [112] have proposed a jet model based on parton phenomenology. The model uses a recursive generation principle introduced by Krzywicki and Petersson[113] and by Finkelstein and Peccei [114]. The jet model is intended to serve as a reference for design and comparison of experiments. It generates exclusive multiparticle final states including resonance production, transverse momenta and finite energy effects. Furthermore, it allows detailed predictions on two-and more particle correlations and on their quantum number dependence.

The model involves one arbitrary function which ultimately determines the momentum distribution of the produced hadrons, and 3 further free parameters; the degree that SU(3) is broken in the formation of new quark-antiquark pairs, the spin of the primary mesons and the mean transverse momentum given to this mesons. In the original version of the model [112], the production of baryons and of heavy quark flavours, like charm or beauty, is neglected.

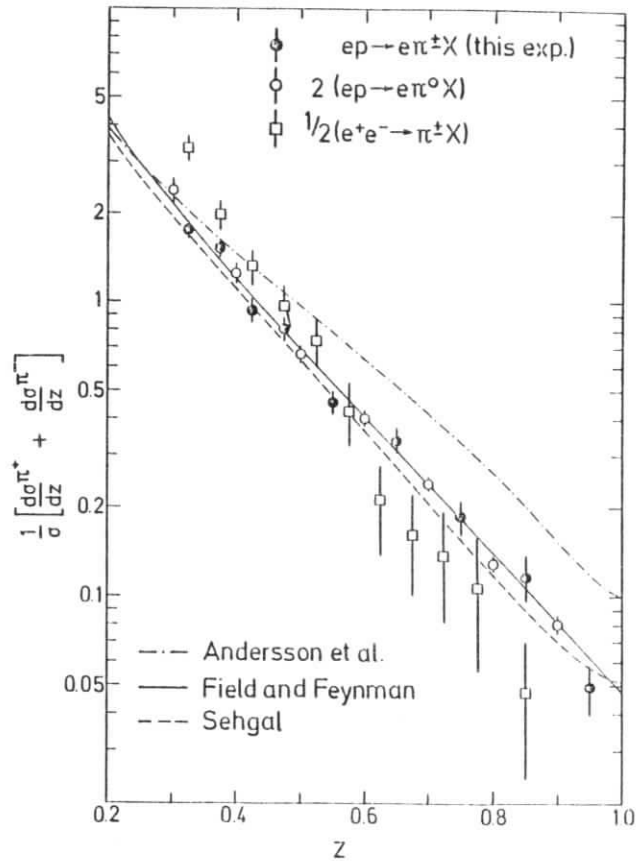

Fig. 4.5
Predictions of varions jet models [109,112,115] compared to quark fragmentation functions measured in deep inelastic lepton nucleon reactions. [116]

The ansatz is based on the idea that a quark of type ‚a' coming out at some momentum p_o creates a color field in which new quark pairs are produced. Quark ‚a' then combines with an antiquark, say ‚b' , from the new pair ‚$b\bar{b}$' to form a meson ‚$a\bar{b}$' leaving the remaining quark ‚b' to combine with a next quark ‚$\bar{c}$' and so on. The primary meson ‚$a\bar{b}$' may be directly observed as a stable meson, or it may be an unstable resonance which subsequently decays. A hierarchy of primary mesons is formed in which ‚$a\bar{b}$' is first in rank, ‚$b\bar{c}$' is second in rank, ‚$c\bar{d}$' is third in rank, etc, as shown in fig. 4.6 (here and in all further diagrams we have adopted the convention to plot antiquarks as quarks moving backwards along their world lines). The chain decay ansatz assumes that, if the primary meson of rank 1 carries away a momentum ξ_1 the further cascade starts with a quark ‚b' with the momentum $p_1 = p_o - \xi_1$ and the remaining hadrons are distributed in the same way as if they came from a jet originated by a quark of type ‚b' with momentum p_1. It is assumed that the momenta are high enough, so that all distributions scale.

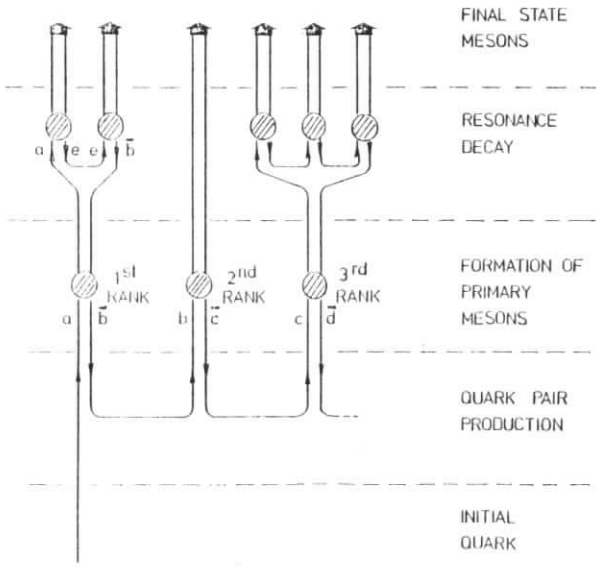

Fig. 4.6
Production of a cascade via sucessive $q\bar{q}$ creation and recombination.

Given this assumptions, and defining f(z) by

f(z) dz = probability that the rank 1 primary meson carries a fraction z of the initial quarks momentum (4.16)

with

$$\int_0^1 f(z)dz = 1 \tag{4.17}$$

the longitudinal structure of the quark jet is uniquely determined. For the single particle density of primary mesons (regardless of its rank)

$$D(z) = \frac{1}{\sigma}\frac{d\sigma}{dz}$$

with

$$z = \frac{p_{meson}}{p_o}$$

we have the integral equation

$$D(z) = f(z) + \int_z^1 \frac{dz'}{z'} f(1-z') \; D\left(\frac{z}{z'}\right) \tag{4.18}$$

(assuming that $zp_o >> m_\perp$).

Generalized to many quark flavours, eqn 4.18 reads

$$D_a^{bc}(z) = \delta_{ab} f_c(z) + \sum_d \int_z^1 \frac{dz'}{z'} f_d(1-z') D_d^{bc}\left(\frac{z}{z'}\right) \tag{4.19}$$

(in the notation of eqn 4.12).

The first term is the probability for the meson to have rank 1, the second term arises from a sum over all higher ranks with the rank 1 meson beeing at z'. Feynman and Field assume that $f_b(z)$ (the probability that a rank 1 meson ‚$a\bar{b}$' is formed at z) can be factorized as follows

$$f_b(z) = f_b^o \cdot f(z) \tag{4.20}$$

where

$$\int_0^1 f(z)dz = 1 \tag{4.21}$$

and

$$\sum_b f_b^o = 1 \tag{4.22}$$

The breaking of the SU(N) flavor symmetry is put in the f^o's, ideally one has in SU(N)

$$f^o_b = \frac{1}{N} \tag{4.23}$$

Guided by experiments, Feynman and Field use

$$f^o_{up} = f^o_{down} = 0.4 \tag{4.24}$$

$$f^o_{strong} = 0.2$$

$$f^o_{charm} = f^o_{bottom} = \cdots = 0$$

in agreement with eqn. (4.15).

In contrast to the model by Anderson et.al., the spin structure of the primary mesons is kept as a free parameter. The best fit to the data is quoted for

probability for spin 0 mesons = $\alpha_p = 0.5$
probability for spin 1 mesons = $\alpha_v = 0.5$
probability for spin ≥2 mesons = $\alpha_T = 0$ (4.25)

The breaking of the SU(N) symmetry and of the spin symmetry can be justified by the fact, that in Schwinger models the production of heavy states (like strange-antistrange pairs or spin 1 mesons) is suppressed by factors like $\exp(-m^2/m_o^2)$, with $m_o \approx 0$ (1 GeV) [112].

Of course, the smaller fraction of vector mesons requires a change of f(z) compared to ref. 109. Feynman and Field use

$$f(z) = (1-a) + 3a\,(1-z)^2$$

with $a = .77$ (4.26)

To incorporate the transverse momentum smearing in the model it was assumed that the quark-antiquark pairs which are produced to discharge the color field conserve transverse momentum in a pairwise fashion and hence have no net transverse momentum. Transverse momenta $\bar{p}_\perp$ and $-\bar{p}_\perp$ are assigned to the quark resp. antiquark of a pair, with a distribution

$$\frac{1}{\sigma}\frac{d\sigma}{dp_\perp^2} \sim e^{-p_\perp^2/(2p_{\perp_o}^2)} \tag{4.27}$$

The transverse momentum of a primary meson is given by the vector sum of the transverse momenta of its quarks. To reproduce the observed mean transverse momentum of the final state pions, $p_{\perp_o} = 350$ MeV is required. The mean transverse momentum of primary mesons is of the order of 440 MeV.

The recursive scheme of jet generation is now evident:

i) choose the momentum fraction of the rank 1 meson from eqn. 4.26
ii) generate a quark pair according to eqs 4.24 and 4.27. The rank 1 meson is made of the old quark and the new antiquark
iii) decide on spin-parity of the meson (eqn 4.25). Use the known pseudoscalar and vector mixing angles to determine the precise type of the meson. If necessary, let it decay.
IV) If there is still enough energy left over, repeat the procedure starting with the residual quark.

The problem is hidden at point IV : the main assumptions put in the model, like scaling, are not valid at low energies. Any low energy cut will lead to irregularities in the plateau (fig. 4.7). Feynman and Field solve this point in a very elegant manner: first they create "master jets" of very large momentum p_∞. Next they reinterpret and rescale the variable z, keeping only those particles which have $z > 0$ afterwards. Physically this is essentially equivalent to boosting the whole jet such that those particles having $y' > 0$ in the new system carry the energy E_o equal to the initial quark momentum. Particles with $y' < 0$ are thrown away (fig. 4.7). To create a full $q\bar{q}$ jet, two such jets with opposite quark momenta are put together.

Since it includes all essential details of hadron physics in a consistent way, the Feynman Field jet model is very well suited to demonstrate the properties of jets in the parton picture.

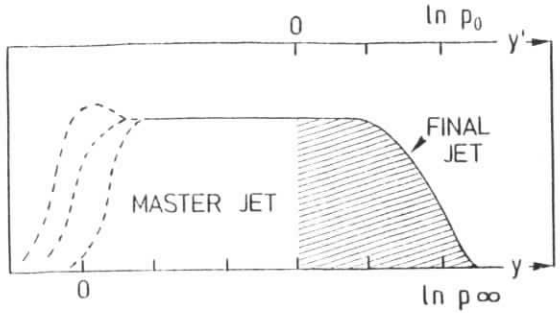

Fig. 4.7
The recursive jet generation leads to problems at y = 0.
To circumvent this problem, only the high-y end of a master jet is used.

Before entering that topic, a few remarks concerning the philosophy of the model have to be made. Regarding the recursive principle, one is tempted to consider the Feynman-Field jet as an "outside-inside" cascade, where e.g. particles of rank 1 are produced first at high y in the overall cms. The authors themselves considered this point as one of the major drawbacks of their model [112]. A comparison of the integral equations (4.19) with the equations describing the inside-outside cascade of Anderson, Gustafson and Peterson (4.12) however proves that both point of views lead to very similar mathematical structures, the eqs. (4.19) being as well compatible with an inside-outside development of the jet. The recursive principle proposed by Feynman and Field thus should not be considered as a physical model, but merely as a mnemonic simplifying the bookkeeping of momenta, quantum numbers etc.

Second, the model deals with probabilities. Quantum field theories usually describe amplitudes and not probabilities, leading to interference terms which don't appear in these semiclassical jet models. Since color confinement is a collective phenomena, these interference terms should be quite important.

On the other hand one may hope that due to the large space time extension of the cascade, interference effects average out on a long range longitudinal scale [117]. The transverse dimensions of jets are strongly influenced by coherent radiation [118], but again it seems that the probabilistic distribution (eqn 4.27) put in by hand represents a realistic average over quantum effects.

The last point is more technical: Since finite momentum jets are produced by cutting off the tails of very high momentum jets, conservation laws are not fullfilled exactly. In the average, there is one quark with its charge, color and transverse momentum left over. In reality, this quantities have to be neutralized by the corresponding ones in the opposite jet. This unbalance of conserved quantities is not a specific failure of the Feynman-Field technique to generate jets, instead it is a reflection of the fact that it is meaningless to talk about a single jet. The only systems of physical relevance are color singlets , like $q\bar{q}$ or qqq states. A division of such systems into single jets is approximately possible for fast particles, it is however completely meaningless and arbitrary for slow fragmentation products.

4.4 Properties of quark jets

In this section we shall discuss the expected properties of quark jets, and compare them to the experiment. The Feynman Field model will be used as the typical parton jet reference. The jet energy should be chosen such that mass effects are negligible, on the other hand it should be low enough so that the QCD corrections to be discussed in the next section will not dominate. This conditions are fullfilled eg. in the lower PETRA energy range.

Consider the fragmentation of u, d and s quarks (the decay of charmed quarks will be discussed later). As "stable" final

state particles we have

$$u,d,s \rightarrow \pi^+, \pi^0, \pi^-; K^+, K^0, K^-, \bar{K^0}; \gamma \qquad (4.28)$$

In principle, there are 3x8 fragmentation functions (plus the corresponding ones for antiquarks).

$$D_q^h(z) = \frac{1}{\sigma_q}\frac{d\sigma}{dz}h \qquad (4.29)$$

Charge conjugation and isospin invariance reduce the number of independent functions:

final state π

$$D_u^{\pi^+} = D_d^{\pi^-}, \quad D_u^{\pi^0} = D_d^{\pi^0}$$
$$D_u^{\pi^-} = D_d^{\pi^+}, \quad D_s^{\pi^0}$$
$$D_s^{\pi^+} = D_s^{\pi^-} \qquad (4.30)$$

final state K

$$D_u^{K^+} = D_d^{K^0}, \quad D_u^{\bar{K}^0} = D_d^{K^-}$$
$$D_u^{K^0} = D_d^{K^+}, \quad D_s^{K^+} = D_s^{K^0}$$
$$D_u^{K^-} = D_d^{\bar{K}^0}, \quad D_s^{K^-} = D_s^{\bar{K}^0} \qquad (4.31)$$

final state γ

$$D_u^{\gamma} = D_d^{\gamma}, \quad D_s^{\gamma} \qquad (4.32)$$

The parton picture gives us additional, approximate relations between the D's. Essentially, there are two main fragmentation mechanisms, usually known as favored and unfavored fragmentation [115]. A fragmentation is favored, if the fragment contains the initial quark. In the language of Feynman and Field it may then be the (fast) meson of rank 1. In the unfavored case,

where the meson does not contain the initial quark, it has to be of rank 2 or higher, implying a smaller mean momentum. Keeping this consideration in mind, we may assume that the ratio w(z) of unfavored to favored fragmentation processes is independent of quark flavour involved

$$w(z) = \frac{D_q^{\text{unfav.}}(z)}{D_q^{\text{fav.}}(z)} \quad \text{e.g.} \quad \frac{D_u^{\pi^-}(z)}{D_u^{\pi^+}(z)} \qquad (4.33)$$

As SU(3) symmetry is probably violated in quark fragmentation, eqn. (4.33) is not fully adequate: as soon as a strange quark is produced, the fragmentation function is suppressed by a factor

$$h(z) = \frac{D^{\text{strange, fav.}}_{\text{non strange}}}{D^{\text{non strange, fav.}}_{\text{non strange}}} = \frac{D^{\text{strange, unfav.}}_{\text{non strange}}}{D^{\text{non strange, unfav.}}_{\text{non strange}}}$$

$$= \text{e.g.} \frac{D_u^{K^+}(z)}{D_u^{\pi^+}(z)} = \frac{D_u^{K^-}(z)}{D_u^{\pi^-}(z)} \qquad (4.34)$$

The value of h is a characteristic property of confinement forces, and should not depend on the rank of a meson.

$$h(z) = \text{const} = \frac{1}{2} \qquad (4.35)$$

Finally, we expect

$$D_q^{\pi^0}(z) = \frac{1}{2}\{D_q^{\pi^+}(z) + D_q^{\pi^-}(z)\} \qquad (4.36)$$

With these simplifications, the D's are fully determined by the knowledge of the three functions $D_u^{\pi^+}(z)$, $D_u^{\pi^-}(z)$ and $D_u^{k^+}(z)$. Eqn (4.33) to (4.36) are only approximately valid because of the presence of a second mechanism for "unfavored" fragmentation: the decay of vector mesons, e.g.

$$u \rightarrow \rho^0 + \text{anything}$$
$$\rightarrow \pi^+ \pi^-$$

which competetes with the direct, suppressed channel.

All this is more easily demonstrated in table 4.1, where the fraction of momentum carried by the various decay products is given, and by fig. 4.8, where the favored and unfavored fragmentation functions of a u-quark into π's and K's are shown, as predicted by the Feynman-Field model.

Table 4.1

Fraction of total momentum carried by the direct-primary (before decay) mesons and direct-plus-indirect (from a decay) mesons resulting from a u-, d- and s-quark.[112]

	Particle	u	d	s
Direct	$\pi^+ = \rho^+$	0.12	0.06	0.06
	$\pi^0 = \rho^0$	0.09	0.09	0.06
	$\pi^- = \rho^-$	0.06	0.12	0.06
	$K^+ = K^{*+}$	0.06	0.03	0.03
	$K^0 = K^{*0}$	0.03	0.06	0.03
	$K^- = K^{*-}$	0.03	0.03	0.09
	$\bar{K}^0 = \bar{K}^{*0}$	0.03	0.03	0.09
	η	0.05	0.05	0.05
	η'	0.05	0.05	0.05
	ω	0.09	0.09	0.06
	ϕ	0.01	0.01	0.04
total = direct + indirect	π^+	0.29	0.19	0.19
	π^0	0.26	0.26	0.20
	π^-	0.19	0.29	0.19
	K^+	0.08	0.06	0.06
	K^0	0.06	0.08	0.06
	K^-	0.04	0.04	0.13
	$\bar{K}^0$	0.04	0.04	0.13
	γ	0.04	0.04	0.04
total	π	0.74	0.74	0.58
total	K	0.22	0.22	0.38

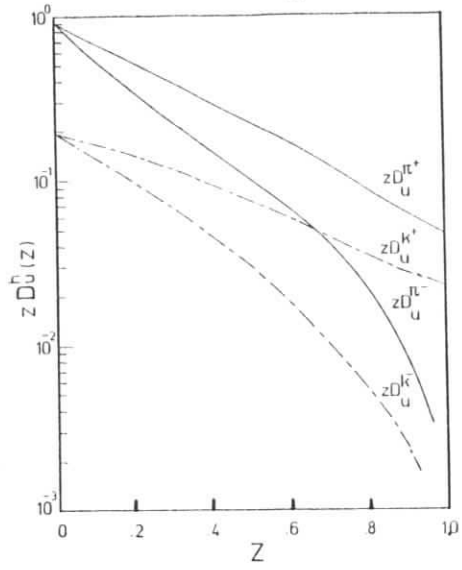

Fig. 4.8
u quark fragmentation function in the Feynman-Field model

Two points are worth to be noted: in contrast to phase space models (chapter 3), the Feynman-Field model predicts a nonzero value of $D_q^u(z)$ at $z \to 1$ even at asymptotic energies. On the other hand, $D_q^\pi = D_q^{\pi^+} + D_q^{\pi^-}$ is remarkable well fitted by the UJM expression $D(z) = (1-z)^2/z$ in a large z range $0 < z < 0.7$.

In e^+e^- annihilations the fragmentation functions of u,d, and s quarks cannot be measured separately. Concerning this topic we shall use data from deep inelastic lepton nucleon interactions for comparison. To reduce contributions from quasielastic channels, cuts on the four momentum transfer Q^2 and on the invariant mass W of the hadronic system have been applied, typically $Q^2 > 2$ GeV^2 and W>4 GeV. Nevertheless the mean energy in the hadronic center of mass <W> = 6 to 7 GeV is fairly small, and phase space effects are still important.

As we shall see in more detail in chapter 6, the choice to the scaling variable is somewhat ambigious in lepton-nucleon interactions, especially as far as show particles are concerned.

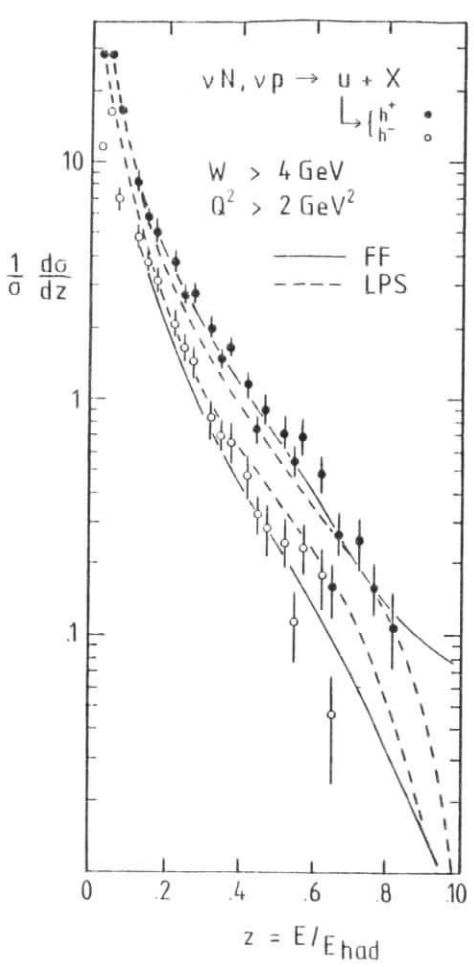

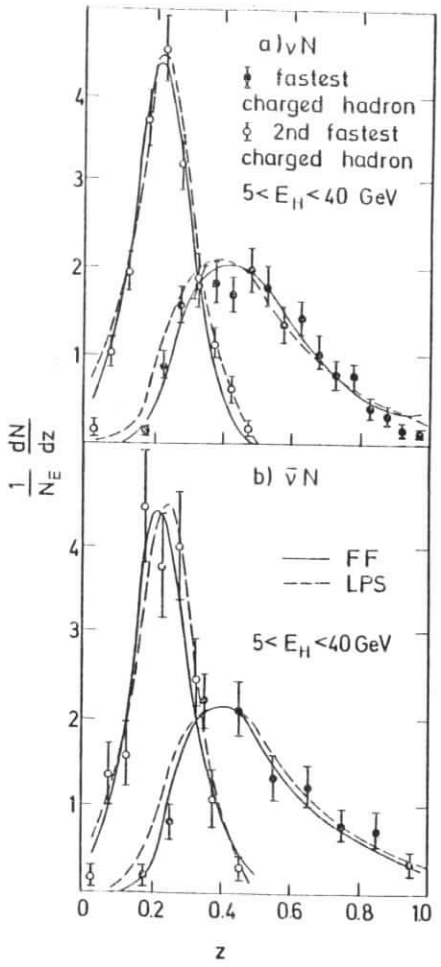

Fig. 4.9. u quark fragmentation functions measured in neutrino nucleus interactions [119] compared to predictions of the Feynman-Fields model (FF) and of a phase space model (LPS).

Fig. 4.10. Distribution in z for the fastest and the second fastest charged hadrons, compared with FF and LPS in a) νN and b) $\bar{\nu}$N interactions. [120]

The most commonly used variable is $z = E/E_{had}$. E is the hadron energy in the laboratory frame, and E_{had} is the total hadronic energy, which is equivalent to the quark energy. For fast hadrons ($z \gtrsim 0.2$), z coincides with $x = 2p_{cms}/W$, or with $x_R = 2E_{cms}/W$.

Fig. 4.5 shows that the model fits rather well the spectrum of favored and unfavored fragmentation modes of u quarks as derived from electroproduction.[116] In fig. 4.9 data from neutrino-nucleus and neutrino-proton interactions,[119] respectively, are compared to the FF model. Again the agreement is good. Included in fig. 4.9 are predictions of a longitudinal phase space model, which demonstrates the influence of energy-momentum and charge conservation. The multiplicity has been constrained to the observed one. Obviously, much of the difference observed between the "favored" and the "unfavored" distribution of positive and negative hadrons, respectively, is accounted for by simple charge conservation. Even the increase of the difference with z is reproduced: events with a particle close to $z = 1$ have a low missing mass and therefore a low multiplicity; effects due to charge conservation are more important than in average events.

A more differential quantity, the distribution of the fastest and second fastest charged hadron, is shown in fig. 4.10.[120] The Feynman Field model as well as the naive phase space model agree with data. Finally, fig. 4.11 illustrates the net charge density in u and d quark jets as a function of the rapidity $y_z = \ln z$.[213] The integrated charge content of the jets is $\langle Q \rangle_u = 0.55 \pm 0.06$ and $\langle Q \rangle_d = -0.12 \pm 0.13$ for u and d-quarks, respectively. The FF model has the tendency to reproduce the observed asymmetry between $\langle Q_u \rangle$ and $\langle Q_d \rangle$.

To summarize so far: the FF model seems to be in reasonable agreement with data from deep inelastic reactions even in details; however, the comparison with the longitudinal phase space model proves that most of this agreement is required by conservation laws, once the multiplicity distribution is correctly adjusted.

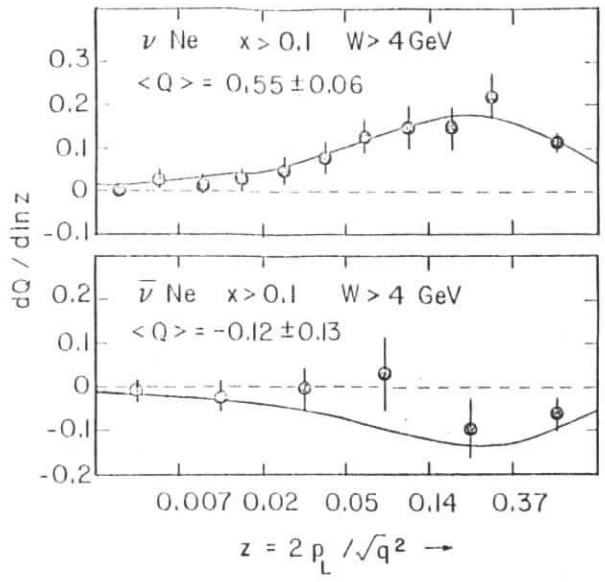

Fig. 4.11 Distribution of the charge dQ/dlnz plotted vs. lnz for u- and d-quark fragmentation[213]. The curve is from Field and Feynman.

Some care is needed when comparing the FF model with data from e^+e^- storage rings. According to its construction, the model is most suited to describe jets at the highest energies. There, however, effects due to charm and bottom quark production and due to gluon bremsstrahlung play an important role. Various extensions of the model have been used to describe the decay of heavy quarks [133] and to account for additional hard processes [103]. All extensions require further, and often unsafe assumptions.

To circumvent this problem, we will use data at $\sqrt{s}$ = 9.4 GeV, below the bottom threshold, for the comparison with FF. There one is far above the charm threshold and it seems reasonable to assume that charm fragmentation doesn't modify the picture too strongly, when averaging over particle types and quantum numbers in the final state.

The following PLUTO-data[41] correspond to measured distributions without acceptance corrections etc. To compare with the FF model, the events were passed through a realistic simulation of the detector and were subjected to the same cuts as real data.[41] Fig's. 4.12 and 4.13 show the inclusive spectra $d\sigma/dx_u$ and $d\sigma/dp_\perp$. In fig. 4.14 the distribution of sphericity is displayed.

In all cases, the FF model describes perfectly the kinematical features of the data; but remember that once the mean multiplicity and the mean $p_\perp$ with respect to a jet axis are fixed, almost any other model will do as well.

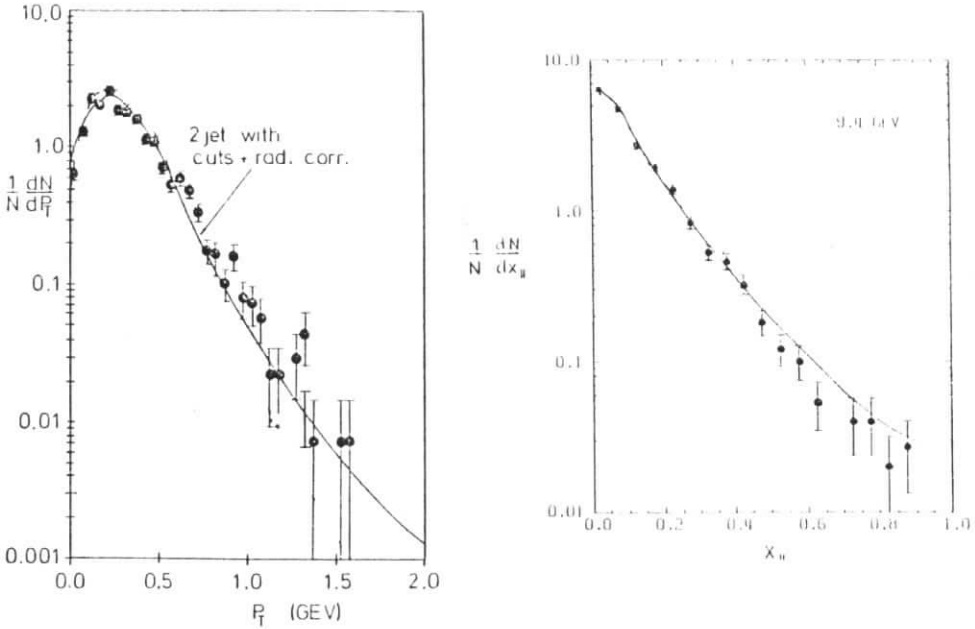

Fig. 4.12 Observed $p_\perp$ distribution of charged tracks (PLUTO data at $\sqrt{s}$ = 9.4 GeV). $p_\perp$ is measured with respect to the thrust axis. The curves correspond to the FF-model for u,d,s quarks.[41]

Fig. 4.13 Same as for fig. 4.12, but for x_u.[41]

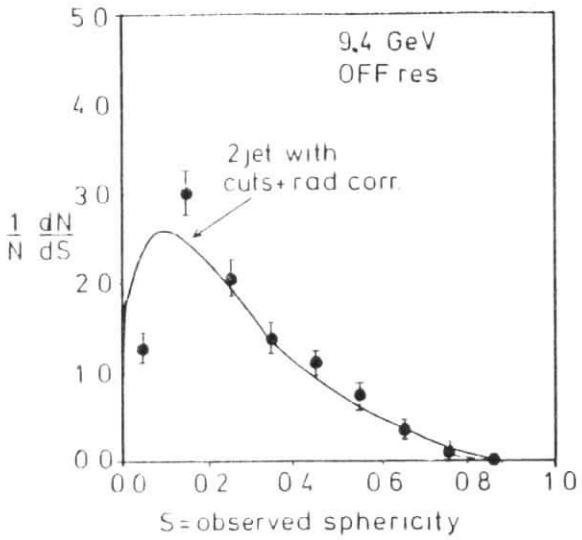

Fig. 4.14. Observed sphericity distribution of charged tracks at $\sqrt{s}$ = 9.4 GeV. The full curve is the FF model including detector simulation and initial state radiation. [41]

Let us now study more in detail the quantum number structure of Feynman-Field jets. We have seen in fig. 4.11 that quark jets tend to retain the charge of the quark at high rapidities. This is the object of a suggestion by Feynman[4]. He conjectured that the total quantum numbers of all the fragments in this region averaged over events should be equal to the (fractional) quantum numbers of the parent quark. This quantum number retention is elucidated by fig. 4.15, which shows the rapidity distribution of the rank 1 mesons containing the original quark compared to the rapidities of the produced particles (for simplicity, $y_z = \ln z = y - \ln \sqrt{s}$ has been used instead of y). Obviously, the rank 1 meson stays in the high y region of the jet. The same is, of course, true for its decay product.

It has been shown, however, that this does not necessarily imply quantum number retention [122-125]. The argument goes as follows: assume we cut the jet somewhere, e.g. at $\tilde{y}_z = -6$, and sum up the quantum numbers of all particles with higher y_z. In nearly

all cases the initial quark is contained among these mesons. Yet, since we start with a quark and count an integer number of mesons, there is always one quark pair whose quark is below $\tilde{y}_z$ and whose antiquark is above. If $\tilde{y}_z$ is low enough, this quark pair will stem from the sea. The sum Λ of quantum numbers for $y_z > \tilde{y}_z$ is then given by

$$\langle \Lambda \rangle = \Lambda_q + \langle \Lambda_s \rangle \qquad (4.37)$$

Λ_q describes the quantum numbers of the initial quark (resp. antiquark) and $\langle \Lambda_s \rangle$ are the mean quantum numbers of an antiquark (resp. quark) from the sea. Exact quantum number retention happens only if $\langle \Lambda_s \rangle = 0$. Let us consider a few examples: a SU(2) sea consisting of $u, \bar{u}, d, \bar{d}$; a SU(3) symmetric sea and the Feynman-Field quark sea with SU(3) broken due to the higher s quark mass. We get for $\langle \Lambda_s \rangle$

sea	charge	strangeness	baryon number	3rd component of isospin
SU(2)	-1/6	0	-1/3	0
SU(3)	0	1/3	-1/3	0
$SU(3)_{FF}$	-1/15	1/5	-1/3	0

(4.38)

In none of these models all quantum numbers are retained. For the Feynman-Field sea, we expect approximate retention of charge and I_z. The mean quantum numbers of their jets are

initial quark	mean jet charge	mean jet strangeness	mean I_z
u	.60	.20	.50
d	-.40	.20	.50
s	-.40	.80	.00

(4.39)

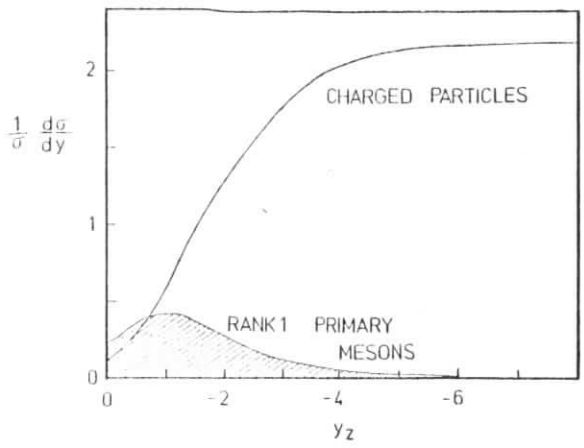

Fig. 4.15
Rapidity distributions of charged particles from a u-quark jet compared to the rapidity of the rank 1 mesons ($y_z = \ln z$)

These numbers are confirmed by the explicit monte carlo simulation of jets,[112] the results for quantum number density in quark jets are shown in fig. 4.16. The most remarkable consequence of this considerations is that even if a jet starts from a non strange quark, it finally aquires a net strangeness. Furthermore, in any jet mechanism leading to a rapidity plateau (that means the decay function f (z) (eqn. 4.16) is finite for $z \to 0$) only the high-y region of the jet is influenced by the parents quantum numbers, and the plateau essentially stays neutral. To get further insight in the dynamics of the cascade mechanism, it is helpful to study correlations of particles within the plateau.

As we have already mentioned, the ordering of primary mesons in rank corresponds to an ordering in their average rapidities; even in infinite momentum jets the rms rapidity difference between mesons adjacent in rank approaches a finite limit as is demonstrated by fig. 4.17. Since primary mesons adjacent in rank contain quarks from one quark pair, there are further correlations between their transverse momenta and quantum numbers. We have

$$\langle \vec{p}_{\perp i} \cdot \vec{p}_{\perp i+1} \rangle = - p_{\perp_0}^2 \qquad (4.40)$$

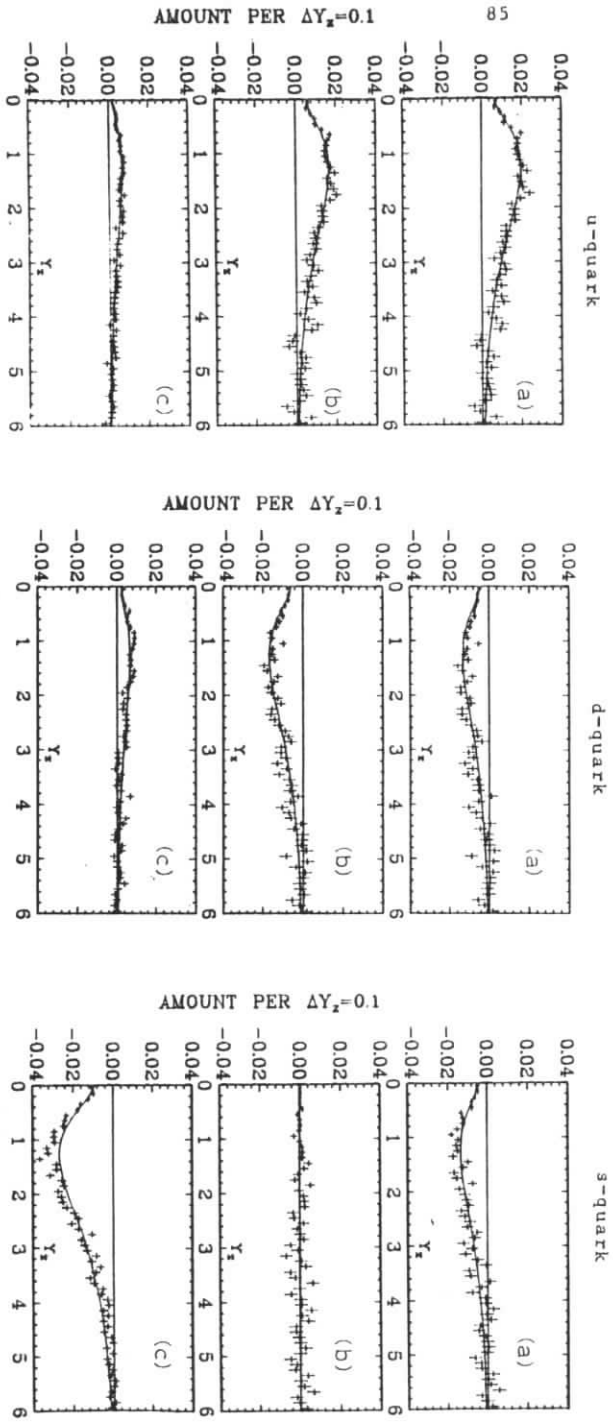

Fig. 4.16
a)
Distribution of (a) charge Q, total Q = 0.6, (b) third component of isospin I_3, total I_3 = 0.5, and (c) strangeness S, total S = 0.2, along the $Y_z (Y_z = -\ln z)$ axis for a u-quark jet.
b)
Same as a) but for a d-quark jet. (a) Total Q = -0.4, (b) total I_3 = -0.5, (c) total S = 0.2.
c)
Same as a) but for an s-quark jet. (a) Total Q = -0.4, (b) total I_3 = 0.0, (c) total S = -0.8.
From ref. 112).

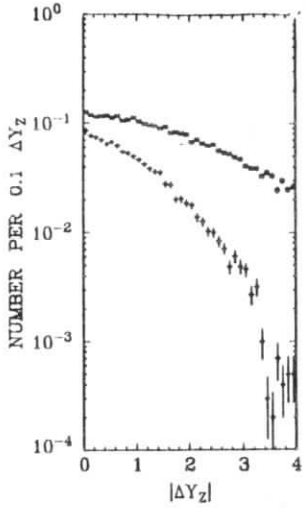

Fig. 4.17
The distribution of distances ΔY_z between the hadrons coming from one primary and those coming from another primary next in rank ✖, $\langle|Y_z|\rangle = 1.8$. The distribution ΔY_z among the secondary hadrons which come from the decay of a single primary ✝, $\langle|Y_z|\rangle = 0.9$. [112]

Relations between their charges are summarized by the probability matrix $W_{q_i q_{i+1}}$

q_i \ q_{i+1}	+	0	−
+	.00	.40	.60
0	.18	.54	.28
−	.60	.40	.00

(4.41)

with the normalization $\sum_{q_{i+1}} W_{q_i q_{i+1}} = 1$

(Note that for $\bar{q}$ - jets q_i and q_{i+1} have to be exchanged, since W is not symmetric!). Similar for strangeness

S_i \ S_{i+1}	+	0	−
+	.00	.20	.80
0	.19	.76	.05
−	.20	.80	.00

(4.42)

Since in (4.41) and (4.42) all elements W_{++} and W_{--} vanish, charge and strangeness must be conserved locally within mesons of neighboured rank. To be more quantitative, we define a correlation length as follows: assume we have a primary meson carring a conserved additive quantity q_1 (charge, strangeness) at a position ξ_1 (e.g. in rank or rapidity). As the plateau as a whole is neutral, the remaining mesons form a system with a net "charge" density $d\sigma_q/d\xi$, normalized via

$$\int d\xi \; (d\sigma_q / d\xi) = - q_1 \qquad (4.43)$$

(for simplicity we treat ξ as a continous variable). A correlation length $\Delta\xi$ may now be defined as

$$\Delta\xi = \int d\xi \; | \xi - \xi_1 | \; (d\sigma_q/d\xi)/(-q_1) \qquad (4.44)$$

In a more model dependent way, $\Delta\xi$ could as well be defined by

$$(d\sigma_q/d\xi) \sim \exp (- |\xi - \xi_1| / \Delta\xi)/(-q_1)$$

The quantity q is conserved locally, if $\Delta\xi$ is finite and not bounded by the range of ξ itself:

$$\Delta\xi << \int |\xi - \xi_1| \; (d\sigma_{MESON}/d\xi)/\sigma \qquad (4.45)$$

In that sense, we get for the correlation lengths in rank

transverse momentum	$\Delta\xi = 1$	
charge	$\Delta\xi = 1.9$	
strangeness	$\Delta\xi = 1.3$	(4.46)

As a finite difference in rank implies a finite average difference in rapidity (fig. 4.17), transverse momentum, charge and strangeness are conserved locally in rapidity in the Feynman-Field cascade. Out of this three, local conservation of charge and strangeness are basic properties of the model, whereas the type of momentum conservation is put in by hand.

The correlation lengths Δy_z can be estimated to be $\Delta y_z = 2$ for charge conservation and $\Delta y_z = 1.5 - 2$ for strangeness conservation. The resonance decay of primary mesons introduces additional short range correlation between the observed mesons. As an example, Fig. 4.18 shows the two particle correlation function

$$C(y_{z1}, y_{z2}) = \frac{1}{\sigma}\frac{d^2\sigma}{dy_{z1}dy_{z2}} - \frac{1}{\sigma^2}\frac{d\sigma}{dy_{z1}}\frac{d\sigma}{dy_{z2}} \qquad (4.47)$$

The peak in $C(y_{z1}, y_{z2})$ for unlike hadron charges is mainly due to the decay of predominantly neutral resonances and not due to a local conservation of charge on the primary meson level. The typical correlation length from resonance decay is $\Delta y_z = 0.9$.

Finally, what about charm fragmentation functions? In the spirit of the Feynman-Field model, the inclusion of charm (or even higher mass quarks) enlarges the number of fragmentation functions considerably. First, there are functions describing charmed meson production by ordinary quarks

$$D_u^{D^+}(z) \quad , \quad D_u^{D^0}(z) \quad , \quad D_u^{D^-}(z) \quad \text{etc.}$$

Since we have learned that in Schwinger - like models the production of high mass states is suppressed by factors like $\exp(-m^2/1\text{GeV}^2)$, charm production by "ordinary" quarks should

be down by factors of the order 10^3 (as long as QCD effects are not dominant) and is negligible even at PETRA energies.

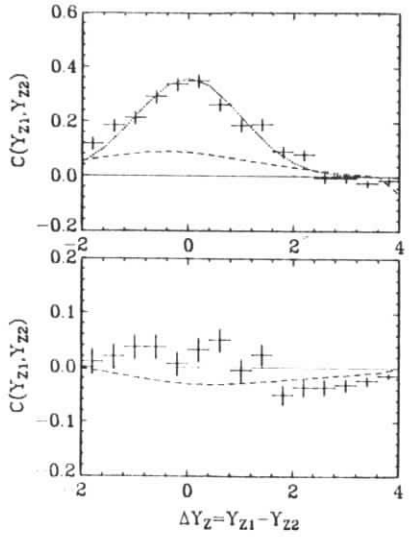

Fig. 4.18
Predicted behaviour of the two-particle correlation function $C(Y_{z1}, Y_{z2})$ defined by (4.2) where $Y_{z1} = 4.0$. C is plotted versus $\Delta Y_z = Y_{z1} - Y_{z2}$. Results are given for h_1 negative and h_2 positive (upper) and h_1 negative and h_2 negative (lower) and are generated using Monte Carlo (points). The dashed curves are the results for $C(Y_{z1}, Y_{z2})$ before the primary mesons are allowed to decay. The dotted curve (to guide the eye) is $0.36\exp(-\frac{1}{2}(\Delta Y_z)^2$. From ref. 112.

A next set of functions describes the emission of normal mesons in the fragmentation of charmed quarks. One is tempted to assume that these meson spectra agree qualitativly with those of normal unfavored decays, up to phase space effects. At the

moment there are no experimental results proving or disproving this conjecture. What stays as a last point is the fragmentation of charmed quarks into charmed mesons. The spectrum of phenomenological predictions ranges from steeply falling functions [126,127] to δ-functions peaked at high z.[128] More recent papers concord in the expectation, that charmed particles should carry out an unusually large fraction of the available energy[129)-131] In fact a detailed analysis of μμ and μe events from the CDHS and BNL neutrino experiments lead to the conclusion, that $D_c^D(z)$ is essentially flat in z.[132] This is in rough agreement with e^+e^- data (section 2.3) which favors a z-dependence between $(1-z)^0$ and $(1-z)^1$.

The prediction from quark fragmentation models, as discussed above, is unambiguous: the charmed meson has to be produced as the rank 1 meson. Further it makes nearly no difference if it is emitted as a pseudoscaler or as a vector meson. Due to its large mass the final charmed meson will carry nearly the whole momentum. So we have

$$D_c^D(z) \sim f(z) \qquad (4.48)$$

where f(z) is the decay function used for the recursive definition of the jet (eqn 4.16). Based on eqn (4.48) the jet model by Anderson et al predicts actually D_c^D to be constant, whereas the Feynman Field choice for f(x) (eqn 4.26) is incompatible with a flat fragmentation function. If the future analysis of experiments confirms the guess of ref.[132] one probably will have to go back to the naive expectation f(z) = const. and provide the "softness" of the normal fragmentation function by increasing the vector/pseudoscalar ratio for primary meson production.

4.5 Summary

Based on the quark-parton model, the space-time evolution of a quark jet can be visualized as an "inside-outside" cascade. Independent of the reference frame chosen, slow fragments are produced earliest. The production of leading fragments, or equivalently the final neutralisation of the primary color charge occurs after a time T proportional to the quark momentum Q. A quantitative description of this process can be given using an analogy to two dimensional QED, or a semi-classical quark model. The recursive scheme for jet generation proposed by Feynman and Field is consistent with these models; it reproduces the measured inclusive particle distributions in quark jets, and the data on correlations, fairly well. One should note, however, that much of this agreement results simply from constraints due to 4 - momentum and charge conservation, and can be obtained as well in an UJM (section 3).

5. Parton jets and QCD

The quark parton model was originally developped to provide a useful and simple description of the physics of deep inelastic phenomena.[1-4,135,136] The modern foundation for the parton model is the gauge theory of strong interactions based on the color degree of freedom: QCD. In QCD scaling of the deep inelastic structure functions, which describe the quark distribution within the nucleon, is predicted to be broken by logarithms of $q^2 = -Q^2$. Physically, these scaling violations are due to the emission or absorption of gluons during the hard scattering process. Thus although the naive parton model, strictly speaking, fails, it is possible to rephrase the parton language by assigning a well specified Q^2 dependence to the parton densities.[137]

$$G(x) \rightarrow G(x,Q^2) \qquad (5.1)$$

Already through the principle of analytic continuation of the scattering amplitude a Q^2 dependence of the structure functions, describing the distribution of partons in a hadron, induces automatically also a Q^2 dependence of the fragmentation functions, which parametrize the distribution of hadrons in a parton.[138,139]

The dynamical mechanisms leading to this scale breaking are sketched in fig (5.1): "before" the quarks emitted e.g. in e^+e^- annihilations reach the surface of the confining bag, they radiate gluons, which may in turn convert into new quark-anti-quark pairs. The bulk of low momentum gluons is reflected at the bag surface and compensates the "vacuum pressure". Gluons and quarks in the high momentum tail of the radiation however deform the surface of the bag and create a number of incoherent final state jets. The "parton shower" inside the bag is described by QCD, whereas the final confining stage has to be described by phenomenological models like the Feynman-Field -jet.

Fig. 5.1 suggests that the perturbative and nonperturbative stages of the process are well separated in space-time. This conjecture has been criticized by Frautschi and Krzywicki [117] with the

argument that the "hard" perturbative matrix elements become large precisly when the energy denominators become small, i.e. when the virtual intermediate states are relativly long lived. As an example, fig. 5.2 shows a space-time diagram of the process

$$e^+e^- \rightarrow q\bar{q}$$
$$\hookrightarrow q\bar{q}g$$
$$\hookrightarrow q\bar{q}\ q\bar{q}\ ,$$

where the splitting of jets happens after a low momentum hadron has been emitted.

Here we shall first discuss the mechanisms of scale breaking at the example of structure functions.
Finally we generalize the results to the case of fragmentation functions.

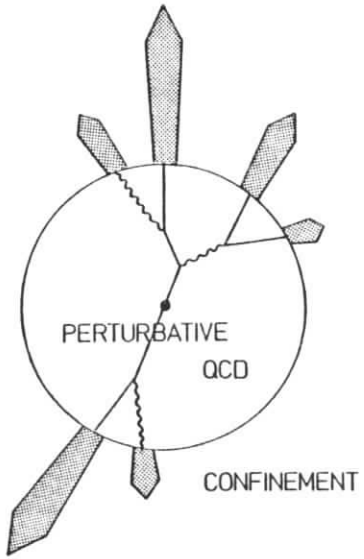

Fig. 5.1
The perturbative QCD scale breaking in parton jets through gluon emission and conversion. Full and wavy lines refer to quarks and gluons, respectivly.

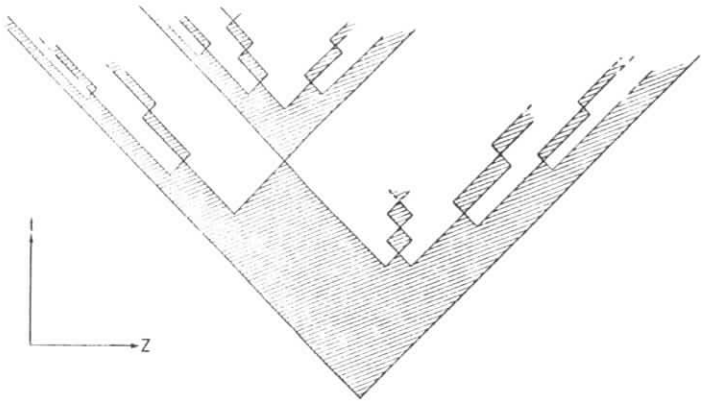

Fig. 5.2
A possible space-time diagram for $e^+e^- \to q\bar{q}\ q\bar{q}$ (in the notation of Anderson et al) .Some hadrons are already emitted before the splitting into four jets occurs.

5.1 Scale breaking in QCD

The formal, and theoretically rigorous derivation of scale breaking in QCD is formulated in the language of renormalization group equations for the coefficient functions of local operators in the light cone expansion for the product of two currents.[140]

A more intuitive model for scaling violations in scale invariant theories has been given by Kogut and Susskind [69], and we shall follow their line of argumentation.[69,142,143] We assume that matter organizes itself into "clusters"[144] For example,

molecules are made of atoms which are made of nuclei which are made of nucleons etc. Each cluster is characterized by a certain size and time scale. The relation between this scales appears to be accidental. However, as smaller and smaller scales are probed in high energy physics some kind of regularities may emerge; certain field theories e.g. suggest that the connections between adjacent scales become universal.

Consider time and length scales of ordinary hadrons, 10^{-13} cm, and denote those as N = 0 clusters which in turn are composite of N = 1 clusters (partons). Renormalization group investigations suggest that the dynamics of clusters of type N which form a cluster of type N-1 can be described by a Hamiltonian H_N without explicitly refering to smaller clusters (N+1, say). In an infinite momentum frame, H_N depends on the fractional momenta x of clusters of the type N and on their transverse momenta. The intuitive picture suggested by Wilson and Polyakov [145,146] was that at large N the coupling constant describing parton-parton interactions becomes constant and thus the ratio of typical scales $R_{N+1}/R_N = \delta$ approaches a constant at large N. In that case, the transformation connecting the Hamiltonians H_{N+1} and H_N is also independent of N.

Imagine now an experiment,which probes hadrons with particles of large four momentum q. Assume the q is space like, e.g.. Then a reference frame can be choosen such that q consists only of a three vector, $q = (0, \vec{q})$. Such a projectile will be able to resolve structures of the order of its wavelength $\lambda = Q^{-1} = (-q^2)^{-1/2}$. As the "target" hadron moves with roughly the speed of light, the time scales probed are of the order Q^{-1} as well. The parton distribution which is relevant for the description of the process is that of clusters with $R_N \approx \lambda$, since clusters of the type N+1 cannot be resolved by the probe, whereas clusters of type N-1 no longer appear pointlike.

This means

$$\lambda \approx R_0\, \delta^N \qquad (5.2)$$

or, with $\lambda \approx Q^{-1}$: $N \approx -\ln (R_0 Q)/\ln\delta$

To calculate the x distribution of clusters of type N within the original hadron

$$G_N(x) = \frac{1}{\sigma_h} \frac{d\sigma_N}{dx} \tag{5.3}$$

we introduce the function $h_{N+1,N}(z)$ which gives the probability per unit z to find a cluster of type N+1 and longitudinal momentum zx' in a cluster of type N and longitudinal momentum x'. Invariance under longitudinal boosts requires that h depends only on z and not on the absolute momenta of the clusters. We neglect transverse momenta for the moment being. The distribution of type N+1 clusters is given by the convolution

$$G_{N+1}(x) = \int_x^1 \frac{dx'}{x'} G_N(x') \quad h_{N+1,N}(\frac{x}{x'}) \tag{5.4}$$

We shall now loosen the assumption of the existence of discrete scales; real field theories may not contain such abrupt transitions between scales. A better description is given using a smooth connection between different N resp. Q. With the replacements

$$\begin{aligned} G_N(x) &\to G(x,t) \\ h_{N+1,N}(z) &\to h(z,t) \\ G_{N+1}(x) - G_N(x) &\to 2\ln(1/\delta)\frac{\partial G(x,t)}{\partial t} \end{aligned} \tag{5.5}$$

and

$$t = \ln(Q^2/Q_o^2) \tag{5.6}$$

we obtain the following equation for $G(x,t)$

$$2\ln\delta^{-1} \frac{\partial G(x,t)}{\partial t} = \int_x^1 \frac{dx'}{x'} \{G(x',t)h(\frac{x}{x'},t) - G(x',t)\delta(1-\frac{x'}{x})\} \tag{5.7}$$

or with the redefinition

$$p(z,t) = 2\ln\delta^{-1}.\ (h(z,t) - \delta(1-\tfrac{1}{z})) \tag{5.8}$$

eqn. (5.7) reads simply

$$\frac{\partial G(x,t)}{\partial t} = \int_x^1 \frac{dx'}{x'} p(\frac{x}{x'},t)\ G(x',t) \tag{5.9}$$

Eqn. 5.9 describes the number density of partons in an object which is probed at a momentum transfer $t = \ln(Q^2/Q_o^2)$. It can be generalized to the case were the probe is only sensitive to the distribution of partons carrying a set of quantum numbers i

$$\frac{\partial G_i(x,t)}{\partial t} = \int_x^1 \frac{dx'}{x'} \sum_j P_{ij}(\frac{x}{x'},t)\ G_j(x',t) \tag{5.10}$$

P_{ij} is the transition matrix between the various species of partons.

To solve eqn. (5.9) it is convenient to rewrite it in terms of moments

$$G(\alpha,t) = \int_0^1 dx\ x^{\alpha-1}\ G(x,t) \tag{5.11}$$

and

$$p(\alpha,t) = \int_0^1 dx\ x^{\alpha-1}\ p(x,t) \tag{5.12}$$

Eqn. (5.9) reads now

$$\frac{\partial G(\alpha,t)}{\partial t} = p(\alpha,t)\ G(\alpha,t) \tag{5.13}$$

resp. for eqn. (5.10)

$$\frac{\partial G_i(\alpha,t)}{\partial t} = \sum_j p_{ij}(\alpha,t)\, G_j(\alpha,t) \qquad (5.14)$$

The structure function G(x,t) can be obtained from its moments via the inverse Mellin transform or by approximative numerical methods.[147]

We shall discuss eqn. 5.13 for the two most interesting cases:

i) fixed point theories

In fixed point theories the dimensionless coupling constant α_s characterizing parton interactions tends to a nonzero constant as t grows. The dynamics and the function p become independent of t.
To solve eqn 5.13 we have further to supply boundary conditions for small, but yet asymptotic t. With the condition

$$G(\alpha,Q_o^2) = G_o(\alpha) \qquad (5.15)$$

we have

$$G(\alpha,Q^2) = G_o(\alpha)\left(\frac{Q^2}{Q_o^2}\right)^{p(\alpha)} . \qquad (5.16)$$

In other words, the moments of G are power behaved in Q^2.
Momentum conservation and unitarity require

$$p(2) = 0;\ p(1) > 0$$

and consequently

$$p(k) < 0 \text{ for } k > 2 \qquad (5.17)$$

That means that the parton distribution shrinks towards lower x with increasing Q^2, and the number of partons, $G(1,Q^2)$, increases.

ii) QCD as an example for asymptotically free gauge theories

In asymptotically free theories the coupling constant tends to zero as Q^2 goes to infinity, eg. in QCD[101,102]

$$\alpha_s(Q^2) = \frac{1}{b \ln (Q^2/\Lambda^2)} \qquad (5.18)$$

with

$$b = \frac{33-2f}{12\pi} \qquad (5.19)$$

f is the number of active flavors.

Due to the weak dependence of α_s on Q^2, fixed point theories are a resonable approximation for QCD within a limited range of Q^2. In the presently accessible region of Q^2, the two models have been shown to be indistinguistable in many aspects. For further calculations we write the transition probability p as a product of the effective coupling constant $\alpha_s(Q^2)/2\pi$ and a term depending only on the momentum ratios

$$p(x,t) = \frac{\alpha_s(t)}{2\pi}\, p(x) \qquad (5.20)$$

Eqn. (5.13)

$$\frac{\partial G(\alpha,t)}{\partial t} = \frac{\alpha_s(t)}{2\pi}\, p(\alpha)\, G(\alpha,t)$$

is now easily solved:

$$G(\alpha,t) = G_o(\alpha)\left(\frac{\alpha(o)}{\alpha(t)}\right)^{p(\alpha)/2\pi b}$$

$$= G_o(\alpha)\left(\frac{\ln(Q^2/\Lambda^2)}{\ln(Q_o^2/\Lambda^2)}\right) \qquad (5.21)$$

Thus QCD leads to logarithmic violations of scaling.
In real QCD, we have not simply one parton structure function G but instead the structure functions q_i and g of 2f quark flavors ($i = u,\bar{u},d,\bar{d},\ldots$) and the gluon. Summing over all color states, we get from eqn. 5.10:

$$\frac{dq_i(x,t)}{dt} = \frac{\alpha_S}{2\pi} \int_x^1 \frac{dx'}{x'} \left(\sum_j P_{ij}\left(\frac{x}{x'}\right) q_j(x') + P_{ig}\left(\frac{x}{x'}\right) g(x') \right)$$

$$\frac{dg(x,t)}{dt} = \frac{\alpha_S}{2\pi} \int_x^1 \frac{dx'}{x} \left(\sum_j P_{gj}\left(\frac{x}{x'}\right) q_j(x') + P_{gg}\left(\frac{x}{x'}\right) g(x') \right) \tag{5.22}$$

This are the well known Altarelli-Parisi master equations [137]. It must be pointed out here that the master equations decribe the t-dependence of the parton distribution function in momentum space. They do not refer to the time development of parton densities during the scattering process. The p functions can be evaluated using standard graph techniques [137] (fig. 5.3). In the leading log approximation all terms containing powers in $\alpha_S \ln Q^2$ are summed up; the direct terms in P_{ii} and P_{gg} are then given through momentum conservation.

$$P_{ij} = \frac{4}{3} \left(\frac{1+x^2}{1-x} \right)_+ \delta_{ij} + 2\delta(1-x)\delta_{ij}$$

$$P_{gi} = \frac{4}{3} \cdot \frac{1+(1-x)^2}{x}$$

$$P_{ig} = \frac{1}{2} \left(x^2+(1-x)^2\right)$$

$$P_{gg} = 6 \left[\frac{1-x}{x} + \left(\frac{x}{1-x} \right)_+ + x(1-x) - \frac{1}{12}\delta(x-1) \right] - \frac{1}{3} f\, \delta(x-1) \tag{5.23}$$

In terms of moments, eqn (5.22) yields a system of coupled differential equations which can be partially diagonalized by choosing suitable combinations of the parton densities: the flavor singlett and flavor nonsinglett (valence) components $q^s(x,t)$ and $q^{ns}(x,t)$

$$q^{ns}(x,t) = \sum_{u,d,s\ldots} q_i(x,t) - \sum_{\bar{u},\bar{d},\bar{s}\ldots} \bar{q}_i(x,t)$$

$$q^s(x,t) = \sum_{u,d,s\ldots} q_i(x,t) + \sum_{\bar{u},\bar{d},\bar{s}\ldots} \bar{q}_i(x,t) \tag{5.24}$$

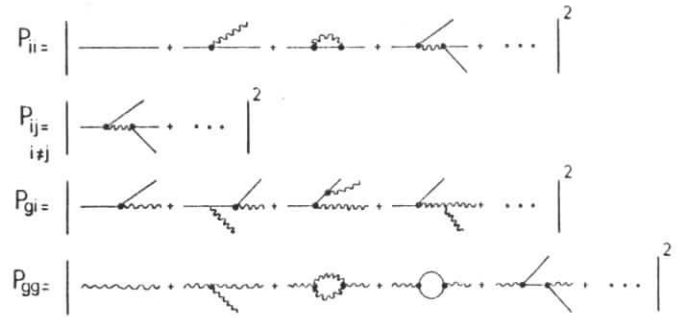

Fig. 5.3
First and second order contributions to the p-functions

Define now G as the vector of the α-th moments of the parton densities

$$G(\alpha,t) = (q^{ns}(\alpha,t),\ q^s(\alpha,t),\ g(\alpha,t)) \tag{5.25}$$

The master equations read then

$$\frac{\partial}{\partial t} G(\alpha,t) = \frac{\alpha_S}{2\pi} A(\alpha)\, G(\alpha,t) \tag{5.26}$$

with the matrix A (α)

$$A(\alpha) = \begin{pmatrix} p_{qq}(\alpha) & 0 & 0 \\ 0 & A_{qq}(\alpha) & 2fA_{qg}(\alpha) \\ 0 & A_{gq}(\alpha) & A_{gg}(\alpha) \end{pmatrix} \qquad (5.27)$$

The coefficients A_{qq} etc. are combinations of the moments of the p functions. The t-dependence of the nonsinglett component is obvious, it is given eqn. (5.21).

The most accurate experimental results on quark structure functions come from deep inelastic neutrino scattering.[149] To compare the QCD predictions with the data, one has to solve eqn. 5.26 including a guess for the unknown gluon structure function; in fact the predictions turn out to be nearly independent on the shape of g (x,t).[148]

Fig. 5.4 compares the predicted Q^2-dependence of $F_2(x,Q^2) \equiv x \sum_{u,\bar{u},d,\bar{d}\ldots} q_i(x,Q^2)$ with the CDHS data.[149] The only free parameter is the constant Λ from eqn. 5.18. The QCD curves shown are calculated for $\Lambda = 0.47$ GeV.

The agreement of experiment and QCD is very impressive; the shrinking of $F_2(x,Q^2)$ towards lower x with increasing Q^2, leading to a decrease of the higher moments, is exactly reproduced.

We are now prepared to discuss the QCD scale breaking of fragmentation functions.[150] Following again the ideas of Kogut, Susskind [69] and Polyakov [146], we assume that in a deep inelastic reaction or in e^+e^- annihilation, a parton of type

$$N = -\ln(R_o Q) / \ln\delta$$

is emitted. This parton "decays" now in a series of N-1 type partons which decay into N-2 type partons etc. Consequently, the distance of the partons four momentum from the mass shell increases with N.[146] So far as quantum numbers etc. are concerned, the partons at different N may well be identical, in QCD e.g. they are all quarks resp. gluons. Accordingly, we

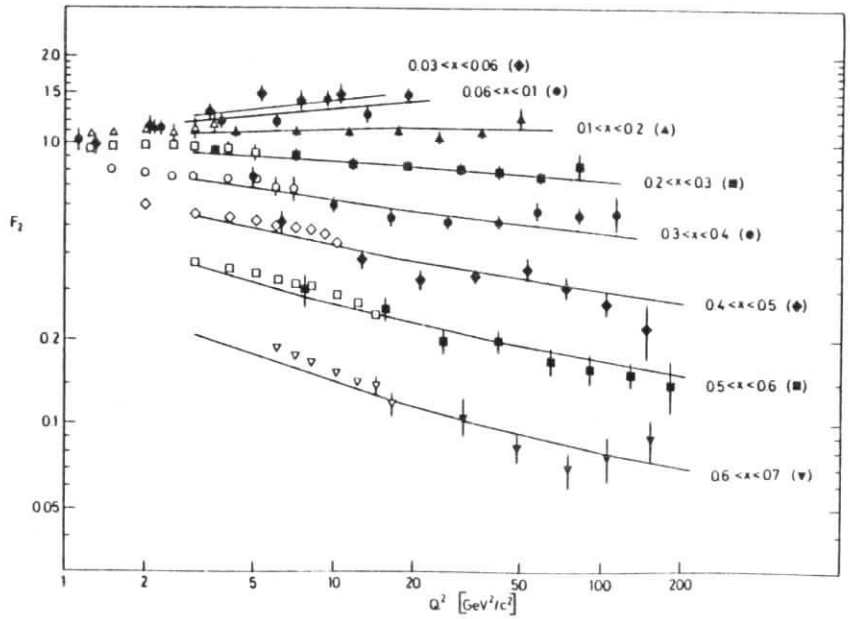

Fig. 5.4
The Q^2 dependence of the structure function F_2 measuring the quark plus antiquark density in the nucleon, as compared to QCD fits with $\Lambda = 0.47$ GeV[149].

get

$$G_{N-1}(x) = \int_x^1 \frac{dx'}{x'} G_N(x)\, k_{N-1,N}(\frac{x}{x'}) \qquad (5.28)$$

or

$$-\frac{\partial G(x,t)}{\partial t} = \int_x^1 \frac{dx'}{x'} r(\frac{x}{x'},t)\, G(x',t) \qquad (5.29)$$

Since we are still dealing with quark and gluon interactions governed by QCD, the r-functions in eqn (5.26) are identical to the p-functions in eqn (5.23). With the definitions of eqs (5.24), (5.25) we arrive at

$$-\frac{\partial}{\partial t} G(\alpha,t) = \frac{\alpha_S}{2\pi} A(\alpha)\, G(\alpha,t) \qquad (5.30)$$

For simplicity, we write the moments of the parton fragmentation functions D as a matrix as well, the element $D_j^i(\alpha,t)$ describing the decay of the j-th parton component (non singlet, singlet, gluon) into the hadron i (π^+, π^o, π^-...). The moments of the final state hadron density are then

$$\sigma(\alpha) = D(\alpha,t)\, G(\alpha,t) \qquad (5.31)$$

There are now two ways to describe the fragmentation of a quark at t_q, as sketched in fig. 5.5: the fragmentation function $D(\alpha,t_q)$ gives a direct mapping of the parton distribution at t_q

$$G(x,t_q) = (\delta(1-x), \delta(1-x), 0)$$

resp.

$$G(\alpha,t_q) = (1,1,0) \qquad (5.32)$$

onto the hadronic final state. On the other hand, $G(\alpha,t_q)$ can be described in terms of a superposition of partons at t_1, $0 \le t_1 \le t_q$. The relation between $G(\alpha,t_q)$ and $G(\alpha,t_1)$ is given by eqn (5.30). The hadronic final state can now be evaluted be applying $D(\alpha,t_1)$ on $G(\alpha,t_1)$. Of course the final state distribution function has to be independent of t_1.

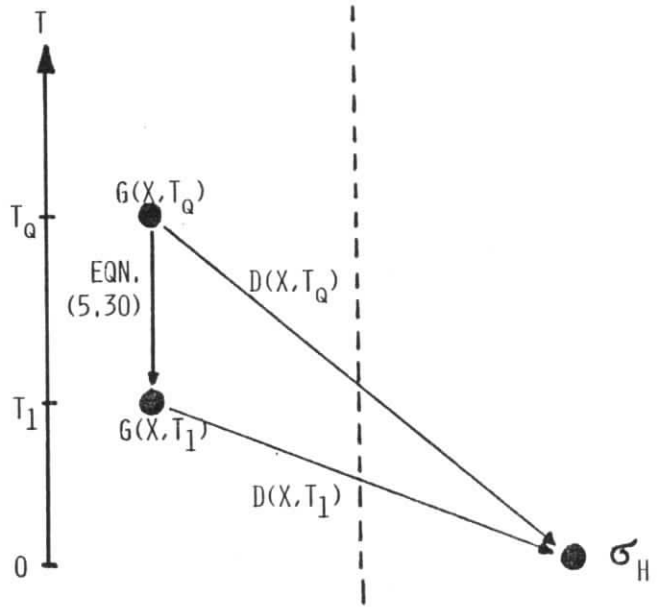

Fig. 5.5
The fragmentation of a quark at t_q can be considered as a mapping of the point $G(x,t_q) = (\delta(1-x), \delta(1-x), 0)$ onto a hadronic final state σ_h. This can be done in two steps: $G(x,t_q)$ is first mapped onto $G(x,t_1)$; next $G(x,t_1)$ is mapped onto σ_h.

So we get

$$\frac{\partial}{\partial t_1} \{ D(\alpha,t_1)\, G(\alpha,t_1) \} = 0$$

or, with eqn (5.30)

$$\frac{\partial}{\partial t} D(\alpha,t) = \frac{\alpha_S}{2\pi} D(\alpha,t)\, A(\alpha) \qquad (5.33)$$

To solve eqn 5.33 one needs a boundary condition at a reference Q^2. We could e.g. use the Feynman Field jet model at $Q^2 = 100\ GeV^2$ where QCD effects should be negligible. The explicit calculation of the scale breaking in parton jets is however complicated by the fact, that a physical quark or gluon is never a pure flavor nonsinglett. Through the singlett term in the quark density $G(\alpha,t_q)$, quark and gluon terms become mixed up. Thus to find the quark fragmentation function, one has to know as well the gluon fragmentation functions at the reference Q^2. To arrive at a more quantitative understanding of the process, we shall consider the parton densities $G(x,o)$ within a jet initiated by a quark at $Q^2 >> Q_o^2$. Q_o^2 is chosen as low as possible (of course, the validity of the perturbative QCD expansion has still to be garanteed). That means, we observe the "parton shower" initiated by a primary quark at a point just before the nonperturbative conversion into hadrons starts. De Grand [151] has shown that in the high Q^2 limit the distributions q^{ns} (favored nonsinglet component), $q^{unf.}$ (unfavored component, e.g. antiquarks) and g (gluons) from eqn (5.30) may be approximated by

$$q_q^{ns}(x,o) \sim (1-x)^{\frac{16}{3}\xi - 1} \qquad x \to 1, \xi > .05$$

$$q_q^{unf}(x,o) \sim (1-x)^{\frac{16}{3}\xi + 1} \qquad x \to 1$$

$$g_q(x,o) \sim (1-x)^{\frac{16}{3}\xi} \qquad x \to 1, \xi > .05 \qquad (5.34)$$

The subscript q refers to the nature of the parent parton, ξ is defined by

$$\xi = \frac{1}{4\pi b} \ln \left(\frac{\alpha_S(Q_o^2)}{\alpha_S(Q^2)} \right) \qquad (5.35)$$

Obviously, as Q^2 goes to infinity, all parton (and hadron) densities concentrate at $x = 0$. The ratio of the various components stays constant. Compared to the valence quark, gluons and sea quarks are suppressed by factors $(1-x)$ and $(1-x)^2$ resp. Thus the leading particle effect, which means the dominance at high x of particles containing the original quark is not destroyed by the QCD corrections. The final hadron spectrum is given by the convolution of eqs. (5.34) with the fragmentation function $D^h(x,o)$. Therefore the steepening of the leading hadron distributions occurs at the same rate as in q_q^{ns}. Comparing e.g. typical DORIS and PETRA energies, we get

$$\frac{x}{\sigma}\left(\frac{d\sigma}{dx}\right)_{Q^2 \approx 1000\ GeV^2} \underset{x \to 1}{\approx} (1-x)^{0.5} \frac{x}{\sigma}\left(\frac{d\sigma}{dx}\right)_{Q^2 \approx 10\ GeV^2} . \qquad (5.36)$$

5.2 Preconfinement

If one compares the QCD results on parton fragmentation (eqn. 5.33) with the results of naive confinement models (chapter 4), a paradoxon seems to emerge: in QCD, the decay of a parton at Q^2 into many partons at lower Q_o^2 is entirely governed by the color charge of the fragmenting parton; the pictorial flux tube connecting the two color sources plays no role at all, a second source is not even needed! Furthermore, the QCD "final" state at t=0 contains a number of color triplet - and octet sources, which are assumed to decay independently according to fragmentation functions D(x,0), wheras naivly one expects a system of color flux tubes joining theses sources. Finally, since the fragments of each t=0 parton cover the y range from y_{parton} to y=0, the

height of the rapidity plateau depends on the choice of reference frame used for description; the results are not lorentz invariant.

The origin of these problems is presumably the following: the confinement- and the QCD picture, respectivly, apply to different stages of the process. The naive confinement picture mainly adresses the question of the formation of the rapidity plateau, whereas the QCD approach describes the distribution of fast fragments in jets. Actually, the leading log approximation on which eqn. (5.33) is based, is invalid for $x \lesssim Q_o^2/Q^2$ because additional terms $(1/x)\ln x$ become important [152]. Therefore eqn. (5.33) makes no predictions on the height of the rapidity plateau, on multiplicities etc.

Nevertheless, the question stays how the two different approaches, the confinement model at low x and at $Q^2 \approx Q_o^2$, and the QCD picture at high Q^2 join smoothly.

Recently, Konishi, Ukawa and Veneziano [153] have proposed a generalization of eqn. 5.33 to describe the t-dependence of n-parton cross section in jets. They describe the parton fragmentation as a branching process [159]; an exact derivation of their method has been given by Kirschner [154], using the leading log approximation. In close analogy to the model of Kogut and Susskind [69], it is shown that in the QCD evolution of a jet, partons of size Q_K decay ("branch") into two partons of size Q_{K-1}. In contrast to the scale breaking of structure functions, this process may be visualized as real decay in space-time. [160] The lifetime Γ_K associated to the propagator of a parton in the K-th generation is [160]

$$\Gamma_K = x_K Q/Q_K^2 \qquad (5.37)$$

in agreement with the naive expectation from the uncertainity relation, $\Gamma_K = \gamma/\Delta E$, with $\gamma = x_K Q/Q_K$ and $\Delta E = Q_K$. From (5.37) we get the total time for jet development

$$\Gamma = \sum_{K=1}^{N} \frac{Q}{Q_K^2} 2^{K-1} \simeq \frac{Q}{Q_o^2} \exp((\ln Q^2/Q_o^2)^{1/2}) \qquad (5.38)$$

The factor 2^{k-1} in eqn. (5.38) arises since the k-th generation contains 2^{k-1} partons. This result is in qualitative agreement with that obtained from the naive fragmentation model of section 4.1.

The jet development by branching of a parton of mass Q_k into two partons close in mass instead of decay by on shell brems-strahlung is a specific feature of the parton formfactor in QCD.

One gets

$$\frac{Q_{k+1}^2}{Q_k^2} \approx \exp(-2(\ln Q_k^2/Q_o^2)^{1/2}) \qquad (5.39)$$

Consequently, a parton of mass Q evolves on the average to [160]

$$\langle n \rangle \approx \exp((\ln Q^2/Q_o^2)^{1/2}) \qquad (5.40)$$

final partons of mass Q_o. The average number of branching steps is

$$\langle N \rangle \approx (\ln Q^2/Q_o^2)^{1/2}/\ln 2 \qquad (5.41)$$

This description gives a very handy, and intuitive picture of the fragmentation of a quark of mass Q into partons of mass Q_o, but does it help to close the gap between the perturbative jet and the rudimentary models of final confinement? This connection was established by a recent work of Amati and Veneziano [155]. They calculated the distribution of color among the n final partons of mass Q_o, with the astronishing result that already perturbative QCD provides a "preconfinement" of color. They discovered that these "final state" partons are grouped into colorless clusters in a number sufficient to "exhaust" the final state, but still posessing a finite average mass of the order Q_o^2. The result is peculiar of QCD, in particular of its non-abelian nature. Let me briefly sketch their derivation. In the axial gauge and at the leading log level, the flow of color during the degradation of a high Q^2 quark into partons at Q_o^2 is determined by planar diagrams, which means that color flow lines must not cross. Nonplanar diagrams are suppressed by $1/N_{color}$ factors.

This is visualized by fig. 5.6; note that a quark corresponds to a single color line whereas a gluon can be displayed as a color triplet-antitriplet state corresponding to two color lines. Obviously, it is always possible to group the "final state" partons into nonoverlapping, colorless clusters.

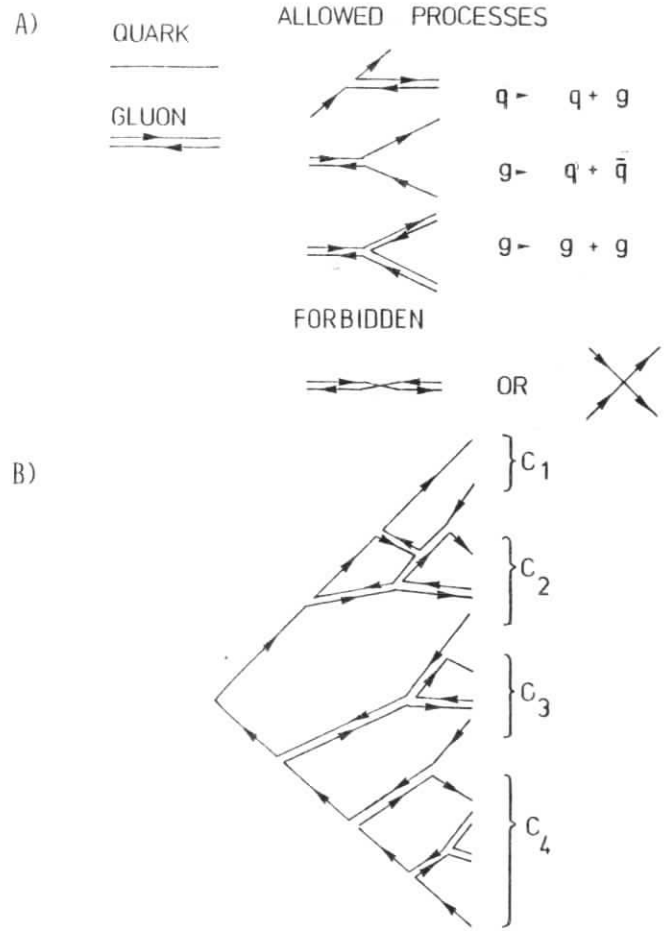

Fig. 5.6

a) Drawing rules for planar QCD graphs

b) Planar graph of the process e^+e^- → hadronic clusters; the "final state" color lines can be grouped into color singlet clusters $C_1 \cdots C_N$

Partons inside each cluster are nearby in the branching-tree structure of the jet. Consequently, the clusters have finite masses. The cluster mass spectrum is cut off in the form [156]

$$\frac{1}{\sigma}\frac{d\sigma}{dM_c^2} = \frac{1}{M_c^2}\left(\frac{Q_o^2}{M_c^2}\right)^{\lambda} \log\left(\frac{M_c^2}{Q_o^2}\right)^{\nu} \qquad (5.42)$$

where λ and ν are of order 1. Thus we get $\langle M_c \rangle \simeq O(Q_o)$; this is a non-trivial result since the $\langle M^2 \rangle$ of two partons chosen randomly grows as $Q^2\, \alpha_S(Q^2)$.

Relative transverse momenta of nearby clusters turn out to be small, but the mean $p_\perp$ of a cluster is of the order $Q/\ln Q$.

The multiplicity of clusters is given by

$$\langle n_c \rangle = \exp\left(2\sqrt{\frac{N_c}{\pi b}}\ln Q^2/\Lambda^2\right)/\exp\left(2\sqrt{\frac{N_c}{\pi b}}\ln Q_o^2/\Lambda^2\right) \qquad (5.43)$$

Notice that $\langle n_c \rangle$ grows faster with Q than any power of logarithms.

The importance of these results is obvious; under the reasonable assumption that confinement at Q_o^2 converts these clusters into hadrons without a large reshuffling of color lines, the final state of the parton evolution is no longer a system of virtual colored objects which are hard to deal with. Instead one has a number of physical objects, which can be treated as on-shell massive states and whose properties are independent of the initial Q.

There are now two philospophies to proceed further. Either one choosen Q_o^2 relatively large, $Q_o^2 \gtrsim 10\ \mathrm{GeV}^2$. In this case the reliability of the QCD calculation is guaranteed, however one has to tackle the question how a cluster of $M^2 = Q_o^2 = 10\ \mathrm{GeV}^2$ fragments. The other way is to use a Q_o^2 as low as possible, $O(1\mathrm{GeV}^2)$ [157]. In this case the final state clusters can be identified as the usual meson resonances, and a simple isotropic

phase space volumes describes their decays with reasonable accuracy. This fragmentation model is once more illustrated in fig. 5.7.

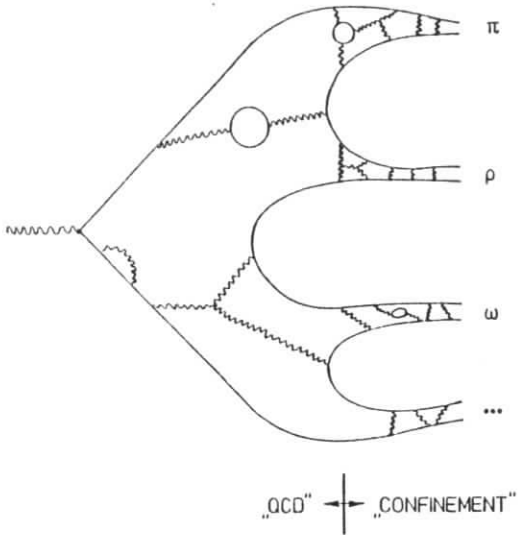

Fig. 5.7 Perturbative and nonperturbative stages of parton confinement.

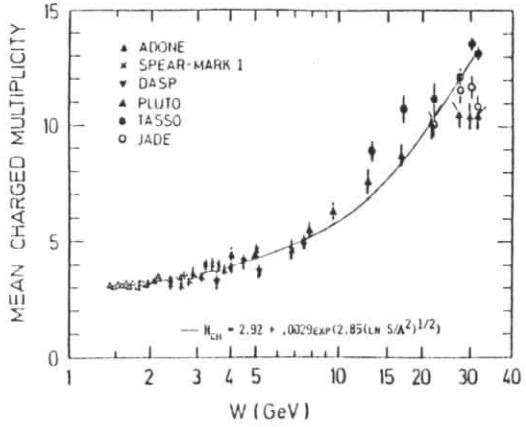

Fig. 5.8 Comparison of measured and predicted hadron multiplicities (eqn. 5.43).

How reliable is this picture? In fig. 5.8 the predicted total multiplicity is compared to the measurements. The final state hadron multiplicity was assumed to be proportional to the cluster multiplicity

$$\langle n \rangle = a\langle n_c \rangle + n_o \quad ;$$

the additional constant n_o accounts for low energy threshold effects. A fit to the data yields [24] (fig. 5.8)

$$\langle n_{ch} \rangle = 2.92 + 0.0029\exp(2.85\sqrt{\ln(Q^2/\Lambda^2)})$$

using $\Lambda = 0.5$ GeV. The factor 2.85 in front of $\sqrt{\ln(Q^2/\Lambda^2)}$ is in good agreement with the estimation by QCD, $2\sqrt{N_c}/\pi b \sim 2.3\text{-}2.5$. These concepts are further supported by recent calculations of Field and Fox who simulated the parton shower in a Monte Carlo model in analogy to simulations of electromagnetic showers, thus keeping trace of all finite mass- and finite transverse momentum effects. Their results are in reasonable agreement with data [158]. At present, however, the idea of preconfinement should be considered as a tool for the consistent treatment of parton fragmentation, and not as a precise quantitative model of jets at subasymptotic energies.

5.3 Production of heavy hadrons

Another essential aspect of scale breaking in quark jets is the production of heavy quark flavors [157]. At sufficiently high Q^2, it is possible that a gluon radiated from the primary quark converts into a pair of heavy quark flavors, like charm etc. The charmed quarks fragment and produce charmed mesons.
In principle, such processes are contained in eqs. (5.30) and (5.33), since the p-functions (eqn. 5.23) explicitly depend on the number of flavors f. Practically, these effects are neglected in most calculations because otherwise the p-functions get an additional Q^2-dependence via

$$f = f(Q^2)$$
$$= 3 + S(Q^2/m_c^2)\,\theta\,(Q^2-m_c^2) + S(Q^2/m_b^2)\,\theta\,(Q^2-m_b^2) + \cdots \qquad (5.45)$$

m_c, m_b are masses of the order of the charmed and bottom quark masses, respectively. $S(Q^2/4m_c^2)$ is a threshold factor going to unity as $Q^2/4m^2 >> 1$. Neglecting S, the Q^2-dependence of the charmed meson production can be calculated from eqn. (5.33)

$$\frac{\partial}{\partial t} D(x,t) = \frac{\alpha_S}{2\pi} D(x,t) A(x,f(t))$$

chosing $\ln\left(\frac{m_c^2}{Q_o^2}\right) \leq t \left(\leq \ln \frac{m_b^2}{Q_o^2}\right)$

and $f = 4$.

As a boundary condition

$$D\left(x, \ln\left(\frac{m_c^2}{Q_o^2}\right)\right) = \delta(1-x) \qquad (5.46)$$

seems natural.

Fig. 5.8 a) shows the results for perturbative charm production by charmed quarks, gluons, and light quarks as given by Georgi and Politzer [161]. The quantity plotted is the second moment of the charmed meson distribution, equivalent to the mean fraction of momentum carried by all charmed fragments. Qualitativly, the curves behave as expected: charmed initial quarks are most effective in producing charmed mesons, only at high Q^2 additional quarks and gluons are produced perturbativly, thus diminuishing the mean "charmed momentum". At first sight, however, the enormous difference between the light quark and gluon fragmentation function seems surprising. The obvious reason

is that a heavy quark can be produced by a primary gluon via pair production; in the light quark case the gluon has to be taken from the steeply falling bremsstrahlung spectrum.

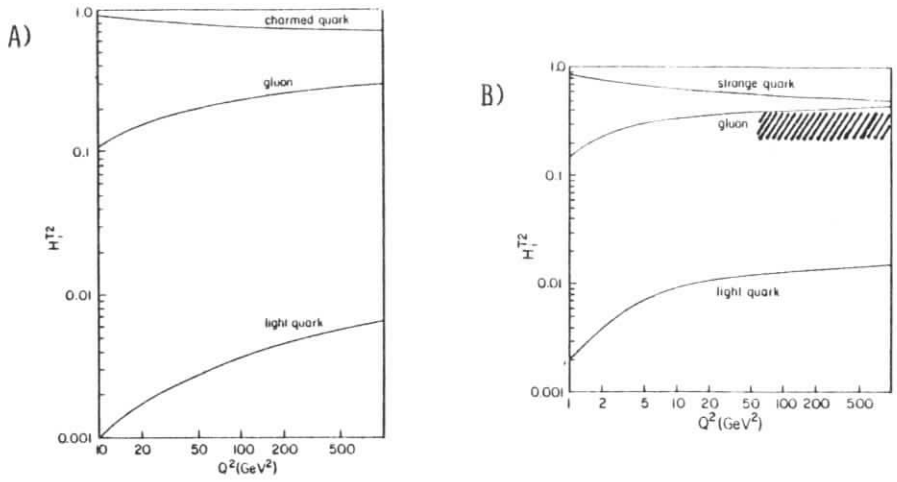

Fig. 5.8

a) The n = 2 moments of the total decay function into charmed hadrons, for charmed quarks, gluons and light quarks versus Q^2.

b) The n = 2 moments of the total decay function into strange hadrons, for strange quarks, gluons, and light quarks versus Q^2. [161]

Adding nonperturbative contributions all curves will be within the shaded area (for u,d and s quarks, the values given in table 4.1 are shown; gluon will be between light, and strange quarks).

Quantitativly, the model does not reproduce the presumably falling fragmentation functions of charmed quarks into a charmed meson. This default is due to the boundary condition of eqn (5.46), and it demonstrates that one has to be very careful

in choosing these limits; the boundary conditions imposed on eqn (5.33) have to be given in a region where the quark fragmentation is dominated by perturbative QCD effects, and where the influence of phase space is negligible. Eqn. (5.46) however is merely a consequence of the limited phase space available.

Georgi and Glashow have as well tried to describe the perturbative production of strange mesons (fig. 5.8 b), using m_s = 500 MeV. In this regime first order perturbative QCD is not expected to hold, so the strong discrepancy to the measured values is not astonishing (use e.g. the Feynman-Field jet as a parametrization of nonperturbative jets at moderate Q^2, one gets D^s_s (2, Q^2 = 100) = 0.38 and $D^s_{u,d}$ (2, Q^2 = 100) = 0.22; gluons should be in between).

5.4 Transverse momentum structure of parton jets

In the naive quark jet models, the lateral width of the jet is essentially determined by the diameter of the color string connecting the primary quarks. The mean transverse momentum of the produced particles is independent of the jet energy resp. Q^2, and of the x of the particles, apart from trivial kinematical effects at very low and at very high x. Such a naive jet represents a cylinder in momentum space.

All these statements become invalid as soon as one includes QCD scale breaking. This is easily visualized in the scale invariant parton model of Kogut and Susskind (see 5.1).[142] Let us calculate the transverse momentum of a parton of size k-1 descending from a parton of size k. Since no other scale is present, the result must be proportional to the parton size

$$\langle p_\perp^2 \rangle_{k-1} = \left(\frac{1}{R_k}\right)^2 f(\alpha_k) \qquad (5.47)$$

f is a function of the strong coupling constant α_k.

In asymptotic free theories one can calculate $f(\alpha_k)$ perturbativly Only those decays, may contribute to transverse momentum fluctuations, where two or more partons of type k-1 are generated. Therefore

$$\langle p_\perp^2 \rangle_{Q^2} = Q^2 \, \alpha^2 \, (Q^2) \quad . \qquad (5.48)$$

In the following stages of the decay, this transverse momentum is smeared out and distributed among the <n> final hadrons. Thus scale breaking effects yield an additional smearing of the final state

$$\langle p_{\perp \text{hadron}}^2 \rangle \sim \frac{\alpha^2(Q^2) Q^2}{\langle n \rangle} \qquad (5.49)$$

Furthermore, this smearing depends on the fraction of momentum carried by the hadron. A hadron at high x must contain partons from "early" stages of the decay and thus carry their large transverse momentum. A hadron at low x, on the other hand, will only contain one of the many fragments in the late stages of the decay and will receive only a small fraction of the early partons transverse momenta. The mean square transverse momentum from perturbative scale breaking is given by

$$\langle p_{\perp \text{hadron}}^2 \rangle_p = x \, \kappa(x) \alpha^2(Q^2) \, Q^2 \qquad (5.50)$$

Phase space factors are included in $\kappa(x)$

$$\kappa(x) = \begin{cases} 0 \text{ for } x \to 1 \\ \sim 1 \text{ else} \end{cases} \qquad (5.51)$$

The total transverse momentum is the sum of perturbative and nonperturbative components

$$\langle p_{\perp hadron}^2 \rangle = \langle p_{\perp p}^2 \rangle + \langle p_{\perp NP}^2 \rangle \qquad (5.52)$$

A QCD jet at very high Q^2 is therefore represented by a cone in momentum space.

There are two ways to calculate the transverse structure of jets explicitly from QCD. First, is it easy to generalize eqn. (5.33) and include transverse momenta in the p functions [162]. Since in this case one has to know how jets look at a reference Q^2, this method is not able to predict the width of QCD jets a priori; or, more precisly, as the estimates given above (eqn (5.49) and (5.50)) in fact represent only lower limits, the method is not even able to prove the existence of finite width QCD jets at all.

A second way was proposed by Sterman and Weinberg, [36] which avoids these problems. They calculated the full QCD cross section in first order of α_s for quark-antiquark production by virtual photons. The diagrams contributing to σ are shown in fig. 5.9. It turns out, however, that this cross section exhibits singularities due to the vanishing gluon mass. However, any cross section which is physically relevant should be stable and free of infrared singularties even in the massless limit.

In fact, the reason for the divergencies is that the fully exclusive cross section evaluated from fig. 5.8 has no physical meaning in the limit $m/\sqrt{s} \to 0$, it is not measurable. For example, no detector is able to distuinguish in the massless limit one particle and several particles moving in the same direction with a vanishing angular divergence.

The Kinoshita-Lee-Nauenberg theorem [164,165] states a way how to avoid this problem: it says that any quantity which could actually be measured is free of infrared divergencies in each order of perturbation theory.

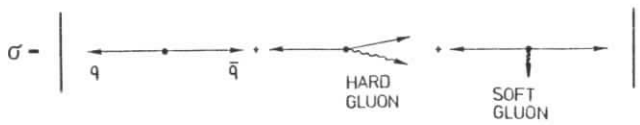

Fig. 5.9
Diagrams contributing to the transverse with of QCD quark jets in first order of α_s [36]

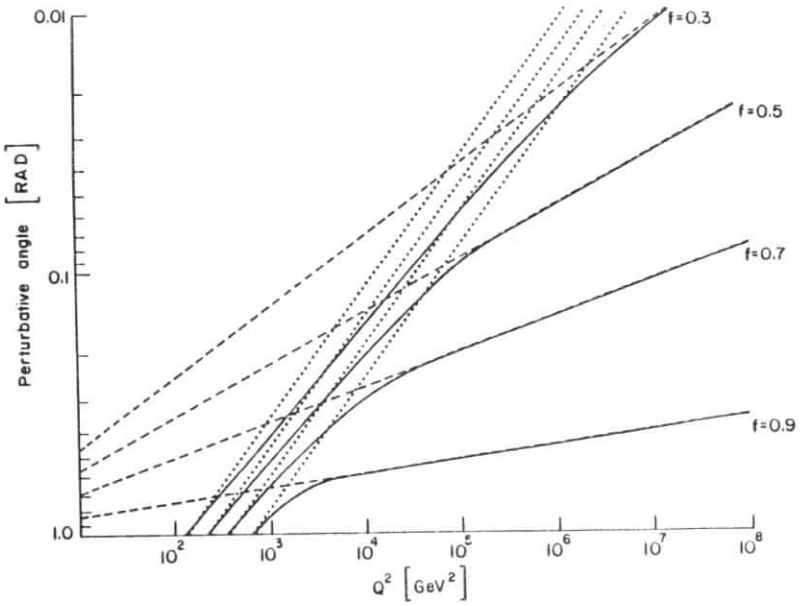

Fig. 5.10
Half opening angle of a double cone containing at least 90 % of the total energy in a fraction f of all events of the reaction $e^+e^- \to$ hadrons. The dotted resp. dashed lines show nonperturbative resp. perturbative contributions.[179]

As a measure of the transverse width of a jet, Sterman and Weinberg calculated the fraction f of events having a fraction ε of their energy outside a pair of oppositly directed cones of half angle $\delta \ll 1$. Their calculation confirmes the conjectures made above. In the final cross section, all singularities from the single diagrams cancel, and one obtains

$$f = 1 - \frac{4}{3\pi}\,\alpha_s(Q^2)\quad [3\ln\delta + 4\ln\delta\ln 2\varepsilon - \frac{\pi^2}{3} - \frac{7}{4}] \tag{5.53}$$

ε and δ must be chosen such that $1 \gg (\alpha_s/\pi)\ln\delta\ln 2\varepsilon$.

Extensions of this formula to a wider range of parameters and calculations in higher orders have been published by several authors [166,177,178], the main results of (5.53) however remain unchanged: neglecting the effects due to confinement, QCD jets are well collimated in angle. At $\sqrt{s}$ = 7 GeV eg. one obtains a fraction of 70 % of all events having more than 80 % of their energy within a double cone of half angle 13°. At increasing energy and constant fractions, this angle decreases as $E^{-1/4}$. Thus the conjecture that jets look narrower at higher energies is supported by QCD. The rate of shrinking of the opening angle is however much less than expected for fixed $p_\perp$ jets. At finite energies, eqn. (5.53) does not describe the final state hadrons, there the nonperturbative smearing of transverse momenta has to be included according to eqn. (5.52). The interplay of the two components is demonstrated in fig. 5.10, which shows results of Monte-Carlo calculations taken from ref. 179) . In fig. 5.10 the half angle of a double cone containing 90 % of the energy in a fraction f of all events is plotted as a function of Q^2. Dotted resp. dashed lines denote the contributions from the nonperturbative resp. preturbative components alone. One recognizes that below Q^2 = 1000 GeV^2 QCD effects are small; above $Q^2 = 10^4 - 10^5$ GeV^2, one has nearly pure QCD jets.

5.5 Gluon jets

Up to now, we have dealt with the simplest type of jets: quark-antiquark jets resulting from the confinement of a color triplet-antitriplet system. However, color confinement is of course not restricted to color tripets; any attempt to separate nonsinglet color systems will produce jets. In QCD, the second basic colored state besides the tripet is an octet, the gluon.

Assume, we generate two color octets of opposite color charge with a high invariant mass Q^2. This could eg. happen in the decay of a heavy quark-antiquark bound state like the Υ into a photon and two gluons.[167] How will the jet look like?

The two most important predictions for hadron production by color octet sources are (referred to the two gluon cms):

i) the multiplicity in the rapidity plateau is increased by a factor 9/4 compared to quark jets [153, 15]

ii) the color octet jet is softer, it contains less fast hadrons than a quark jet. Asymptotically one expects [151, 15]

$$D_g^h(x,t) \underset{\substack{x\to 1\\ t\to\infty}}{=} (1-x)\, D_q^h(x,t) \tag{5.54}$$

Both features are already evident from the Schwinger model presented in section 4.2. Assume, the primary partons have a color charge g' different from the coupling g which ties two fermious together to form a boson of the mass

$$m = \frac{g}{\sqrt{\pi}}\ .$$

From eqn. (4.10) we obtain now

$$\frac{1}{\sigma}\frac{d\sigma}{dy} = \frac{1}{(2\pi)^2}\left|\int d^2x\, e^{ipx} g\,\phi'_{ext}\right|^2 = \frac{g'^2}{\pi m} = \frac{g'^2}{g^2} \tag{5.55}$$

Now remind that in SU(N) the squares of charges of the N-plet resp. N x $\bar{N}$-plet are given by the structure constants of the group

$$g_N^2 = \frac{1}{N} \sum_a t^a t^a = \frac{N^2-1}{2N} = \frac{4}{3} \quad \text{for SU(3)c}$$

$$g_{N\times\bar{N}}^2 = \frac{1}{N^2-1} \sum_{abc} C_{abc} C_{abc} = N = 3 \quad \text{for SU(3)c} \tag{5.56}$$

So we expect

$$\left(\frac{1}{\sigma}\frac{d\sigma}{dy}\right)_{8\times\bar{8}} \Big/ \left(\frac{1}{\sigma}\frac{d\sigma}{dy}\right)_{3\times\bar{3}} = g'^2/g^2 = 9/4 \tag{5.57}$$

The relative softness of the gluon jet is now required by simple energy-momentum conservation.

In the QCD language these results are obtained by integrating eqn (5.30)

$$-\frac{\partial}{\partial t} G(\alpha,t) = \frac{\alpha_S}{2\pi} A(\alpha)\, G(\alpha,t) \tag{5.58}$$

from the starting point $t=t_{quark}$ and $t=t_{gluon}$ down to a low reference scale $t_o = 0$. With the trivial boundary conditions (compare eqn. 5.25)

$$G_q(\alpha, t_{quark}) = (\underset{\text{density}}{\overset{\text{nonsinglet}}{\text{quark}}}, \underset{\text{density}}{\overset{\text{singlet}}{\text{quark}}}, \underset{\text{density}}{\overset{\text{gluon}}{\text{gluon}}}) = (1,1,0)$$

and

$$G_g(\alpha, t_{gluon}) = (0,0,1) \tag{5.59}$$

we obtain for the numbers $G_q(1,0)$ and $G_g(1,0)$ of t=0 partons in quark and gluon jets, respectivly

$$G_q(1,0) = (1, \tfrac{4}{9} q(t_{quark}), \tfrac{4}{9} g(t_{gluon}))$$

$$G_g(1,0) = (0, q(t_{gluon}), g(t_{gluon})) \tag{5.60}$$

In an infinite momentum frame, q(t) and g(t) diverge due to the 1/x spectrum of non valence components. At a finite jet momentum, q(t) and g(t) are limited since partons of wavelength greater than the typical hadron size decouple. In this case, q(t) and g(t) can be approximated as a product of the length of the rapidity plateau and a function power behaved in t, which is roughly of the order of 1 for Q_o^2 chosen as low as possible in QCD ($Q_o^2 = 2\cdots5$ GeV^2) and usual Q^2. At all t, we have g(t) >> q(t).

So we see that the density of partons in the gluonic plateau is 9/4 times the density in the quark plateau. Correspondingly the number of final state hadrons should by larger by roughly the same factor. It has been pointed out by Brodsky that the last assumption may be only approximately valid.[169] Due to the higher density of partons in rapidity, the average mass of the hadronic clusters formed in the last stage of confinement should be smaller, and as well their decay multiplicity. Nevertheless, the height of the plateau of gluon jets should be roughly twice as large as in quark jets.

The hadron spectrum at high x from gluon jets can be estimated from the parton spectrum at $x \to 1$. In the limit of high Q^2, we get[151] in analogy to eqn. 5.34:

$$q_g(x,0) \sim (1-x)^{\frac{16}{3}\xi}$$

$$g_g(x,0) \sim (1-x)^{12\xi-1} \qquad x \to 1, \xi > .05 \tag{5.61}$$

Eqn. 5.61 demonstrates the striking fact that the quark spectrum within a gluon is much flatter than the spectrum of gluons within a gluon jet. Thus the leading particle within a gluon jet at high Q^2 is a quark!

Actually, though the number of quarks is small compared to the number of gluons in a gluon jet (eqn. 5.60) the fraction $x_{q/g}$ carried by t=0 quarks in a gluon jet is roughly 50%

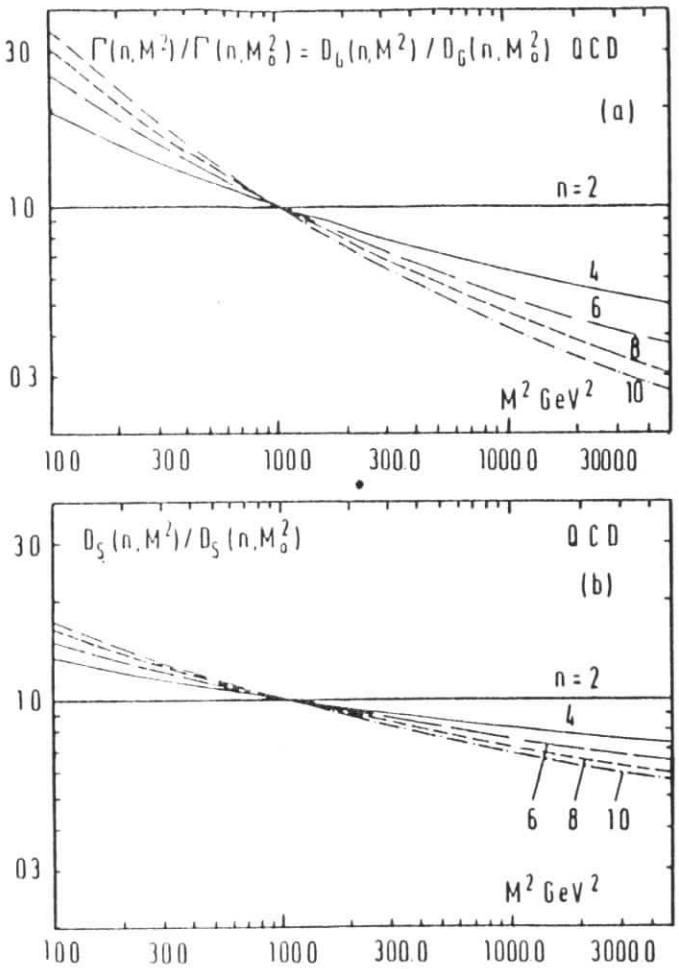

Fig. 5.11
Q^2-dependence of the n^{th} moment of the fragmentation function of gluons (a) and quarks (b), normalized at $Q^2 = M^2 = 100\ GeV^2$. 376)

$$x_{q/g}\Big|_{t\to\infty} = \frac{3f}{16+3f} = 0.43 \text{ for } f = 4 \qquad (5.62)$$

(If is further interesting to note that $x_{q/Jet}$ is independent of the parent parton for $t \to \infty$)

The explanation for eqs. (5.61) and (5.62) is simple: the coupling of gluons to gluons is stronger than the coupling of quarks to gluons; so once a quark is produced it degrades much slower in momentum than e.g. the parent gluon.

Since fast hadrons from gluon jets stem mostly from quarks, we have

$$\frac{D_g^h(x,t)}{D_q^h(x,t)} \sim \frac{q_g(x,0)}{q_q^{ns}(x,0)} \underset{x\to 1}{\sim} (1-x) \qquad (5.63)$$

The stronger coupling of gluons to gluons further leads to a different pattern of scaling violations: first, the mean perturbative opening angle of gluon jets is 9/4 of the opening angle of a quark jet at the same Q^2 [170,171]. Second, the effects of longitudinal scale breaking are increased by roughly the same factor. This is evident from fig. 5.11, where the Q^2 dependence of the n-th moment of the final state hadron density (n=2,4,6,8,10) is shown for gluon jets (a) and for quark jets (b) (taken from ref. 376).

An interesting interpretation of gluon jets is suggested by topological models [153,180,181]: in the limit of infinitely many colors, the ratio of gluon multiplicities within color octet jets and color triplet jets is given by (eqn 5.59)

$$\left(\frac{1}{\sigma}\frac{d\sigma}{dy}\right)_{8\times\bar{8}} \Big/ \left(\frac{1}{\sigma}\frac{d\sigma}{dy}\right)_{3\times\bar{3}} = \frac{g'^2}{g^2} = \frac{2N}{N^2-1} \cdot \underset{N\to\infty}{N=2}$$

The plateau of a gluon jet is thus represented by the sum of the plateaus of two quark jets. In the $N \to \infty$ limit, a gluon jet can be visualized by two diagrams like fig. 5.6 b) put on top of each other.

This model describes as well the distribution of the leading quarks within the gluon jet, assuming that the "dissoziation" of the color octet into a triplet plus an antitriplet is equivalent to the decay of the leading gluon into two quarks. From eqn. 5.23 we known that the distribution of quarks at high Q^2 within a gluon jet is approximated by

$$q_g(x,t_g-\varepsilon) \approx \varepsilon\,(x^2 + (1-x)^2) \simeq \text{const.} \qquad (5.64)$$

Convoluting the quark spectrum (5.64) with the quark fragmentation function $D_q^h(x,t_g-\varepsilon) \approx D_q^h(x,t_g)$ we obtain the well known result

$$D_g^h(x,t_g) \sim (1-x)\, D_q^h(x,t_g) .$$

A further consequence of this model is that in gluon jets coherent effects, like the Bose-Einstein attraction (s.3.6) of identical particles should gain in importance. Finally, what about the gluon fragmentation function at low $Q^2 \approx Q_o^2$? Intuitively one would assume that the gluon fragmentation function falls steeper with increasing x than a quark fragmentation function, simply because to built a meson the gluon has first to convert into a quark pair which in turn decays. There is however an interesting speculation[172-174] : due to the self coupling of gluons, stable particles could exist whose wavefunction does not contain quarks. The mass of such a glueball should be of the order of 1 GeV [173]. Alternativly, such glueballs need not exist as pure states, instead they could mix with normal mesons. From the breaking of chiral SU(3) symmetries on could expect that e.g. the η' contains a glueball admixture of more than 60 % : [175,176]

$$\eta' = c\,(-\sin\theta'|\,\eta_8\rangle + \cos\theta'|\eta_1\rangle + \varepsilon'\,|G\rangle) \qquad (5.65)$$

If these models are realistic, the initial gluon could decay into a glueball with a rather flat fragmentation function. However, even then the fragments of the glueball will have comparably low x due to the mean decay multiplicity of ~ 4.

To conclude: in QCD we expect that gluon jets at high Q^2 have an increased decay multiplicity; the leading hadron spectrum is steeper by factor (1-x) compared to quark jets. Since gluons are flavor neutral, there is no "favored" leading flavor in a gluon jet, except perhaps mesons containing a strong glueball admixture.

5.6 Quantitative test of QCD predictions for jets in e^+e^- reactions

The main effect of QCD corrections in parton jets is a redistribution of the energy flux - longitudinal spectra are steepened, and transverse spectra are widened.

In chapter 3 is was shown that a scale breaking of longitudinal distributions could as well be induced by nonasymptotic, nonperturbative effects. Furthermore, the expected size of QCD corrections to $d\sigma/dx$ is small (eqn. 5.36) and beyond the accuracy of present measurements.

Therefore, quantitative tests of QCD corrections mainly deal with the transverse broadening of jets. Among the main questions

i) is the effective coupling constant α_s governing scale breaking in quark jets compatible with the values obtained in lN scattering at a similar Q^2?

ii) is gluon bremsstrahlung described by the QCD matrix element for spin - 1 boson emission?

iii) determination of the gluon fragmentation function

quantitative results available up to now concern point i).

As discussed in chapter 2, the increase in the mean $p_\perp$ of secondaries with respect to a fitted jet axis can be traced to the appearance of events containing three planar jets. The number of such events with noncollinear jets, or equivalently the number of tracks in the tail of the $p_\perp$ distribution is proportional to α_s.

Fig. 5.12 proves that the increase of $\langle p_\perp^2 \rangle$ is well accounted for by QCD predictions.

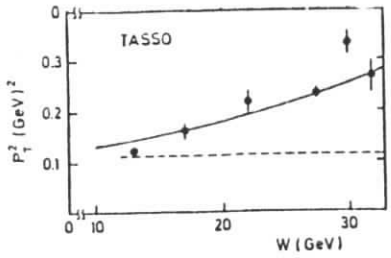

Fig. 5.12
Mean transverse momentum squared with respect to the jets axis, as a function of $\sqrt{s}$ [24], compared to QCD predictions [103].

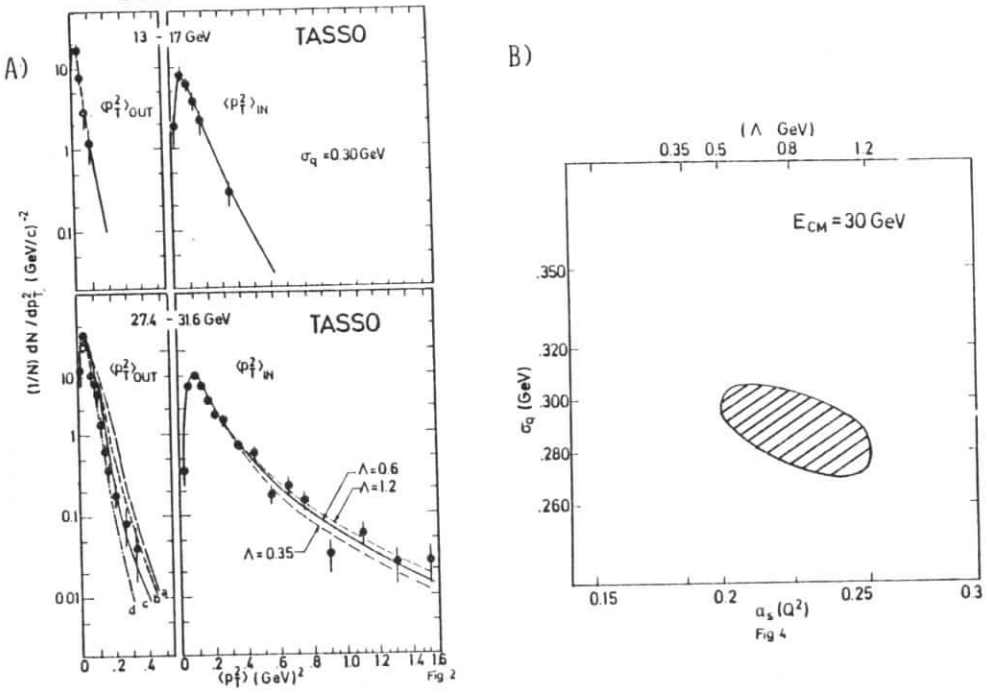

Fig. 5.13
a) Distribution of the mean momentum squared in and out of the event plane at $\sqrt{s}$ = 13-17 GeV and at $\sqrt{s}$ = 30 GeV [24], as compared to QCD predictions [141], assuming an average nonperturbative transverse momentum of fragments σ_q = 300 MeV.
b) Allowed domain for the parameter σ_q and the QCD scale parameter Λ.

Perturbative and nonperturbative components of p_t^2 can be seperated, when transverse momenta in and out of the "event plane" are considered; the momenta out of the plane are determined by nonperturbative processes, whereas momenta in the event plane also receive contributions from a third jet emitted at large angles. Fig. 5.13 a) shows the distribution of the mean $\langle p_t^2 \rangle_{IN}$ and $\langle p_t^2 \rangle_{OUT}$ per event[24], also indicated are predictions for different values of the scale parameter Λ in QCD.[141] The range of parameters compatible with data is given in fig. 5.13 b); data are fully consistent with $\Lambda \approx 0.5$ GeV, as determined from lN scattering[215], and with a constant non-perturbative transverse momentum of the order 300 MeV, as obtained for jets at lower energies.

Similar conclusions are obtained by studying the "oblateness" of the distribution of transverse momentum vectors in jets[259], or simply by counting the number of non cylindrical planar events.[65,220]

5.7 Summary

At large Q^2, where α_s is small, the evolution of jets, as discussed in chapter 4 in a very phenomenological way, can be calculated perturbativly in QCD. The characteristic feature of these "QCD-jets" is a broadening of the transverse size of a jet proportional to $Q^2/\ln Q^2$, and a steepening of longitudinal distributions. The QCD contributions to the transverse jet size should be relevant at $Q^2 \gtrsim 1000\ \mathrm{GeV}^2$. The effects seen at highest PETRA energies are compatible with QCD predictions, both qualitativly and quantitativly.

The QCD model can be applied also to gluon fragmentation. The main predictions concerning gluon jets are

- the longitudinal distribution of fragments is softer than in quark jets, the opening angle of a gluon jet is larger
- the production of heavy quark flavors is enhanced.

6. Jets from parton systems

In the chapters 2 and 4 , we considered interactions where a large four momentum q is transferred to a single parton, giving rise to the production of jets. We restricted our attention to very simple initial conditions: the systems studied consisted of a parton and an antiparton of opposite color. Furthermore, only elementary, irreducible partons were considered-quarks resp. gluons. These limitations reduce the number of variables: the resolution power $1/\lambda \approx \sqrt{|q^2|}$ of the probe[69] is identical to the invariant mass $\sqrt{s}$ of the hadronic final state. In the picture of color flux strings, the geometry of the color field connecting the two partons is well defined. Experimentally, these conditions are fullfilled only in one type of reaction: the decay of a heavy (timelike) state into quark or gluon pairs. Other deep inelastic reactions, like the scattering of quarks out of a nucleon by probes of large spacelike momenta create more complex final states which cannot be fully described by the tools discussed above. In this chapter we shall try to give a phenomenological description of these reactions.

6.1 Deep inelastic lepton-nucleon scattering

As as first example let us study processes where the nucleon structure is probed by a photon or a weak vector boson of high, space like momentum. Various interactions are possible. In the simplest case, the probe is absorbed by a valence quark. Fig. 6.1 compares the corresponding diagrams of parton resp. color flux lines with those obtained for quark production in e^+e^- annihilations. The main difference of the parton final state is that in fig. 6.1 b) the antiquark is replaced by the diquark system ("spectator") remaining after the "active" quark is scattered. The diquark forms a color antitriplet

$$3 \times 3 = \bar{3} + 6 \qquad (6.1)$$

The sextet state is excluded because the whole system has to be a color singlet. The (transverse) mass of the spectator diquark is determined by the primordial (transverse) mass of the active quark, $m_{\perp q} = (m_q^2 + p_\perp^2)^{1/2}$, and by its momentum fraction x [182]

$$m_{\perp qq}^2 = (1-x)(m_n^2 - \frac{m_{\perp q}^2}{x}) \qquad (6.2)$$

For x not too small, the diquark invariant mass is of the order of the nucleon mass m_n. Thus it seems natural to assume that they still form a coherent state [188].

Also indicated in fig. 6.1 are radiative corrections leading to preconfinement. The diagrams are identical for e^+e^- annihilations and lepton-nucleon scattering, respectivly; the physical difference is that in the e^+e^- case quark and antiquark radiate after the hard process, whereas in the latter case the quark radiates immediately before and after the hard scattering.

Due to the analogy of diagrams, the hadron distribution in the final state (fig. 6.2b). should be identical to that observed in e^+e^- annihilations, except that the antiquark fragmentation region is replaced by a diquark fragmentation region.

Another possible interaction is the interaction of the "pointlike" current with a sea parton belonging to the primordial Fock state of the nucleon (fig. 6.3a). Then the final state hadrons populate a rapidity region of the size

$$Y = \ln(W^2/m_\perp^2) \qquad (6.3)$$

The invariant mass W of the hadronic final state is given by

$$W^2 = (p_n+q)^2 = Q^2(\frac{1}{x}-1)+m_n^2 \qquad (6.4)$$

$m_\perp$ is a typical transverse mass of hadrons in jets, $m_\perp \approx O(0.5\ GeV)$.

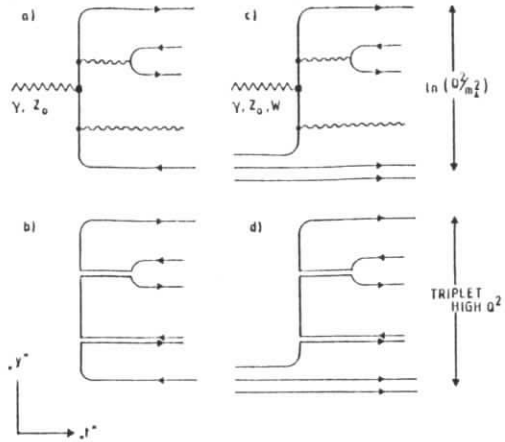

Fig. 6.1
Schematic representation of hadron production in e^+e^- reactions (a,b) and in lepton-valence quark scattering. Figs. b) and d) show the planar diagrams of color flux corresponding to a) and c).

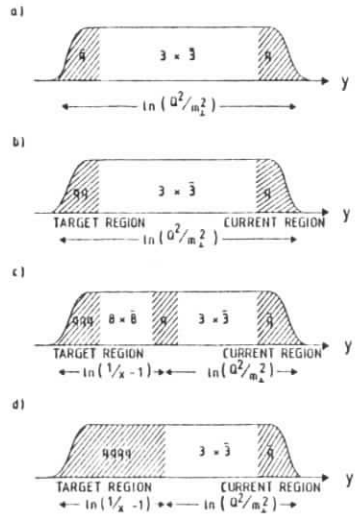

Fig. 6.2
Structure of the hadronic final state
a) in e^+e^- annihilations
b) in lepton-valence quark scattering
c) in lepton-sea quark interactions resulting in an incoherent spectator
d) in lepton-sea quark interactions resulting in a coherent spectator . In lepton nucleon interactions the rapidity axis is defined by the three momentum of the current.

The range Y is exhausted by two types of fragments: those arising from the confinement process of the active quark are spread over a region $Y_q = \ln (Q^2/m_\perp^2)$, like in e^+e^- annihilations. The residual region $Y_T = \ln (1/x-1)$ is populated by spectator fragments [123-125,183,186,187] (fig. 6.2c).

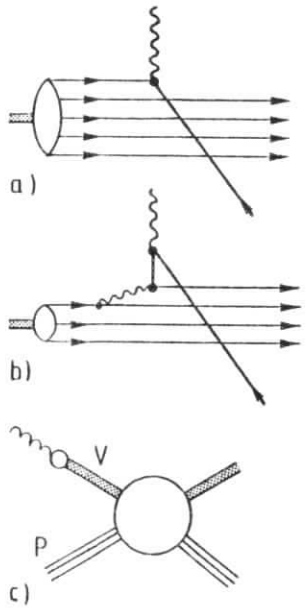

Fig. 6.3
Possible interactions between a spacelike current and nonvalence partons

a) Scattering off a sea quark belonging to the primordial hadron wave function
b) Scattering off a sea quark created dynamically during the interaction
c) Interaction with the vector meson component of the current by soft exchange of wee partons.

Details of the structure of the final state can be derived by considering the configuration of color sources. For definiteness let us use rapidities in the target rest frame, and assume that an antiquark has been struck. The scattered quark represents an antitriplet at $y_{LAB} = Y$, the opposite color pole beeing the spectator at $y_{LAB} \lesssim \ln (1/x-1)$. In analogy to e^+e^- reactions, we thus expect to see a plateau region of the length $= Y-\ln (1/x-1)-2\cdots3$ followed by a shoulder at $y_{LAB} = Y$ containing the direct fragments of the active quark.

Predictions concerning the region of the target, or spectator fragments are less evident. The standard assumption [183,186-187] is the following: quark-antiquark pairs from the sea have low invariant masses, and the rapidities of quark and antiquark are similar. So the sea quark left over is localized at the primordial rapidity of the active quark, $y_{LAB} = \ln (1/x-1)$ (in analogy to the Dirac picture of antiparticles as hole states in a neutral continuum, this quark is often referred to as the quark hole). At $y_{LAB} = 0$, the three valence quarks form a color octet since long time ago one of them had emitted the gluon which created the sea quark pair. Consequently, one may expect to find the valence and hole fragments at $y_{LAB} = 0$ and at $y_{LAB} = \ln (1/x-1)$, respectivly, connected by a hadronic plateau created by the octet color field.

It was pointed out by Brodsky [188] that this model may not be appropriate. The initial 5 quark fock state is a soft, coherent, and long lived fluctuation of the nucleon core. In a coherent state, however, it is impossible to further localize color charges.

This is easily demonstrated in the parton picture: the relatively small mass of a nucleon implies that the mean transverse mass of sea quarks goes to zero as x goes to zero. [87] Then, however, the rapidity spread of a low mass $q\bar{q}$ pair may be arbitrarily large.

Under these conditions, any further subdivision of the target region seems unmotivated (fig. 6.2d). We shall return to this point later when discussing specific models of the fragmentation of multiquark states.

Besides the scattering off a primordial sea parton, a quark pair may be created dynamically as an integral part of the scattering process, due to the pointlike coupling of the current to a quark line (fig. 6.3b). In this case, the residual quark is off shell of the order $O(Q^2)$, and is localizable within the target nucleon. Because of its large distance to the mass shell, and its short life time, this quark hole is an incoherent part of the spectator wave function and fragments independently. Through the exchange of hard quanta, even the coherence of the nucleons valence core may be partly destroyed. This process should dominate lepton nucleon interactions at high Q^2; the resulting final state will resemble fig. 6.2 c).

Of course the strict division between coherent and incoherent sea partons, between primordial quarks and those created dynamically, between nonperturbative and perturbative effects is somewhat arbitrary; in reality one will have a smooth transition between the two regimes [193].

At low Q^2, $Q^2 \lesssim O(1\ \mathrm{GeV}^2)$, coherent soft interactions between current and target compete with the above hard processes. At low Q^2 and W^2 quasielastic scattering of the lepton may occur, resulting in the production of excited nucleon states. At higher W, the vector meson component of weak or electromagnetic currents may interact with the nucleon by exchanging wee partons (fig.6.3c). Both target and current region form coherent states.

Obviously such interactions are not suited to study parton jets. In the experimental data quoted in the following discussion, quasielastic events are removed by cuts in Q^2 and in W (typically $Q^2 > 2\ \mathrm{GeV}^2$, $W > 4$ GeV). The cut in Q^2 as well suppresses coherent interactions. For almost all applications, the requirement $Q^2 > 2\ \mathrm{GeV}^2$ is selective enough.

Before going into a more detailed discussion, a few words concerning the choice of reference frames and variables.

The three momentum component of the current defines a preferred axis, along which the color sources involved are more or less aligned. This fixes the reference frame except for longitudinal

boosts. Four conventions are usual

- the laboratory frame in which the target was at rest before the interaction. The usual scale variable for jet studies is $z = E_{hadron}/\text{total hadronic energy } E_H$
- the center of mass frame of the hadronic final state. Scaling variable is $x_F = 2\, p_\parallel^*/W$.
- the Breit frame, in which the probe carries only momentum, but no energy. Scaling variable is $z_B = 2p_\parallel^B/|q|$
- the rest frame of the active quark after scattering

Neglecting nucleon and quark masses, the frames are connected by the boosts (fig. 6.4) (with Q measured in ~ GeV).

$$\begin{aligned} y_{cms} &= y_{LAB} + \ln(Q^2(\tfrac{1}{x}-1))^{1/2} \\ y_{BREIT} &= y_{LAB} + \ln(Q\,(\tfrac{1}{x}-1)) \\ y_{QUARK} &= y_{LAB} + \ln(Q^2(\tfrac{1}{x}-1)) \end{aligned} \qquad (6.5)$$

Obviously, the laboratory and the quark rest frame are suited to study the fragmentation of the valence core of the target, and of the scattered quark, respectivly. $y_{BREIT} = 0$ characterizes the center of the color triplet plateau.

The scaling variables quoted above are used to describe the fragmentation of the scattered quark. For fast fragments, $p_\parallel \gg m_\perp$, the variables agree asymptotically.

The study of interactions of pointlike probes with hadrons provides the opportunity to check our ideas on quark fragmentation in a more complex environment compared to e^+e^- annihilations, and it further provides information on the fragmentation of compound parton systems, like diquarks.

To arrive at a unified description of the various hard processes, and to enable quantitative predictions, we shall discuss the principles of scaling, environmental independence, factorisation and jet universality.

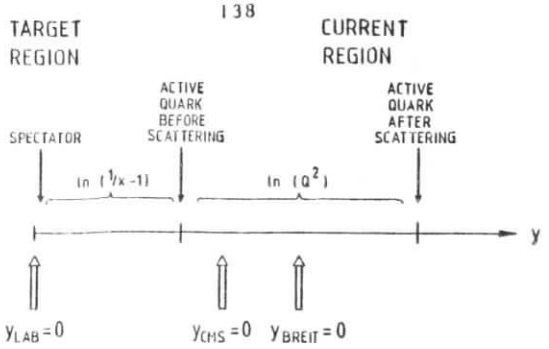

Fig. 6.4
Interrelation of the various reference frames used to describe the hadronic final state in lepton nucleon interactions.

6.2 Environmental independence and factorisation

The hypothesis of environmental independence is implicitely contained in the genuine quark parton model[1-4,108], it has first been stated explicitely by Seghal[115]. Environmental independence means, that the distributions of hadrons in the parton fragmentation region of a specific process is expressible as

$$\frac{1}{\sigma}\frac{d\sigma^h}{dz} = \sum_i \varepsilon_i D_i^h(z) \qquad (6.7)$$

where ε_i is the probability that the fragmenting parton is of type i ($\sum_i \varepsilon_i = 1$) and $D_i^h(z)$ is the fragmentation function depending on a scaling variable z. This means that for the purposes of calculation, we may assume that the primary interaction creates a "parton beam" with a composition given by the probabilities ε_i, and that each parton variety i decays into hadrons of type h with a distribution $D_i^h(z)$, which is independent of the origin of the parton.

The probabilities ε_i characterize the process under investigation In e^+e^- annihilations e.g. the ε_i are proportional to the quark

charges squared, whereas in lepton nucleon interactions they further depend on the fractional momentum x of the interacting parton.

In eqn. (6.7) the fragmentation functions are assumed to scale. The scaling variable used by Seghal to describe quark fragmentation in lepton nucleon reactions was z defined as the ratio of the actual and the maximum hadron energy in the laboratory frame. In general, the choice of the "suited" reference frame is ambigous, fig's 6.2 and 6.3 suggest e.g.to use z_B in the above case, whereas naivly one may vote for x_F.

This problem disappears at infinitely high energies. Here the relation

$$p_h = z p_q$$

between the four momenta p_h and p_q of quark and hadron, respectivly holds in all frames with the same z. At finite energies, eqn (6.7) should hold for those hadrons wich are fast ($E \gg m_h$) in each of the various frames.

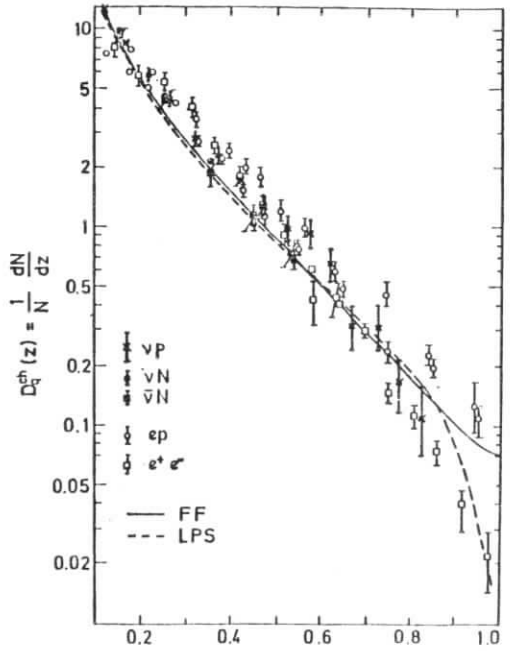

Fig.6.5
The fragmentation $D_q^{h\pm}(z)$ for charged hadrons in various hard reactions[119].

What is the experimental evidence for factorisation? We have seen in chapter 4 that in fact the fragmentation functions measured in e^+e^- annihilations, in electroproduction and in neutrino-nucleon interactions can be described by one unique parametrisation. This is once more demonstrated by fig. 6.5, where the z-distribution of charged hadrons is summarized for the various reactions.[119] The measurements agree at not too high z within the error bars. At $z > 0.8$ a slight discrepancy seems to develop. One should however bear in mind, that the distributions have been measured using drastically different detectors, that acceptance corrections and selection criteria (e.g. on the minimum number of reconstructed tracks per event) have been applied, and last not least that the Q^2 range and the final state masses differ, with typical Q^2 beeing as low as 2 GeV^2 in the neutrino reactions compared to $Q^2 \approx 0$ (25 GeV^2) in the e^+e^- case. All these differences influence mainly the region close to $z = 1$.

In all types of quark jets, typical transverse momenta with respect to the axis turn out to be of the order 300···400 MeV/c, and all show the seagull effect.[195]

On the other hand, do we expect exact environmental independence and scaling for quark jets? It has been pointed out that phase space effects lead to nonscaling of fragmentation functions even if the basic matrix element is scale invariant. Thus we get

$$D_i^h(z) \underset{\text{phase}}{\rightarrow} \underset{\text{space}}{} D_i^h(z,W) \quad . \qquad (6.8)$$

Following the argumentation of Kogut and Susskind (s. chapter 5), a scattered parton furthermore is not fully described by the parton type; one has to know as well its "size" Q^2.

$$D_i^h(z) \underset{\text{field}}{\rightarrow} \underset{\text{theory}}{} D_i^h(z,Q^2) \quad . \qquad (6.9)$$

The scale breaking leads to a shrinking of the z distribution and to a broadening of $p_\perp$ distribution within the jet.

Moreover, we have seen in section 6.1 and in chapter 5, that the quark composition of the target, as probed by a pointlike current, depends on q^2 as well, and that the clean separation of target structure and interaction is no longer possible.
Does this imply the total breakdown of the idea of environmental independence?
Fortunately, QCD provides us with the equivalent principle of factorisation, as far as the Q^2 dependence of the process is concerned. Consider fig. 6.6a). This diagram describes the interaction of a probe with a hadron observed with a resolution just enough to see the parton structure. The incoming nucleon dissociates into a primordial quark and a spectator. The interaction of probe and active quark is described by a formfactor $F(Q^2)$.

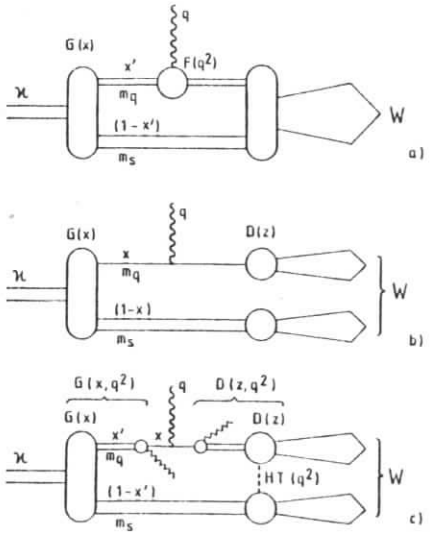

Fig.6.6
Lepton nucleon interactions seen at various levels of complexity. The most general diagram a) can be simplified using the naive quark parton model (b). QCD corrections are indicated in fig.6.6 c). Double lines refer to the propagators of hadrons or dressed partons; "pointlike" partons are represented by single lines.

Both scattered quark and spectator decay into the final state hadrons. The simplification made by the naive parton model, leading to environmental independence, is evident from fig.6.6b). The quark is assumed to be pointlike, $F(Q^2) \equiv 1$, and active quark and spectator are assumed to decay independently. Finally, the QCD version of the process is shown in fig. 6.6c). The incoming hadron dissociates into a primordial quark and a spectator according to the structure function $\sigma(x')$. Before the interaction with the probe, the quark radiates and becomes off shell of order Q^2. It absorbs the probe and again radiates quanta to approach again the mass shell. The practically on-shell quark and the spectator decay with fragmentation functions $D(z')$, where z' is the ratio of the hadron and the dressed quark energies. The exchange of soft gluons in the final state[196] and target mass effects lead to Q^2 and x dependent corrections of the fragmentation functions.[197,198]

Of course, fig. 6.6c) is fully equivalent to fig. 6.6a) except that now a detailed prescription is given how to calculate $F(Q^2)$. In the past years, however, a different approach to recover the naive model of fig. 6.6b) has been followed. It has been proven that the violations of scaling induced by radiation before and after the hard scattering process are independent of the precise nature of the hard process [199-201]. The naive model of scale breaking a la Kogut and Susskind as well suggests such a behaviour.

The scaling violations can be absorbed in the definition of now Q^2-dependent structure and fragmentation function. In lepton nucleon scattering, the cross section factorizes as

$$\frac{d\sigma}{dxdz} = \frac{d\sigma}{dx}(x,Q^2)\cdot D(z,Q^2) \quad . \qquad (6.10)$$

The factorisation was shown to hold for the leading QCD-terms ($\sim \alpha_S(Q^2)\ln Q^2$) and in the leading log approximation.[199] So factorisation is the QCD-analogon of the naive parton models environmental independence.

Recent investigations have shown that factorisation, however, is only approximate in QCD, and is violated by terms $O(\alpha_S)$[202-204]. This is demonstrated by fig. 6.7 where to effective quark fragmentation functions as calculated by QCD up to $O(\alpha_S)$ for deep inelastic scattering processes are compared for different x.[204] The fragmentation functions depend on x as well as on z, the violations of scaling beeing strongest at large x and z. Although the effects of nonfactorisation are small in those regions where the bulk of present data lies, on should be aware that this effect signalizes the point were the intuitive parton picture breaks down; is makes no longer sense to treat quark distributions and fragmentation functions as separate entities.

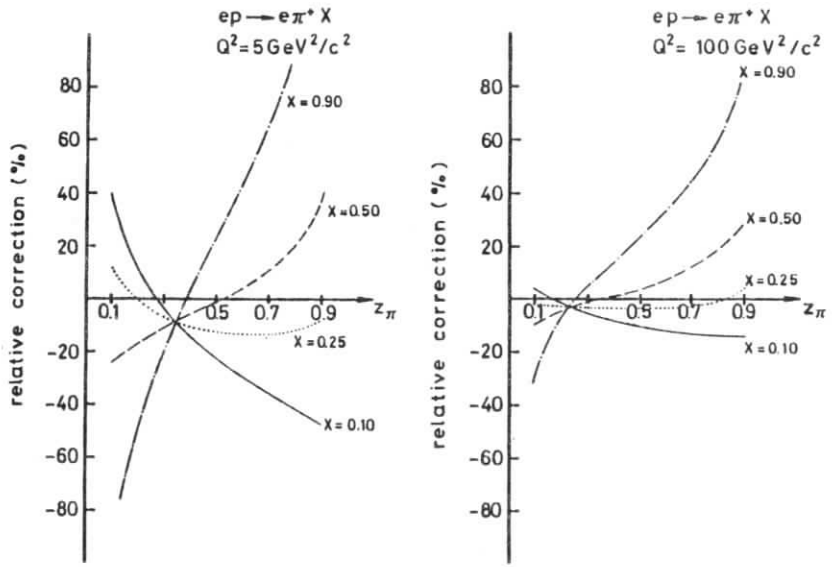

Fig. 6.7
Relative correction to the fragmentation function D_q^h of order $\alpha_S(Q^2)$ for the reaction $ep \to e\pi^+ + x$ as a function of z for different values of the Bjorken scaling variable x at $Q^2 = 5$ GeV^2 and at $Q^2 = 100$ GeV^2.[204]

What is the experimental situation? From fig. 6.5 we learned that factorisation is at least approximately true. However, experimental uncertainities make a definite conclusion hard. A better test of factorisation is possible in lepton-nucleon scattering where $d^2\sigma/dxdz$ can be measured for various x using the identical detector and acceptance corrections. Even in this case, however, the interpretation of data is not unambigious. Because of

$$W^2 = Q^2(\frac{1}{x}-1) \qquad (6.11)$$

any variation of x with Q^2 fixed (to test factorisation) or of Q^2 with x fixed (to measure $D(z,Q^2)$ to compare with QCD predictions) changes W as well, giving rise to scale breaking due to phase effects.

Fig. 6.8 shows the distribution of masses W of the hadronic final state as measured by a typical neutrino-nucleon scattering experiment, performed at the Fermilab wide band beam using the 15 ft hydrogen bubble chamber.[205] The bulk of data lies below W < 5 GeV; in e^+e^- reactions however this is the point were a jet structure starts to be visible, averaged over many events! In that region, the structure of a single event is dominated by phase space effects. This is once more visualized in fig. 6.9 where the mean multiplicities in the quark fragmentation region z > 0.2 are plotted vs. W.[205] Scaling implies that these multiplicities should be constant. The deviations are due to threshold effects and are well explained by a phase space model (solid lines). Using a cut W >4 GeV to exclude the influence of phase space limitations, the experimentalists claim to see no significant violations of scaling or factorisation.

The same result was obtained with higher statistics by an electroproduction experiment at Cornell[206,207]. Fig. 6.10 shows $d^2\sigma/dxdz$ for various x, normalized to the average $d\sigma/dz$. Cuts on the four momentum transfer $Q^2 > 2$ GeV^2 and on W > 3 GeV suppress kinematical effects at low masses and reject

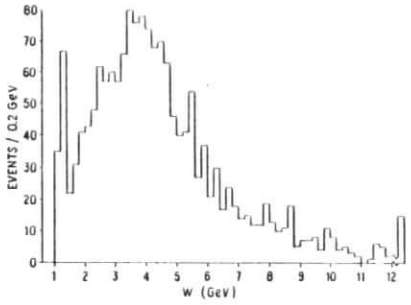

Fig. 6.8
Distribution of invariant mass of the hadronic system for neutrino charged current events[205].

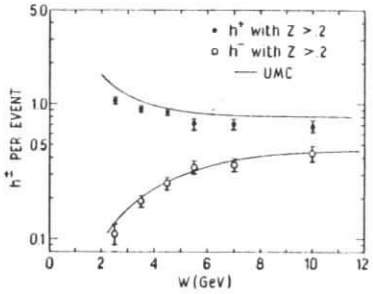

Fig. 6.9
The rate of production of positive and negative hadrons with z > 0.2 as a function of W for neutrino proton interactions. The curves are the result of a longitudinal phase space model[205].

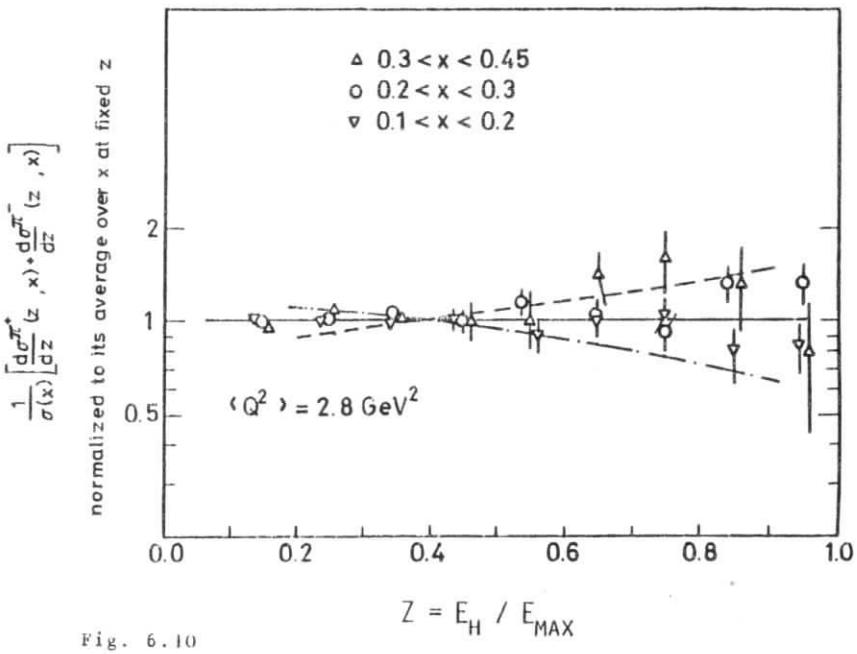

Fig. 6.10

The cross section $d\sigma/dxdz$ for electroproduction normalized to its average over x at fixed z.[206,207] The curves illustrate the expected violation of factorisation, calculated in O (α_s)[204], for x = 0.15 (-.-.), x = 0.25 (—) and x = 0.37 (---).

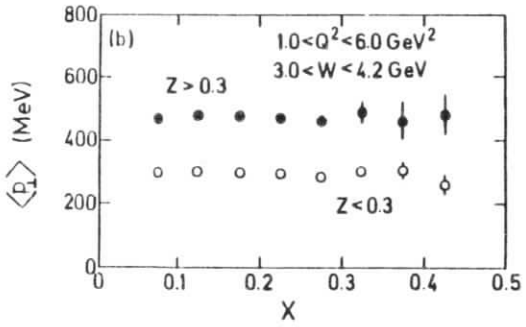

Fig. 6.11

Mean transverse momentum of hadrons in electroproduction as a function of x.[206,207]

quasielastic events. Within the x range covered, no significant violations of factorisation are seen, the upper limits beeing compatible with QCD predictions (fig. 6.8). Fig. 6.11 shows that at fixed W the mean transverse momentum of fragments is independent of x as well.

More recently, high statistics data from the bubble chamber BEBC on νp interactions became available[208-210]. Fig. 6.12 shows the inclusive distribution $(1/\sigma)(d\sigma/dz)$ for two ranges of Q^2, averaged over all W. Significant differences are observed when going from $Q^2 \approx 1$-2 GeV^2 to $Q^2 \approx 5$-40 GeV^2. Because of the interrelationship of x, Q^2, and W this signalizes either a breakdown of factorisation or of scaling, or the dominance of phase space effects. To investigate this in more detail, the moments

$$D(n,Q^2) = \int_0^1 z^{n-1} D(z,q^2)\,dz \qquad (6.12)$$

have been calculated and compared to QCD predictions[202]. Fig. 6.13 shows the x dependence of the 3rd moment of the density of positive particles in the quark fragmentation region $x_F > 0$ for three intervals of Q^2. For $Q^2 \approx 1$ to 5 GeV^2, a clear violation of factorisation is observed, $D^+(3,Q^2)$ depends strongly on x at fixed average Q^2. Note, however, that the final state mass W ranges between 1 and 3 GeV for $x > 0.3$ and $Q^2 \approx 2$ GeV^2! It would be rather astonishing if factorisation in the sense of QCD holds at these masses. In fact, if $D^+(3,q^2)$ is plotted vs x resp. q^2 for W fixed, data agrees with scaling in Q^2 resp. factorisation. Thus the effects seem to be induced by phase space effects depending on W (fig. 6.14).

This is once more explicitly shown in figs. 6.15 a) and b). Fig. 6.15 a) shows the moments 2-7 of the nonsinglet fragmentation function $D^+(z,q^2)-D^-(z,q^2)$, averaged over all x. The observed nonscaling is in rough agreement with the QCD predictions based on eqn (5.33), however the fit yields a rather large scale parameter $\Lambda \approx 0.6$ GeV. However, with an additional cut in W, $W > 4$, as used by other experiments, the Q^2 dependence of the moments disappears completely (fig. 6.15 b).

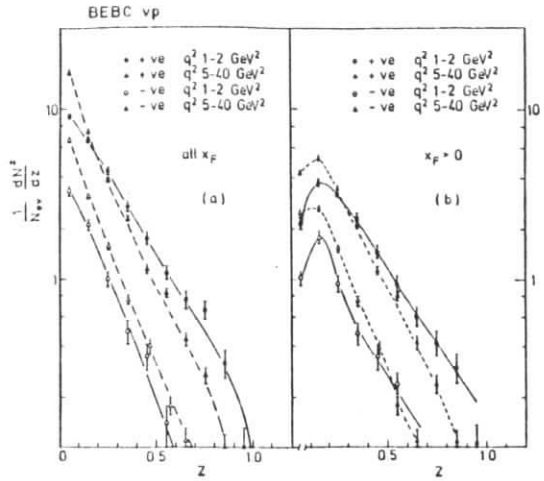

Fig. 6.12
z distributions ($z=E_h/E_{MAX}$) of positive and negative hadrons for two ranges of low and high Q^2 from BEBC νH_2 [208] a) for all hadrons b) for hadrons going forward in the cms ($x_F > 0$).

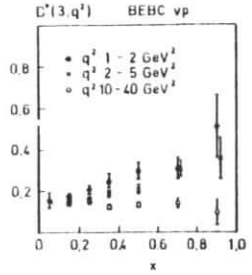

Fig. 6.13
Third fragmentation moment of positive hadrons with $x_F > 0$ vs Bjorken x for three intervals of Q^2, from BEBC νH_2 [208]

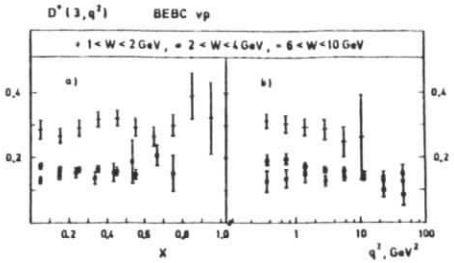

Fig. 6.14
Third fragmentation moment of positive hadrons with $x_F > 0$ vs. Bjorken x (a) and vs. Q^2 (b).

Is it possible, that the good agreement with QCD, as obtained in fig. 6.15 a) by fitting only one free parameter Λ, is faked by phase space effects?

This question has been investigated by Engels et.al. [211] at the example of jets in e^+e^- annihilations. They compared the shape of $D(n,Q^2)$, as predicted by QCD, with scaling violations given by a longitudinal phase space model, as described in chapter 3 (fig. 6.16). The shape of the two sets of curves is very similar; at low Q^2, or S the phase space model predicts an even stronger variation of $D(n,Q^2)$ with Q^2. So this model would even explain, why no violations of scaling are observed above W = 4, whereas in QCD one expects scaling violations to be independent of W, at least if $O(\alpha_S)$ corrections are neglected.

To summarize so far, the violations of scaling and factorisation observed in longitudinal distributions in quark jets are compatible with kinematical threshold effects, which vanish above W = 4 GeV. Such a behaviour is, within the limited

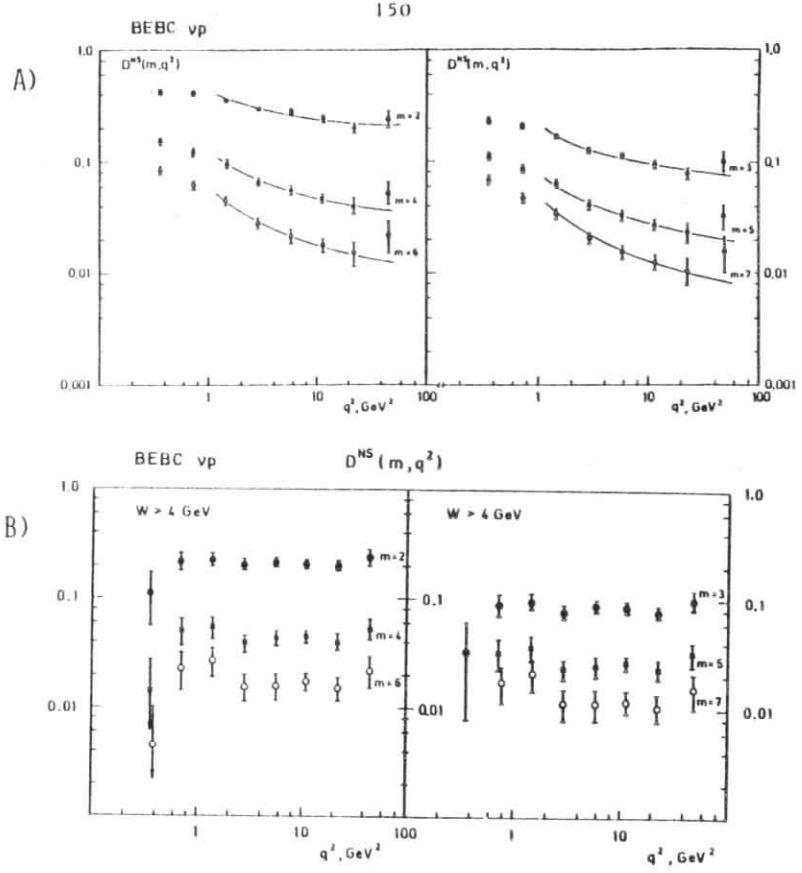

Fig. 6.15
Non-singlet moments $D_{ns}(n,Q^2) = D^+(n,Q^2)-D^-(n,Q^2)$ vs. Q^2 for m = 2...7 [208].
a) averaged over all W. The curves show fit of the QCD formula (5.33) to the data points above $Q^2 = 1$ GeV^2.
b) for W > 4 GeV

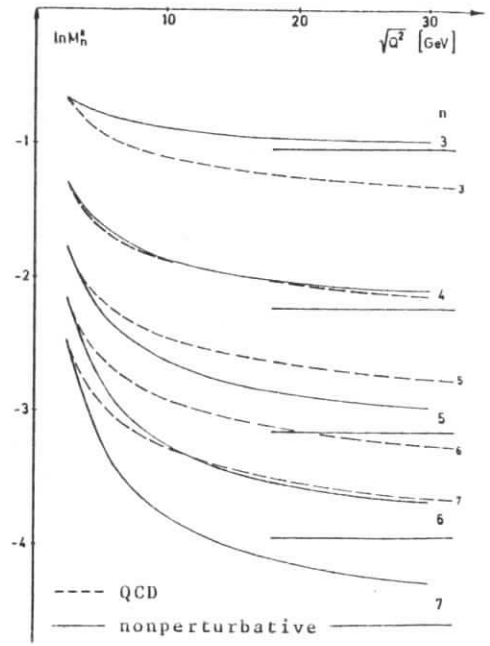

Fig. 6.16
Q^2-dependence of the logarithms of moments from nonperturbative quark fragmentation with respect to the scaling variable x_F, compared to perturbative QCD prediction calculated with $\Lambda^2 = 0.5$ GeV^2. Horizontal lines indicate the scaling limits of the nonperturbative moments[211].

statistics of data still consistent with QCD, since QCD corrections to longitudinal fragmentation functions are relatively small (see eqn. 5.36).

We have seen in chapter 2 that the transverse size of jets exhibits nonscaling at the highest PETRA energies. Nevertheless, in most cases only tails of distributions are concerned, and a constant mean $p_\perp$ for fragmentation is still a reasonable assumption.

Thus we conclude that at present energies the principles of scaling and factorisation provide a good description of the main features of quark jet systems.

A direct consequence of factorisation is the retention of quark quantum numbers, up to a constant term, at high rapidities of the current fragmentation region. This has been demonstrated qualitativly in chapter 4; here we will briefly summarize quantitative results.

Clean "beams" of one quark species can be produced in the following reactions:

a) neutrinoproduction $\nu N \to l^- + u + x$

$\bar{\nu} N \to l^+ + d + x$

for $x > 0.1$

b) electroproduction $lp \to l + u + x$

for $x \to 1$

l refers to an electron or muon. The cuts in x are necessary to suppress interactions with sea quarks in a). The limit $x \to 1$ in b) makes use of the fact that for $x \to 1$ a proton consists of pure u-quarks, in addition to the fact that the u-quark cross section is enhanced by a factor 4 compared to d quarks because of its charge.

The main experimental limitations of the study of quantum number retention comes again from the low masses of the hadronic final state, which induce a considerable spill over between the target and the current fragmentation region. This is evident from fig. 6.17: the total negative charge in the d quark fragmentation region in $\bar{\nu}N$ reactions increases with W since then the contamination due to positive fragments of the target nucleon becomes less important.[212] The real mean charge of quark fragments was derived from fig's 6.17 by extrapolation linear in W^{-1} to $W = \infty$ (fig.6.18). The result, $\langle Q \rangle_d = -(0.46 \pm .08)$, is in good agreement with the expectation based on the Feynman-Field jet model, e.g..

The experimental information on charge retention in quark jets is summarized in table 6.1.

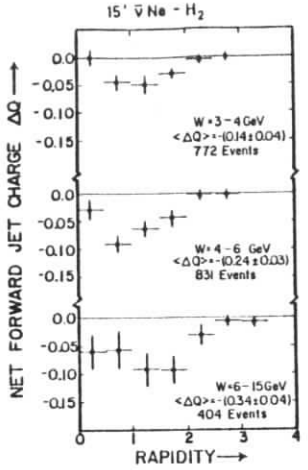

Fig. 6.17
Distribution of charge per event in the cms rapidity for hadrons going forward in the cms in events with $x > 0.1$ and $Q^2 > 1\ GeV^2$ for three intervals of W. From 15' $\bar{\nu}Ne-H_2$ [212]

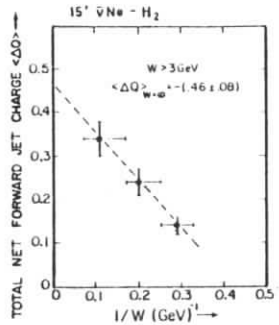

Fig. 6.18 Total net charge <Q> per event of hadrons going forward in the cms vs 1/W. From 15' $\bar{\nu}Ne-H_2$ [212].

Table 6.1

Measured net charges in the u,d fragmentation region

Exp., Ref.	Selection criteria and cuts (in units of GeV, GeV^2 etc.)	$\langle Q_u \rangle$	$\langle Q_d \rangle$
15' $\bar{\nu}H_2Ne$ 212)	$W\to\infty, x>.1, Q^2>1, x_F>0$		-0.46 ± 0.08
BEBC νH_2 208)	$W\to\infty, x>.1, Q^2>1, x_F>0$	0.59 ± 0.10	
BEBC νH_2 208)	$W\to\infty, x>.1, Q^2>1, Z_B>0$	0.52 ± 0.08	
BEBC $\nu, \bar{\nu} NeH_2$ 213)	$W>4, x>.1, Q^2>1, Z_B>0$	0.55 ± 0.06	-0.12 ± 0.08
BEBC $\nu, \bar{\nu} NeH_2$ 213)	$W\to\infty, x>.1, Q^2>1, Z_B>0$		-0.3 ± 0.1
DECO ep 206)	$W>2.5, x+1, Q^2>1, x_F>0$	0.48 ± 0.05	

In the high energy limit, all data are in qualitative agreement with the expectation of approximate charge retention. Quantitativly, the data tend to confirm an SU(3) breaking for sea quarks as used in the Field-Feynman model.

6.3 Jet universality

At moderate energies the jet physics is dominated by the parton fragmentation regions investigated in the last section. At asymptotic energies, however, the direct quark, or spectator fragments populate only a relatively small region of the whole rapidity range; the dominant contribution to particle production comes from the plateau region.
The ideas of jet universality try to relate the structure of the rapidity plateaus observed in the various deep inelastic reactions.

The idea of an "universal" plateau, whose properties are asymptotically independent of target and current in current induced reactions was first suggest by Bjorken and Kogut[214] based on correspondence principles. In a universal plateau the density of each particle species $(1/\sigma)(d^2\sigma/dydp_\perp^2)$ is independent of the final state mass and the reaction considered. Consequently one predicts a universal behaviour of multiplicities

$$\langle n \rangle = n_o \ln W^2 \qquad (6.13)$$

Taking into account our present ideas on parton fragmentation, this model has to be modified slightly. In two dimensional quark gluon bremsstrahlung models, as discussed in chapter 4 and 5, the mean multiplicity per unit of rapidity grows with the square of the partons color charge. This observation lead Brodsky and Gunion[15,215] to the following universality principle: the properties of the hadronic plateau are uniquely determined by the type of color charges separated, independent of the flavor content of the color sources.

In QCD, the two basic sources of color are triplets, like quarks or diquarks, and octets, like gluons or quark-antiquark pairs.

In current nucleon interactions at high Q^2, e.g., one should observe a triplet plateau of the length $Y_{3\times\bar{3}} = \ln Q^2$, and an octet plateau of the length $Y_{8\times\bar{8}} = \ln (1/x-1)$ (fig. 6.2 c), thus yielding the asymptotic multiplicity

$$\langle n \rangle \underset{\substack{x \to 0 \\ Q^2 \to \infty}}{=} n_{3\times\bar{3}} \ln Q^2 + n_{8\times\bar{8}} \ln(1/x-1) \qquad (6.14)$$

More general, and taking into account scaling violations, we get

$$\langle n \rangle \underset{\substack{x \to 0 \\ Q^2 \to \infty}}{=} N_{3\times\bar{3}}(Y_{3\times\bar{3}}, Q^2_{3\times\bar{3}}) + N_{8\times\bar{8}}(Y_{8\times\bar{8}}, Q^2_{8\times\bar{8}}) \qquad (6.15)$$

with the asymptotic prediction from QCD

$$N_{3\times\bar{3}} = \frac{4}{9} N_{8\times\bar{8}} \quad .$$

Unifying models based on dual unitarisation schemes [216,217] and on dual topological unitarisation [218,219] arrive at similar conclusions [187].

Referring to a comparison of hadronic events in e^+e^- annihilations and in current-nucleon reactions, the predictions of eqs. (6.14, 6.15) are obvious:

- same height of the rapidity plateau, as measured at
  $Y_{CMS} = 0$ (e^+e^-) and at
  $Y_{BREIT} = 0$ (lN), respectivly
- for valence quark scattering, the total multiplicities observed in the two reactions should be identical for same W, up to a small additive constant from a possible difference in quark and diquark fragmentation
- in lN reactions the total multiplicitiy at fixed W increases with decreasing x, because then the relative contribution of the color octet part grows.

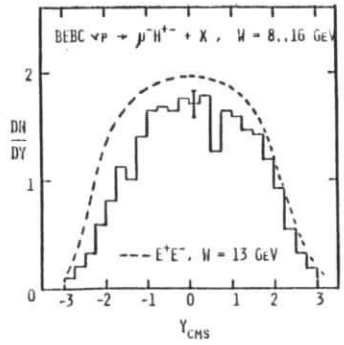

Fig. 6.19
Rapidity distributions in the cms of secondaries in νp reactions at W = 8···16 GeV,[208] and in e^+e^- annihilations at $\sqrt{s}$ = 13 GeV[24]

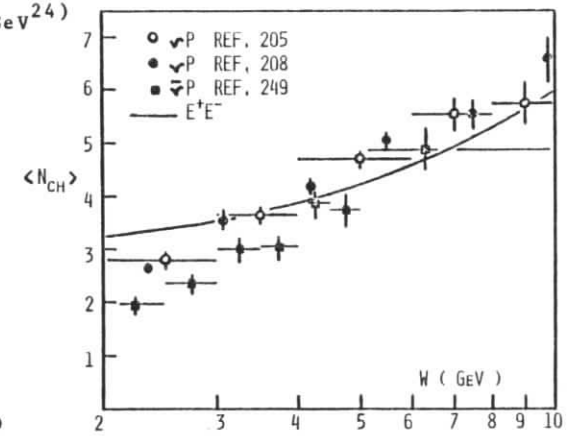

Fig. 6.20
Mean charged hadronic multiplicity measured in νp reactions and in e^+e^- annihilations.

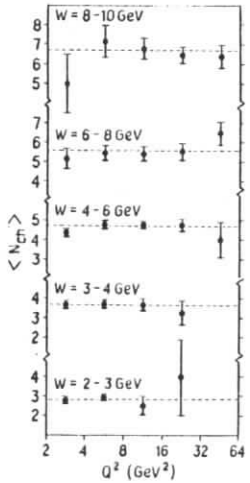

Fig. 6.21
Mean number of charged hadrons produced in νN interactions, as a function of Q^2 for fixed W.[205]

Fig. 6.19 shows dσ/dy from νp reactions [208] for 8 ≤ W ≤ 16 GeV, compared to e^+e^- annihilations at $W = \sqrt{s} = 13$ GeV.[24] The height of the charged particle plateau, (dn/dy) = 2, is in fact consistent. In fig. 6.20 the total multiplicity measured in νp reactions [205,208] is compared with data from e^+e^--annihilations (see chapter 2). Again the values agree surprisingly well, except at very low energies, where the phase space available to fragments is significantly reduced in νp interactions, due to the existence of a final state nucleon.

Fig. 6.21 demonstrates the dependence of $\langle n_{ch} \rangle$ on Q^2 (or, equivalently, x) at fixed W, for νp interactions. In contrast to the expectation based on eqs. (6.14) and (6.15), $\langle n_{ch} \rangle$ shows no significant dependence on Q^2. This feature is basically agreed upon by other experiments studying deep inelastic lepton nucleon interactions [221-223].

When interpreting figs. 6.19-6.21 in terms of jet universality one should note that at these energies the multiplicity is far from being dominated by the plateau region. Below W = 5 GeV, e.g., the multiplicity is more or less fixed once the transverse momentum smearing of the produced particles is given, and is nearly independent on the choice of matrix elements. The invariance of n_{ch} with Q^2 will be partially due to this fact, it may further indicate that at these Q^2 either reactions with a coherent spectator system dominate, and no octets are separated, or that the typical multiplicities of triplet and octet plateaus are similar.

Clearly, the present data are not sufficient to decide wether jet universality holds exactly; nevertheless data are consistent with universality, so we shall keep it as a working hypothesis.

6.4 Spectator fragmentation

Present data seems to be consistent with the hypothesis of approximate factorisation and jet universality. In a certain sense lepton-nucleon reactions therefore don't give qualitativly new information on quark jets, as compared to e^+e^- annihilations.

Lepton nucleon reactions, however, offer the unique possibility to study the fragmentation of compound quark states, like diquarks. It will be shown that the measurement of their fragmentation functions reveals information on the wavefunction and dynamics of multiparton states. Furthermore, once the fragmentation properties of multiquark systems are known, e.g. from νN reactions, the mechanisms of other deep inelastic phenomena, like muon pair production in hadron-hadron interactions can be reconstructed by studying the quark contents of the spectators left over after the hard process.

A spectator system can be described by its flavor content, its color state, its mass and by the degree of coherence of its wavefunction. Table 6.2 gives a list of possible spectators in charged current neutrino-nucleon interactions.

Table 6.2

Spectator systems in $\nu, \bar{\nu}N$ interactions. Coherent subsystems of the spectator are put in brackets. Only u and d sea quarks are taken into account.

Reaction	Spectator flavor	color	mass
ν-valence quark (fig. 6.1)	(uu)	$\bar{3}$	0 (m_n)
$\bar{\nu}$-valence quark (fig. 6.1)	(ud)	$\bar{3}$	0 (m_n)
ν-primordial sea (fig. 6.3a)	(uud$\bar{d}$) or (uudu)	$\bar{3}$ 3	m_n ($\frac{1}{x}$ -1)
$\bar{\nu}$-primordial sea (fig. 6.3a)	(uu$\bar{u}$d) or (uudd)	$\bar{3}$ 3	m_n ($\frac{1}{x}$ -1)
ν-pointlike sea (fig. 6.3b)	(uud)$\bar{d}$ or (uud)u	(8) $\bar{3}$ (8) 3	m_n ($\frac{1}{x}$ -1)
$\bar{\nu}$-pointlike sea (fig. 6.3b)	(uud)$\bar{u}$ or (uud)d	(8) $\bar{3}$ (8) 3	m_n ($\frac{1}{x}$ -1)

The spectator is thus a much more complex object than a single active quark. To reduce the number of variables, we shall assume the following simplifications, based on our knowledge on quark jets.

First, the studies of QCD jets presented in chapter 5 have shown that the fragmentation function of a system consisting of incoherent components can be represented as the incoherent sum of their fragmentation functions, at least as far as fast ($x \gg 0$) fragments are concerned.

Second, we shall assume that factorisation holds here as well. That means that the distribution of fast fragments depends only on the flavor contents of the spectator, whereas its color contents influences the plateau region.

We are now ready to define the spectator fragmentation function $D_s^h(z)$ which refers to the decay of a coherent parton system. We use a reference frame where the initial nucleon has a large momentum p_o. Since the maximum momentum available to fragments is $p_{\parallel MAX} = p_o\ (1-x)$, the natural scaling variable is $z = p_\parallel / p_o(1-x)$. In the cms, we have $z = -x_F$, with x_F defined in the usual way as $2\ p_\parallel / W$.

Do we expect scaling to hold for spectator fragmentation? The picture of asymptotic freedom, together with the diagrams of fig. 6.1 suggests that the spectator completely ignores the hard process. The energy used to built up the preconfinement plateau is radiated by the active quark; the color charge of the spectator participates only in the final confining step at fixed Q_o^2. Does this imply that the spectator fragmentation function is independent of Q^2?

In fact, a Q^2 dependence of spectator fragmentation arises in a rather indirect, and process dependent way, as can be seen from fig. 6.6c). The incoming proton dissociates into the active quark at x' and the spectator at (1-x'). The active quark radiates an energy fraction (x'-x) and is then hit by the hard probe. Therefore, the maximum momentum fraction of spectator fragments is (1-x'), and not (1-x), as naivly expected. Since the amount of radiation, (x'-x), increases with

increasing Q^2, the spectator fragmentation function D(z) shrinks with increasing Q^2, and the particle density at low z increases. Qualitativly these effects of scale breaking equal those observed in quark fragmentation; quantitativly they differ and depend on x as well as on Q^2. This difference of the perturbative jet structures in e^+e^- and in lN reactions has been emphasized by various authors[224-227].

In reality, however, these differences are small compared to nonperturbative effects, at least at present values of Q^2 and W. This is evident from fig. 6.22 where the distribution of sphericity is compared for e^+e^- events and for lN reactions in two bins of W. The distributions agree within the error bars. Therefore we feel that in the following discussion scale breaking effects can be neglected without introducing much bias.

Let us now consider the fragmentation of the coherent part of the spectator. Its decay is governed by soft, collective processes, and one may ask if the perturbative quark parton

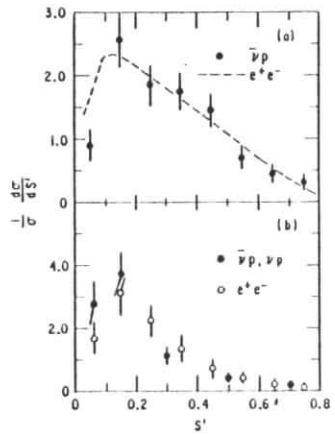

Fig. 6.22

a) sphericity distribution for $\bar{\nu}p$ reactions with W = 6.6 GeV and for e^+e^- annihilation at W = 7 GeV

b) sphericity distribution for νp plus $\bar{\nu}p$ reactions at W = 10.5 GeV and for e^+e^- annihilation at W = 13 GeV. From 15' $\bar{\nu}H_2$.185)

model, or, more general, the concept of individual quarks, may be applied. Consider the decay of the spectator (mass m_s) into a parton b and a core of mass m_x. Let z be the fractional momentum of b, and $p_\perp$ its transverse momentum. From simple kinematics, we get

$$p_b^2 = -\frac{p_\perp^2 + z\, m_x^2}{(1-z)} + z\, m_s^2 \quad . \qquad (6.16)$$

If the core z contains valence constituents of the spectator, its mass should be of the order O(GeV)[189-191]. That means, however, that for $z \to 1$ the active parton is far off shell. A fragment which contains this parton thus actually tests the parton structure at large Q^2 and the application of the perturbative parton concept appears to be justified.[192]

This result, as well as eqn. (6.16) seems to disagree with the conclusions of chapter 4, that fast particles in jets are produced last. We found, that the production coordinates of particles ly on a hyperbola in space-time

$$t^2 - r^2 = \text{const} \quad . \qquad (6.17)$$

This corresponds to a fixed production time of each particle, as measured in its own rest frame. Eqn. (6.16) forces us to modify this statement:

$$t^2 - r^2 = \frac{1}{p_b^2} = \text{const.}(1-z) \qquad (6.18)$$

The production time of a fast particle is then

$$t \sim z\sqrt{1-z} \qquad (6.19)$$

measured e.g. in the core rest frame. This modification concerns only fast particles; it does not destroy the principal scheme of an inside-outside cascade, but simply introduces a

variable cut off for the evolution of the cascade.

To conclude: although spectator fragmentation is basically a soft process, the quantum numbers of fast fragments should reflect the constituent structure of the spectator.

Unfortunately, experimental data at sufficiently high Q^2 and W, suited to test these ideas is rare. Fig. 6.23 shows the x_F distribution of positive and negative fragments observed in νp reactions in the 15' bubble chamber [205] for events with $W > 4$ GeV and $x > 0.05$, with typical Q^2 of the order of 2...10 GeV^2. Similar results have been reported by BEBC[208]. In fig. 6.23, target fragments populate the region $x_F \to -1$. For comparison, the distributions observed in the proton fragmentation region in inelastic $\pi^+ p$ reactions at $\sqrt{s} = 5.6$ GeV[229] are included as dotted lines.

The similarity of the pion spectra obtained in the two reactions is striking ; furthermore in each case proton production dominates for $x_F \to -1$. The absolute proton yield, however is a factor 5 down in the deep inelastic reaction, for $x_F \to -1$. A dominant production of neutral baryons can be excluded. Baryon number conservation requires then the proton distribution to peak at lower x_F, in contrast to the $\pi^+ p$ events.

The full lines in fig. 6.23 are the result of a phase space model (UJM). The model uses constant matrix elements to describe pion production; the matrix element for proton production has been adjusted to fit the experimental proton spectrum. In addition, experimental values for the multiplicities have been used as an input. The agreement between data and the simple model is surprisingly good; this demonstrates once more that a those energies jet physics is still governed mainly by phase space effects.

Nevertheless, the following facts have to be explained by fragmentation models

- the spectrum of positive pions agrees with that obtained from normal $\pi^+ p$, or pp interactions at similar energies. The ratio of positive to negative pions increases for fast pions. The

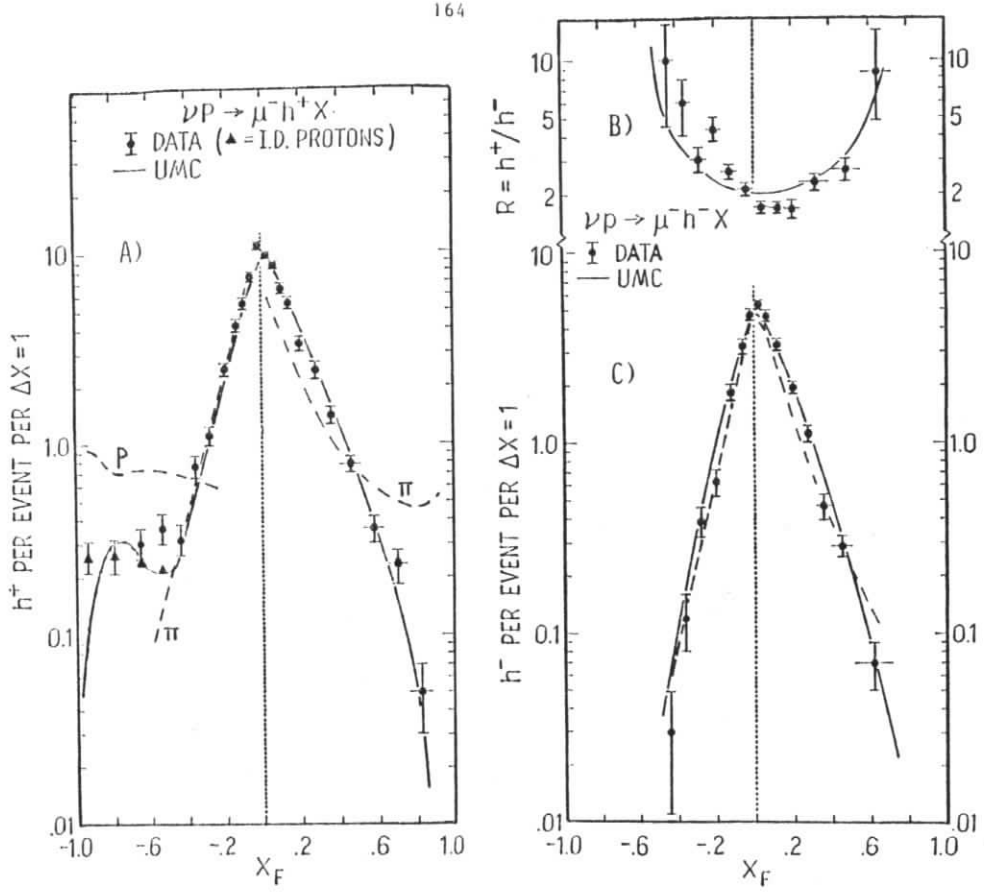

Fig. 6.23
a) Density of positive particles vs. Feynman x_F in the hadronic rest frame, for νp interactions with x > 0.05, and W > 4 GeV. From 15' νp[205]. Full lines refer to a longitudinal phase space model. Dotted lines show the hadron distribution in $\pi^+ p$ interactions at $\sqrt{s}$ = 5.6 GeV[229].
b) Ratio of positive to negative hadrons vs x_F
c) Density of negative hadrons vs x_F.

increase is slightly stronger than observed in normal interactions. However, most of this second effect, if not all, may be accounted for by charge conservation.

- the production of fast protons is suppressed compared to normal inelastic interactions.

Various models have been proposed to describe the fragmentation of multiquark systems, like generalisations of the Feynman-Field model[230], multi component fusion models[231], etc.. We shall discuss two models which rely on a minimum number of additional assumptions, which are most commonly accepted and are well documented, and which have proven useful for the description of normal inelastic reactions: the quark recombination model[14] and the dimensional counting rules[232,233].

6.5 The quark recombination model (QRM)

The quark recombination model is based on a recent observation by Ochs[13] that the x_F distributions of fast mesons produced in proton-proton collisions closely resemble the x distributions of quarks known from deep inelastic lepton nucleon scattering. If these mesons were produced from fast quarks by fragmentation, as in e^+e^- annihilations, the meson spectra would fall much more steeply in x_F than is observed, since one would have to convolute the quark fragmentation function over the probability distribution for quarks in a proton.

This observation lead Goldberg,[234] and later Das and Hwa[14] to propose that fast mesons are produced in hadronic reactions by the recombination of valence and sea quarks, at x_q and $x_{\bar{q}}$, respectivly, into a meson $q\bar{q}$ at $x_M = x_q + x_{\bar{q}}$. Thus the production of fast mesons measures the combined probability $G(x_q, x_{\bar{q}})/(x_q x_{\bar{q}})$ of finding two quarks in the wave function of the proton:

$$\frac{1}{\sigma} E \frac{d^3\sigma_M}{dp^3} = \int \frac{dx_q}{x_q} \frac{dx_{\bar{q}}}{x_{\bar{q}}} G(x_q, x_{\bar{q}}) R(x_M, x_q, x_{\bar{q}}) \qquad (6.20)$$

σ is the total nondiffractive cross section, and R is a recombination function which parametrizes the fusion process. R can be decomposed into a presumably scale invariant two body piece and a many body piece

$$R(x_M, x_q, x_{\bar{q}}) = R_2(\frac{x_q}{x_M}, \frac{x_{\bar{q}}}{x_M}) \delta(x_M - x_q - x_{\bar{q}}) + R'(x_M, x_q, x_{\bar{q}}) \qquad (6.21)$$

Because of the difficulty of many body recombination, R' is assumed to be negligible except for x_M very close to 1, where it gives rise to Regge behaviour . This is visualized by a "competition" argument[235]: fast hadrons are produced after the rapidity plateau at x = 0 has been built up[108]. At that time however, most of the hard gluons which could participate in a multi body recombination will already be "used" by other fragments, respectivly will have turned into quark pairs feeding the particle production at low x.

$R_2(x_q, x_{\bar{q}})$ can be determined from plausibility arguments. One expects recombination to be of short range in rapidity; thus R_2 will be zero for $|Y_q - Y_{\bar{q}}| >> 1$. It seems further natural to assume that the probability for two quarks at $x_q, x_{\bar{q}}$ to recombine into a meson at x_M is proportional to the probability to find the two valence quarks of a meson at x_M at x_q and $x_{\bar{q}}$, respectivly.

That means

$$R_2(\xi_q, \xi_{\bar{q}}) = G_\pi(\xi_q, \xi_{\bar{q}}) / (\xi_q \xi_{\bar{q}}) \qquad (6.22)$$

with $\xi_q = x_q / x_M$ and G beeing the two valence quark structure function of the pion. Eqn. (6.22) can be fullfilled by chosing

$$R_2(\xi_q, \xi_{\bar{q}}) = \alpha \xi_q \xi_{\bar{q}} \qquad (6.23)$$

Eqn. 6.23 yields a single quark structure function of the pion

$$G_\pi(x_q) \underset{x_q \to 1}{\sim} (1 - x_q) \qquad (6.24)$$

in approximate agreement with experiments[236]. Probability conservation requires $\alpha \leq 4$ [237].

In practice, σ_M is nearly independent of the specific choice of R_2 , once the condition of short range recombination is obeyed[238].

For proton-proton interactions where antiquarks are concentrated at low x, $G(x_q, x_{\bar{q}})$ can be approximated as [237]

$$G(x_q, x_{\bar{q}}) = \lim_{\varepsilon \to 0} G_q(x_q) \bar{x}_{\bar{q}} \delta(1 - \varepsilon)/\varepsilon \qquad (6.25)$$

$\bar{x}$ is the average momentum fraction carried by the quark species $\bar{q}$. Eqs. (6.20) and (6.25) explain Ochs observation, they yield

$$\frac{1}{\sigma}(x_M \frac{d\sigma_M}{dx_M}) = \bar{x}_{\bar{q}} \alpha G_q(x_M) \qquad (6.26)$$

Using e.g. the Feynman Field parametrisation of parton structure functions,[239] the QRM describes extremely well the cross sections for $\pi^\pm$ and K^+ production by proton beams for $0.5 \leq x_M \leq 0.9$ [14,237]. Vice versa,the structure functions of sea quarks in the proton were determined using eqn (6.20) and data on valence distributions as an input.[240] The shapes of sea quark distributions obtained in this way agree with results from lepton nucleon scattering, proving the consistency of the model.

With less theoretical justification, the QRM can be extended to lower values of x_M, including thus e.g. the production of K^- in proton-proton interactions via recombination of two sea quarks[241]. At low x_M however difficulties arise due to hadron production by resonance decays. At high x, $x \gtrsim 0.4$ resonance contributions to the inclusive spectra were shown to be negligible both experimentally[242] and theoretically[243]. Though the QRM gives a good description of the shape of inclusive particle spectra, the absolute magnitudes of the cross sections turn out to be considerably below the data, when calculated for the standard amount of sea quarks. To fit the data, the momentum fraction carried by the quark sea of the nucleon has to be 20 to 50 % [14,237,240]; taking into account that the quark antiquark system has to be a spin-0 color singet would increase the required number of sea quarks by another order of magnitude[235].

The enhancement of the sea is usually explained by the following mechanism[235,240]: in an undisturbed hadron, sea quarks and gluons form an equilibrium state. During the interaction, this equilibrium is disturbed since quark-antiquark pairs "condense" into mesons. Consequently, new quark pairs are created etc., until all gluons are used. Therefore the momentum fraction carried by the effective sea should be of the order 50%, or somewhat less, depending on the time scales governing the quark-gluon equilibrium and the recombination mechanism. Finally, it is not unnatural to assume that the spin and color states of the final mesons will be adjusted by emission and absorption of soft gluons, without modifying the z distribution of the mesons.

The ideas nicely dovetail with the probabilistic quark model approach to proton fragmentation by Pokorski and Van Hove[244-246]. They assume that in hadronic collisions the gluon clouds of the hadrons interact and generate the rapidity plateau, whereas the incident valence quarks fly through without change of momentum and recombine to leading baryons and fast mesons.

The QRM has been applied to deep inelastic reactions by De Grand et.al.[241,247]. The situation is only slightly more complicated in this case; here one measures the combined probability for seeing three quarks (fig. 6.24) in the wave function of the proton.

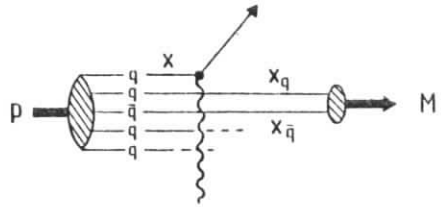

Fig. 6.24
Quark recombination in reactions initiated by pointlike probes measures the three quark distribution in the nucleon.

For instance, the meson spectrum in the target fragmentation region in deep inelastic electron-hadron scattering is

$$\frac{1}{\sigma(x)}\ \frac{d\sigma(x,z)}{dz} = \frac{\sum_i q_i^2 \int \frac{dx_q}{x_q} \frac{dx_{\bar{q}}}{x_{\bar{q}}} G(x,x_q,x_{\bar{q}}) R_2\left(\frac{x_q}{x_M}, \frac{x_{\bar{q}}}{x_M}\right) \cdot \delta(x_M-(1-x)z)}{\sum_i q_i^2\ G(x)} \qquad (6.27)$$

where q_i is the charge of the i-th quark. z is the fraction of the recoiling core's momentum (in an infinite momentum frame) carried off by the meson. The cross section is normalized by the total cross section at fixed Bjorken x, i.e. it describes the number of mesons per event. Similar expressions hold for neutrino-nucleon scattering.

So far the discussion has been quite general. In order to make quantitative predictions, however, one has to make models for the multiquark distributions in the target, like the Kuti-Weisskopf model[248].

A Kuti-Weisskopf model assumes that the instantaneous probability distribution F of partons in the proton factorizes as

$$F = F_u(x_u)F_u(x_{u'})F_d(x_d)F_o(1-\sum_{u,u',d} x) \equiv \frac{G(x_u,x_{u'},x_d\cdots)}{x_u\cdot x_{u'}\cdot x_d\cdots} \qquad (6.28)$$

The sea wave function F_o is a sum over all possible numbers of sea partons

$$F_o(\tilde{x}) = \left(\sum_{n=0}^{\infty}\frac{g^n}{n!}\prod_1^n F_s(x)\right)\delta(\tilde{x}-\sum_{sea} x) \qquad (6.29)$$

Eqn. (6.29) is written for one type of sea partons, its generalisation to n quark flavors and gluons is obvious. The coupling constant g determines the mean number of sea partons.

After summing over all unseen partons, one obtains for the inclusive distribution of the valence quarks and of m sea partons[238]

$$F_m = F_u(x_u)F_u(x_{u'})F_d(x_d)\prod_{i=1}^m F_s(x_i)\,C_{uud}(\bar{x}) \qquad (6.30)$$

with

$$\bar{x} = 1-\sum_{u,u',d,sea} x_i$$

The function C_{uud} expresses the damping close to $x = 1$ and depends on the mean number of sea partons, i.e. on g. Approximately one has

$$C_{uud} = \bar{x}^{g-1} \qquad (6.31)$$

In general, g stands for the sum of the coupling constants of the various species of sea quarks.

The functions F_u, F_d, F_s and the coupling constant g are to be determined from data. The connection to the fully inclusive single valence quark spectra is given by

$$G_u(x) \underset{x\to 1}{\approx} (1-x)^g F_u(x)$$

$$G_d(x) \underset{x\to 1}{\approx} (1-x)^g F_d(x) \qquad (6.32)$$

In addition, Regge behaviour suggests that

$$F_u(x),\ F_d(x) \underset{x\to 0}{\sim} \frac{1}{x^{\alpha_R}} \sim \frac{1}{\sqrt{x}} \qquad (6.33)$$

The small x behaviour of the sea quark distribution is determined by the pomeron trajectory

$$F_s(x) \underset{x\to 0}{\sim} \frac{1}{x^{\alpha_P}} \sim \frac{1}{x} \qquad (6.34)$$

Under the conditions of eqn (6.32) to (6.34), a fit of the measured structure functions can be obtained e.g. by choosing 238)

$$F_u(x) = x^{-1/2}(1+3.5x)$$

$$F_d(x) = x^{-1/2}(1+5.0x)(1-x)$$

$$F_{\bar{u},\cdots}(x) = x^{-1}(1-x)^3$$

$$F_g(x) = x^{-1}$$

and

$$g_{\bar{u},\bar{d}} \cdots = 0.12$$
$$g_{s,\bar{s}} = 0.09$$
$$g_{g} = 2.84 \qquad (6.35)$$

for the sea quark and gluon coupling constants, respectivly. These parametrisations are not unique; other combinations (which fit the measured structure functions as well) were chosen e.g. in ref. 241. The predictions of the QRM, as quoted in the following also turn out to be insensitive to the acual choice of the model parameters.

Let us now specify the predictions of the QRM for νp scattering (fig. 6.23). The basic features can be derived without explicit calculation. In Kuti Weisskopf models, the two quark wavefunctions factorize approximately, as can be seen from eqs. (6.30), (6.31), and (6.35):

$$G(x_1,x_2) \sim G(x_1)G(\frac{x_2}{1-x_1}) \qquad (6.36)$$

Taking x_1 as the x of the quark beeing scattered, $x_2/(1-x_1)$ is identical to the scaling variable z describing the fragmentation of the spectator. That means that the distribution of a valence quark of the spectator is identical to its distribution in the initial proton, if written in the correct scaling variable.

For νp interactions at very low x, the current will mostly scatter off a sea quark, and the spectator contains all three initial valence quarks. Consequently, because of eqn (6.36), the distribution of fast mesonic fragments should be identical to that observed in normal inelastic interactions. Furthermore, the distribution of π^+ and π^- will be similar, except for a normalisation factor 2 since there are two u quarks, and a factor (1-x) reflecting the dominance of u quarks at large x. As the x of the scattered quark increases, the neutrino will mostly interact with the d quark; therefore the π^+ distribution will remain unaffected, whereas the π^- distribution steepens since a π^-

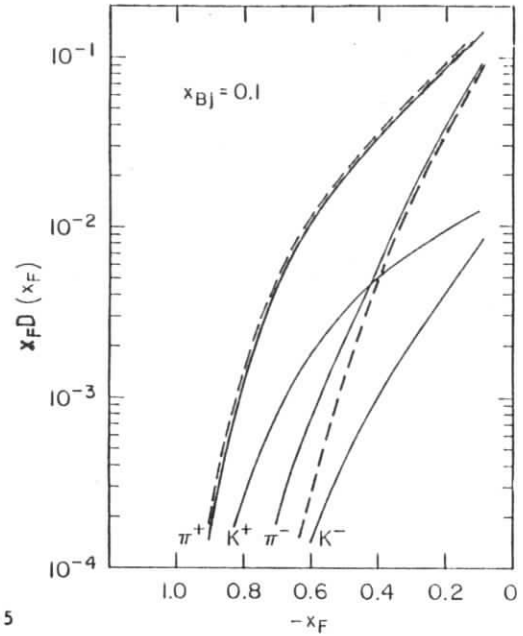

Fig. 6.25
Invariant cross section for meson production in the spectator fragmentation region in $\nu p \to \mu^- h^\pm x$ reactions as a function of x_F. Full curves are predictions of the QRM[241], absolutely normalized. Dotted curves are predictions of dimensional counting rules (DCR), arbitrarily normalized.

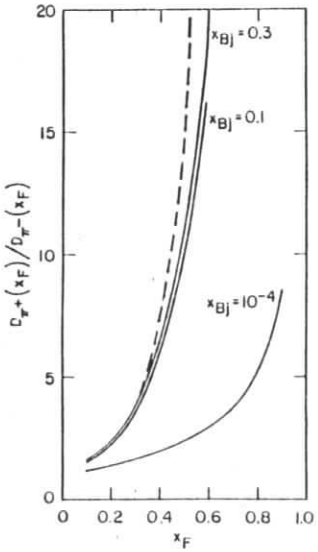

Fig. 6.26
Ratio of positive to negative pion density in the spectator fragmentation region in $\nu p \to \mu^- h^\pm x$ as a function of x_F, for different values of Bjorken x. Curves as in fig. 6.25

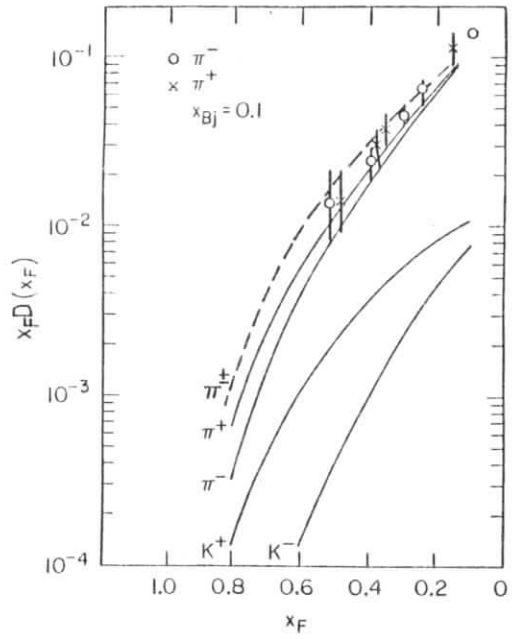

Fig. 6.27
As in fig. 6.25, but for $\bar{\nu}p \to \mu^+ h^\pm x$. Data from ref. 249.

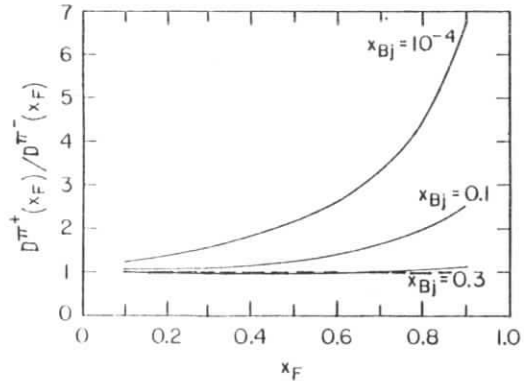

Fig. 6.28
As in fig. 6.26, but for $\bar{\nu}p \to \mu^+ h^\pm x$.

cannot longer be produced by recombination of a valence quark with a sea parton.

The pion and kaon spectra resulting from the exact evaluation of eqn (6.27) [241] are shown in figs. 6.25 and 6.26, for charged current νp interactions. The curves represent the lorentz invariant cross section $(2/\pi W) \int dp_\perp^2 E d^3\sigma/dp^3$, and the predictions are extended to low x_F using empirical corrections and sea enhancement factors[241]. The normalisation has been adjusted to a electroproduction experiment at lower energies[222]. In fig. 6.26 the ratio of π^+ to π^- production is compared for various Bjorken x, nicely demonstrating the transition from sea quark scattering (low x) to valence quark scattering ("high" x). The corresponding spectra for $\bar{\nu}p$ scattering are shown in figs. 6.27 and 6.28, including data from a $\bar{\nu}$ scattering experiment at lower energies. As in the latter case the spectator always contains both u and d quarks, the spectra of π^+ and π^- are similar.

As far as baryon production is concerned, the predictions of the QRM are rather ambugious since there are various competing production mechanisms. For scattering of a sea quark at low x, the possibilities are depicted in fig. 6.29 a)-d). The two extrema are the recombination of all valence quarks to a baryon, and the recombination of the valence quarks into three mesons with the baryon being formed by the sea quarks left over. The corresponding graphs for spectators containing two valence quarks of the initial proton are shown in fig. 6.29 e)-g). Obviously, for $z \to 1$, the graphs with the maximum number of valence quark lines collected in the baryon will dominate.

The relative probabilities can be estimated by noticing that the processes shown in fig. 6.29 a) are presumably identical to those describing proton fragmentation in normal proton-proton interactions.

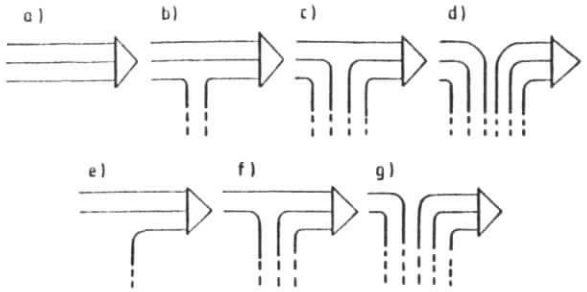

Fig. 6.29 Diagrams for baryon production by spectator systems containing all three initial valence quarks (a-d), and two valence quarks, respectivly (e-g).

An analysis of such interactions in terms of the graphs shown above is reported in ref. 246. It is stated that the probability T that two incident valence lines emerge in a single hadron is about 0.65. Assuming that T has a universal value for all "soft" hadronic processes [246], we are now able to predict the shape of proton spectra in the spectator fragmentation region. For sea quark scattering, the terms dominant at large z, fig. 6.29 a) and b) generate T^2 and (2T)/2 protons per event, in the mean. The factor 1/2 in 6.29 b) arises since roughly half of baryons will be neutrons. For valence quark scattering, fig. 6.29 e) dominates at high z, yielding an integral number of T/2 protons per event. The QRM can be easily generalized to this type of recombination, yielding

$$\left(\frac{d\sigma_p}{dz}\right) \underset{z\to 1}{\sim} G_i(z) \qquad (6.37)$$

with $G_i(z)$ beeing the distribution of the momenta of parton

systems containing i valence quarks. The normalisation is given by

$$\int E\frac{d^3\sigma_p}{dp^3}\,\frac{d^3p}{E} = T^2 \;;\; T \;;\; \frac{T}{2} \qquad (6.38)$$

fig.6.29 a) b) e)

e.g.

We are now able to compare the QRM with the high statistics data from the 15' νp experiment (fig. 6.23). The cut $x > 0.05$ provides a rather clean sample of ν-valence quark interactions. Fig. 6.30 shows the data compared to absolute QRM predictions. The shape of the pion spectra, and the charge ratios are well described. The absolute normalisation seems to be a bit too low, however taking into account that the model refers to scaling spectra at very high energies, and does not contain nonasymptotic corrections, the agreement is fairly good. The proton distribution seems to drop slightly too fast as $|x_F| \to 1$. However one should note that for the mean W of this data the kinematical limit for proton production is $x_F = -.90\cdots -.95$, so at least the data point at highest $-x_F$ appears somewhat questionable. Secondly, the excess at high x may be due to a small remaining fraction of diffractive events. This is supported by the BEBC data (fig. 6.31) which indicates that the proton cross section drops at $x_F \to -1$ as Q^2 increases.

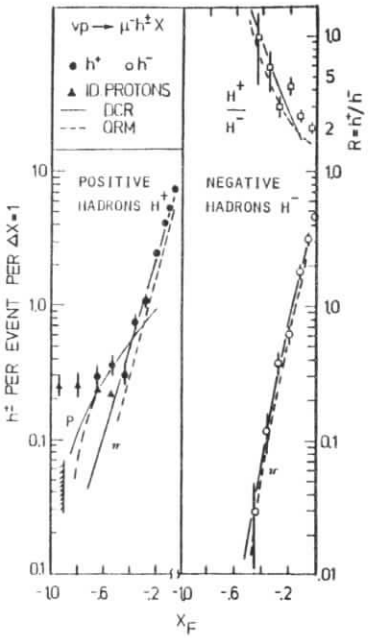

Fig. 6.30
Same data as fig. 6.23, compared to model predictions for the spectator fragmentation region $0 \geq x_F \geq -1$. Dotted lines: QRM, absolutely normalized[241].
full lines: Dimensional counting rules. Proton spectra are absolutely normalized; one normalisation constant for meson spectra chosen to fit the data.

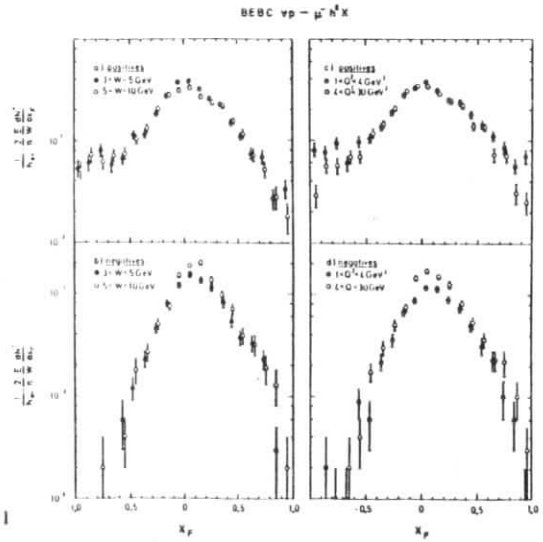

Fig. 6.31
Normalized lorentz invariant cross section for positive (a,c) and negative (b,d) particle production in νp charged current interactions from BEBC νH_2[208] for 2 intervals of W and of Q^2.

6.6 Dimensional counting rules

A second, and widely used approach to describe the fragmentation of multiparton systems is based on dimensional counting technics[250-254]. The dimensional counting rules (DCR) developed by Brodsky, Blankenbecler, Gunion, and Farrar[255-258] refer to the inclusive spectra of the fragment a in the fragmentation process

$$A \to a + X \tag{6.39}$$

As usual, the process is decribed in a frame where the momenta p_A and p_a are large. DCR predict

$$\frac{1}{\sigma} \int E\frac{d^3\sigma_a}{dp_\perp^2}\, dp_\perp^2 \sim z\,\frac{1}{\sigma}\frac{d\sigma_a}{dz} = z\, D_A^a(z) \underset{z\to 1}{\sim} (1-z)^m \tag{6.40}$$

with $z = p_a/p_A$, and $m = 2n_x - 1$, where n_x is the minimum number of quarks left behind in X.

Eqn (6.40) can be derived using the Bethe-Salpeter equation to describe an n-quark bound state.[256,253,241] If such a state decays into a particle a and n_x residual quarks, the mean momenta of the residual quarks go to zero as (1-z) for $z \to 1$, giving rise to a phase space-like suppression factor $(1-z)^{n_x}$ in the transition amplitude, or $(1-z)^{2n_x}$ in the decay probability. In the overall expression, one factor (1-x) is canceled by an energy denominator refering to the core energy.

The spectrum of fragments a is then given by

$$\frac{1}{\sigma}\, z\,\frac{d\sigma_a}{dz} = \sum_{i=n_x}^{\infty} f_i (1-z)^{2i-1} \tag{6.41}$$

with f_i beeing the probability that i quarks are left behind.

Eqn. 6.41 holds only for 1-z small, e.g. $z \gtrsim 0.5$.[241,257] In this limit, σ_a will be dominated by the leading term shown in eqn (6.40).

There are basic differences between the DCR-ansatz and the QRM[241]: in the counting rule scheme, no distinction is made between sea- and valence quarks of the incident particles, both are treated on equal footing, and with identical matrix elements. The different shape of valence quark structure functions arises from the summation over the different Fock states, in any of which the valence quarks are present whereas the mean number of sea quarks, equivalent to the relative importance of higher Fock states, is small. Consequently, for semiinclusive deep inelastic scattering we assume that the nucleon breaks up into a quark c (which is struck by the current) and a core A of n_A quarks; this core then breaks up into a meson a and a recoiling core of n_x quarks. Thus we get in analogy to eqn (6.41)

$$\frac{1}{\sigma(x)} z \frac{d\sigma_a(x,z)}{dz} \underset{z\to 1}{\sim} \frac{\sum_{n_A} f_{n_A} (1-x)^{2n_A-1} (1-z)^{2n_x-1}}{\sum_{n_A} f_{n_A} (1-x)^{2n_A-1}} \qquad (6.42)$$

This implies however that between the hard scattering and the fragmentation the quark core A again reaches an equilibrium state.

Note that in eqs (6.41) and (6.42) the power in (1-x) may increase by one unit due to spin effects.[253,260]

Let me demonstrate the application of DCR in a few examples.

Fig. 6.32 shows the leading graphs contributing to the proton- and pion structure functions. For $x \to 1$, we predict

$$\begin{aligned} G_p^{u,d} &\sim (1-x)^3 \\ G_p^{\bar{u},\bar{d},..} &\sim (1-x)^7 \\ G_{\pi^+}^{u,\bar{d}} &\sim (1-x) \\ G_{\pi^+}^{\bar{u},d,..} &\sim (1-x)^5 \end{aligned} \qquad (6.43)$$

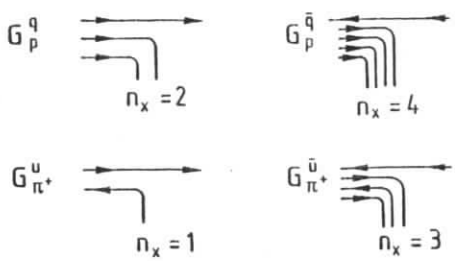

Fig. 6.32
Counting rule graphs describing nucleon and meson structure functions. n_x is the number of residual quarks

in reasonable agreement with the experimental values. Fig. 6.32 can as well be read as defining quark fragmentation functions (from right to left). Obviously one gets

$$G_A^a(x) \underset{x\to 1}{\sim} D_a^A(x) \qquad (6.44)$$

as required by rather general correspondance arguments[138,139].

The discrepancy between the prediction $D_u^{\pi^+} \to (1-z)$, and the experimental results, close to $(1-z)^2$ can be explained by spin effects. The predicted suppression factor for unfavored decays, $(1-z)^4$ however is in clear disagreement with the observed behaviour (1-z). The explanation is simple: the DCR don't include effects like resonance production. Favored production of ρ mesons by a u quark, followed by a decay into $\pi^+\pi^-$ yields a π^- spectrum suppressed just by (1-z) as compared to the

p spectrum. These modes have to be taken into account when applying DCR; they are especially important in quark jets where the ratio of vector meson to scalar meson production is of the order 1.[112] On the other hand, resonance effects can be neglected in the high z region of favored soft fragmentation processes.[242,243]

Let us now calculate the distribution of spectator fragments in νp and $\bar{\nu} p$ charged current interactions with valence quarks. We obtain

$$\nu p: \quad \int dp_\perp^2 E\frac{d^3\sigma}{dp^3} \sim \begin{cases} zD_{uu}^{p}(z) \sim (1-z) & \text{for protons} \\ zD_{uu}^{\pi^+}(z) \sim (1-z)^3 & \text{for } \pi^+ \\ zD_{uu}^{\pi^-}(z) \sim (1-z)^7 & \text{for } \pi^- \end{cases}$$

and

$$\bar{\nu} p: \quad \int dp_\perp^2 E\frac{d^3\sigma}{dp^3} \sim \begin{cases} zD_{ud}^{p}(z) \sim (1-z) & \text{for protons} \\ zD_{ud}^{\bar{u}\pm}(z) \sim (1-z)^3 & \text{for } \pi^\pm \end{cases} \qquad (6.45)$$

Figs. 6.25 - 6.28 show these curves together with the QRM predictions, a comparison with νp data is included in fig. 6.30. In the last case, the proton cross section has been normalized to give 0.5 protons per event. The pion spectra are arbitrarily normalized, however the same normalisation constant is used for both π^+ and π^- spectra (although this is not necessarily required by DCR). Except for the proton spectra at high $|x_F|$, the agreement with data is excellent.

Unfortunately, the fact that both QRM and DCR roughly agree with data doesn't help to shed light on the underlying fragmentation mechanism. The two models are even contradictory: the QRM assumes that the final mesons reflect the quark distribution immediately after the interaction, whereas the interpretation of the DCR requires the spectator partons to

reach a new equilibrium state. We shall return to this point in chapter 7.

Let me now briefly go through a few recent extensions of DCR. The influence of spin effects has been clarified in a recent work by Brodsky[134]. If the helicities of parent and fragment differ by Δh, an additional factor $(1-z)^{2|\Delta h|}$ arises in $d\sigma/dz$. This correction e.g. improves the agreement with experiment for the favored quark fragmentation into mesons.

Furthermore one has to ask what scaling counting rules mean in a world where scaling seems to be violated at least as far as structure functions are concerned. It has been shown by Frazer and Gunion[262] that using the DCR-approach via the Bethe-Salpeter equation reproduces the Altanelli-Parisi equations. A heuristic picture to this is given in the model of scale breaking by Kogut and Susskind (chapter 5): increasing Q^2 yields an improved resolution of the system under study so that effectivly the system appears to have more constituents, resulting in a steepening of the structure- and fragmentation functions.

$$zD(z) = (1-z)^{2n_{eff}(Q^2)-1} \qquad (6.46)$$

Additional violations of scaling which appear in system with an even number of constituents, and which vanish like $1/Q^2$ have been discussed by Vainstain and Zacharov[260].

Finally, the question of the time scales involved in parton fragmentation has been investigated by Gunion[192]. As already mentioned, there seems to be a disagreement between the requirement of an intermediate equilibrium state in DCR, and the fact that particle production at x close to 1 involves off shell partons (eqn 6.16), resulting in short decay times (measured in the rest system of the fast fragment). Since this process will contain large momentum transfers, the quark pairs required for the fragmentation can be created in a pointlike manner during the decay (fig. 6.33 a). This quarks don't

participate in the momentum sharing among partons belonging to the n quark Fock state of the parent system, the suppression per quark line left over is smaller than in the original DCR. Using these "pointlike" counting rules one obtains

$$D_A^a(z) \sim (1-z)^{2n_x+n_{pl}-1} \qquad (6.47)$$

n_x is the number of those quarks in X which are completely unaffected by the decay. n_{pl} is the number of quarks in X which participate in a hard creation process. In the case of νp scattering at not too small x, one obtains now (fig. 6.33 b-d)

$$D_{uu}^{\pi^+} \sim (1-z)^3$$

$$D_{uu}^{\pi^-} \sim (1-z)^5$$

$$D_{uu}^{p} \sim (1-z)^1 \qquad (6.48)$$

The x dependence in (6.48) has been calculated assuming that the emission of a fast fragment immediately follows the hard scattering, and that consequently quark distributions are identical to those in the incident proton. To derive multi-quark distributions, factorisation in the sense of eqn. (6.36) was used.

Within the limited statistics available, and due to the restricted x range for negative fragments, "standard" and "pointlike" counting rules cannot yet be distinguished experimentally.

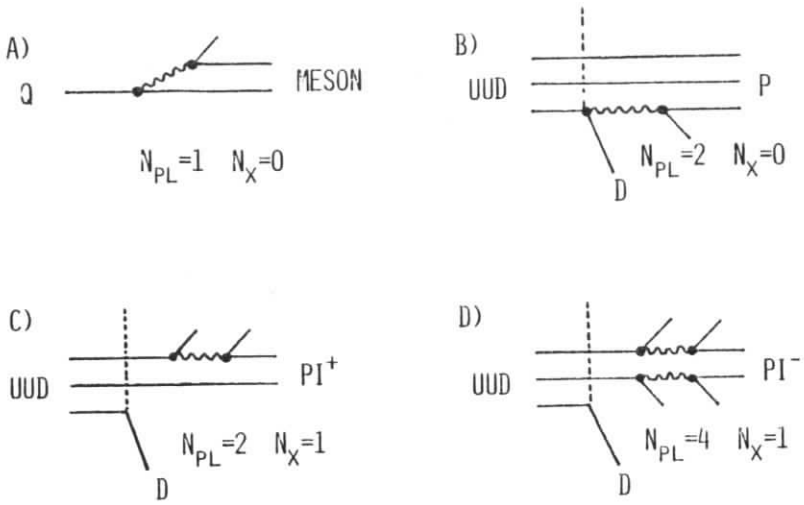

Fig. 6.33 a) Counting rule graph involving a pointlike creation process b)-d) corresponding graphs for the fragmentation of a uu-diquark into p, π^+, and π^-. n_{pl} is the number of residual quarks which participated in the pointlike process. n_x is the number of passive residual quark fields. The quark which interacts with the external current belongs to the primordial wave function and counts as a passive constituent.

6.7 The 3 gluon decay of the T

Up to now we restricted our attention to parton systems where in a suited reference frame the momenta of color sources are more or less collinear. The principles of factorisation and universality were used to describe the fragmentation of these systems; QRM and DCR provide convenient, however not yet fully understood parametrisations of the fragmentation functions of multiquark systems. There is no ambiguity of chosing the "best" reference frame for the description of the fragmentation, except for longitudinal boosts. The situation changes drastically as soon as three or more color sources are distributed in space.

As an example, we shall discuss the decays of heavy quark-antiquark bound states like the Υ or the Υ'. These mesons were discovered[265] as broad enhancements in the mass spectrum of muon pairs produced in proton-nucleus collisions. The interpretation as bound states of a new quark flavor has been confirmed by production experiments[266-269] using the upgraded storage ring DORIS at DESY[270] (fig. 6.34). The charge of the new quark can be determined from the leptonic decay widths of the Υ and the Υ', which turn out to be consistent with $|q| = 1/3$ (fig. 6.35)[273]. The best estimate of the total decay width of the Υ is $\Gamma = 50$ KeV, as calculated from Γ_{ee} and the leptonic branching ratio $B_{ee} = B_{\mu\mu} = 2.6 \pm 1.4\%$ [271,292]. The narrow width implies that the quarks in the Υ carry a new, conserved flavour, called bottom, and that the Υ-mass is below the threshold for production of naked bottom. Allowed decay modes are annihilations into an odd number of strong, electromagnetic, or weak vector bosons. Relevant decays are the annihilation into a virtual photon, $\Gamma \approx O(\alpha)$, and the annihilation into the simplest color singlet formed of an odd number of gluons, $\Gamma \approx O(\alpha_s^3)$ (fig. 6.36). Modes with more than 3 gluons are suppressed since $\alpha_s(M_\Upsilon^2)/\pi < 1$. In principle, the Υ may also decay into a large number of soft gluons, which correspondingly have large couplings. This process in generally assumed to be negligible[274,275,289], as those

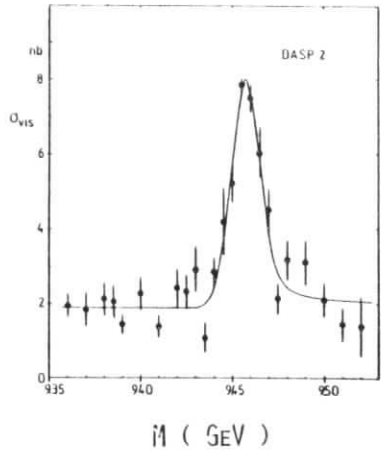

Fig. 6.34
Visible cross section of the reaction e^+e^- → hadrons. The solid curve describes a single resonance with gaussian energy resolution and radiative corrections. The width of the peak is consistent with the energy resolution, $\sigma = 7.6$ MeV.[271]

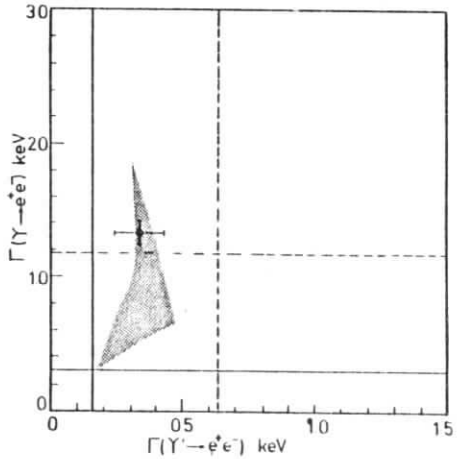

Fig. 6.35
Quarkonium model expectation[273] for the leptonic widths of Υ and Υ' for quark charges $|q| = 1/3$ compared to the mean values measured at DORIS [266-269,292].

gluons would have a wavelength large compared to the size of the Υ. Therefore the Υ acts effectivly as a color singlet and decouples. Since α_S is very large compared to α, the three gluon decay of the Υ essentially will saturate the hadronic cross section.[290] The hadronic decays of the Υ offer the up to now unique opportunity to study decay properties of noncollinear arrangements of basic color sources; in parallel we may hope to get further insight into the way a gluon fragments.

The matrix element for the decay has been calculated by various authors[276-281]

$$\frac{1}{\sigma}\frac{d^2\sigma}{dx_1 dx_2} = \frac{1}{(\pi^2-9)}\left[\frac{(1-x_3)^2}{x_1 x_2} + \frac{(1-x_2)^2}{x_1 x_3} + \frac{(1-x_1)^2}{x_2 x_3}\right] \qquad (6.49)$$

where x_i is the fractional momentum of the i-th gluon, $x_i = 2|\vec{p}_i|/M_\Upsilon$. The inclusive x distribution of gluons is shown in fig. 6.37; their angular distribution is illustrated by the Dalitz plot (fig. 6.38). In general, the gluons will be noncollinear. Note, however, that the matrix element (6.49) refers to massless gluons, whereas in the preconfinement picture they are expected to be off shell, $p^2 = 0\ (M_\Upsilon^2)$.

How do this gluons transform into hadrons? As a first step, use the picture that colored objects at large distances from each other built up tubes of color fields. In the case of two partons the tube is obviously along the line connecting them, and the jet axis will coincide with this line. For three partons in a noncollinear configuration, the color field tubes emanating from the partons have to join somehow in order to form a color singlet. It seems natural to assume that the system is in the energetically most favorable state, with a minimum of energy stored in the gluon field.

The actual configuration depends on the properties of the color strings, especially on their tension which is defined by the

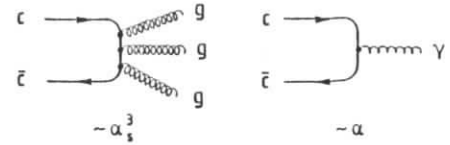

Fig. 6.36
Allowed decay modes of the Υmeson into vector bosons.

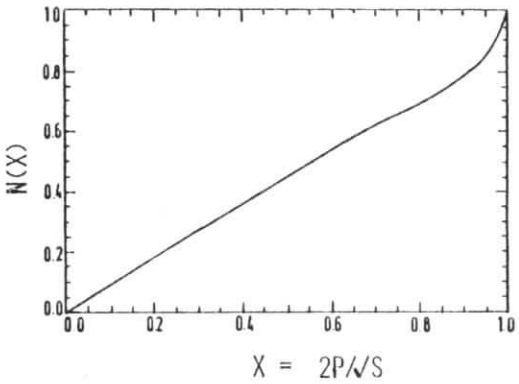

Fig. 6.37
The inclusive momentum distribution of on shell gluons from the Υ decay, according to eqn (6.49).

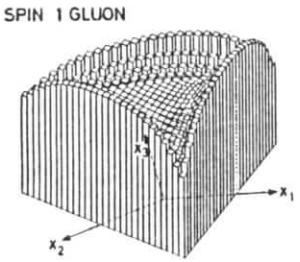

Fig. 6.38
Dalitz plot for the decay of the Υ into three on shell gluons, according to eqn (6.49).

energy per unit length at rest. In the MIT-bag model the tension of an octet, or gluon tube is r = 3/2 times bigger than that of a triplet tube [282], lattice gauge theories predict r > 2 [283].
In the latter case, it is more favourable for an octet, or gluon, to split into triplet tubes.

For the Υ decay, possible configurations of flux tubes are shown in fig. 6.39. In case of $r < 2$, the octet tubes join in the middle, and a "color center frame" can be defined as that frame, where the tensions of the three strings are in an equilibrium[284]. In the center of color frame, the gluons are emitted with angles of 60° relative to each other [284].

For $r \geq 2$ the octet tubes split up and the gluons are connected by three triplet tubes.[283,284]

Corresponding diagrams are obtained e.g. for $q\bar{q}g$ states resulting from e^+e^- annihilations (fig. 6.40). In the limit $r \geq 2$, the gluon may be identified as a "kink" in the triplet string joining the quarks. This interpretation of a gluon has been discussed extensivly in ref. 285; it offers a bridge to topological models[219] where gluons don't appear explicitely. From this point of view, one may even think of the 3 gluon intermediate state in the Υ decay as a closed triplet tube with 3 kinks!

In analogy to the Schwinger model (section 4.2) the hadron distribution may be calculated as the four dimensinal Fourier transform of the color field strength (eqn 4.10). Equivalently, we may say that the color tubes decay into hadrons with limited momentum transverse to the color-anticolor axis, rather than to the jet axis in the overall cms. In the following, we shall refer to three models for the Υ-decay:

model I each gluon fragments as a color octet, and the process is described in the overall cms. If a gluon has a momentum p, on octet-antioctet jet is generated with an invariant mass $M_{8\times\bar{8}} = 2p$, and one half of it is taken as the gluon jet. This straight foreward

picture has been used by many authors [276,277,279].

model II Assume $r \leq 2$. The octet octet strings join symmetrically in the center of color frame. Gluon fragmentation is described as above, but in the center of color frame.

model III Assume $r \geq 2$. Then the octet strings split into three triplet strings, the fragmentation of each is described in its own center of mass frame. The triplet strings are treated as quark-antiquark jets, the "decay" of the gluon into quarks being described by the usual QCD cross section.

In models II and III, the lorentz transformation to the overall cms will lead to an increase of the mean transverse momentum squared with respect to the new jet axis in the cms, and will modify the distribution of energy flux[286]. However, the factorisation property (eqn 6.7) will still hold for fast particles, since the scaling variable transforms as

$$z_{CMS} = z_{COLOR\ CENTER} + O\left(\frac{m_{\perp cms}}{p_{\parallel cms}}\right) + O\left(\frac{m_{\perp}}{p_{\parallel}}\right) \qquad (6.50)$$

where $m_{\perp}$ and $p_{\parallel}$ refer to quantities in the color center frame.

A more sensitive quantity is the mean decay multiplicity of the Υ. For model I we get

$$\langle n \rangle = \frac{1}{\sigma} \int_0^1 dx \left(\frac{d\sigma_g}{dx}\right) \frac{1}{2} n_{gg}(x\sqrt{s}) \qquad (6.51)$$

$n_{gg}(\sqrt{s})$ is the mean multiplicity of a gluon - "anti"gluon jet system of mass $\sqrt{s}$. In model II, the expression simplifies to

$$\langle n \rangle = 3 \cdot \frac{1}{2} n_{gg}\left(\frac{2}{3}\sqrt{s}\right) \qquad (6.52)$$

Finally for model III we have

$$\langle n \rangle = \frac{1}{\sigma} \int_0^{\sqrt{s}} dm \left(\frac{d\sigma}{dm}\right) n_{q\bar{q}}(m) \qquad (6.53)$$

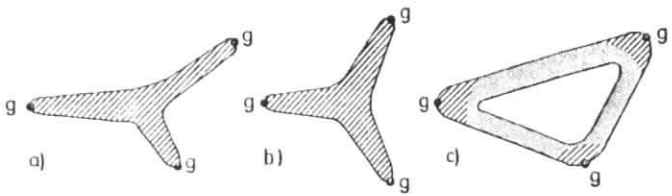

Fig. 6.39 Configuration of color flux strings in the T decay a) r ≤ 2, cms frame b) r ≤ 2, color center frame c) r ≥ 2, cms frame. Shaded and dotted regions are octet and triplet tubes, respectivly.

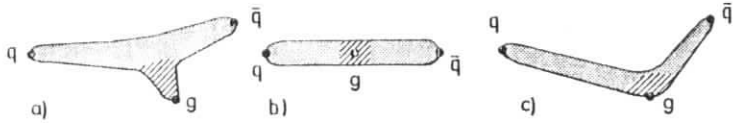

Fig. 6.40 As in fig. , but for $q\bar{q}g$ jets

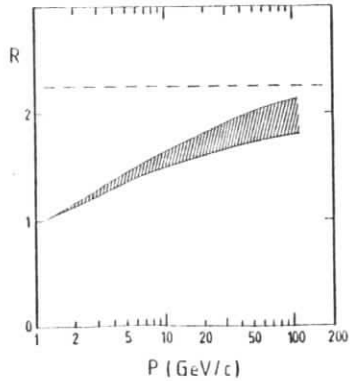

Fig. 6.41 Ratio of gluon to quark jet multiplicities as a function of the partons momentum p from longitudinal phase space models, adjusted to give $R(\infty) = 9/4$.

with $d\sigma/dm$ being the mass distribution of the quark-antiquark subsystems. In the limit of on shell gluons, and neglecting transverse momenta in the process $g \to q\bar{q}$, $(d\sigma/dm)$ is independent of the choise of the reference frame.

Defining now R(p) as the ratio of gluon to quark jet multiplicities for a parton momentum p,

$$R(p) = n_{gg}(2p)/n_{q\bar{q}}(2p) \qquad (6.54)$$

we estimate for <n> from T decays

model I $\quad \langle n \rangle = (1.10 \pm .02) R\, n_{q\bar{q}}(M_T)$

model II $\quad \langle n \rangle = (1.20 \pm .05) R\, n_{q\bar{q}}(M_T)$

model III $\quad \langle n \rangle = (1.50 \pm .10)\, n_{q\bar{q}}(M_T)$

R is to be taken at $p \approx 0\ (M_T/3)$.

Using the canonical value from QCD, R = 9/4, the models I and II predict a tremendous rise in multiplicity on the γ resonance, as compared to the two jet continuum. At modest energies, however, phase space effects will decrease the value of R. This is easily seen: the mean number of particles produced is given by $\langle n \rangle = \sqrt{s}/\langle E_h \rangle$. Two terms contribute to the mean hadron energy $\langle E_h \rangle$: the momentum distribution parallel to the jet axis, depending on the scale invariant matrix element, and the transverse momentum smearing. At moderate energies, the latter is dominant term, and <n> becomes independent on the matrix element. Fig. (6.41) shows R as a function of p, as obtained from phase space models described in chapter 3. The matrix elements were adjusted to yield $R(\infty) = 9/4$. The approach to asymptotic values is extremely slow, in our range of interest we obtain R ≈ 1.2 - 1.3. This leads to the expectation for the relative change in multiplicity on the T, compared to the continuum

$$\Delta n/n_{q\bar{q}} \approx \begin{cases} 30 - 45\ \% & \text{model I} \\ 40 - 60\ \% & \text{model II} \\ 40 - 50\ \% & \text{model III} \end{cases} \qquad (6.55)$$

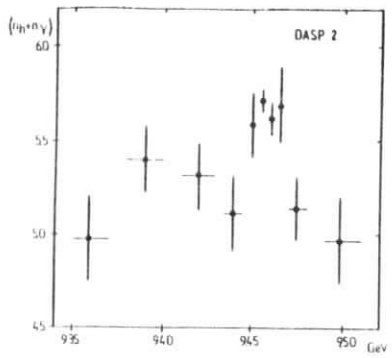

Fig. 6.42

Average visible multiplicity of charged particles and converted photons in the DASP inner detector.[271] The values are not corrected for acceptance.

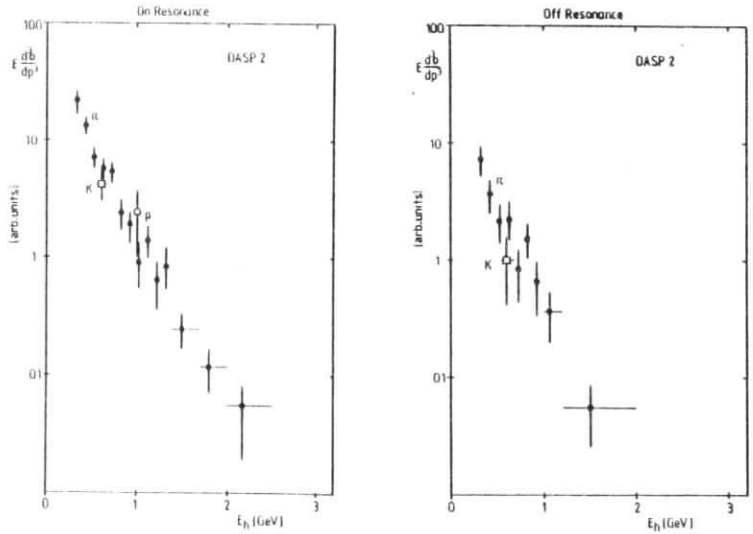

Fig. 6.43

Invariant production cross section for the inclusive reactions $e^+e^- \to \pi^\pm x$, $k^\pm x$, $p^\pm x$ on and off the T(9.46) resonance. From DASP II.[271]

Consequently, one expects the momentum distribution to steepen slightly.

Let us now consider the experimental data. As evident from fig. 6.34, the T resonance sits on a continous background from $q\bar{q}$ jets. Since the events cannot be separated on an event to event basis, all experimental quantities refer to a mixture of $q\bar{q}$ and 3 gluon jets. It is however possible to subtract the contribution of $q\bar{q}$ jets from the continuum and from electromagnetic decays of the T itself on a statistical basis. In the following, we shall refer to uncorrected values as to "on the T" and to corrected ones as to "T direct".

Fig. 6.42 shows the mean observed multiplicity in the DASP detector as a function of energy [271]. A slight increase in $\langle n_{obs} \rangle$ is seen in the T region. The present data on multiplicities is summarized in table 6.3

Table 6.3

Increase of multiplicity for direct T decays compared to two jet events

Group	Ref.	δ(%)	remarks
DASP II	271	12 ± 3)	not corrected for acceptance effects, however corrections should be small (±1)
DHHM	288	13 ± 3)	
PLUTO	287	27 ± 8	corrected values

This values are incompatible with the predictions of model III, they can be accommodated to models I and II only by chosing R ≈ 1.0.

Fig. 6.43 shows the invariant cross section for the reactions

$$e^+e^- \to \pi^\pm x,\ k^\pm x,\ p^\pm x$$

as a function of the particle energy on and off the resonance, respectivly, as measured by the DASP II group.[271] Above the

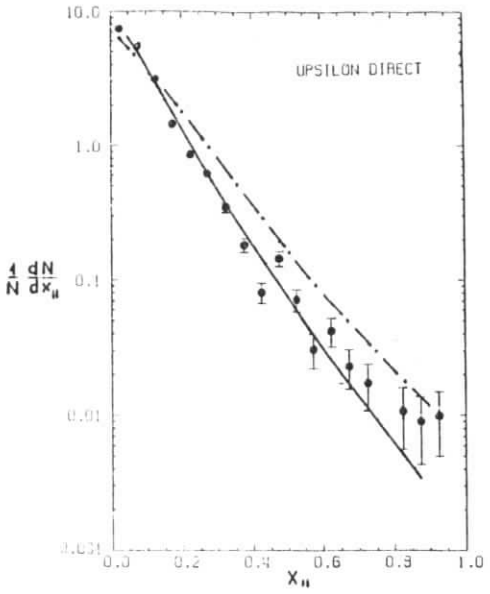

Fig. 6.44
Observed $x_{\parallel}$ distribution with respect to the thrust axis from direct T decays. The point-dashed curve gives the distribution off the resonance. The full line is a model prediction assuming $D_g^h(z) = D_q^h(z)$. From PLUTO[41]

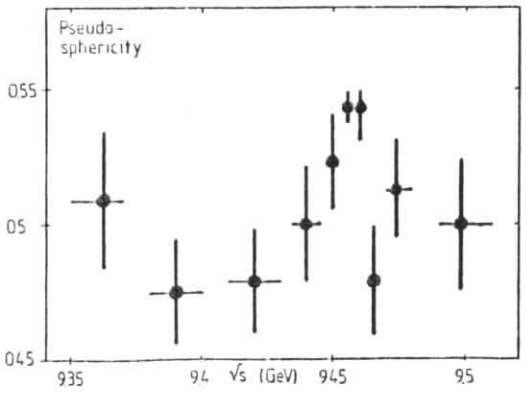

Fig. 6.45
Mean pseudospherocity as a function of energy. From DASP II[271]

momentum cutoff of 200 MeV/c, the pions show a purely exponential spectrum $Ed^3\sigma/dp^3 \sim \exp(-E/E_0)$ with

$$E_0(\text{on resonance}) = (260 \pm 25)\ \text{MeV}$$
$$E_0(\text{off resonance}) = (240 \pm 25)\ \text{MeV}$$

Within the statistical accuracy, there is no difference between the values on and off the resonance.

More precise (preliminary) data are available from the PLUTO detector. Fig. 6.44 shows the distribution of momenta parallel to the thrust axis compared to $d\sigma/dx_{\parallel}$ off the resonance[41]. Direct Tdecays yield a smaller number of particles at high $x_{\parallel}$. Assuming that factorisation holds, a model independent guess for particle spectra is obtained by convoluting $d\sigma/dx_g$ over the gluon fragmentation function $D_g^h(z)$. Justified by the small value of (R-1), we chose as a first approximation $D_g^h(z) = D_q^h(z)$. The resulting spectrum $d\sigma/dx_{\parallel}$ is included in fig. 6.43, it fits data quite well.

The above data dont allow to decide wether the T really decays dominantly into three jets, instead one has to study topological quantities like sphericity or thrust. At this place it should be pointed out that T decays will not show a pronounced 3 jet structure, since the mean energy per jet, $\langle E \rangle \approx 3$ GeV, is just at the threshold where it is possible to recognize a jet structure on a statistical basis, averaged over many events. The following results rely on a comparison with Monte-Carlo models, taking into account the detector acceptance, the reliability of the track recognition and last not least radiative corrections.

Let me first discuss results from DASP II[271,291]. Since the DASP detector measures directions of particles, but no momenta, four "pseudo" topological variables have been used:

Pseudosphericity $= \frac{3}{2} \min \langle \sin^2\theta \rangle$

Pseudospherocity $= ((4/\pi)\min \langle |\sin\theta|^{\gamma} \rangle)^2$

Pseudothrust $= \max \langle |\cos\theta| \rangle$

Pseudoacoplanarity $= 4(\min \langle |\cos\theta| \rangle)^2$

where θ is the angle of each track with respect to the preferred axis, or, for pseudoacoplanarity, with respect to the preferred plane. $\langle\ \rangle$ means the average over particles of one event. Fig. 6.45 shows the mean pseudosphericity as a function of $\sqrt{s}$. Obviously, events from τ decays is less jet like. Table 6.4 summarizes the relative changes of these variables on and off the Υ resonance, compared to a Monte Carlo calculation. The model, based on the Field-Feynman algorithm assumes that gluons are produced according to eqn (6.49), and that they decay exactly like quark jets.

Table 6.4

Change on/off resonance	Exp.[291]	Model[291]
<Pseudoacoplanarity>	18.8 ± 4.0	23.0
<Pseudosphericity>	9.1 ± 1.8	9.8
<Pseudospherocity>	9.5 ± 2.0	14.0
<Pseudothrust>	- 2.8 ± 0.6	- 3.1
<Multiplicity>	8.4 ± 2.0	7.0

The agreement is fairly good, $\chi^2 = 1.4/NDF$. τ decays are definitivly different from normal two jet events, a fit in terms of two jet models gives $\chi^2 = 22/NDF$. The DASP II group pointed out that, if the Υ decays into three gluons, the decay properties of these gluons are identical to those of quarks. A change of the parameter 'a' governing the behaviour of the model for $z \to 1$ (eqn 4.26) from $a = 0.88$ to $a = 1$ completely spoils the agreement, yielding $\chi^2 = 11/NDF$ although the effective change in $D_g^h(z)$ is smaller than for the asymptotic QCD prediction, $D_g^h(z) \sim (1-z)\, D_q^h(z)$ (fig. 6.46). Similarly, a significant change in the mean transverse momentum with respect to the jet axis can be excluded.

Recent, and very detailed studies of the hadron distribution from τ decays by the PLUTO[292] and DHHM[288] groups strongly support this picture of a three jet decay of the Υ. This is e.g.

demonstrated by a three jet analysis using the triplicity method[293], as performed by the Pluto group. The triplicity method assigns three jet axis to each event by grouping the detected particles into three disjunct groups in a way as to maximize the sum of the momenta of the jets. Let $x_1 \geq x_2 \geq x_3$ be the normalized jet momenta, and $\theta_1 \leq \theta_2 \leq \theta_3$ the angles between the jets. Fig. 6.47 shows the experimental distributions of thrust, x_1, x_3, θ_1, and θ_3, for direct τ decays and for two jet events from the continuum[292]. Included are Monte Carlo model predictions for two jet, three jet, and phase space like events. Consider first the two jet data off resonance. An attempt to assign three jet axis to a two jet event will lead to one jet axis coinciding with one of the jets, and the two other axis pointed opposite. Consequently, x_1 is peaked close to 1, and θ_3 is close to 180°. The distribution in x_3 should be rather flat, since the momentum of one original jet is shared among two reconstructed jets, and the angle between this jets, θ_1, should be small. This is exactly what is observed. For direct τ decays, θ_3 decreases, and θ_1 increases, proving that it is reasonable to assign three distinct axis. Data are in good agreement with the 3 gluon decay model (which assumes that gluon jets behave like quark jets); a description by pure phase space seems to be ruled out.

It has been pointed out that the spin of the 3 decay partons can be determined from the angular distribution of the axis of the fastest jet with respect to the beam axis.[289] In the limit $x_1 \to 1$, the distribution of the angle θ between the event axis and the beam direction is given by

$$d\sigma/d\cos\theta \sim 1 + a\cos^2\theta \qquad (6.56)$$

with

$a = 1$ for spin 1 partons
$a = -1$ for spin 0 partons.

Averaged over all values of x_1, one predicts $a = 0.39$[289] for spin 1 partons, and $a < 0$ for spin 0 partons. The distribution of the sphericity axis of direct Υ decays is shown in fig. 6.48 as measured by the PLUTO and DHHM detectors. Taking into account

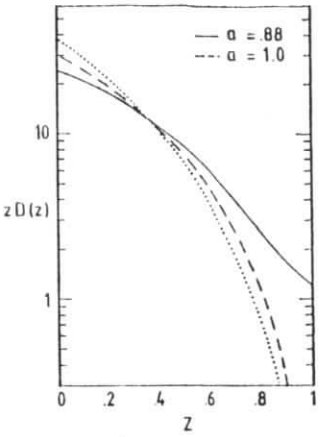

Fig. 6.46

Fragmentation functions $D^h(z)$ in the Feynman Field model for a = 0.88 (quark jets), a = 1.0, and the function $(1-z)D_q^h(z)$ (dotted line)

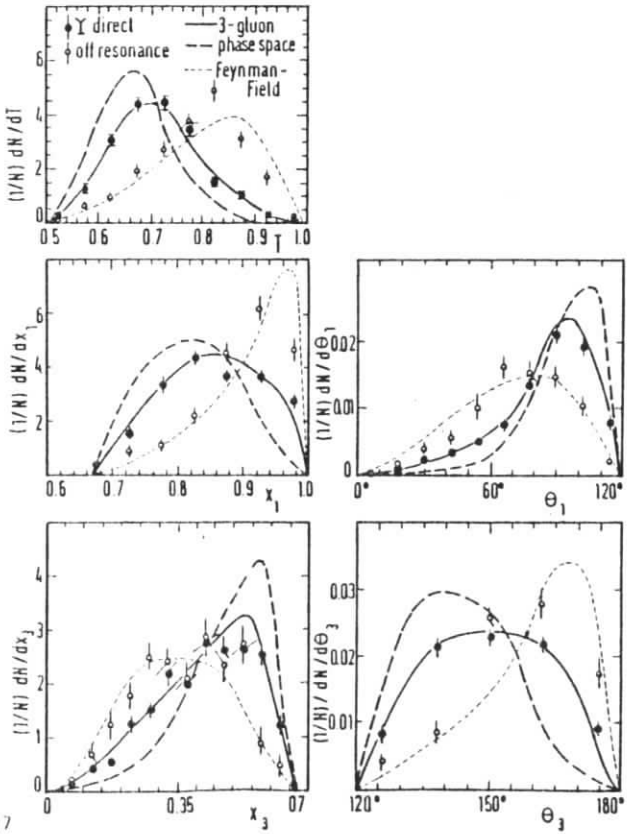

Fig. 6.47

Experimental distributions of thrust T, reconstructed gluon energies x_1, x_3 and reconstructed angles θ_1, θ_3 between gluons compared to various models. From PLUTO [292].

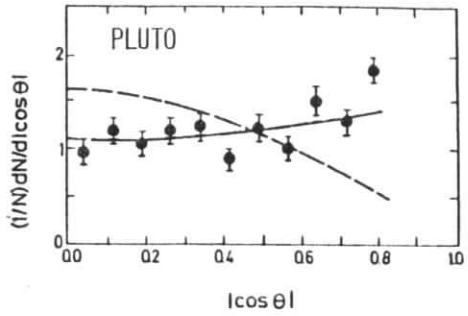

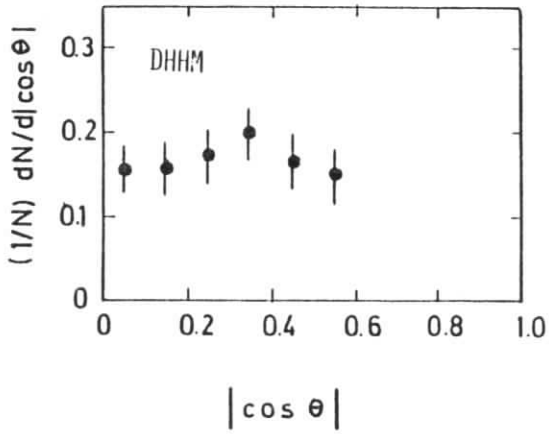

Fig. 6.48

Angular distribution of the sphericity axis in direct Υ decays with respect to the beam axis. Full and dashed lines refer to predictions for spin 1 and spin 0 gluon, respectivly. From PLUTO [292] and DHHM [288].

that the DHHM detector does not allow a precise measurement of the momenta of fast charged hadrons and thus has the tendency to smear the distribution towards isotropy, the spin 1 assignment seems to be slightly favored.

Let me briefly discuss another prediction from QCD: since the gluon couples to all quark species with roughly the same strength, in contrast to a virtual photon, the production of strange quarks should be enhanced. However, as pointed out in chapter 5, the effective change will be small. Fig. 6.43 demonstrates that in fact no abnormal production of charged kaons is observed on the T. In fig. 6.49 the cross section for neutral kaon production is compared to the total cross section. The relative increase on the T is statistically not very significant, but would be compatible with the expectations.

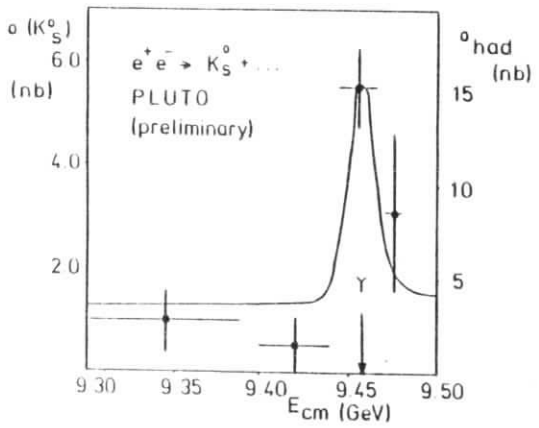

Fig. 6.49
Cross section for k^0 production compared to $\sigma_{hadr.}$ as a function of $\sqrt{s}$. From PLUTO [292]

6.8 Summary

The fragmentation of systems containing more than two elementary color sources, resp. color sources composed of two or more quarks, is studied.

As far as quark jets produced in lepton nucleon interactions are concerned, the principles of scaling, factorisation - or environmental independence -, and universality hold approximately and can be used to relate quark jets from different sources, and at different energies. Small violations of scaling and factorisation are observed, and agree qualitativly with QCD predictions, where $O(\alpha_s)$ terms are taken into account. However, regarding the low mean W, it seems more likely that these effects correspond to the "scale breaking" seen in e^+e^- annihilations at very low energies, which result from phase space effects due to the non negligible particle masses.

The fragmentation of the multiquark spectator systems in lN interactions is shown to be described by quark counting rules, or by a quark recombination model.

Let me now summarize what we learned from the study of T decays. The dominance of a three parton decay mode, probably with spin 1 partons, seems to be established. Although present data have a limited statistical accuracy, there seems to be a disagreement between the expected properties of gluon jets, and the observed fragmentation modes, which are identical to those of quarks, especially as far as multiplicities are concerned. However, parton fragmentation at these energies is expected to be strongly influenced by phase space effects. Because of these problems, it is hard to draw definite conclusions on the dynamics of systems with noncollinear color sources. Only models where the gluon splits up into two incoherent quark jets seem to be excluded.

Assuming that the decay partons of the T fragment like quarks, data is consistent with factorisation.

7. Jets in hadron-hadron interactions with particles of large transverse momentum

Both in e^+e^- annihilations and in lepton-nucleon scattering jets are produced since a parton interacts with a current of large Q^2. The four momentum transfer is given by the change in momentum of the lepton and is well defined experimentally (fig.7.1a) In close analogy, one predicts interactions of two partons inside two colliding hadrons via the exchange of a vector boson[11]; simply by replacing the lepton at the upper vertex in fig. 7.1a by another quark (fig. 7.1b). The main difference is that the current now may be a gluon, as well.

As a result of the hard scattering, four color sources are distributed in the plane defined by the collision axis of the incoming hadrons and by the three momentum component of the current. In general, the two active partons will be scattered at large angles in the overall cms, and the spectator systems will move along the directions of the primary hadrons.

When the color sources start to separate in space, flux tubes are built up which in turn "decay" and form jets. From our present knowledge, the configuration of these flux tubes cannot be calculated, it depends on the kinematics of the interaction and on the specific tensions of color octet- and triplet strings. In addition, one may have the possibility to group the color sources into two colorless clusters [284]. It seems natural to assume that the flux tubes are formed in a way as to minimize the energy stored in the field.[283] Fig. 7.2 shows examples for the case of quark-quark scattering. Depending on the ratio r of the tensions of octet and triplet flux tubes, different configurations are favored. Since, however, the final distribution of fast fragments depends only on the state of the color field in the proximity of the color charge and on the boost connecting charge and cms, factorisation is still expected to hold; the change of the field for $r \lesssim 2$ concerns only those slow particles in regions of phase space where the four jets join.

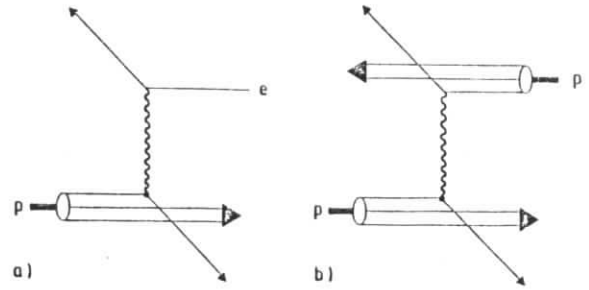

Fig. 7.1 Quark diagrams for
a) deep inelastic lepton-nucleon interactions
b) quark elastic scattering in proton-proton collisions

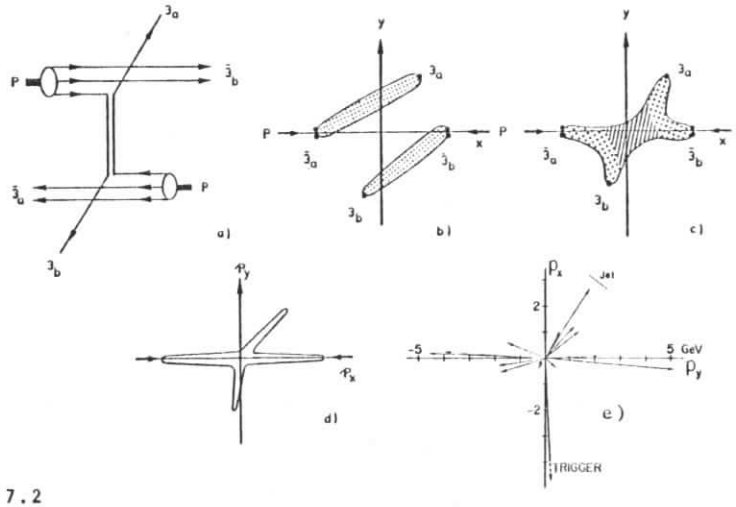

Fig. 7.2
a) Flow of color lines for elastic scattering of valence quarks
b,c) Possible configuration of color sources and flux tubes after the scattering for $r \gtrless 2$. Dotted and shaded regions denote triplet and octet strings, respectivly.
d) Final 4 jet event in momentum space.
e) A real large $p_\perp$ event. Momenta are projected into the scattering plane. From BFS.[311]

The resulting configuration consists of two jets containing particles with large transverse momentum with respect to the collision axis, and of two jets of low $p_\perp$ particles (fig. 7.2d). At sufficiently large $p_\perp$, such processes should dominate the particle production in hadronic interactions.[11]

This prediction was confirmed in 1973 by three experiments studying proton-proton interactions at the CERN-ISR[8-10]. They measured a considerable excess of particles at transverse momenta above 1 GeV/c as compared to the extrapolation of low $p_\perp$ data. For meson production, the invariant cross section can be approximated by

$$E\frac{d^3\sigma}{dp^3} \sim p_\perp^{-8\cdots9}$$

for $2 \lesssim p_\perp \lesssim 5\cdots7$ GeV.

After this discovery, a large amount of theoretical and experimental work set in, concentrated on the following questions

- do high $p_\perp$ particles really result from a two body hard scattering process?
- are the active partons identical with quarks and gluons, and is their interaction described by asymptotically free field theories, like QCD?
- can one obtain further information on mechanisms of parton fragmentation and confinement, and is there a link between these events and normal inelastic hadron-hadron interactions, where only low $p_\perp$ particles are produced?

The experimental investigation of events with high $p_\perp$ particles (in the following we consider the high $p_\perp$ regime as starting at $p_\perp$ around 2 GeV/c) is complicated by the complexity of the multijet final state. In each jet, the bulk of particles produced will have longitudinal momenta which are comparable to their momenta transverse to the jet axis. These particles are no longer aligned along the jet axis and in general cannot be attributed

to a specific jet. Consequently, the momentum transfer q is no longer directly accessable to the experiment, in contrast to lN charged current interactions.

The following discussion is concentrated on the last two of the questions mentioned above, which of course cannot be treated independently of each other.

This chapter is subdivided as follows. The large variety of experiments makes it necessary to discuss the main types of experiments. This will be done in the remainder of the introduction. In section 7.1, the predictions of the parton model are discussed on a very elementary level. In section 7.2, the main features of high $p_\perp$ events are compared with parton model predictions. The properties of the jets at high $p_\perp$, and of the spectator fragmentation are discussed in detail in sections 7.3 and 7.4, respectivly.

The data discussed in sections 7.3 and 7.4 will mainly come from proton-proton interactions at the highest ISR energies, since there a reliable separation of the jets starts to be possible; in addition the amount of final state interactions is minimized in proton-proton interactions, as compared to hadron-nucleus collisions.

To avoid additional complications, the discussion of jet properties will be restricted to jets produced in hadron-hadron collisions, although we are aware that with the advent of more detailed and precise data, jet production off nuclei will be an important tool in studying the development of jets, because the interaction with other nucleons tests the jet structure at early stages of confinement.[294,295]

Experiments investigating events with particles of large $p_\perp$ can be grouped into four main categories:

i) Experiments measuring inclusive single particle cross sections at highest $p_\perp$ and $\sqrt{s}$, with the aim to study parton parton interactions in the asymptotic region where corrections due to masses, finite transverse momenta and higher twists are negligible. The tiny cross section requires large aperture spectrometers, which are usually realized by lead glass walls detecting high $p_\perp$ π^0's.

ii) Experiments comparing large $p_\perp$ cross sections for different particle species, and different beam or target types. Particle ratios at large $p_\perp$ reflect the quantum numbers of the scattered partons, and thus help to pin down the basic scattering mechanism. Such experiments commonly use magnetic spectrometers of very limited acceptance.

iii) Experiments studying correlations between particles in events with a large $p_\perp$ secondary. Most of the results quoted in the following discussion come from this kind of experiments, which can be set up in very different ways, ranging from two small aperture spectrometers to 4π detectors. Since most of the recent detectors of type i) are equipped with a vertex spectrometer, they contribute to this field as well.

Experiments of type i) to iii) use a large $p_\perp$, single particle trigger. Their ability to measure parton-parton cross sections is restricted by the fact that one has to unfold an a priori unknown parton fragmentation function. A more reliable way to "detect" a scattered parton is to measure the whole jet, e.g. by determining the energy flux into a suited region of solid angle.

iv) Experiments measuring jet cross sections. These experiments are equipped with calorimeters measuring the amount of energy emitted at large angles in the cms. Although in

principle being superior to other types of experiments measuring parton cross sections, these experiments suffer from the fact that even at ISR energies jets are far from being pencil like, and that a cut in solid angle is a somewhat inefficient way to collect particles from one jet. Consequently, acceptance corrections are large, and there are ambiguities in interpreting the data.

Table 7.1 gives a list of large $p_\perp$ experiments, and summarizes their main characteristics.

Table 7.1 Main characteristics of some large $p_\perp$ experiments

	Collaboration		Apparatus	Type of Exp.	Beam, Target	$\sqrt{s}$ (GeV)	type	Trigger $p_\perp$(GeV/c)	θ_{cms}	some ref.s
ISR	Saclay-Strasbourg	R 102	Single arm spectrometer	i)	pp	23-53	$h^\pm,\pi^0$	1-5	90^0	9)
	CERN-Columbia-Rockefeller (CCR)	R 103	Lead glass	i)	pp	53	π^0	2-8	90^0	10,300)
	British-Scandinavian (BS)	R 203	Single arm spectrometer	ii)	pp	23-63	$\pi^\pm,k^\pm,p$	0-5	45^-90^0	8,301)
	Pisa-Stony Brook	R 801	Lead glass + scint.hodoscope	iii)	pp	23-63	π^0	0-4	$90^0,17^0,8^0$	302)
	CERN-Columbia-Rockefeller-Saclay (CCRS)	R 105	Two arm spectrometer	i,iii)	pp	23-63	$\pi^0,\pi^\pm$	2.5-8	90^0	303)
	CERN-Daresbury-Liverpool-Rutherford	R 205	Spectr. + scint. hodoscope	iii)	pp	23-63	$\pi^\pm,k^\pm,p^\pm$	0-3	45^0-90^0	304)
	Aachen-CERN-Heidelberg-Munich (ACHM)	R 701	Streamer chamber	iii)	pp	45-63	π^0	0-4	53^0-90^0	305)
	CERN-College de France-Heidelberg-Karlsruhe (CCHK)	R 407, R 408	Split Field Magnet spectr.	iii)	pp	53	$\pi^\pm,k^-,p$	1-4	$20^0,45^0$	7,306,307)
	CERN	R 412	Split Field Magnet spectr.	iii)	pp	53	π^0	1.5-4	90^0	308)
	British-French-Scandinavian (BFS)	R 413	Split Field Magnet spectr.	iii)	pp	53	$\pi^\pm,k^\pm,p^\pm$	0.5-4	90^0	309-311)
	CERN-Columbia-Oxford-Rockefeller (CCOR)	R 108	Solenoid + lead glass	i,iii)	pp	31-63	π^0	3-14	90^0	312)
	CERN-Saclay (CS)	R 702	Magnet spectr. + lead glass	i,iii)	pp,pd,dd	53-63	π^0	3-15	90^0	313)
	Athens-Brookhaven-CERN-Syracuse (ABCT)	R 806	Argon calorimeter	i,iii)	pp	53-63	π^0	3-15	90^0	314)
	Annecy-CERN-College de France-Dortmund-Heidelberg-Warsaw (ACCDHW)	R 416	Split Field Magnet spectr.	iii)	pp	23-63	π,k,p	3-8	45^0	
FNAL	Chicago-Princeton	E 100A	Single arm spectrometer	i,ii)	pN	19-27	$\pi^\pm,k^\pm,p^\pm$	1-8	90^0	315)
	Chicago-Princeton	E 300	Single arm spectrometer	i,ii)	pp,pN	19-27	$\pi^\pm,k^\pm,p^\pm$	1-7	90^0	316)
	Brookhaven-Caltech-LBL	E 268, E 350	γ-Calorimeter	ii)	$p,k^-p,\bar{p}$ p	14-19	π^0	1-5	50-110^0	317)
	Caltech-UCLA-Fermilab-Chicago-Indiana	E 260	Calorimeter + spectrometer	iv)	$\pi^\pm p,k^-p,pN$	19	$\pi^\pm,k,p,$ jet	1-4	60- 90^0	318)
	Fermilab-Lehigh-Pennsylvania-Wisconsin (FLPW)	E 395	Calorimeter	iv)	$\pi p,pp$	16-27	jet	2-4	50-100^0	319-321)
	Columbia-FNAL-Stony Brook	E 494	Double arm spectrometer	ii)	pN	19-27	$\pi^\pm,k^\pm,p^\pm$	1-5	90^0	322)
	FNAL-Michigan-Purdue	E 357	Double arm spectrometer	ii)	pN	27	$\pi^\pm,k^\pm,p^\pm$	1-3,5	110^0	323,324)

7.1 Parton-parton scattering

In this section we discuss the kinematics and cross sections for parton-parton scattering.

As a first approximation, and to enable a transparent presentation, we neglect parton masses and finite transverse momenta in the structure and fragmentations functions. Assume that the basic process is a two body interaction

$$q_1 q_2 \to q q' \tag{7.1}$$

where q_1, q_2 are partons inside the primary hadrons h_1, h_2, carrying momentum fractions x_1 and x_2, respectivly.

In the cms of h_1 and h_2, the kinematics of the reaction is fully described by three "observables": the rapidities y and y' of the outgoing partons

$$y = \ln\left(\frac{E+p_\parallel}{m_\perp}\right) = -\ln\tan\left(\frac{\theta_{cms}}{2}\right) \tag{7.2}$$

and their transverse momenta $p_\perp = p_\perp'$, or transverse masses $m_\perp = m_\perp' = p_\perp$. x_1 and x_2 are given by

$$x_{1,2} = \frac{m_\perp}{\sqrt{s}}\left(\exp(\pm y)+\exp(\pm y')\right) \tag{7.3}$$

where s is the total cms energy.

For the Mandelstam invariants $\hat{s},\hat{t},\hat{u}$ of the subprocess we get

$$\begin{aligned}
\hat{s} &= (q_1+q_2)^2 = x_1 x_2 S = 4m_\perp^2\cosh^2\left(\frac{y-y'}{2}\right)\\
\hat{t} &= (q-q_1)^2 = -m_\perp^2(1+\exp(y'-y))\\
\hat{u} &= (q'-q_1)^2 = -m_\perp^2(1+\exp(y-y'))
\end{aligned} \tag{7.4}$$

where q_1, q_2, q, q' denote parton momenta.

The rapidities y and y' are related to the scattering angle $\hat{\theta}$ in the two parton cms

$$\hat{\theta} = 2 \arctan \exp((y-y')/2) \tag{7.5}$$

In analogy to the treatment of lepton nucleon interactions we assume that the cross section $d^3\sigma/dydy'dp_\perp$ for the production of two partons q and q' factorizes:

$$d\sigma(h_1h_2 \to qq') = \sum_{q_1,q_2} d\sigma(h_1 \to q_1)d\sigma(h_2 \to q_2)d\sigma(q_1q_2 \to qq') \tag{7.6}$$

The first two terms are the well known hadron structure functions

$$d\sigma(h \to q) = G_h^q(x)\, dx/x \tag{7.7}$$

For the cross section we write

$$d\sigma(q_1q_2 \to qq') = \frac{d\sigma^{12}}{d\hat{t}}(\hat{s},\hat{t})\, d\hat{t} \tag{7.8}$$

yielding finally[325] (for simplicity, we omit the sum over q_1, q_2)

$$d\sigma = G_{h_1}^{q_1}(x_1) G_{h_2}^{q_2}(x_2) \frac{d\sigma}{d\hat{t}} \frac{dx_1}{x_1} \frac{dx_2}{x_2} d\hat{t} \tag{7.9}$$

or, with $(dx_1/x_1)(dx_2/x_2)d\hat{t} = dydy'dp_\perp^2)$ (7.10)

$$\frac{d\sigma}{dydy'dp_\perp^2} = G_{h_1}^{q_1}(x_1) G_{h_2}^{q_2}(x_2) \frac{d\sigma}{d\hat{t}} \tag{7.11}$$

Writing σ as

$$\frac{d\sigma}{d\hat{t}}(\hat{s},\hat{t}) = \alpha_s \hat{s}^{-n} f(\frac{\hat{t}}{\hat{s}}) = \alpha_s \hat{s}^{-n} f(\hat{\theta}) \tag{7.12}$$

We obtain the scaling law

$$\frac{d\sigma}{dydy'dp_\perp^2} = \alpha_s\, F(y,y',x_\perp) p_\perp^{-2n} \tag{7.13}$$

where the angular dependence of $d\sigma/d\hat{t}$ and the structure functions are summarized in F, and the term $p_\perp^{-2n}$ reflects the $\hat{s}$ dependence of $d\sigma/d\hat{t}$ at fixed angle $\hat{\theta}$.

Eqn. (7.1) suggests that for a single dominant subprocess the $\hat{s}$ dependence of σ can be determined directly by measuring the inclusive single jet cross section $Ed^3\sigma/dp^3 = \int dy'(d\sigma/dydy'dp_\perp^2)$ at two cms energies s_I, s_{II}, but for fixed $x_\perp$:

$$\frac{(Ed^3\sigma/dp^3)_I}{(Ed^3\sigma/dp^3)_{II}}_{x_\perp} = (\frac{s_{II}}{s_I})^n \tag{7.14}$$

However this result holds only up to corrections arising from the $\hat{t}$ dependence of the structure functions and of the coupling α_s as predict in asymptotically free theories[326,327].

Neglecting this effect, n is given by dimensional arguments

$$[\frac{d\sigma}{dt}] = [\alpha_s]\, [\frac{1}{\hat{s}}]^n \tag{7.15}$$

yielding n = 2 for theories with a dimensionless coupling constant.

The cross sections (7.12) and (7.13) refer to the production of large $p_\perp$ partons, or jets. The single particle cross section σ^h is given by a convolution of σ over the parton fragmentation function D(z)

$$E\frac{d^3\sigma^h}{dp^3}(\vec{p}_\perp) = \int \frac{dz}{z^2} E\frac{d^3\sigma}{dp^3}(\frac{\vec{p}_\perp}{z}) D(z) \tag{7.16}$$

In order to enable simple analytical calculations, we parametrize σ locally as $E(d^3\sigma/dp^3) = Ap_\perp^{-k}$, and chose a rather general ansatz for $D(z)$

$$D_q^h(z) = (B/z)(1-z)^{m+L+T\delta(1-z)} \qquad (7.17)$$

The δ-term takes into account that for certain subprocesses stable hadrons may emerge. From (7.16) and (7.17) we obtain for the ratio of inclusive single particle and jet cross sections 328 - 330)

$$(E\frac{d^3\sigma^h}{dp^3})/(E\frac{d^3\sigma}{dp^3}) = 2B\,\frac{m!(k-3)!}{(k+m-2)!} + \frac{L}{(k-1)} + T \qquad (7.18)$$

Within our approximation the single particle spectrum has the same slope in $p_\perp$ as the distribution of jets, however the absolute yield is much smaller, choosing e.g. the standard quark fragmentation function with $m \approx 2\cdots3$, $L \ll 1$ and $T = 0$ (fig. 7.3). This fact is easy to explain: for a large k, and a given $p_\perp^h$ it is less "expensive" to pick up a hadron at $z \approx 1$ from a jet with $p_\perp \approx p_\perp^h$, than to use a slow fragment of a parton at very large $p_\perp$. As k increases, the mean z of the trigger hadron approaches 1

$$\langle\frac{1}{z}\rangle = \frac{\langle p_\perp\rangle}{p_\perp^h} = \frac{\int \frac{dz}{z^2}\, E\,\frac{d^3\sigma}{dp^3}(\frac{\bar{p}_\perp^h}{z})D(z)\frac{\bar{p}_\perp^h}{z}}{\int \frac{dz}{z^2}\, E\,\frac{d^3\sigma}{dp^3}(\frac{\bar{p}_\perp^h}{z})D(z)\bar{p}_\perp^h} \qquad (7.19)$$

$$= \left(\frac{Bm!(k-4)!}{(k+m-3)!}+\frac{L}{k-2}+T\right)/\left(\frac{Bm!(k-3)!}{(k+m-2)!}+\frac{L}{k-1}+T\right) \qquad (7.20)$$

and σ^h drops (fig. 7.4). Experiments triggered on a single hadron at large $p_\perp$

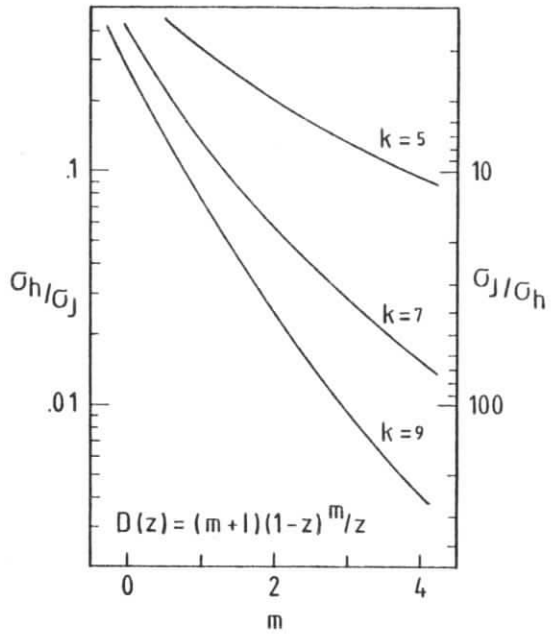

Fig. 7.3
Ratio of jet to single particle cross section for a fragmentation function $D(z) = (m+1)(1-z)^m/z$ vs m. Typical slopes of the inclusive cross sections are $k \approx 9$ at medium $p_\perp$.

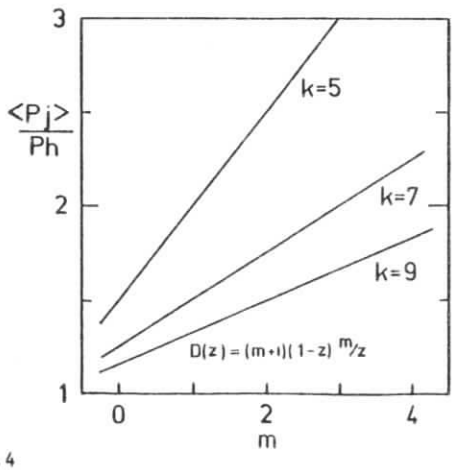

Fig. 7.4
Mean fraction z of the jet momentum carried by the trigger particle h, for a fragmentation function $D(z) = (m+1)(1-z)^m/z$. The quantity shown is $\langle P_j\rangle/P_h = \langle 1/z\rangle$.

thus select a special type of parent jets: those consisting essentially of one very fast fragment. This effect is known as the trigger bias [329,330]. Experiments triggered by jets of large $p_\perp$ are not subjected to this bias, however a similar bias is introduced if the solid angle covered by the jet detector is comparable to the jet size: then the trigger condition enhances narrow, well collimated jets [318].

Another important consequence of the trigger bias is that for a mixture of different parent partons the species with the flattest fragmentation function is favored by the single particle trigger condition.

Of course, only the jet containing the trigger particle is affected by the trigger bias; the recoiling parton in the opposite azimuthal hemisphere decays unbiased, within the limits imposed by energy-momentum conservation. The fragmentation of this second "away" jet is usually described in terms of a variable x_E referring to the trigger momentum $p_\perp^h$

$$x_E = p_\perp^{h'}/p_\perp^h \qquad (7.21)$$

where h' is a hadron in the away jet. Neglecting transverse momenta in the parton fragmentation, x_E is related to the "correct" scaling variable $z^{h'}$ referring to the momentum of the away jet

$$z^{h'} = x_E\, z^h \qquad (7.22)$$

(Note that x_E may exceed 1.)
The particle density $(1/\sigma)(d\sigma/dx_E)$ is obtained from

$$\frac{1}{\sigma}\frac{d\sigma}{dx_E} = \frac{\int \frac{dz}{z} E\frac{d^3\sigma}{dp^3}\left(\frac{\bar{p}_\perp^h}{z}\right) D(z) D'(x_E \cdot z)}{\int \frac{dz}{z^2} E\frac{d^3\sigma}{dp^3}\left(\frac{\bar{p}_\perp^h}{z}\right) D(z)} \qquad (7.23)$$

D(z) and D'(z) are fragmentation functions of the towards and the away jet, respectivly. Two points should be kept in mind: since $d\sigma/dx_E$ depends both on D(z) and on the inclusive jet cross section $d^3\sigma/dp^3$, scaling of the fragmentation functions does not necessarily imply scaling of $d\sigma/dx_E$ in x_E. Furthermore, the dependence of $d\sigma/dx_E$ on the trigger-side fragmentation function D(z) may induce correlations between the towards and the away jet. Compare e.g. events were scattered u- or d quarks create $\pi^\pm$ and k^- trigger particles. Since $D^{k^-}_{u,d}$ falls steeper in z than $D^{\pi}_{u,d}$, the mean momentum of the towards jet is larger for the k^- trigger, and $d\sigma/dx_E$ is flatter. Care is needed not to confuse such kinematical effects with dynamical correlations due to the scattering mechanism itself.

To complete this discussion, let me quote the relations concerning the two spectator jets at low $p_\perp$. The energy available to the spectators is reduced when compared to the total cms energy. The sum of the energies resp. momenta of the spectator jets is

$$E' = \sqrt{s} - m_\perp(\cosh y + \cosh y')$$
$$p' = \quad - m_\perp(\sinh y + \sinh y') \qquad (7.24)$$

Hence the usual Feynman variable $2p_\parallel/\sqrt{s}$ is no longer suitable to describe the fragmentation of spectators. The most natural choice is to use a reduced energy $\sqrt{s'}$ for the system of the two spectator jets

$$\sqrt{s'} = (E'^2 - p'^2)^{1/2} \quad .$$

The appropriate scaling variable is then the reduced longitudinal momentum of a secondary in the spectator system [307]

$$x' = 2p'_\parallel/\sqrt{s'} \quad . \qquad (7.25)$$

The QCD approach. In a hard scattering picture, the favored candidates for the active partons are of course quarks and gluons, with their interactions governed by QCD. The main ingredients of the model are shown in figs. 7.6 to 7.8. The basic subprocesses are quark-quark, quark-gluon, and gluon-gluon scattering, with the cross sections [331,332]

$$\frac{d\sigma}{d\hat{t}}(q_1 q_2 \to qq') = \pi \alpha_s^2(Q^2)\frac{f(\hat{\theta})}{\hat{s}^2}\delta_{q_1 q}\delta_{q_2 q'} \qquad (7.26)$$

whose angular dependence $f(\hat{\theta})$ is displayed in fig. 7.5. The δ-function in (7.26) refers to parton flavors only, color factors are included in $f(\hat{\theta})$. Since the effective color charge of a gluon is 3/2 times that of a quark, we get

$$\sigma_{\text{gluon gluon}} > \sigma_{\text{gluon quark}} > \sigma_{\text{quark quark}} \qquad (7.27)$$

As factorisation holds in QCD at the leading log level,[199-201] the parton structure functions and fragmentation functions are identical to those measured in lepton-nucleon reactions, up to corrections $O(\alpha_s)$ which mainly affect the distribution of sea quarks. The Q^2 evolution of $G(x,Q^2)$ and $D(z,Q^2)$ is governed by the Altarelli-Parisi equations (eqs 5.26, 5.33). However, the large mass scale Q^2 characterizing the hard scattering is not uniquely determined in a leading log calculation, the naive choice $Q^2 = -\hat{t}$ e.g. is not fully adequate to describe a quark-gluon compton effect. Forms used in the literature are [326,332-334]

$$Q^2 = \frac{2\hat{s}\hat{t}\hat{u}}{(\hat{s}^2+\hat{t}^2+\hat{u}^2)}\,,\quad Q^2 = (\hat{s}\hat{t}\hat{u})^{1/3},\quad Q^2 = p_\perp^2$$

$$Q^2 = -\hat{t},\quad Q^2 = \hat{s},\quad Q^2 = (\hat{s}-\hat{t}-\hat{u})/3 \qquad (7.28)$$

resulting in uncertainities of the single particle cross section of the order 20-30 %.

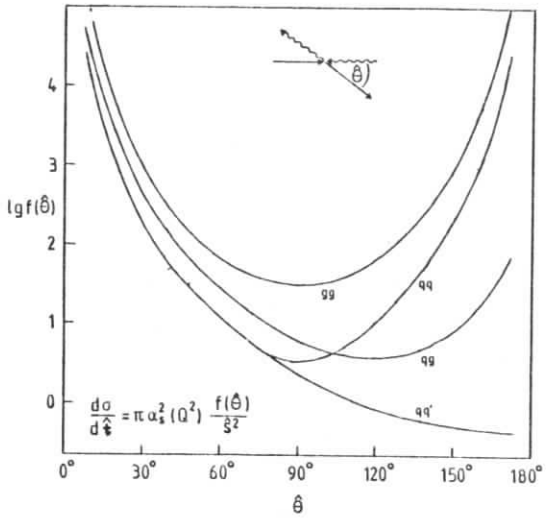

Fig. 7.5
Angular dependence of parton-parton cross sections in first order of QCD [331,332]

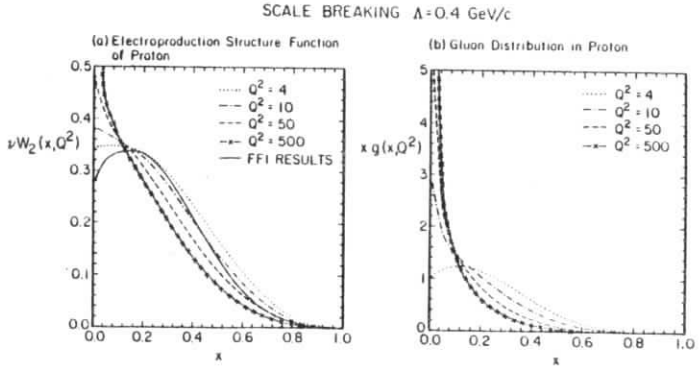

Fig. 7.6
Typical parametrisation of quark and gluon structure functions of the proton for various Q^2. [326]

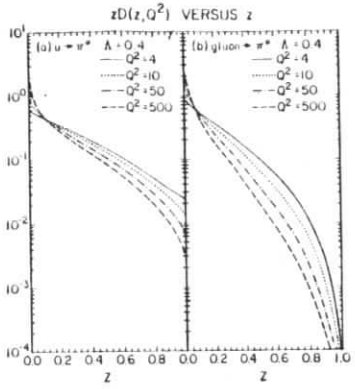

Fig. 7.7
As fig. 7.6, but for fragmentation functions.

Typical examples for structure functions and parton fragmentation functions are shown in figs. 7.6 and 7.7

Although the basic cross section (7.26) scales as $\hat{s}^{-2}$, scale breaking effects increase the effective power in $p_\perp$ of the single particle cross section by about 2 units, yielding [335]

$$E(d^3\sigma/dp^3)\Big|_{x_\perp} \sim p_\perp^{-6\cdots7} \qquad (7.29)$$

in contrast to the naive expectation $p_\perp^{-4}$ (fig. 7.8).

Whereas the distribution of quarks in a nucleon is determined rather precisely from lN scattering experiments, the gluon density is accessable experimentally only through scaling violations in the distributions of sea quarks, and is not determined very well. Nevertheless most authors agree that at moderate $Q^2 = 2 - 4$ GeV^2 the gluon distribution in the proton more or less coincides with the counting rule prediction

$$G_p^g(x) \sim (1-x)^{4-5} \qquad (7.30)$$

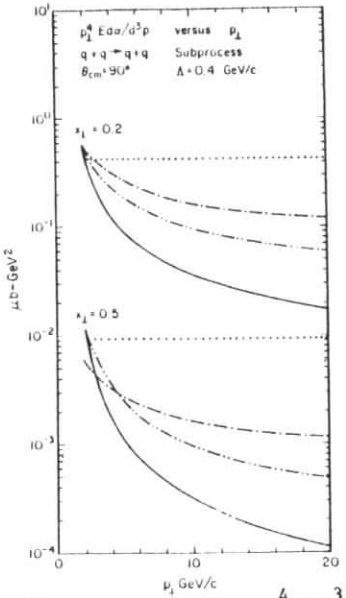

Fig. 7.8
QCD predictions for the cross section $p_\perp^4\, Ed^3\sigma/dp^3$ for $pp \to \pi^0 X$ at 90° in the cms, at ISR energies.[335] Dotted curve: "QCD" without scale breaking. Dot-dashed: with running coupling constant $\alpha_s(Q^2)$. Dot-dot-dashed: with running coupling and nonscaling structure functions. Solid curve: QCD including all scale breaking effects

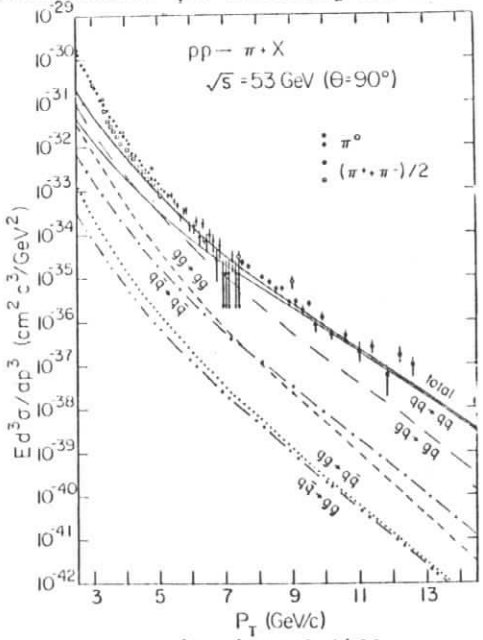

Fig. 7.9
QCD prediction for the contribution of different subprocesses to the cross section $pp \to \pi X$ at $\sqrt{s}$ = 52 GeV, compared to experimental data [327].

with the normalisation $\int dx\, G_p^g(x) = 0.5$. Based on theoretical prejudices, the gluon fragmentation function is typically chosen a factor (1-z)steeper than the quark fragmentation function.

Fig. 7.9 shows a QCD prediction for the inclusive pion cross section at large angles for the reaction pp → π + X, subdivided into different subprocesses. The calculation is in fair agreement with data for $p_\perp \gtrsim 5$ GeV/c, at lower $p_\perp$ the theory falls considerably below the data, indicating that additional scale breaking or higher twist effects have to be taken into account. Such corrections could arise from a non negligible transverse momentum of partons in the nucleon, or from additional subprocesses involving non-elementary constituents with form factors, as are e.g. postulated by the constituent interchange model (CIM) [250-256, 338].

Parton transverse momentum. In the naive parton model, the partons q_1 and q_2 move collinear with their parent hadrons h_1 and h_2. There is however considerable evidence, particularly from dilepton production experiments, that the partons can have a sizeable transverse momentum. It has been pointed out that these effects are very important in large $p_\perp$ calculations, where the steeply falling cross section is sensitive to the transverse configuration of the initial state partons [7, 336, 337].

Although the qualitative effect of parton transverse momentum is fairly well understood-triggering on a large $p_\perp$ hadron favors configurations where both the active constituents move in the transverse direction of the trigger hadron, thereby reducing the effective $\hat{t}$ and enhancing the cross section- there is no common consensus how to incorporate these effects into the calculation of cross section, and quantitative predictions show major discrepancies. [326, 333, 339-342]

Two components contribute to the parton transverse momentum $k_\perp$: a primordial $k_\perp$ inherent to the initial wave function, and a component created through hard bremsstrahlung during the

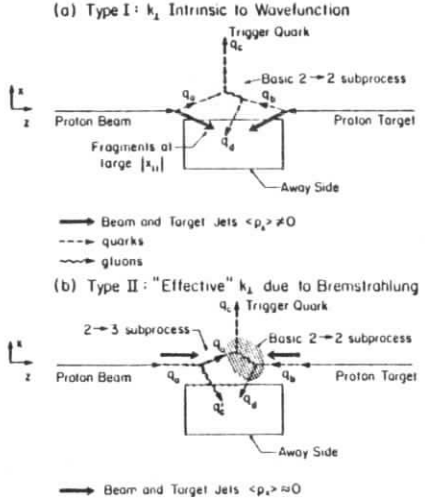

Fig. 7.10
Effect of a parton transverse momentum in parton elastic scattering processes a) primordial transverse momentum intrinsic to the wave function b) transverse momentum due to gluon bremsstrahlung. The trigger condition (a large $p_\perp$ hadron) selects configurations were the parton transverse momentum is aligned with the final hadrons momentum. [326]

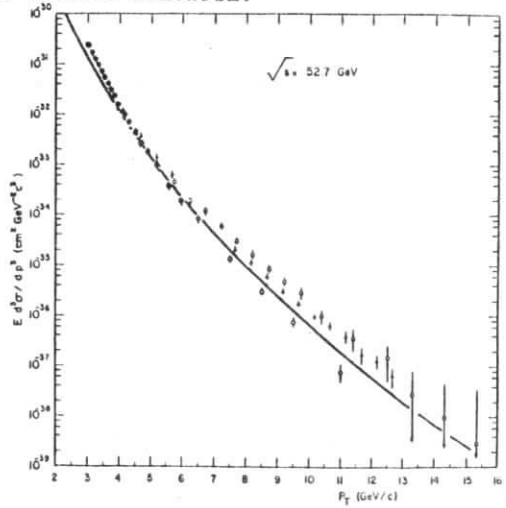

Fig. 7.11
QCD prediction for the single particle cross section at large $p_\perp$ for proton-proton interactions at ISR energies, using a mean parton transverse momentum of 850 MeV/c. [335]

interaction (fig. 7.10). Naivly, one expects the primordial $k_\perp$ to be of the order 300 MeV, whereas the hard component grows as $Q^2/\ln(Q^2/\Lambda^2)$. To circumvent problems arising in the calculation of higher order QCD diagrams,[360-362] most authors parametrize both components by one effective $k_\perp$ distribution. Chosing a mean $k_\perp$ of 850 MeV, independent of x and Q^2, the theory can be tuned to agree with data over the whole range of $p_\perp$ (fig. 7.11)

The phenomenological way to include parton $k_\perp$ raises several new problems. Consider e.g. the diagram shown in fig. 7.12. It can be regarded either as a quark-quark scattering, with the effect of the bremsstrahlung gluon beeing parametrized by the parton $k_\perp$, or as a quark-gluon compton effect; the same process appears to be counted twice.

In the context of parton $k_\perp$, another point becomes evident: it is no longer possible to keep all partons on shell.[189,190] Two ways are followed in the literature: either the active partons are massless and kept on shell[326], with the fate of the spectators being neglected, or it is argued that the spectator essentially carries the initial hadron mass, since it is subjected only to confining forces which have an appreciable effect only after a rather long time.[190,342] Consequently, the active partons are off shell (eqn 6.2). This procedure has the advantage that the pole of the scattering amplitude at $\hat{t} = 0$ moves into the unphysical region and cannot be reached. In the case of on shell partons, an arbitrary regularizing mass $\hat{t} \to \hat{t} - M^2$ has to be introduced to avoid divergencies.[7,326]

In the spirit of a preconfinement model, none of these methods is fully adequate. Here the active partons become more and more off shell through successive emission of gluons, reaching a mean momentum squared of the quark line at the hard vertex up to $O(Q^2)$. After the scattering, the active parton initiates a "parton shower" and successivly cascades down to the mass shell.

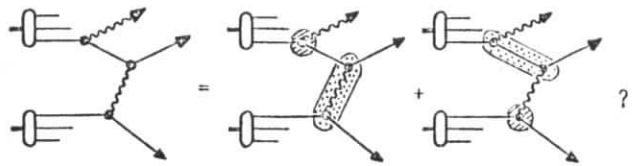

Fig. 7.12
QCD diagram which can be counted either as quark-quark scattering or as a quark-gluon compton effect. The dotted region characterizes the two body process, the shaded region denotes the interaction responsible for the large parton $k_\perp$.

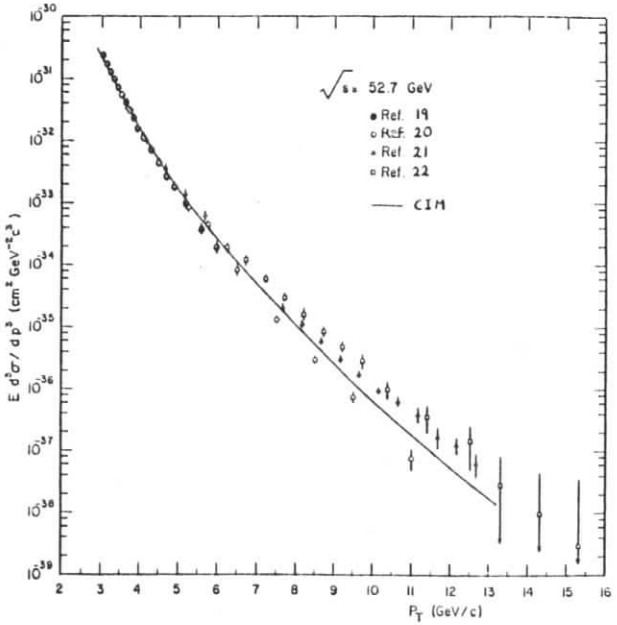

Fig. 7.13
CIM predictions[351] for the inclusive π^0 cross section at $\theta_{cms} = 90^0$, as compared to data.[312-314]

Recent works start to deal with this problem[346], e.g. by choosing the parton mass as the mean mass of a Sterman-Weinberg jet of corresponding momentum, with the result that the QCD jet cross section is fairly insensitive to such manipulations.

Anyhow, all these ambiguities in the interpretation of the QCD calculus concern mainly the region below $p_\perp \approx 5$ GeV, and it is commonly agreed upon that the inclusion of parton transverse momentum improves the agreement between theory and experiment in the medium $p_\perp$ range.[7,326,339-342]

Constituent Interchange Model (CIM). The QCD interpretation of large $p_\perp$ phenomena requires a rather large parton transverse momentum. The phenomenological representation of these fluctuations by an effective $k_\perp$ instead by a sum over Feynman diagrams rises various problems, part of which can be traced back to the fact that a moderate $p_\perp$ the lifetime of a large $k_\perp$ fluctuation is of the same order as the timescales set by the hard interaction. In this case, effects due to the coherence of the initial wave function have to be taken into account, resulting in subprocesses involving more than two quark partons.

The CIM model [250,251,254,256] assumes that particle production in the region below $p_\perp = 5$ to 7 GeV/c is governed by such 'higher twist' or 'natural' mechanisms. Typical subprocesses and their $p_\perp$ dependence are

$$\left.\begin{array}{l} qM \to qM \\ q\bar{q} \to MM \end{array}\right\} p_\perp^{-8} \qquad qB \to qB \quad p_\perp^{-12} \tag{7.31}$$

The labels M, B and q denote partons with meson, baryon, or quark quantum numbers, respectivly, which are treated as having a negligible primordial $k_\perp$.

It has been argued[347,349] that a systematic treatment of all hard scattering processes including both elementary quark and gluon contributions and higher order constituent interchange processes is given by the "hard scattering expansion"[348] accounting for gluon corrections to the basic QCD process, constituent transverse momenta, higher twist effects etc. The inclusive meson cross section e.g. is represented by

$$E\frac{d^3\sigma^h}{dp^3}(h_1h_2 \to hX) = \underbrace{\frac{F(x_\perp,\theta)}{p_\perp^4}}_{qq \to qq \quad qg \to qg} + \underbrace{\frac{G(x_\perp,\theta)}{p_\perp^6}}_{gM \to gM \quad qg \to qM} + \underbrace{\frac{H(x_\perp,\theta)}{p_\perp^8}}_{qM \to qM \quad qq \to MM} + \cdots \tag{7.32}$$

The intrinsic transverse momentum of the partons in (7.32) is small and reflects non-leading contributions. The validity of this expansion has been proven rigorously in a ϕ^3 toy theory[348]; it is presently not clear if it is appropriate to asymptotically free theories.

The $p_\perp^{-4}$ terms in (7.33) correspond to the asymptotic QCD predictions; the $p_\perp^{-8}$ terms represent the classical CIM mechanisms. The $p_\perp^{-6}$ processes are suppressed by a suble cancellation related to gauge invariance[347].

The normalisation of the different processes can be derived from meson form factors and elastic scattering cross sections[350]. The resulting cross section is in fair agreement with data (fig. 7.13), the dominant mechanism below $p_\perp \approx 5 \cdots 7$ GeV beeing qM→qM.

From the experimentalists point of view, QCD and CIM mainly differ in three points

i) in the CIM model, the "jet" containing the trigger particle is formed by decay products of a meson resonance.

ii) mesons which do not contain one of the incident valence quarks are likely to be produced via $q\bar{q} \to MM$. For $pp \to k^- X$ e.g. one obtains [347]

$$\frac{\sigma(q\bar{q} \to k^- M)}{\sigma(qM \to k^- q)} \approx \frac{0.15}{(1-x_\perp)^2} \quad \text{for } \theta = 90^\circ \text{ and } x_\perp > .15 \qquad (7.33)$$

Compared to large $p_\perp$ π^- triggers, which are in the CIM almost entirely due to $qM \to \pi^- q$, the away jet for a k^- trigger should be different, and its contents of k^+ should be enhanced, in contrast to QCD where no strong flavor correlation exists between the two jets at large $p_\perp$.

iii) if one of the colliding hadrons contains a valence antiquark, the $q\bar{q} \to MM$ subprocess will considerably enhance the cross section at large $x_\perp$, as compared to QCD predictions.

7.2 General characteristics of high $p_\perp$ events

Scattering of quark or gluon partons was shown to account for single particle yields at large $p_\perp$, once higher order- and higher twist effects are taken into account. In this section, we shall discuss further evidence for a basic two body scattering process, using two sets of data which are insensitive to details of parton fragmentation. The mechanisms of fragmentation and the properties of jets in large $p_\perp$ events will be discussed in sections 7.3 and 7.4.

Particle and beam ratios. Ratios of single particle or jet cross sections at large $x_\perp$ for different particle species, beam and target types essentially test the ratio of structure functions of

the interacting partons. They have the great advantage that both theoretical and experimental uncertainities tend to cancel.

The ratio of jet to single particle cross sections (fig. 7.14) tests the idea that scattered partons carry color and hence have to fragment, yielding a tremendous ratio $\sigma^{Jet}(p_\perp)/\sigma^h(p_\perp)$ of the order 10^3 at large $x_\perp$ [326] (eqn. 7.18). The measured ratio is in good agreement with QCD predictions. For pure CIM processes which directly produce color singlet mesons, the jet cross section is lowered by about one order of magnitude [347,349] as compared to QCD. In the subprocess expansion (eqn. 7.32) combining QCD and CIM graphs, the relative abundance of processes can be adjusted such that the major contributions to the jet cross section come from QCD graphs, whereas CIM terms dominate single particle production, favored by the trigger bias. Within present experimental errors, [318,320,352] such a combination is indistinguistable from pure QCD.

Figs. 7.15 and 7.16 show π^+/π^-, k^+/π^+ and k^-/π^- ratios at large $p_\perp$, for proton-proton collisions. In almost any hard scattering model refering to quark partons, π^+,k^+ and π^- mesons at large $x_\perp$, or x contain a u and d valence quark, respectivly, from one of the incident hadrons. Consequently, the π^+/π^- ratio at large $x_\perp$ reflects the ratio $1/(1-x)$ of u and d quark structure functions, k^+/π^+ should be constant for $x \to 1$, and k^-/π^- will drop with increasing $p_\perp$. Data show all these features, proving that the standard valence quarks are involved in large $x_\perp$ particle production.

The same argument shows that the beam ratio $pp \to Jet + X/\pi p \to Jet + X$ falls with increasing $x_\perp$, since the x distribution of valence quarks is flatter in a pion, as compared to a proton, simply because momentum is shared by only two valence quarks. Again data agrees with the QCD ideas (fig. 7.17). The CIM prediction, where the process $qM \to qM$ is considerably enhanced due to the incident meson, falls below the data.

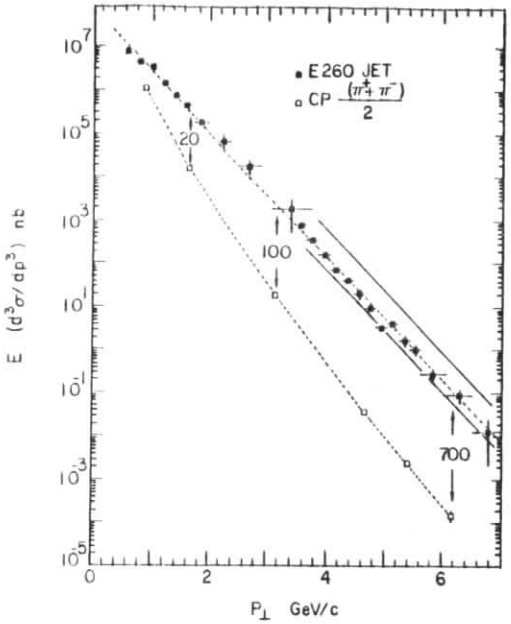

Fig. 7.14

Jet cross section at $\sqrt{s}$ = 19.4 GeV compared with the single particle cross section.[318] The full lines refer to a QCD calculation for fixed jet energy and fixed jet momentum, respectivly.[363]

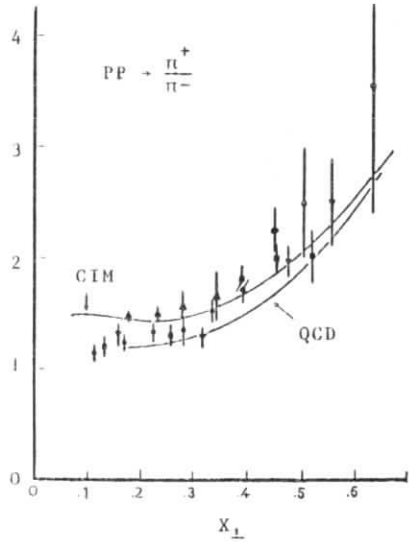

Fig. 7.15

Particle ratio pp → π^+/π^- + X at θ_{cms} = 90° from refs 316 (▲$\sqrt{s}$ = 19 GeV, ■$\sqrt{s}$ = 23 GeV, ●$\sqrt{s}$ = 27 GeV) and 353 (▽ $\sqrt{s}$ = 19 GeV) compared to QCD[326] and CIM[338] predictions.

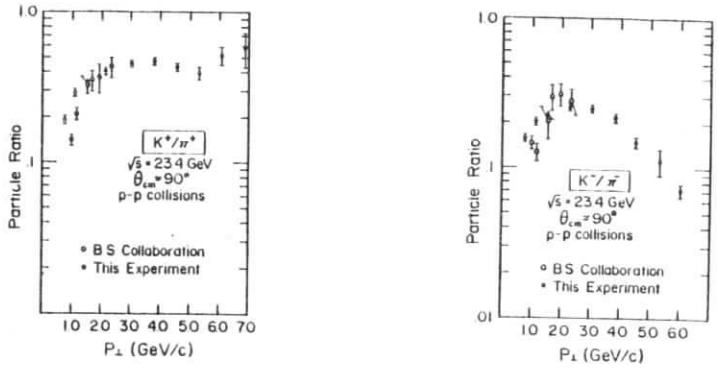

Fig. 7.16

Particle ratios pp→K^+/π^+ + X and pp→K^-/π^- + X at θ_{cms} =90° vs $P_\perp$ for $\sqrt{s}$ = 23.4 GeV (o ref. 301, • ref. 316)

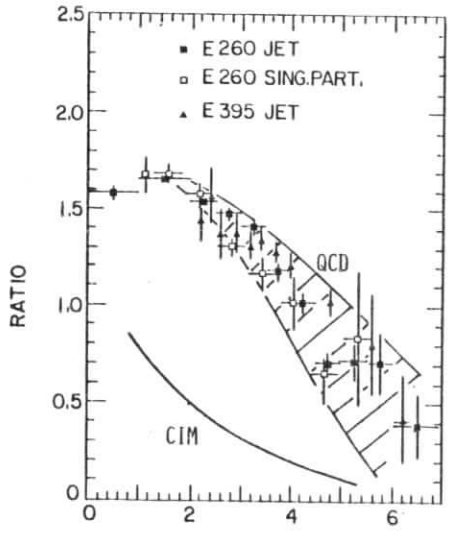

Fig. 7.17

Beam ratio pp→π^0+X/πp→π^0+X and pp→Jet +X/πp→Jet +X,[319,354] compared to QCD[351] and CIM[338] predictions. The shaded area gives the QCD prediction for jet ratios, the single particle ratio is given by the lower boundary. The CIM prediction refers to single particles.

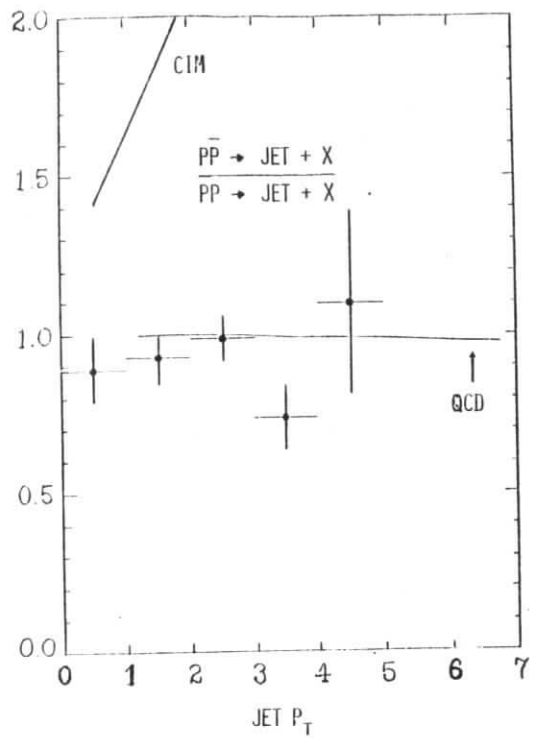

7.18

Beam ratio $p\bar{p}$→Jet +X/pp→Jet +X vs $p_\perp$ at $\sqrt{s}$ = 19 GeV [354] compared to QCD [351] and CIM [338] predictions.

Finally, there is a simple way to decide wether the underlying process is a scattering ($\hat{t}$-channel) or fusion ($\hat{s}$-channel) mechanism: the ratio $p\bar{p} \to$ Jet X/pp → Jet + X should be about 1 in the first case, and large compared to unity else. The conclusion from fig. 7.18 is evident.

Structure of large $p_\perp$ events. The inspection of particle and beam ratios supports the idea that in events with a secondary at large $x_\perp$ a valence quark is struck out of one of the incident hadrons. What stays to prove is that this happens by a two body process, i.e. that a large $p_\perp$ event contains four jets of particles, two at large $p_\perp$ and two low $p_\perp$ jets made of spectator fragments.

Fig. 7.19 shows the ratio of particle densities observed in pp collisions with a large $p_\perp$ particle at $y^t \approx 0$, to those observed for normal inelastic events [310], as a function of the rapidity y and the azimuthal angle ϕ. The observed structure is not too far from what one expects in a hard scattering model: near the trigger hadron, the particle density is enhanced, indicating the existence of a "towards" jet. The increase in density opposite in azimuth to the trigger is commonly interpreted as due to the away jet. Since the momenta of the colliding partons vary, particles from the away jet are smeared out over a wide range in y, when averaged over many events.

Contributions from the two jets at large $p_\perp$ are more clearly seen in fig. 7.20: in the central rapidity region, the particle density peaks at $\phi = \phi_{trigger} = 0$, and at $\phi = \pi$. With increasing $p_\perp$ of the secondaries, the flat background of spectator fragments diminishes, and the jets are better collimated in angle [312].

Fig. 7.21 and 7.22 demonstrate, that the increase of particle density in the towards region $\phi \approx \phi^t$ follows the trigger rapidity, whereas the density of away secondaries stays symmetrical around y = 0.[7] Since both particles of same and opposite charge as the trigger show a narrow correlation, the effect cannot be entirely

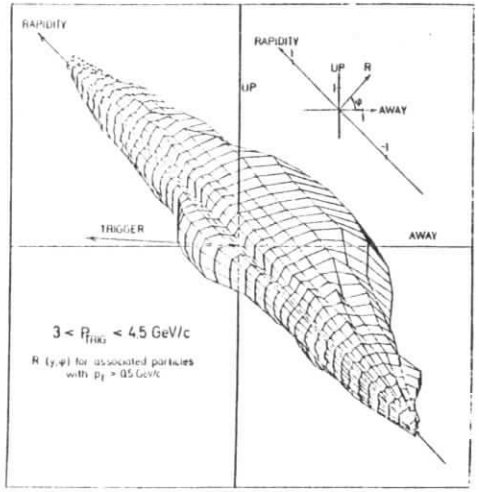

Fig. 7.19
Ratio of particle densities in large $p_\perp$ events and in normal inelastic events as a function of y and ϕ. From BFS [310]

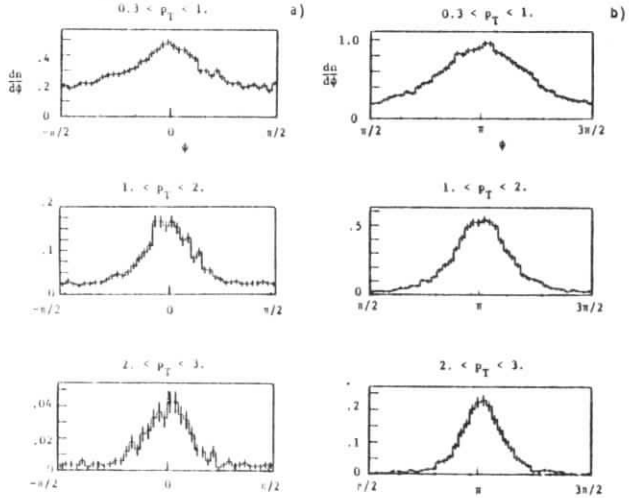

Fig. 7.20
Density of additional secondaries produced in events with a large $p_\perp$ (>7 GeV/c) π^0 at ϕ = 0 as a function of azimuthal angle, for different $p_\perp$ of the secondaries. From CCOR [312].

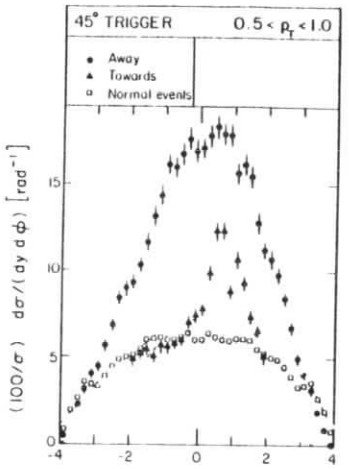

Fig. 7.21
Rapidity distributions of secondaries, integrated over $p_\perp$ from 0.5 to 1.0 GeV/c. Shown are the distributions of away ($\phi \approx \phi^t + 180^o \pm 40^o$) and towards ($\phi \approx \phi^t \pm 25^o$) secondaries for a trigger particle at y ≈ 0.8 - 1.0, and of particles produced in normal events. The mean $p_\perp$ of the trigger hadron is 2.4 GeV/c. From CCHK [306]

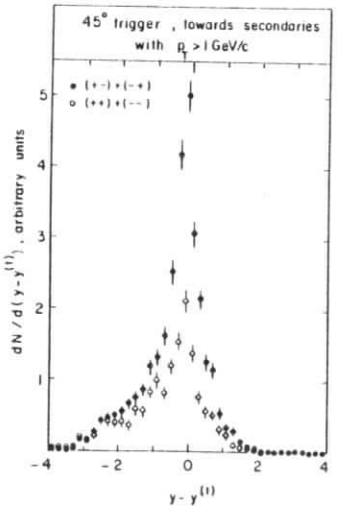

Fig. 7.22
Same data sample as in fig. 7.23. Shown is the distribution of toward secondaries with $p_\perp$ > 1 GeV/c, in rapidity relative to the trigger rapidity. Full circles represent secondaries of charge opposite to the trigger charge, open circles refer to secondaries with the same charge as the trigger. From CCHK [306]

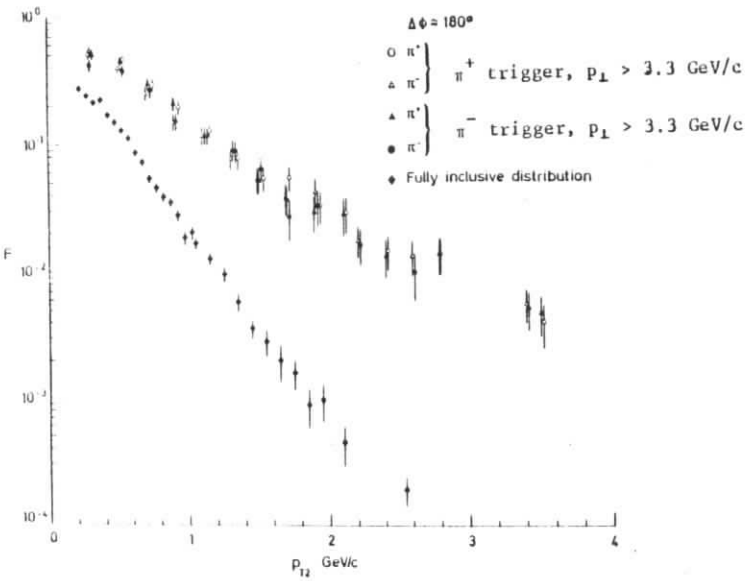

Fig. 7.23
Density of particles produced opposite in ϕ to the trigger particle, as a function of the transverse momentum of secondaries, compared to the inclusive cross section. From CCRS[303].

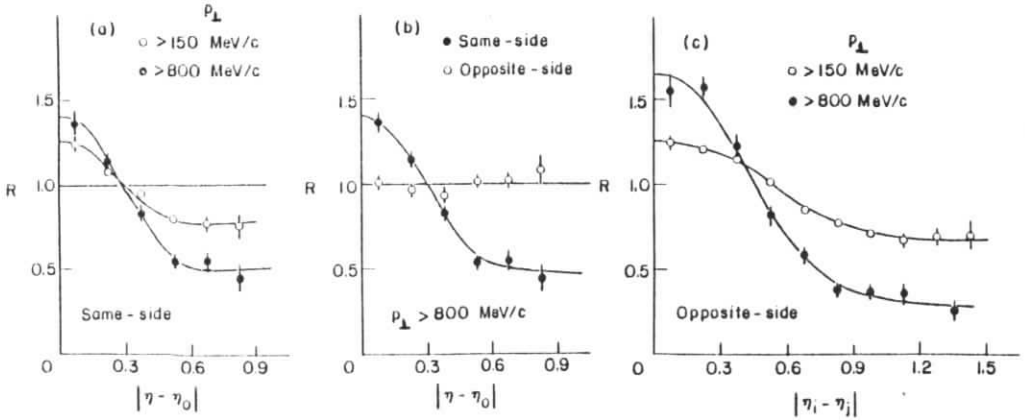

Fig. 7.24
Pair correlation functions for rapidities of towards and away secondaries.
a) between the trigger π^0 and charged particles on the same side
b) between the trigger π^0 and charged particles with $p_\perp$ > 800 MeV/c
c) between charged particles in the away region
From CS[313].

due to the decay of low lying resonances like ρ.[306,368]

Consider now the azimuthal region opposite to the trigger. A comparison of the $p_\perp$ spectrum of particles with the inclusive spectrum proves that not only the number of particles, but as well their mean $p_\perp$ is increased (fig. 7.23[303]). If the excess observed in fig. 7.23 is attributed to the "away" jet, two particles in this region are expected to show strong correlations in rapidity, since both are more or less aligned along the jet axis. Such a correlation, whose strength increases with the $p_\perp$ of particles is in fact observed (fig. 7.24[313]). The shape of the correlation function is similar to that observed for towards particles. No correlation is seen between the trigger rapidity and away particles. Regarding the strength of the two particle correlation function $C(y_1,y_2)$ at $y_1 = y_2$ as a measure for the probability to find the away jet at y, one concludes that its rapidity range is limited to $|y| < 2\text{-}3$ at ISR energies (fig. 7.25)[306]. Note further that the correlation shown in fig. 7.25 is practically independent of the trigger rapidity.

In hard scattering models, one expects the two jets to be coplanar. It is however not clear, if the back - to - back structure of jets seen in fig. 7.20 is not merely a consequence of momentum conservation. This question has been investigated by studying events with two π^0's of large $p_\perp$.[314] Fig. 7.26 shows their difference in azimuth for events having a fixed value of E_T. E_T is defined as the sum of the pion transverse momenta, plus the $p_\perp$ of another object necessary to ensure the $p_\perp$ balance. $\vec{p}_\perp x = -\vec{p}_{\perp\pi 0} - \vec{p}_{\perp\pi 0}'$. For uncorrelated emission of particles as described by the UJM (chapter 3) , the production probability depends only on $E_\perp$ and not on the angle between the π^0s. Fig. 7.26 proves that even at fixed $E_\perp$ the distribution peaks at $\Delta\phi = 0^\circ$ and at $\Delta\phi = 180^\circ$.

Finally, is there exactly one away jet in each event, and does it compensate the whole $p_\perp$ of the trigger particle? Fig. 7.27 shows the momentum distribution of the away jet,

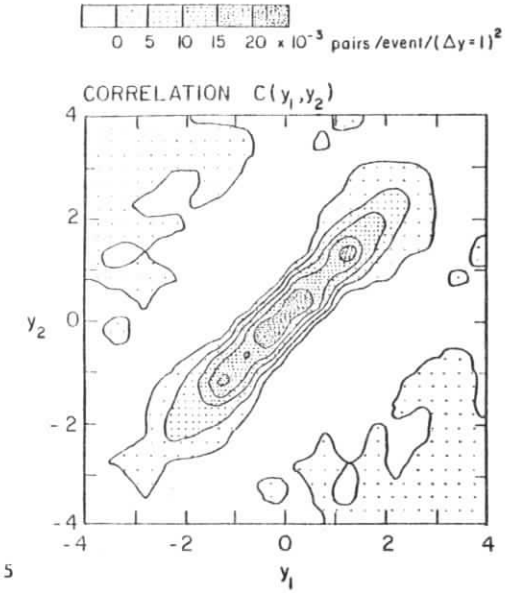

Fig. 7.25
Contour plot of correlation between away particles with $p_\perp$ > 800 MeV/c, for a mean trigger $p_\perp$ of ~ 2.5 GeV/c. From CCHK[306].

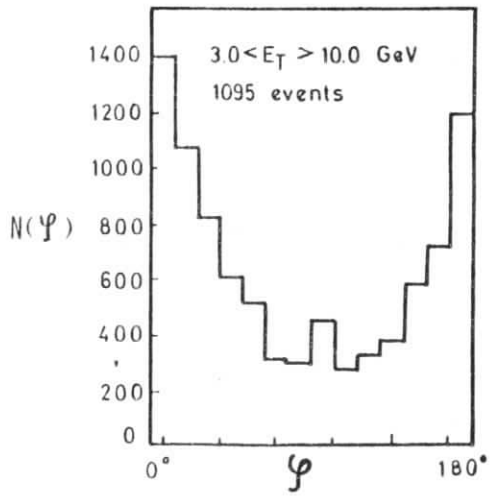

Fig. 7.26
Distribution of azimuthal angle between to large $p_\perp$ π^0's, for 8 ≤ $E_\perp$ ≤ 10 GeV/c. From ABCY[314].

as obtained from a calorimeter experiment[319-321]. The discrepancy between the trigger $p_\perp$ and the mean momentum of the away jet cannot be explained by the limited acceptance of the calorimeter[352]. A natural explanation is given by assuming a parton transverse momentum of ~ 1 GeV/c; in this case, the transverse motion of the active partons is aligned along the trigger direction, with the recoil beeing taken by the spectators. This interpretation is supported by the investigation of spectator fragmentation[7,309] (section 7.4).

In fig. 7.28 the frequency of reconstructed away jets with $p_\perp$> 1.5 GeV/c is plotted as a function of the trigger $p_\perp$. As a reference, two curves from a monte-carlo simulation of the jet reconstruction procedure are shown, one for zero parton transverse momentum, and one assuming a momentum difference between trigger and away jet of ~ 0.8 GeV/c, due to parton $k_\perp$. The away jet was chosen to resemble those observed in e^+e^- annihilations. The result for nonzero parton $k_\perp$ supports the idea, that an away jet is present in each large $p_\perp$ event.

To conclude: correlation data are fully consistent with the assumption of an underlying two body hard scattering process. But note that this does not necessarily give new information compared to the investigation of inclusive cross sections: it has been pointed out [356,357] that e.g. in an uncorrelated jet model (section 3.1) whose matrix element is chosen power behaved in $p_\perp$, a large transverse momentum is likely to be compensated by a single particle, or cluster. If such a model is used to describe parton thermodynamics, all kinematical features of large $p_\perp$ events are reproduced once the single parton matrix element is matched to describe the inclusive spectrum.

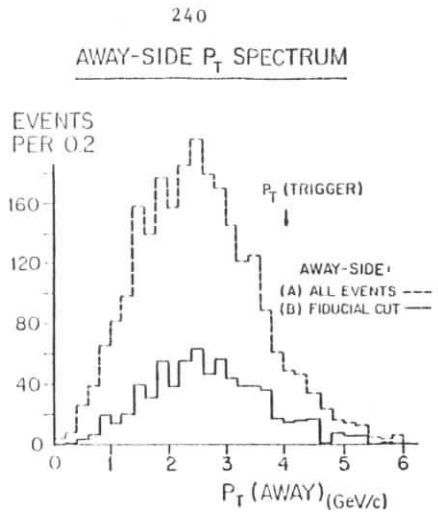

Fig. 7.27
Transverse momentum detected in the away side calorimeter when triggering on a jet with $3.95 < p_\perp < 4.2$ GeV/c.
From E 395 [352].

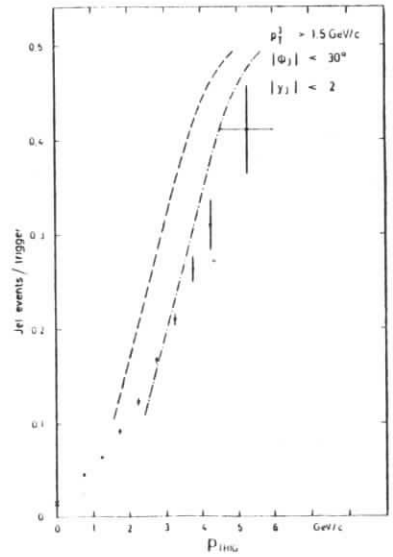

Fig. 7.28
Frequency of reconstructing a jet on the away side. The curves refer to a Monte-Carlo simulation assuming either perfect momentum balance the jets (---) or an imbalance of 0.8 GeV/c due to parton transverse momenta (-.-.-). From BFS [311].

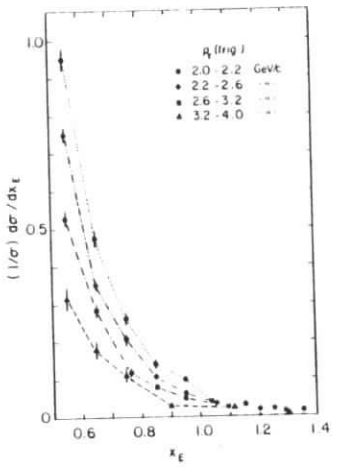

Fig. 7.29
Distribution in x_E of away secondaries, $(1/\sigma)d\sigma/dx_E$, for four intervals of transverse momentum of the trigger. From CCHK [7].

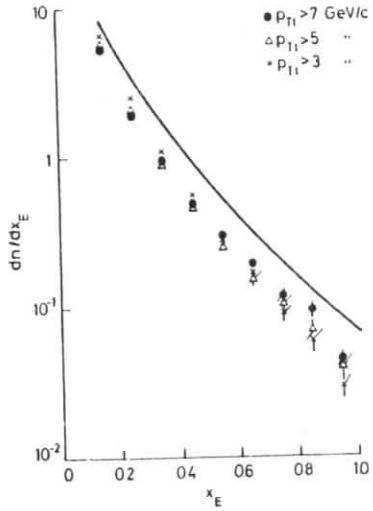

Fig. 7.30
Distribution in x_E of away side charged secondaries for three sets of trigger $p_\perp$. The solid line is calculated from eqn (7.23) using quark fragmentation functions, with a normalisation such that charged particles carry 60% of the jet momentum.
From CCOR [312].

7.3 The jets at large $p_\perp$

The investigation of properties of the two jets at large $p_\perp$ is concentrated on the following questions

- does factorisation hold, i.e. does a quark fragment in the same way in e^+e^- annihilations and in such a complex environment of color sources as is given in large $p_\perp$ reactions.
- are the fragmentation functions of the towards- and away jets identical? According to QCD, the away side parton is likely to be a gluon, whereas the towards parton is more often a quark[326],
- is there any evidence for scale breaking effects, or for gluon bremsstrahlung?
- is there a nontrivial correlation between the flavors of the towards and the away parton? Such a correlation would be a hint that additional mechanisms are active besides the basic QCD graphs.

Consider first the parton fragmentation functions, which can be studied via the x_E distribution of particles in the unbiased away jet (eqn. 7.23)

Figs. 7.29 and 7.30 show x_E distributions for lower (< 4 GeV/c) and higher (> 3 GeV/c) $p_\perp$ of the trigger particle. The cross sections $(1/\sigma)(d\sigma/dx_E)$ scale for $p_\perp^t$ > 3 GeV, the onset of scaling being evident from fig. 7.31. In the scaling region, x_E spectra from different experiments, and for charged and neutral secondaries agree remarkably well (fig. 7.32), and are described by $(1/\sigma)(d\sigma/dx_E) \sim \exp(-3.7x_E)/x_E$.

The scaling violations at low $p_\perp^t$ can be understood as a consequence of a nonzero parton transverse momentum, and partly as a contamination by spectator fragments[7].

Since these effects are negligible at sufficiently large $p_\perp^t$, it seems justified to use eqn (7.23) to predict x_E spectra for the known quark fragmentation function. For this purpose, the jet

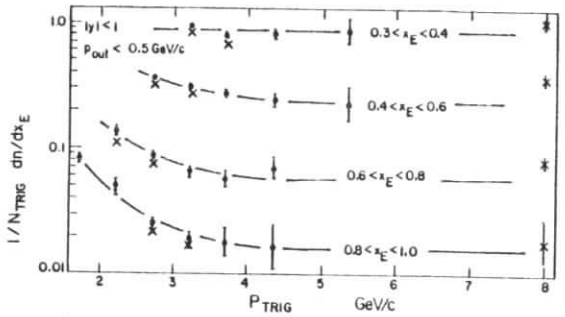

Fig. 7.31
Approach to scaling of $(1/\sigma)(d\sigma/dx_E)$. The lines are drawn to guide the eye. From BFS[310] and CCOR[312].

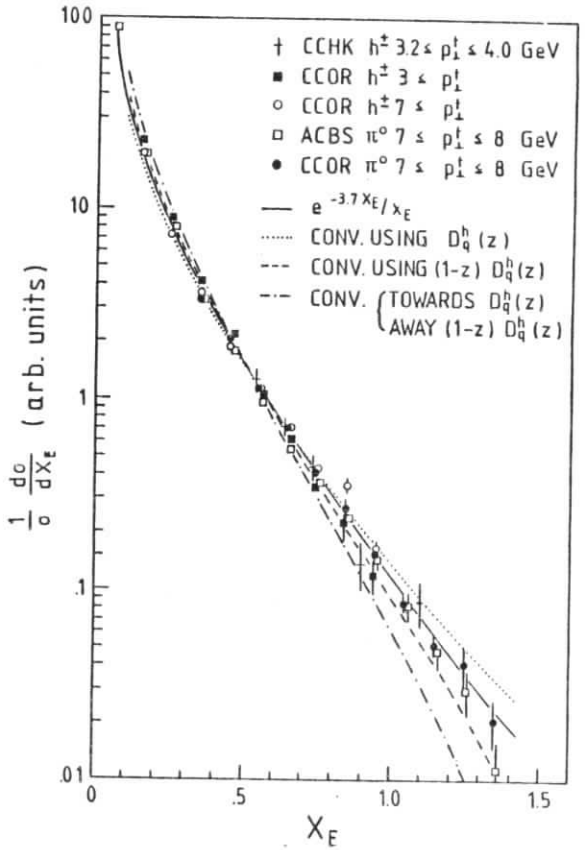

Fig. 7.32
x_E distributions for charged and neutral hadrons for different ranges of trigger $p_\perp$, from CCHK[7], CCOR[312], ABCY[314]. Data are normalized at x_E=0.5. The curves shown are calculated from eqn (7.23) using a quark fragmentation function D_q^h for both jets (••), a "gluon" fragmentation function $D_g^h(z)=(1-z)D_q^h(z)$ for both jets (---) and D_q^h and D_g^h for the towards and away jet, respectivly (-.-.).

cross section was taken as the measured inclusive cross section [312-314] times the jet to single particle ratio predicted by QCD [326]. The quark fragmentation function was parametrized as $D_q(z) \sim \exp(-4.5z)/z$. Alternativly, a "gluon" fragmentation function $D_g(z) = (1-z)D_q(z)$ was used. The agreement between data and the naive calculation is surprisingly good (fig. 7.32). Data ly between the curves for quark and for gluon jets; for definite conclusions the calculation certainly is not precise enough.

It is interesting to note the similarity of the predictions using $D_q(z)$ and $D_g(z)$. The reason is that these fragmentation functions were used both for the towards and the away jet. In the "gluon" case, of course the distribution of fragments in z is steeper, on the other hand, the mean z of the trigger hadron decreases (eqn 7.19, fig. 7.4) and thus the momentum of the parent jets is increased for fixed trigger $p_\perp$, thereby just cancelling the additional power (1-z) in $D_g(z)$. The situation changes once towards and away jets are taken to fragment in different ways; for a towards quark and an away gluon jet the prediction falls below the data at large x_E. As far as absolute rates are concerned, data typically lie a factor 2 below the predictions (fig. 7.30). Note, however that the normalisation is essentially given by momentum conservation; using the extrapolation $(1/\sigma)(d\sigma/dx_E) \sim \exp(-3.7x_E)/x_E$, only 35% of the trigger momentum is compensated by charged particles in the away jet, for the data shown in fig. 7.30!

Finally to demonstrate what x_E scaling really means, consider fig. 7.33 where the inclusive spectrum of particles is shown together with (dn/dx_E) at $x_E = 1$. For uncorrelated emission of toward and away hadrons, the particle density at $x_E = 1$ would drop by 5 orders of magnitude when changing the trigger $p_\perp$ from 2 to 5 GeV/c. Instead, the correlation between towards and away jet momenta keeps (dn/dx_E) constant within 20-30%!

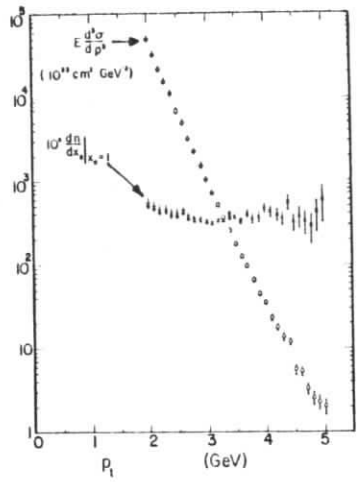

Fig. 7.33
Single hadron invariant cross section and away side multiplicity $(1/\sigma)(d\sigma/dx_E)$ for $x_E = 1$ plotted vs. $p_\perp$, for p-Be interactions at 400 GeV. From E 494 [322].

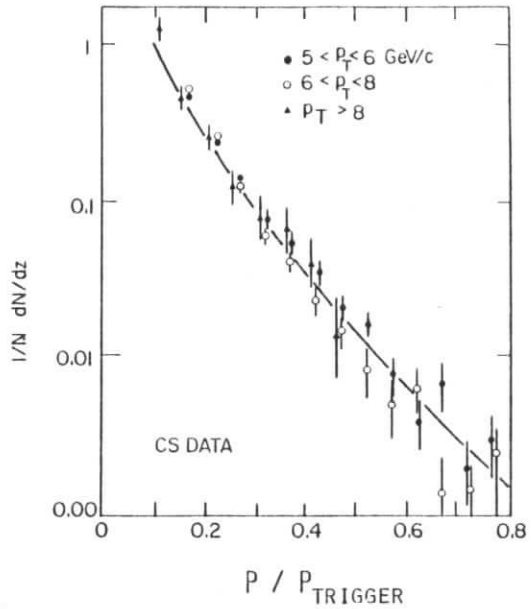

Fig. 7.34
Longitudinal distribution with respect to the jet axis of charged particles associated with a high $p_\perp$ neutral trigger. Longitudinal momenta are scaled according to the trigger momentum. From CS [313]. The solid line is calculated from eqn (7.34) using quark fragmentation functions, and is normalized arbitrarily.

Note in passing that at $x_E = 1$ the scaling limit is reached very early, since the event is in a fully symmetrical configuration, and the influence of a parton $k_\perp$ nearly disappears [366].

In analogy to eqn (7.23) the spectra of additional particles in the towards jet are given by

$$\left(\frac{d\sigma}{d|x_E|}\right)_{towards} = \int \frac{dz}{z} E\frac{d^3\sigma}{dp^3}\left(\frac{\vec{p}_\perp^{\,h}}{z}\right) D(z, |x_E|z) \qquad (7.34)$$

For a first check, the two particle fragmentation function $D(z_1, z_2)$ can be written as a product of the inclusive fragmentation functions,

$$D_q(z_1, z_2) = \theta(1-z_1-z_2)\exp(-4.5(z_1+z_2))/z_1 z_2 \qquad (7.35)$$

yielding a rather good representation of the measured spectra (fig. 7.34). Although the inclusive distribution seems to scale for different trigger $p_\perp$, the fraction of momentum carried by additional particles of the towards jet decreases with increasing trigger $p_\perp$ (fig. 7.35). This is equivalent to an increase of the mean z of the trigger hadron with $p_\perp^t$, and to an increase of the jet to single particle ratio (eqn. 7.16). The effect is well accounted for by eqn (7.19), with $D_q(z)$ as chosen above. The 20% difference in normalisation is explained by the azimuthal cuts used in the experiment.

The mean z of the trigger particle depends both on the steepness of the jet cross section, and on the shape of D(z). With increasing steepness of D(z), <z> increases and less momentum is left over for other hadrons in the trigger jet. The BFS

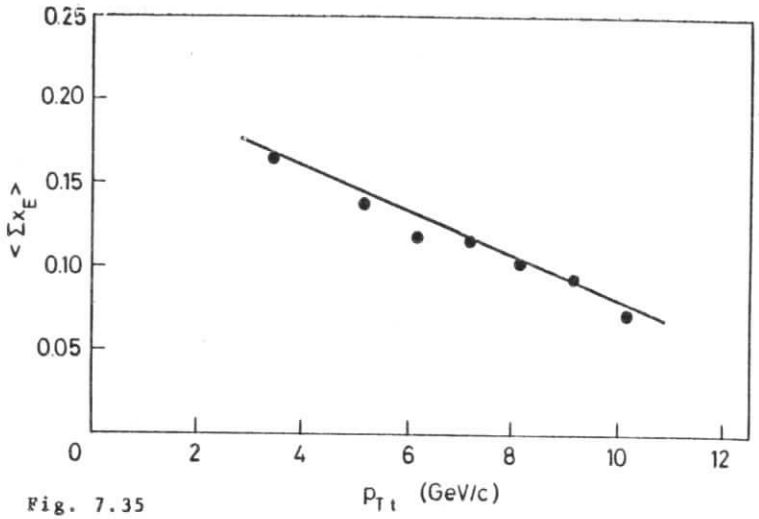

Fig. 7.35
Sum of the momenta of same side charged particles with $|\phi - \phi^t| < 60^o$, scaled to the trigger momentum, vs. trigger $p_\perp$. From CCOR [312]. The solid curve is calculated from eqn (7.19) using quark fragmentation functions, and is renormalized by 0.8.

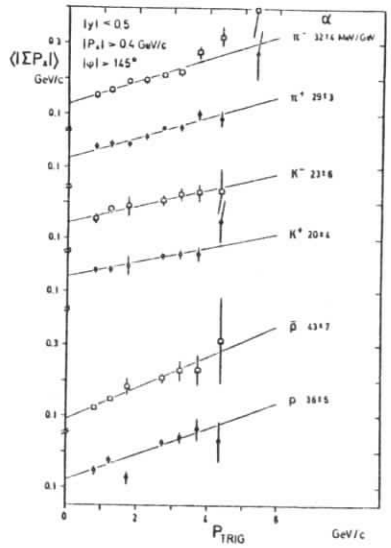

Fig. 7.36
Sum of momentum components along the trigger axis of same side charged particles with $|\phi - \phi^t| < 45^o$, and $|y - y^t| < 0.5$, for different trigger types, vs. trigger $p_\perp$. The solid lines represent a fit of the form $\langle|\Sigma p_x|\rangle = \alpha p_\perp^t + \beta$. From BFS [310].

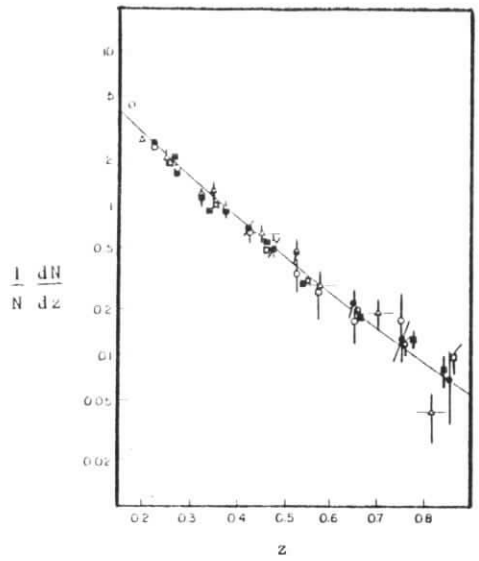

Fig. 7.37
Jet fragmentation function D(z), for the towards jet (● $p_\perp^t$ < 6 GeV/c, ○ $p_\perp^t$ > 6 GeV/c, from CS [313]) and for the away jet (■ $p_\perp^t$ > 5 GeV/c, ▲ $p_\perp^t$ > 7 GeV/c, from CCOR [312]), compared to data from νN reactions [364] (Δ), and e^+e^- annihilations [22] (-).
Distributions are normalized to unity in the interval 0.2 < z< 0.8.

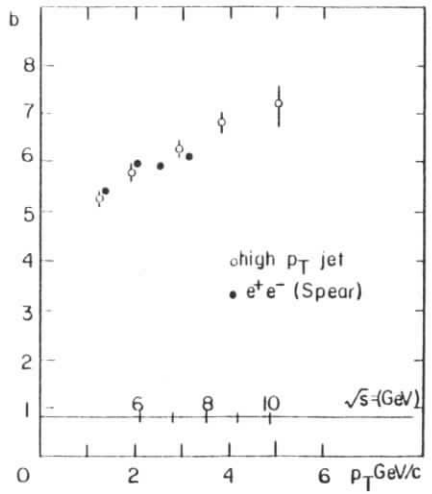

Fig. 7.38
Slope parameter b of an exponential fit to the jet fragmentation function, D(z) = exp(-bz), for 0.2 ≤ z≤ 0.8, compared to data from e^+e^- annihilations [22]. From BFS [311].

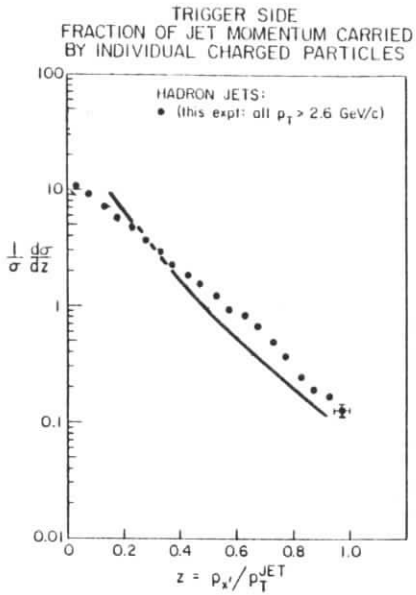

Fig. 7.39
Distribution in transverse momentum fraction z, scaled to the jet momentum, for charged particles in the trigger jet. Corrections due to the hadronic-neutral component of the jet lead to an additional uncertainity of 20% at large z. From E 260 [318]. The full line shows the distribution in $z = {}^{2P}/_{\sqrt{s}}$ obtained for quark jets in e^+e^- annihilations at $\sqrt{s}$ = 6 to 13 GeV.[55,24]

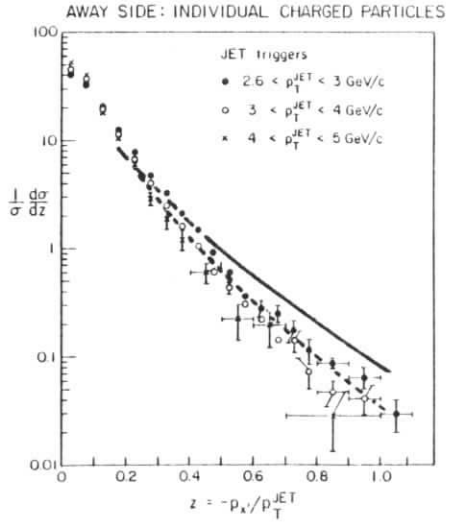

Fig. 7.40
As fig. 7.39, but for the away jet. Momenta are scaled to the trigger jet transverse momentum. The dashed curve corresponds to the full line, but with z ≡ 0.8 ·2P/$\sqrt{s}$.

collaboration has measured the amount of momentum carried by additional particles of the towards jet, for different trigger types (fig. 7.36). Since background from the spectator jets is not subtracted, only the change with the trigger $p_\perp$ is significant. Antibaryons seem to be produced by an unfavored fragmentation process, and their mean z is smaller than that of mesons.

As we have seen above, it is rather hard to determine the shape of fragmentation functions from x_E distributions. A more promising way is to detect as many jet fragments as possible, so that the total momentum of the jet is known. Results from such attempts are shown in figs. 7.37 and 7.38: both towards and away jet fragmentation agree with each other and with lepton induced quark jets. However, some caution is needed: since the experiments do not manage to detect all jet fragments, large corrections are applied which in turn depend on the jet properties, and it is not fully clear how unique the final, seft consistent solution really is.

Figs. 7.39 and 7.40 show fragmentation functions obtained from the calorimeter experiment E 260 [318] using a jet trigger, as compared to jets in e^+e^- reactions. The distribution of particles in the trigger jet is definitely flatter than in "standard" quark jets. Unfortunately, however, this does not allow definite conclusions: due to the limited solid angle of the calorimeter, the trigger bias selects jets consisting of a few, fast particles and rejects less collimated jets containing many slow particles. The problem of trigger bias disappears when the away jet is considered, nevertheless a real comparison is possible only by extensive, and model dependent simulations, since we know (fig. 7.27) that the away jet in the average carries about 1 GeV/c less transverse momentum that the trigger jet, according to which momenta are scaled. In addition, particle momenta refer to the jet momentum, and not to the jet energy, as in e^+e^- (this effect has been corrected for the CS data shown in fig. 7.37). The first effect can roughly be accounted for by chosing the scaling variable

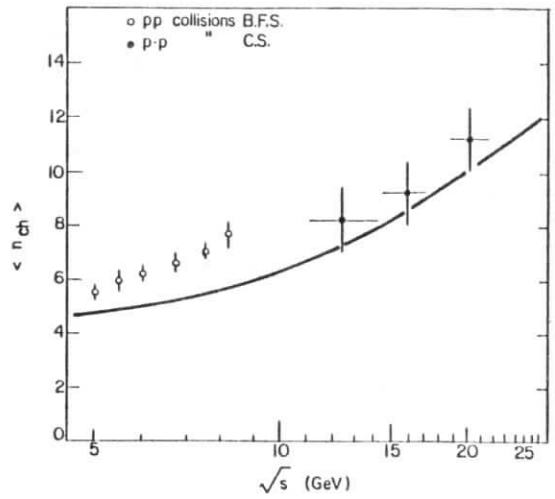

Fig. 7.41
Mean multiplicity measured for large $p_\perp$ jets per jet pair together with a fit to data from e^+e^- annihilations (compare to fig. 2.2) From BFS [311] and CS [312].

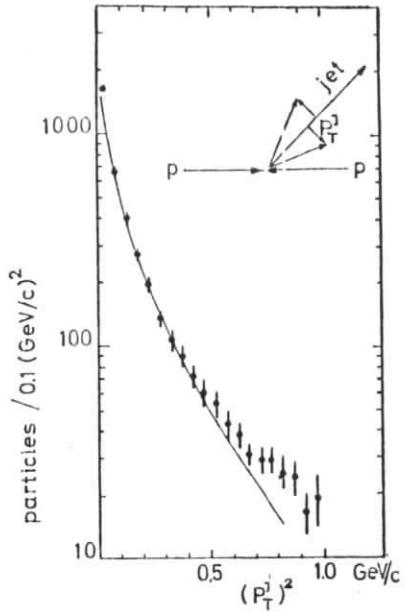

Fig. 7.42

Distribution of transverse momentum with respect to the jet axis for fast secondaries in the trigger jet, for $p_\perp^t \approx 2$ GeV. Uncorrelated background is subtracted on a statistical basis. The solid line represents the $p_\perp$ - distribution of secondaries in normal inelastic events, $d\sigma/dp_\perp^2 \sim \exp(-6p_\perp)$. From CCHK [358].

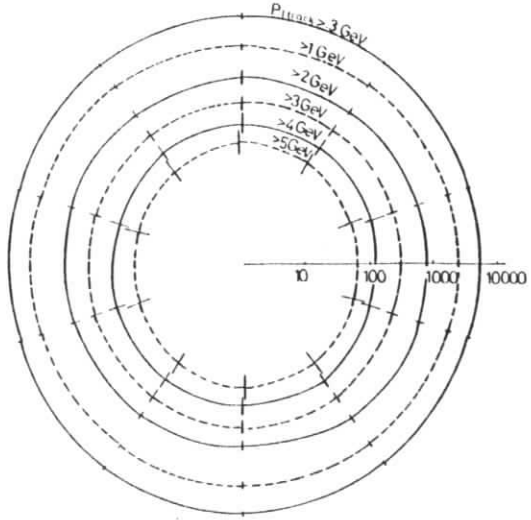

Fig. 7.43

Angular distribution of jet fragments around the reconstructed axis of a jet at large $p_\perp$, for different cuts in the transverse momentum of the secondaries. Since the jets are detected at 90° in the cms, these cuts in $p_\perp$ correspond to cuts in the momentum fraction parallel to the jet axis. From CCOR [312].

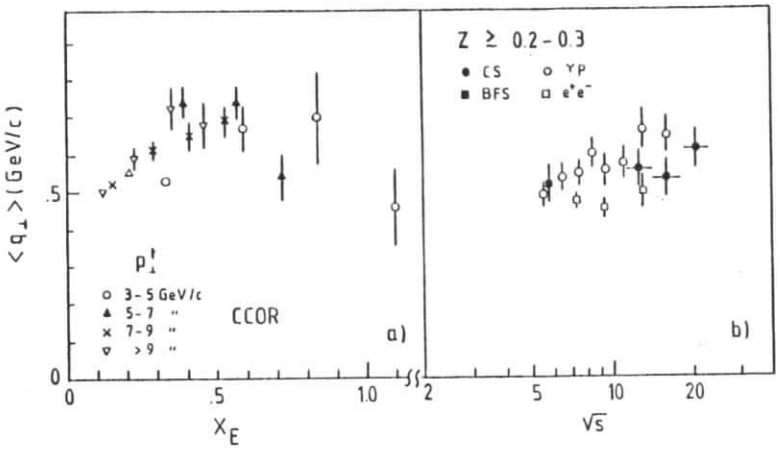

Fig. 7.44

Mean transverse momentum with respect to the jet axis

a) as a function of x_E. From CCOR [312]

b) as a function of the cms energy of the two large $p_\perp$ jets. Only hadrons at large z are taken into account. From BFS [311] and CS [313]. As a comparison points from lN interactions [367] and e^+e^- annihilations [22,41] are added.

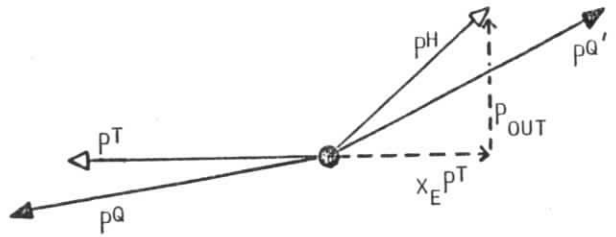

Fig. 7.45

Definition of p_{out}. All momenta are projected into the transverse momentum plane. p^t, p^h, p^q and $p^{q'}$ are the momenta of the trigger particle, of a hadron in the away jet, and of the two scattered partons, respectivly.

$z \equiv 0.8 \ast 2P/\sqrt{s}$ for the jet seen in e^+e^- annihilations, and $p_\perp^{Jet} \approx 3$ to 4 GeV/c. With this choice, the distributions agree reasonably (fig. 7.40). Fig. 7.41 compares the mean charged multiplicity of jets in large $p_\perp$ events with data from e^+e^- annihilations. Although the overall agreement is not bad, especially the BFS data [311] for low $\sqrt{s}$ show an increase of the mean multiplicity by slightly more than one unit. The excess can be traced to an increase of particle density by a factor 2 for $z \approx 0$ to 0.2, and the authors claim, that the effect cannot be accomodated within a model with "standard" quark jets. It could be regarded as a sign for gluon jets; on the other hand, $z \approx 0.1$ corresponds to particle momenta of about 0.5 GeV/c in the cms of the two jets of large $p_\perp$, and factorisation is not expected to hold for such fragments. In the spirit of the QRM e.g. other explanations are possible: picturally, quarks in e^+e^- reactions produce a chain of quark pairs, which "recombine" into hadrons. In large $p_\perp$ events, and at small z, this chain overlaps with the primordial quark sea of the incident hadrons, and the multiplicity will be enhanced; although such particles in principle do not "belong" uniquely to a large $p_\perp$ jet, they are close to it in rapidity and are counted by the reconstruction procedure.

Let us now turn to the dependence of the fragmentation functions on the transverse momentum with respect to the jet axis, $q_\perp$. Figs. 7.42 and 7.43 prove that the distribution of particles is sharply cut off in $q_\perp$, and that in large $p_\perp$ jets particles are distributed uniformly in azimuth around the jet axis. If $\langle q_\perp \rangle$ is plotted as a function of the track momentum, or x_E (fig. 7.44a) a seagull effect is visible.

Although it has been argued [225,226] that $O(\alpha_s)$ corrections lead to a stronger broadening of jets in hadronic interactions, as compared to jets in e^+e^- annihilations, no clear effect is seen up to now. This is astonishing since QCD effects manifest

themselves clearly in the nucleon structure functions, where they give rise to a large parton $k_\perp$.

The Q^2, or $p_\perp$ dependence of $k_\perp$ can be measured directly in two ways. Either the component of $k_\perp$ in the scattering plane is determined by measuring the transverse momentum imbalance of the two jets, or one studies the component out of the scattering plane, which gives rise to a noncollinearity of the jet transverse momenta. This is usually done by investigated the momentum component p_{out} out of the scattering plane defined by the trigger momentum and the collision axis (fig. 7.45). Obviously, the mean square of p_{out} is given by the following relation

$$p_{out}^2 = \frac{1}{2} \langle q_\perp^2(1,Q^2) \rangle + x_E^2 \left(\frac{1}{2} \langle q_\perp^2(x_E,Q^2) \rangle + \langle k_\perp^2(x,Q^2) \rangle \right) \qquad (7.36)$$

where $q_\perp^2(z,Q^2)$ is the mean transverse momentum squared of a jet fragment carrying a fraction z of the jet momentum, and $k_\perp^2$ is the effective transverse momentum of a parton of fractional momentum x in the incident hadron. The trigger hadron has been assumed to have $z \approx 1$. The factor 1/2 enters, since only one component of transverse momentum is used. For practical purposes, $\langle p_{out}^2 \rangle$ is often replaced by $\langle |p_{out}| \rangle^2$.

Whereas for a trigger transverse momenta between 2 and 4 GeV no significant variation of $\langle |p_{out}| \rangle$ was found for fixed x_E [7], more recent experiments [312,314] report an increase of $\langle |p_{out}| \rangle$ with the trigger $p_\perp$ for trigger momenta between 3 and 10 GeV/c (fig. 7.46 and 7.47). Since $q_\perp$ is known not to depend strongly on Q^2, the variation of $\langle |p_{out}| \rangle$ can be interpreted as in increase of $\langle k_\perp^2 \rangle$ with Q^2. Unfortunately this explanation is not unique since at fixed $\sqrt{s}$ $x_\perp$, and x increase also with Q^2, or $p_\perp^t$. To exclude a x-dependence of $k_\perp$, measurements at

different energies are necessary. Fig. 7.48a) summarizes the values of $\langle k_\perp \rangle$ as derived from $\langle |p_{out}| \rangle$, and from the jet momentum balance. At fixed energy, $\langle k_\perp \rangle$ increases with the trigger $p_\perp$, or Q^2. As shown in fig. 7.48 b), the $x_\perp$ dependence of $\langle k_\perp \rangle$ cannot be responsible for this effect. It is interesting to note that for $p_\perp^t \to 0$ all curves extrapolate to $\langle k_\perp \rangle \approx 300$ to 400 MeV, in agreement with the naive guess for transverse momentum fluctuations of partons in a nucleon of size O (1 fm). It is tempting to attribute the rise of $\langle k_\perp \rangle$ with $p_\perp^t$ to QCD bremsstrahlung effects; actually first calculations of the higher order graphs involved succeed in reproducing the slope of the p_{out} distribution for large p_{out} .[361]

To summarize so far: the fragmentation functions D(z) obtained for fast ($p \gg m$) fragments of the scattered partons in large $p_\perp$ events agree with the properties of quark jets measured in e^+e^- annihilations, within the experimental accuracy; also the transverse size of jets is similar and mainly determined by nonperturbative effects. A large asymmetry between the fragmentation of the towards and away jets, as expected in the CIM model, is excluded. On the other hand, a dominant contribution from gluons jets with a fragmentation function $D_g^h(z) = (1-z)D_q^h(z)$ seems to be hardly compatible with data.

QCD effects are visible as an increase of $\langle k_\perp \rangle$ with Q^2. However there is no evidence for a broadening of the large $p_\perp$ jets, or for a sizeable fraction of events containing more than four jets.

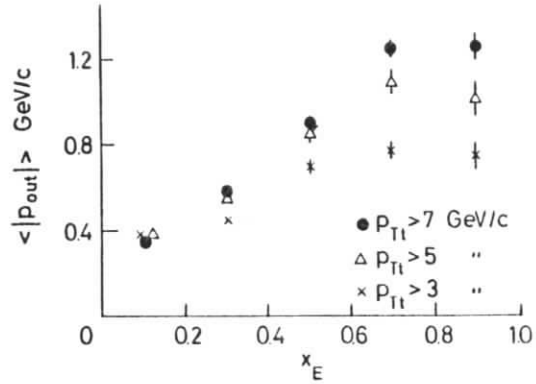

Fig. 7.46
Mean value for $|p_{out}|$ as a function of x_E for different ranges of trigger $p_\perp$. From CCOR [312]

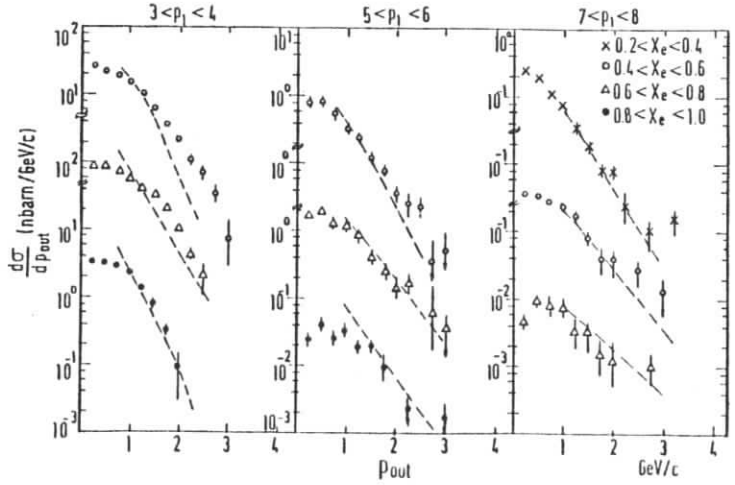

Fig. 7.47
p_{out} distribution for different x_E regions and trigger momenta. From ABCY [314]. The dashed curves are results of a QCD calculation. [361]

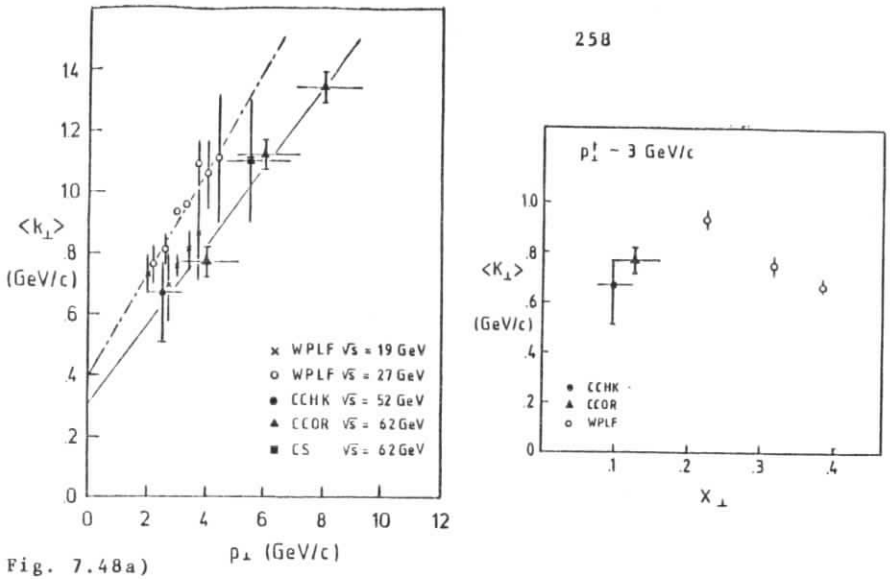

Fig. 7.48a)

Mean parton transverse momentum as determined from the $\langle |p_{out}| \rangle$ (CCHK[7], CCOR[375], CS[313]) and from the momentum imbalance of large $p_\perp$ jets (WPLF[352]), vs. trigger $p_\perp$. For the WPLF data, $\langle k_\perp \rangle$ has been calculated from $\langle k_\perp^2 \rangle$ assuming an exponential distribution in $k_\perp$. Some of the error bars include systematic uncertainities (CCHK, CS), other refer to statical errors only (CCOR). The WPLF data is corrected for detector resolution. Additional corrections[352] were suggested which would systematically decrease the mean $k_\perp$ by 10-15%.

b) Mean parton $k_\perp$ as a function of $x_\perp$, for fixed trigger $p_\perp$ of ~ 3 GeV/c.

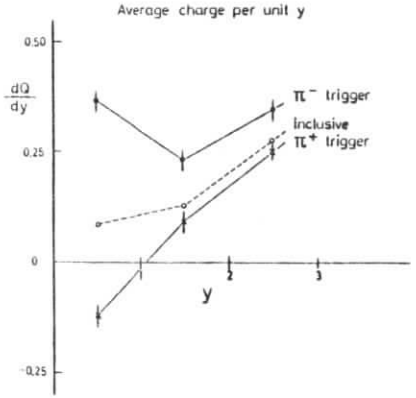

Fig. 7.49

Average charge density dQ/dy for events with a large $p_\perp$ π^+ or π^- trigger at y = 0, compared to the charge density in normal inelastic events. From BFS[310].

The next step in the investigation of jets in large $p_\perp$ events is to study correlations between quantum numbers of particles emitted within one jet, and in different jets, respectivly. Correlations in normal hadronic interactions are governed by the principle of "short range order" which states that flavour quantum numbers of secondaries tend to be conserved locally.[377,194,372] The situation differs drastically for large $p_\perp$ events. In the hard scattering process, both confined quantum numbers - like fractional charge, or color - and non confined quantum numbers like strangeness propagate over large distances in phase space and give rise to long range quantum number correlations.

In the remainder of section 7.3 we discuss correlations between the trigger flavour and hadrons in the opposite jet of large $p_\perp$. In contrast to the constituent interchange model, QCD predicts the flavours in the towards and the away jet to be uncorrelated, since in QCD subprocesses no flavour exchange occurs.

Consider first the influence of the trigger charge. Fig. 7.49 shows the net charge density $(1/\sigma)(d\sigma^+/dy - d\sigma^-/dy)$ for events with a positive and negative large $p_\perp$ particle at $y^t = 0$.[310] σ^+ and σ^- are the cross sections for production of additional positive and negative particles, respectivly. It seems that the charge of the trigger particle is balanced by other particles close to it in rapidity.

A precise measure for the correlation is given by the difference of the two curves in fig. 7.49, the so called "associated charge density balance" $\Delta q(y|y^t)$.[372] Naivly speaking $\Delta q(y,y^t)$ is the answer to the question "which particles in a high $p_\perp$ event know about the trigger charge?" or "where do the valence constituents in the trigger particle come from?". Fig. 7.50 displays $\Delta q(y,y^t)$ for events with a large $p_\perp$ hadron at $y \approx -0.9$.[368] The peak in Δq follows the trigger rapidity; the whole distribution looks quite similar compared to the compensation of the charge of a low $p_\perp$ "trigger" particle in normal events.[372] Fig. 7.51 shows Δq as a function of the azimuthal angle ϕ and the difference $y-y^t$, for two event configurations, with the two jets of large $p_\perp$ being in the same rapidity hemisphere ("back-antiback") and with

the two jets in opposite hemispheres ("back to back"). The rapidity of the away jet is given by the secondary with largest $p_\perp$ ("jet leader") in the away wedge $150^o \leq \phi \leq 210^o$. The trigger hadron is emitted at $\phi \sim 0^o$, and $y \sim -0.9$.

In fig. 7.51, three components of Δq can be distinguished: part of the charge of the trigger hadron is balanced by secondaries in the towards jet, with $\phi \sim \phi^t$ and $y \sim y^t$. A second component peaked at $\phi \sim 180^o$ follows the away jet rapidity and can be assigned to fragments of the away parton. Finally, a third component flat in ϕ is most naturally attributed to spectator fragments.

A contribution of away jet hadrons to Δq does not contradict QCD predictions since it may arise from soft hadrons in the region where the jets overlap, and hence will exchange flavors (fig. 7.2), while the charge of the scattered parton, as measured e.g. by the charge of the away jet leader remains unaffected. Fig. 7.52a) shows the mean charge of the away jet leader for "back to back" configurations (see fig. 7.51), for positive and negative trigger particles.[307] In order to exclude cases where an undetected neutral is the leading particle in the away jet, transverse momentum balance was checked by calculating the ratio $x_J = \Sigma p_x^{tow} / \Sigma p_x^{away}$, which measures the fraction of the trigger jet transverse momentum compensated by away side charged particles. In the limit $x_J \to 1$, the mean charge of the jet leader $\langle q_F \rangle$ measures the average charge of the away side parton.

In a simple quark model a value $\langle q_F \rangle = 1/3$ is expected, since the average charge of a valence quark in a proton is 1/3. A more sophisticated calculation of valence quark scattering, based on exact structure and fragmentation functions[326] confirms this value. The presence of gluon contributions should decrease $\langle q_F \rangle$. However, the "back to back" configuration selects events where $\hat{s}$, x_1 and x_2 are large, and valence quarks are preferred. In addition, the condition $x_J \to 1$ acts similar to a trigger bias and favors quark jets as compared to QCD gluon jets.

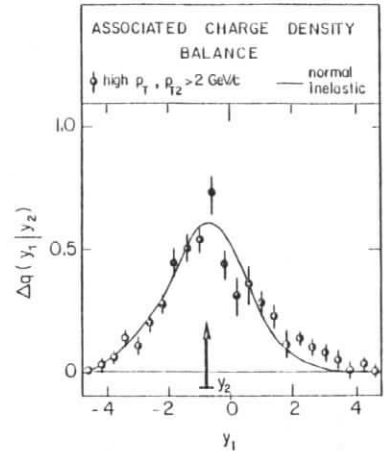

Fig. 7.50
Charge density balance $\Delta q\ (y, y^t)$ as a function of the rapidity y, associated with a large $p_\perp$ trigger at $y^t = -0.9$. The full line shows the corresponding distribution for nondiffractive inelastic events. From CCHK[368].

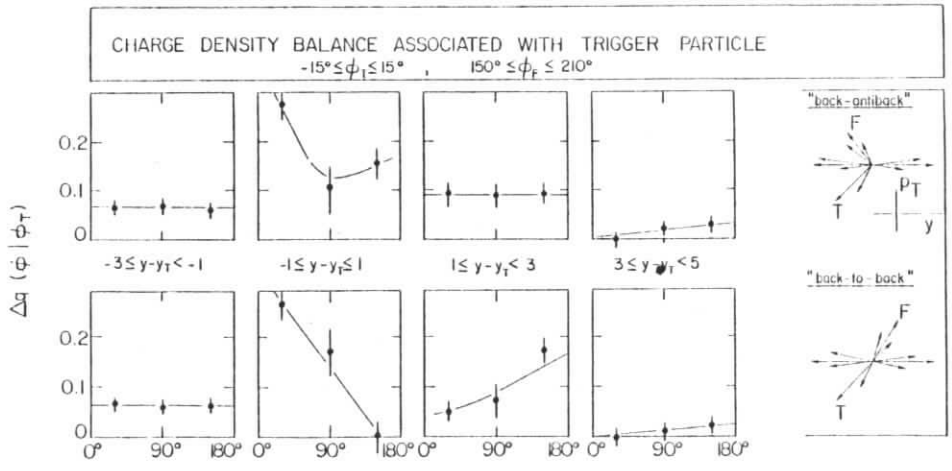

Fig. 7.51
Charge density balance $\Delta q(\phi, \phi^t)$ of particles associated with a large $p_\perp$ particle, for different intervals in rapidity relative to the trigger, and for two event configurations
-large $p_\perp$ jets are in the same rapidity hemisphere ("back-antiback")
-large $p_\perp$ jets are in opposite hemispheres ("back-to-back")
From CCHK[368].

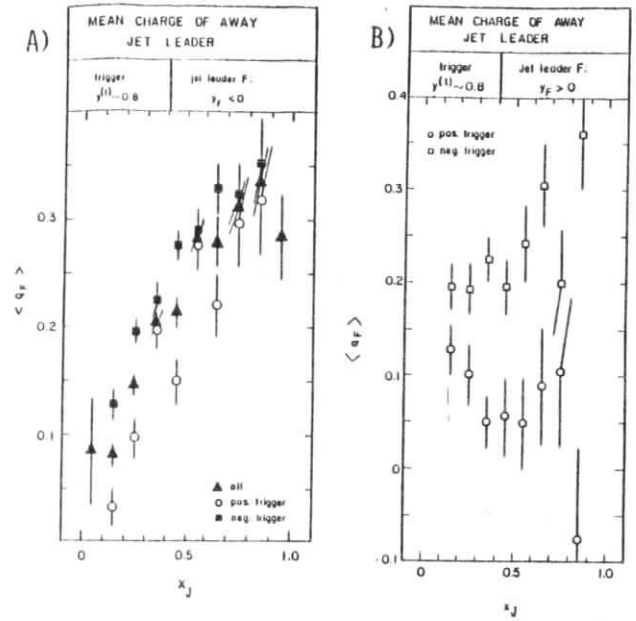

Fig. 7.52
Mean charge of the fastest particle in the away jet, as a function of the visible momentum of the away jet, scaled to the trigger $p_\perp$, for positive and negative trigger particles at $y^t \approx -0.9$.
a) back-to-back configuration
b) back-antiback configuration (comp. fig. 7.51)
From CCHK [307].

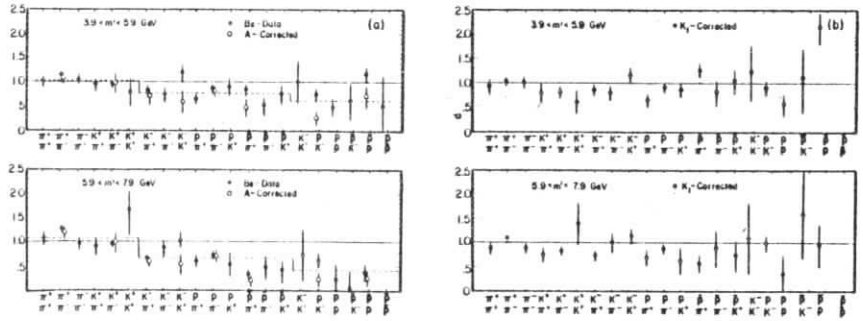

Fig. 7.53
Correlation function R for two hadrons emitted with large, and opposite transverse momenta for two ranges of the "mass" $m' = p_{\perp 1} + p_{\perp 2}$. a) • Data from pBe collisions, o corrected for nuclear enhancements. b) The same correlation function, corrected for effects due to parton transverse momenta. R is defined in a way that the flavors of the hadrons are uncorrelated if R=1. From E 394 [322].

Data are consistent with $\langle q_F \rangle \to 0.3 - 0.35$ for $x_J \to 1$. At large x_J, no significant dependence of $\langle q_F \rangle$ on the trigger charge is seen.

Fig. 7.52b) shows the same plot for the "back-antiback" event configuration. Here the charge of the away jet leader is correlated to the trigger charge. Although precise predictions are missing, this correlation will be difficult to accomodate in the QCD model; possible excuses are that the "back-antiback" event type corresponds to the lowest values of $\hat{s}$ for fixed $p_\perp$. Non asymptotic exchange processes will be strongest in this configuration. Furthermore, the positive triggers contain a sizeable fraction of protons [307], whose production mechanism will been shown to differ from meson production.

Flavor correlations between towards and away particles at $y \approx 0$ were investigated by two experiments at FNAL [322-324], which detected and identified pairs of hadrons with large and opposite transverse momenta, and by the BFS group at the ISR. [310,311] Fig. 7.53 displays the flavor correlation function $R_{h_1h_2}$ obtained in the E 494 experiment. [322] $R_{h_1h_2}$ is defined as the two particle correlation function C normalized to its mean value when averaged over opposite charged hadron pairs:

$$R_{h_1h_2} = C_{h_1h_2} / C_{h^+h^-} \qquad (7.37)$$

and

$$C_{h_1h_2} = \frac{(E_1E_2\frac{d^6\sigma_{12}}{dp_1^3dp_2^3}/\sigma_{tot})}{(E_1\frac{d^3\sigma}{dp_1^3}/\sigma_{tot})(E_2\frac{d^3\sigma}{dp_1^3}/\sigma_{tot})}$$

From fig. 7.53, one reads a significant correlation for hadron pairs containing one or two k^- or $\bar{p}$.

However the authors have shown that the definition of R may not be fully appropriate, for the following reason: one knows that for inclusive particle production at large $p_\perp$, the hadron $p_\perp$ is augmented by about 1 GeV of additional transverse momentum $\Delta p_\perp$ from the parton transverse momentum. Symmetric pair production is not biased by $k_\perp$ because of symmetry. Thus the species composition in symmetric pairs of transverse momentum $p_\perp$ corresponds to the single particle composition at $p_\perp' = p_\perp + \Delta p_\perp$, and the correlation function R is to be modified

$$C'_{h_1 h_2} = \frac{\sigma_{12}(p_{\perp 1}, p_{\perp 2})/\sigma_{tot}}{(\sigma_1(p_{\perp 1}+\Delta p_\perp)/\sigma_{tot})(\sigma_2(p_{\perp 2}+\Delta p_\perp)/\sigma_{tot})} \qquad (7.38)$$

This change influences only those hadrons whose relative abundance depends strongly on $p_\perp$, namely k^- and $p,\bar{p}$ (fig. 7.17). Actually, all systematic deviations from unity disapear in the $k_\perp$ corrected correlation function R' (fig. 7.53b). The authors consider remaining fluctuations as not significant.

A contradictory result was obtained by the experiment E 357 [324] studying hadron pairs of lower $p_\perp$ = 1··1.8 GeV/c. In this case a correlation function was defined without referring to inclusive spectra, simply by comparing e.g. the abundance of protons compared to the total positive particle yield h^+ on the away side, for a towards antiproton $\bar{p}$ and an arbitrary towards hadron h

$$R = \frac{(p/h^+)_{\bar{p}}}{(p/h^+)_h} \qquad (7.39)$$

This definition avoids the $\Delta p_\perp$ bias, but is still sensitive to a change in the towards fragmentation function (s.eqn 7.23).

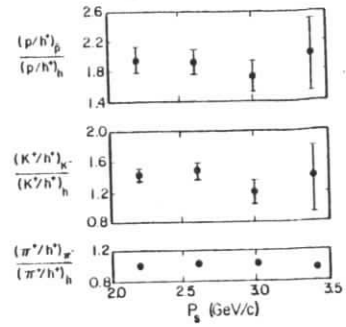

Fig. 7.54
p_s dependence of the particle-antiparticle correlation in pBe collisions. p_s is the sum of the magnitudes of the transverse momenta of the two particles. Errors are statistical only. From E 357 [324].

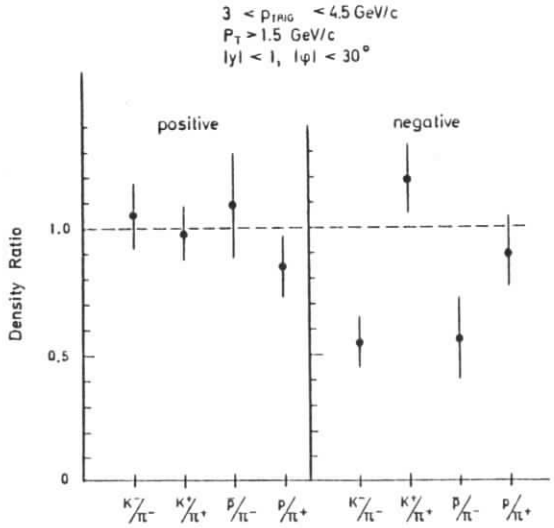

Fig. 7.55
Ratio of the average number of hadrons in the away region for different combinations of trigger particles, and for positive and negative secondaries. From BFS [310].

Strong correlations between p and $\bar{p}$ and between k^+ and k^- are observed (fig. 354). Such a correlation is expected e.g. for CIM fusion mechanisms. It should be noted that this experiment does not really test the large $p_\perp$ domain. Mean invariant masses of the particle pairs are 2-3 GeV; thus the correlation can be explained as due to the decay of a flavor singlet, low $p_\perp$ cluster into $p\bar{p}$, or k^+k^-. To arrive at a definite conclusion, more precise data on the $p_\perp$ dependence of the correlation is required.

A similar correlation for k^- and $\bar{p}$ triggers has been observed by the BFS group at the ISR. Fig. 3.55 shows that the number of negative particles in the away jet decreases for events with a k^- or $\bar{p}$ triggering particle. The effect is observed for large $p_\perp$ (> 3 GeV/c) and fast ($p_\perp$ > 1.5 GeV/c) secondaries. The observation cannot be explained by a change of the fragmentation function of the towards jet, since this should influence both positive and negative fragments in about the same way.

To summarize: all experiments agree that for "non exotic" large $p_\perp$ meson triggers no significant correlation between the flavors of the towards and the away parton is seen (here the CCHK data from fig. 7.52 b) are omitted, since a considerable fraction of triggers is known not to be mesons). For exotic triggers (i.e. particles which do not contain a beam or target valence quark) the situation is unclear; data are sometimes contradictory and lack of statistical significance. Furthermore, the effect seen by the BFS group is not what is expected in the CIM model. For $q\bar{q} \to k^-M$ e.g. the meson M has a comparable flat fragmentation function and the number of positive away fragments should be considerable enhanced, as compared to $qM \to \pi^- q$.

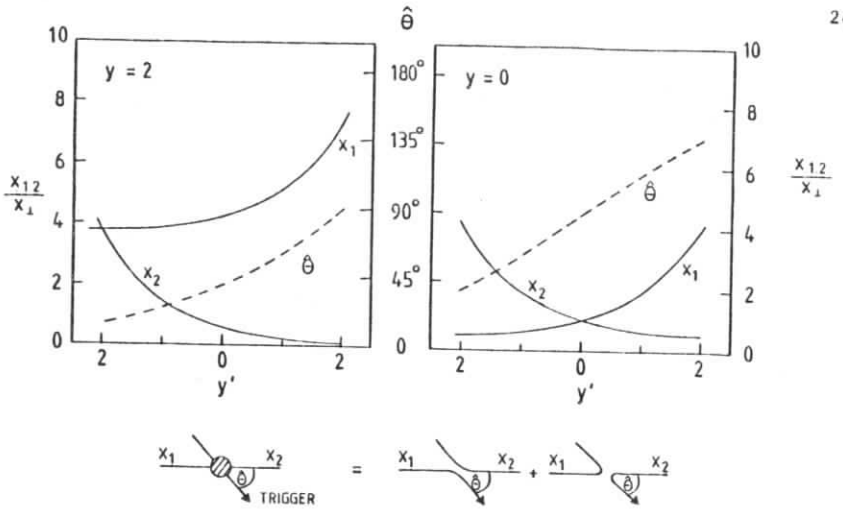

Fig. 7.56
Kinematics of the two body subprocess for trigger rapidities y = 0 and 2, as a function of the away jet rapidity y'. Shown are x_1, x_2 and the scattering angle $\hat{\theta}$. x_1 is the parton moving in the same direction as the trigger particle, and $x_\perp = 2\,p_\perp/\sqrt{s}$ measures the $p_\perp$ of the jets at large $p_\perp$. Based on eqs (7.2, 7.3, 7.5) neglecting masses and parton $k_\perp$. More refined calculations including these effects show no major differences[7].

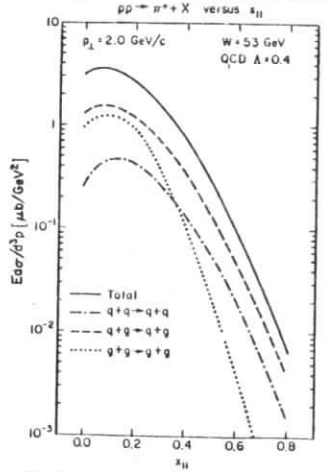

Fig. 7.57
Contributions of quark-quark, quark-gluon and gluon-gluon scattering to single particle inclusive cross sections at $p_\perp \approx 2$ GeV/c and $\sqrt{s} = 52$ GeV as a function of x_{II}, according to ref 326.

7.4 Spectator fragmentation

In the previous discussion of properties of the jets at large $p_\perp$, the two spectator jets at low $p_\perp$ were mainly considered as a nasty source of background. Since however the active partons are missing in the spectator systems, and since models like QRM or DCR predict the distribution of spectator fragments to depend crucially on its quark contents, the investigation of spectator decay offers an independent, and complementary way to check the parton model concepts.

As compared to studies of spectator fragmentation in lepton nucleon interactions, high $p_\perp$ events at ISR energies offer the advantage that the mass of the spectator system is increased by factors of 10 as compared to the mean W in lN reactions, and it is certainly justified to use asymptotic concepts like DCR. Spectator fragmentation has been investigated by the CCHK/ACCDHW[307] [368] and BFS [309] groups using the Split Field Magnet detector at the ISR. In both experiments the detector was triggered by particles of $p_\perp \approx 2$-3 GeV/c, which were produced in proton-proton collisions at $\sqrt{s} = 52$ GeV. The trigger hadron was identified by cerenkov counters.

The BFS group selected trigger particles at $y \approx 0$, whereas the CCHK collaboration used a forward trigger at $y \approx 2$, or $\theta \approx 20^\circ$. As a result, the kinematics of the two body subprocess differs appreciably (fig. 7.56): for the central trigger, with $x_\perp \approx 0.1$, the active partons are likely to be gluons (fig. 7.57)[326, 327]. Because of the symmetrical configuration, the parton creating the towards jet can come of each of the incident protons.

For a trigger angle of 20°, the active parton in the proton moving in the same longitudinal direction as the trigger particle has to be in the valence quark region, at $x \approx 0.4$. Here, qq and especially qg processes are expected to be relevant. Since in QCD the forward cross sections are large compared to the probabilities for backward scattering (fig. 7.5), the towards parton will always be the quark scattered out of the proton in the same rapidity hemisphere as the trigger. The spectator fragments of this proton will be called the "accompanying spectator", as compared to the "away spectator" opposite in rapidity to the trigger.

The forward trigger condition has yet another consequence: at a fixed small angle the inclusive cross section falls more steeply in $p_\perp$ than at $\theta = 90^\circ$, and the trigger bias pushes the mean z of the trigger hadron up to $z \approx 0.8$ -0.9 (eqn 7.19). Thus favored fragmentation modes like $u \to \pi^+$, $d \to \pi^-$ are strongly preferred - this allows to determine the flavor of the scattered quark.

For such events with a forward large $p_\perp$ particle, the predictions of the quark parton model are evident

- in most cases, the accomanying spectator contains two quarks, e.g. two u quarks for a π^- trigger, and a u and a d quark for a π^+ trigger
- quantum numbers of the trigger particle and of the away spectator are uncorrelated
- the away spectator is likely to contain all three incident valence quarks

General characteristics of the spectator. Fig. 7.58 shows the distribution of spectator fragments in Feynman x for a central large $p_\perp$ trigger, as compared to the particle density in normal inelastic events. [309] With increasing $p_\perp^t$ of the trigger, the distributions drop more rapidly at large x. This can be understood simply as a consequence of energy conservation - the maximum energy of the spectators diminuishes with increasing trigger $p_\perp$. Introducing a new scaling variable $\hat{x} = p_\parallel / (p_{beam} - a p_\perp^t)$,

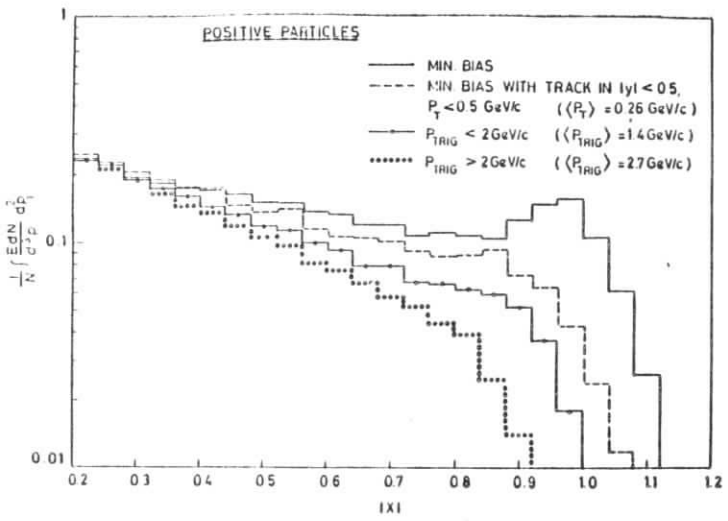

Fig. 7.58
Distribution of positive spectator fragments in Feynman x for events with a large $p_\perp$ particle. Full and dashed lines refer to the corresponding distributions in inelastic and in non-diffractive proton-proton interactions. From BFS.[309]

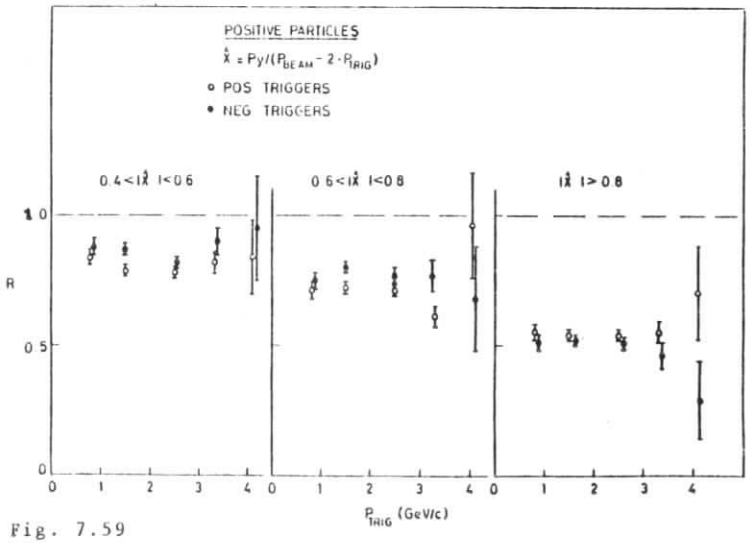

Fig. 7.59
Density of positive spectator fragments in $\hat{x}$, scaled to the corresponding yields in normal inelastic interactions, as a function of the trigger $p_\perp$.[309]

the BFS collaboration found scaling for a = 2 (fig. 7.59). This value means that the amount of energy carried by the jets at high $p_\perp$ is twice the minimum amount required by momentum conservation. This may seen embarrasing, however Monte Carlo studies prove that for a = 2 the variable $\hat{x}$ is a good approximation to the "correct" variable x' defined in eqn (7.25), when averaged over the away jet rapidities. So Feynman scaling seems to hold for spectator fragmentation.

Let us now turn to transverse momentum distributions in spectator jets. Fig. 7.60 shows the ratio R of particle densities in spectator jets and in normal inelastic events as a function of $p_\perp$ with respect to the collision axis. Once more the transversely cut off distribution of momenta proves to be a universal feature of jets, the mean transverse momenta in the two classes of events deviate by less than 10%! Assuming that the basic fragmentation mechanisms are identical, the small difference in $\langle p_\perp \rangle$ can be explained in different ways

- contamination by particles from the jets at large $p_\perp$. Since the rapidity of such particles is essentially restricted to $|y| \lesssim 2\text{-}3$, the effect should be negligible for $|x| \geq \frac{2m_\perp}{\sqrt{s}} \sinh(y_{max}) = 0.3 - 0.4$, for $p_\perp \lesssim 1$ GeV.
- gluon bremsstrahlung of the active quark before the scattering
- the spectator axis of flight deviates from the collision axis, since the active parton recoils against the spectator

Such a recoil has in fact been observed [7] as a pronounced asymmetry in the azimuthal distribution of fast spectator protons in high $p_\perp$ events (fig. 7.61). Fig. 7.62 a) shows the mean transverse momentum component opposite to the trigger $p_\perp$ as a function of x, for a central trigger. The amount of recoil carried per particle saturates for higher $p_\perp$ of the trigger (fig. 7.62 b). Such a saturation is expected for the primordial component of parton $k_\perp$. The comparison of the recoil component

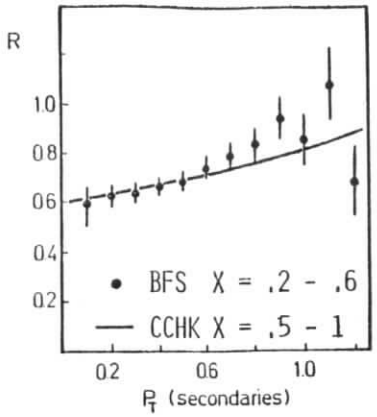

Fig. 7.60
Ratio of particle densities in the spectator fragmentation region of large $p_\perp$ events to particle densities observed in normal inelastic interactions as a function of the particles $p_\perp$. From BFS [309] and CCHK [365].

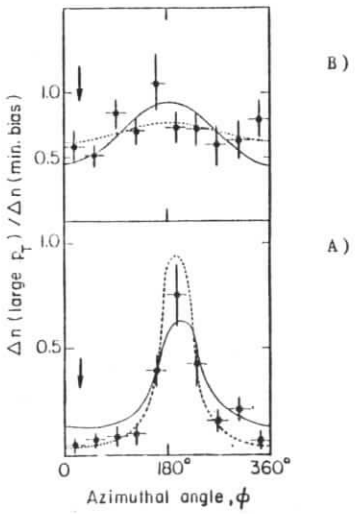

Fig. 7.61
Azimuthal distribution of fast positive particles
(a) in the accompanying spectator in large $p_\perp$ events, normalized to the particle density in normal inelastic events. Full and dotted lines refer to parton model calculations including parton $k_\perp$. From CCHK [7,365]
(b) in the away spectator.

and of the effective $k_\perp$ measured by the imbalance of momenta of the large $p_\perp$ jets (fig. 7.48) offers the possibility to separate soft gluon contributions (primordial $k_\perp$?) from hard gluon effects (QCD) - only soft gluons are expected to be reabsorbed by the spectators; hard gluons should materialize as separate jets. Present data indicate a different dependence on the trigger $p_\perp$ for the two components, for definite conclusion more precise data on the recoil momentum for larger $p_\perp^t$ are needed.

Concerning the third possibility listed above, the BFS group claims that the increase of the mean $p_\perp$ of spectator fragments cannot be fully explained by a momentum smearing due to the recoil.

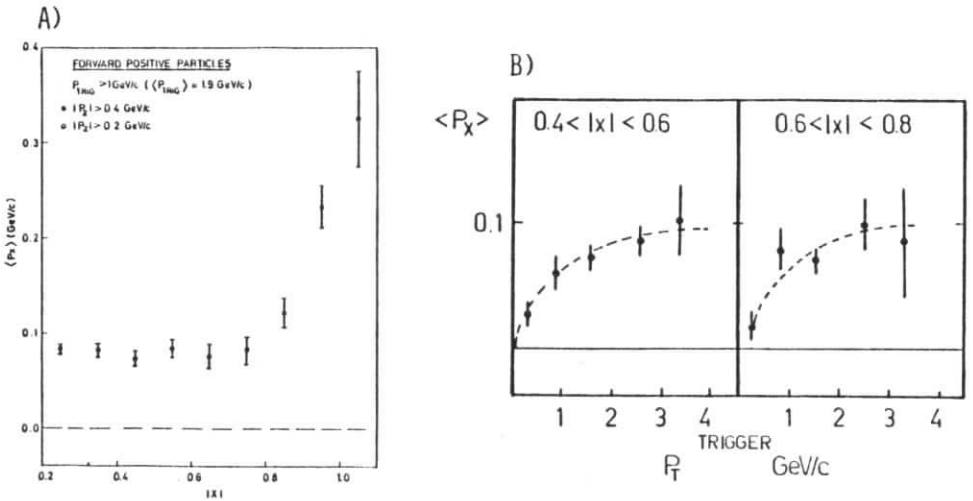

Fig. 7.62
Mean component of transverse momentum opposite to the trigger $p_\perp$, as a function of Feynman x of the secondary (a) and as a function of the trigger $p_\perp$ (b). From BFS. [309]

Quantum number correlations. As already discussed, the quark parton model predicts strong correlations between trigger and spectator quantum numbers. Fig. 7.63 shows the ratio of rapidity distributions of positive secondary particles for a π^+ trigger to those with a π^- trigger and similarly for negative secondaries. The trigger particle at $y^t \approx 2$ has a mean $p_\perp$ of 2.5 GeV/c. Similarly, the corresponding ratios for p/π^+ triggers and for k^-/π^- triggers are given in fig. 7.64 and 7.65 (note that the "k^- triggers" contains a certain - ~30% - contamination of large $p_\perp$ antiprotons, and that the "p trigger" includes some k^+ - ~ 20%)[307]. A clear correlation is seen between the nature of the trigger particle and charged particles in the accompanying spectator jet; for y > 2, where spectator fragments dominate, the ratios deviate markedly from unity.

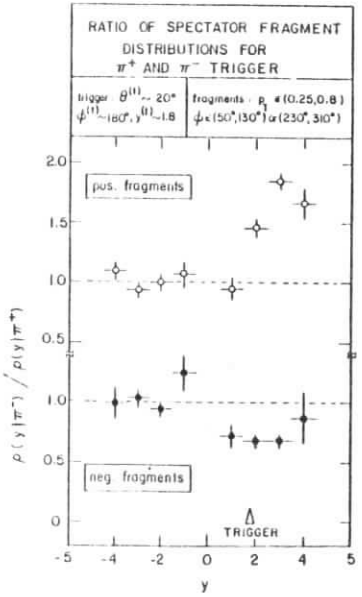

Fig. 7.63
Ratio of the distributions of spectator fragments for a π^+ trigger ($((1/\sigma)(d\sigma/dy)_{\pi^+ \text{ trigger}} \equiv \rho(y|\pi^+)$) and for a π^- trigger ($\rho(y|\pi^-)$) as a function of rapidity. The region y > 0 is populated by fragments from the accompanying spectator. From CCHK. 307)

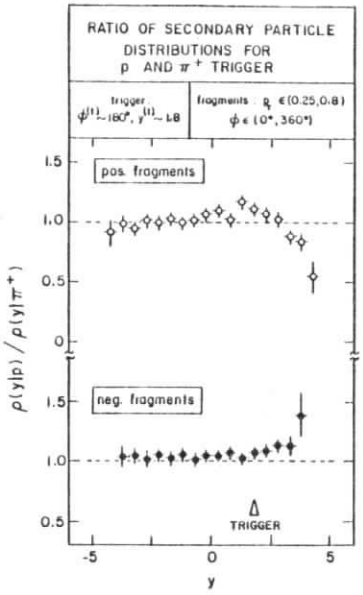

Fig. 7.64
As fig. 7.63, but for proton and π^+-trigger. From CCHK [307].

Spectator fragmentation functions. For a forward π^+ and π^- trigger particle, the quark composition of the accompanying spectator is known to be ud and uu, respectivly. Using dimensional counting rules, or the quark recombination model, the scaling distribution of fast fragments can be predicted and compared with the experiment. Vice versa, one can try to identify the scattering mechanism by inspecting the quark composition of the spectator, an application which is particularly interesting for the proton and k^- triggers.

As a scaling variable, we use x' as defined by eqn (7.25), and make the following approximations for y, y' and $m_\perp$:

$y = y^t$ (trigger rapidity)
$y' = 0$ (experimentally: $\langle y' \rangle = 0.05$)
$m_\perp = 1.1\ p_\perp^t$

The effects of these approximations have been simulated, showing that an initial distribution $Ed^3\sigma/dp^3 \sim (1-x)^\beta$ can be regained with an error in β of less than 10-15%. For ratios of cross sections, these errors tend to cancel.

To compare with data, we use the QRM as defined by eqn (6.27). Numerical values for meson production are taken from ref. 241. Predictions for ratios of particle densities are absolutely normalized.

In addition predictions from counting rules are quoted, calculated via $x'd\sigma^h/dx' \sim (1-x')^{2n-1}$, where n is the minimum number of quarks left over after the hadron h is emitted (s. sections 6.5, 6.6). The normalisation is arbitrary. In apparent contradiction with experiments[369], such a counting rule predicts the distribution of π^+ and π^- from proton fragmentation to be identical. To correct for this effect, we use an ad hoc modification[307,192] of the counting rule recipe: the predicted power is increased by one unit whenever the fragment contains a valence d quark out of one of the primary protons.
The same modification has been applied to the DCR predictions assuming pointlike particle creation (eqn. 6.47).
DCR predictions are summarized in table 7.2.

Table 7.2

Dimensional counting rule predictions
for spectator fragmentation spectra

trigger type	hard scattering process	spectator contents	fragment charge and type	predicted spectrum "standard" DCR	"pointlike" DCR
π^+	$qq \to qq, qg \to qg$	ud	+ p_+ − π^-	$(1-x)_4$ $(1-x)^4$	$(1-x)_4$ $(1-x)^4$
π^-	$qq \to qq, qg \to qg$	uu	+ p_+ − π^-	$(1-x)_7$ $(1-x)^7$	$(1-x)_5$ $(1-x)^5$
K^-	$qq \to qq, qg \to qg$	uu, ud	+ p_+ − π^-	$(1-x)_4$ $(1-x)^4$	$(1-x)_4$ $(1-x)^4$
	$q\bar{q} \to q\bar{q}, q\bar{g} \to \bar{q}g$	$uud\bar{s}$	+ p_+ − π^-	$(1-x)_8$ $(1-x)^8$	$(1-x)_{4-8}$ (**) $(1-x)^{4-8}$ (**)
	$gg \to gg, gq \to gq$	uud	+ p_+ − π^-	$(1-x)^0_6$ (*) $(1-x)^6$	$(1-x)^0_4$ (*) $(1-x)^4$

(* the straight forward prediction $(1-x)^{-1}$ is obviously not adequate)

(** depending on wether the sea quark belongs to the primordial wave function or not)

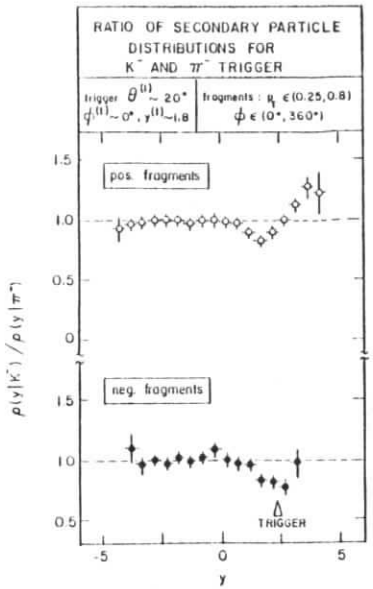

Fig. 7.65
As fig. 7.63, but for K^- and π^- triggers. From CCHK[307].

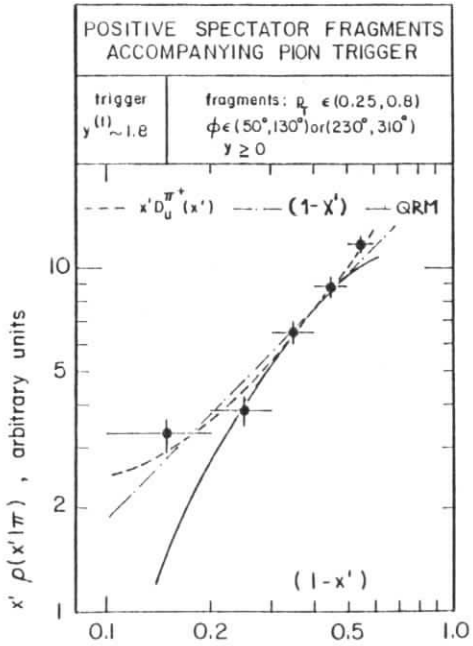

Fig. 7.66
Distribution in x' of positive fragments in the spectator accompanying large $p_\perp$ pions, compared to favored quark fragmentation functions $D_u^{\pi^+}$, the counting rule prediction $(1-x')$ and the prediction of the QRM, for a diquark-quark recombination. From CCHK[307].

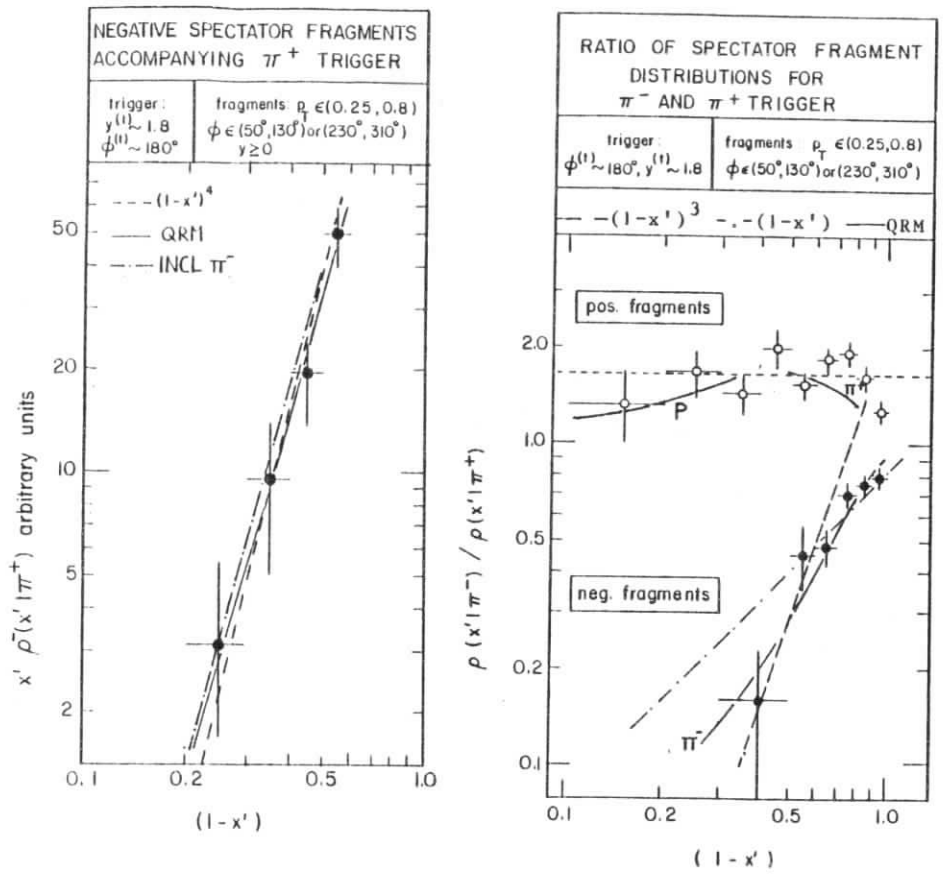

Fig. 7.67
Spectrum of negative particles in the spectator accompanying a π^+ trigger, compared to model predictions, and to the fully inclusive π^- spectrum. From CCHK [307].

Fig. 7.68
Ratios of distribution of spectator fragments in events with a π^-, and a π^+ trigger, respectivly. The QRM prediction for negative fragments refers to pions; for positive fragments, pions were assumed to dominate at small x', and protons at large x'. From CCHK [307].

For the K^- trigger, three possibilities have been considered
- scattering of a valence quark , followed by an unfavored fragmentation into a K^-
- scattering of a $\bar{s}$ sea quark
- scattering of a gluon

Fig. 7.66 shows the distribution of positive fragments in the spectator accompanying a pion trigger. The DCR prediction fits data reasonably well, whereas the QRM distribution drops slightly too fast at large x - an effect which had been observed already in lN interactions (fig. 6.30). As a less model dependent comparison, the quark fragmentation function $D_u^{\pi^+}$ is shown, assuming that the fragmentation of a quark into a meson will be similar to the fragmentation of a diquark into a baryon.

The spectrum of negative particles in the spectator accompanying a π^+ trigger is given in fig. 7.67. The shape of the spectrum coincides with the fully inclusive pion distribution in proton-proton collisions [369], and is reproduced by both QRM and DCR models.

To demonstrate the influence of the trigger charge the ratios of x' distributions for secondaries in the spectator jet accompanying a π^- trigger and a π^+ trigger are shown in fig. 7.68 for both positive and negative secondaries. As expected, there are less fast negative fragments in π^- triggered events than for π^+ triggers, proving that in the first case the valence d quark has been struck. The model calculations included in fig. 7.68 are straight forward as far as negative secondaries are concerned; the QRM model describes data well even at low x'. The prediction based on 'standard' DCR seems to be too steep at low x', but below x' ≈ 0.3 - 0.4 the model anyhow is not expected to hold. The QRM values for positive particles include three components: at low x', the ratio is dominated by π^+ production. At large x' the ratio is determined by the proton yields from

i) $ud \to p + X$ for trigger π^+
ii) $uu \to p + X$ for trigger π^-
iii) $uu \to \Delta^{++} + X$ " "
$\Delta^{++} \to p\pi^+$

Based on the direct terms i) and ii) alone, one expects the ratio plotted in fig.7.68 to increase with increasing x', since in the average the uu system has a larger momentum than the ud spectator. Contributions from iii) however increase the ratio to values larger than 1, in agreement with experiment. Note that the prediction is not sensitive to the assumption that all baryons are produced in their ground states.

The corresponding ratios of particles produced in association with a k^- and π^- trigger are shown in fig. 7.69. In the k^- events, positive spectator fragments are enhanced and the density of negative particles falls even steeper with increasing x than for a π^- trigger. This result is compatible with the counting rule prediction for scattering of strange sea quarks against quarks or gluons. It is however hard to accomodate these observations in the framework of a recombination model. Since the k^- contains no d quark, it seems impossible to imagine any scattering mechanism which picks up the valence d quark with the same efficiency than for π^- triggers. Without such a mechanism, the ratio shown in fig. 7.69 is predicted to increase with x', for negative secondaries!

Consider now events with a proton at large $p_\perp$. Classical QCD processes like quark and gluon scattering don't explain the comparably large yield of protons at transverse momenta up to a few GeV [326] (fig. 7.70), instead CIM contributions like quark-diquark or quark-baryon scattering have been suggested.[347]

Fig. 7.71 shows the density of positive fragments in the spectator accompanying a proton trigger. As for a pion trigger, the spectrum is similar to $D_u^{\pi^+}(x')$. The ratio of densities of positive and negative fragments is shown in fig. 7.72, it falls like (1-x'). This cannot be explained consistently by a quark recombination mechanism, since the net slope of the distribution of negative fragments is flatter than the distribution in x' of spectator d quarks,

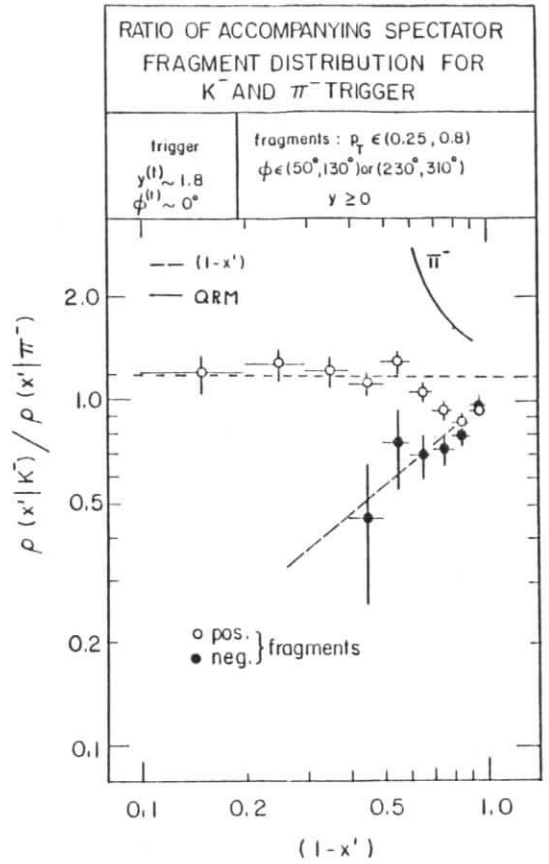

Fig. 7.69
As fig. 7.68 but for K^- and π^- triggers.

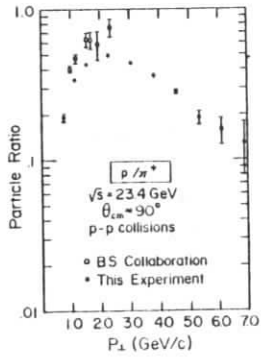

Fig. 7.70
Ratio of inclusive pion and proton cross sections as a function of $p_\perp$, measured at $\theta = 90^o$ at FNAL energies.[316]

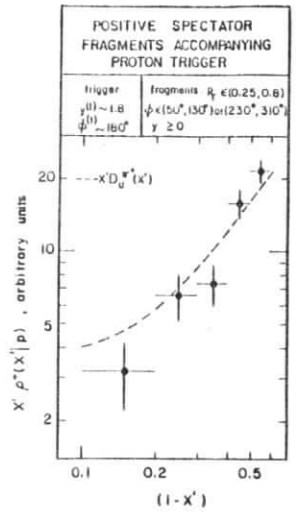

Fig. 7.71
Distribution in x' of spectator fragments accompanying a large $p_\perp$ proton trigger. From CCHK.[307]

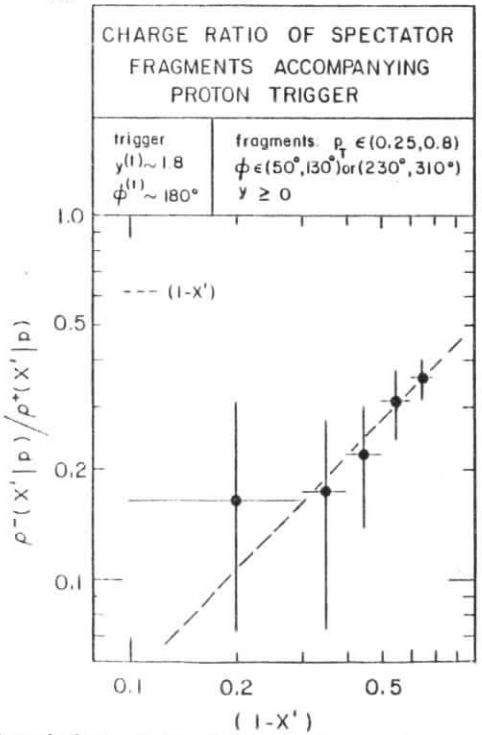

Fig. 7.72
Ratio of densities of positive and negative particles in the accompanying spectator in events with a large $p_\perp$ proton. From CCHK.[307]

as obtained for the π^+ trigger. DCR predictions are summarized in table 7.3, for cases where the trigger proton contains one, two, and three valence quarks of the projectile moving in the same longitudinal direction as the trigger particle.

Table 7.3

DCR predictions for spectator fragmentation function in events with a proton trigger

No. of valence quarks common to projectile and trigger	spectator	fragment charge	fragment type	predicted spectrum "standard DCR"
1	uu or ud	+	p	$(1-x')$
		−	π^-	$(1-x')^4$
2	u or d	+	π^+	$(1-x')$
		−	π^-	$(1-x')^2$
3	"gluon"	+	π^+	$(1-x')^3$
		−	π^-	$(1-x')^3$

Assuming that one of these mechanisms dominates, data are consistent with a diquark common to projectile and trigger. Such a configuration could e.g. result from scattering of a quasi-bound diquark out of the projectile. As an extended system, such a diquark will show a form factor

$$F(\hat{t}) \sim 1/(1+|\hat{t}|/0(1\ \mathrm{GeV}^2))$$

which explains why the ratio of inclusive proton to pion cross section drops at larger $p_\perp$ (fig. 7.70). A more natural

explanation however is that for large parton $k_\perp$, sometimes the spectator and the "active" quark exchange their roles, and that a large $p_\perp$ proton trigger favors such configuration due to the trigger bias. For a parton $\langle k_\perp \rangle$ of ~ 800 MeV, this process qualitativly describes to measured cross sections.[370)]

Let me summarize so far: using the standard dimensional counting rules, the shape of particle spectra in the accompanying spectator can be described. The quark recombination model using a Kuti-Weiskopf matrix element fits the distribution of spectator mesons in events with pion triggers quite well, but fails drastically for "exotic" large $p_\perp$ particles like k^- or protons. There are two possible reasons for this failure.

a) The Kuti-Weisskopf model for the proton wave function makes a somewhat artifical distinction between valence quark and sea quark matrix elements. It may happen that although the model accounts for correlations between valence quarks, it underestimates the correlation between a valence quark and a fast sea quark.

b) In the QRM the fragments reflect the instantaneous distributions of quarks at the moment of the scattering. There, the spectator is far from its equilibrium; after scattering a quark at x = 0.3, 70% of the spectator momentum turn out to be carried by gluons, e.g.. Assuming that this system regaines its equilibrium before the fragmentations starts, the qualitative agreement with experiments can be improved. A quantitative fit has not been tried, since of course the matrix elements of quarks in the spectator state will differ from those used to describe the proton.

The quark gluon compton effect. One peculiar feature of the QCD description of hard scattering processes is that a major contribution to the inclusive meson cross section at $p_\perp$ = 2-3 GeV/c

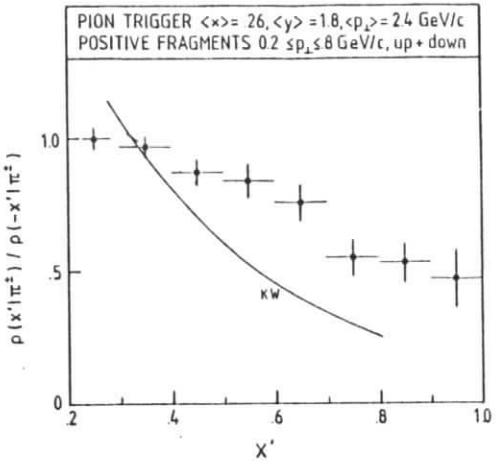

Fig. 7.73
Ratio of the densities of positive particles in the accompanying and in the away spectator jet, for events with a large $p_\perp$ meson trigger. The curve shows the ratio predicted by a recombination model , assuming that the accompanying and the away spectator contain 2 and 3 valence quarks, respectivly. From CCHK.

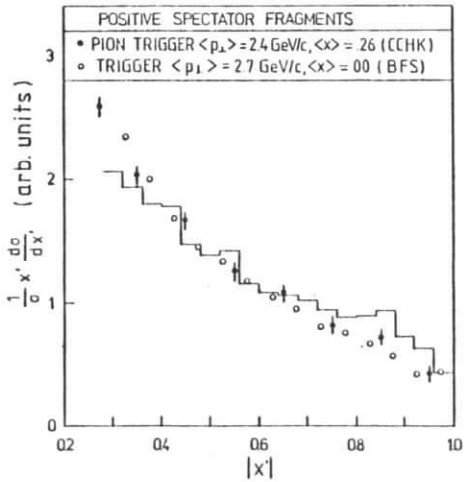

Fig. 7.74
Density of positive particles in the away spectator for a forward trigger at $x_\perp$ ~ 0.1 (•, from CCHK), for a central trigger at $x_\perp$ ~ 0.1, and for normal nondiffractive interactions (o and -, from BFS)[309)]

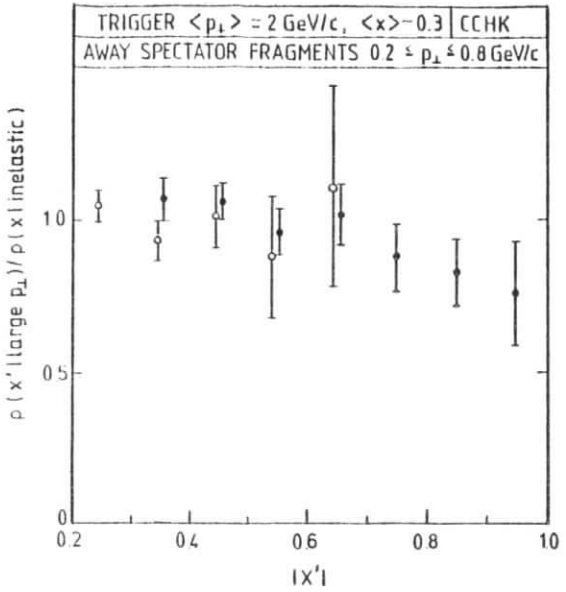

Fig. 7.75
Ratios of particle densities in the away spectator of large $p_\perp$ events and in normal nondiffractive events, for positive and negative secondaries, as a function of x'. From CCHK.

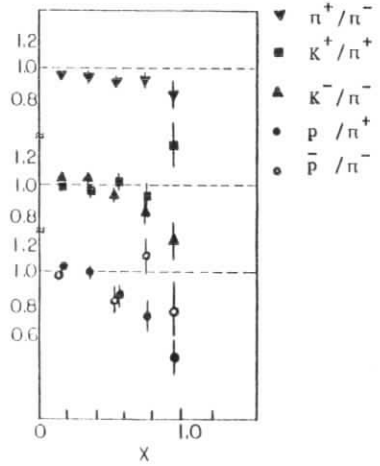

Fig. 7.76
Ratio of densities of positive spectator fragments for events with a large $p_\perp$ π^+/π^-, K^-/π^-, K^+/π^+, p/π^+ and $\bar{p}/\pi^-$ emitted at y = 0. From BFS.[309]

comes from quark gluon scattering.

The experimental investigation of this prediction suffers from the fact that there is no clear way how to identify gluon jets, and that indirect tests - e.g. by studying particle ratios in the away jet region - rely heavily on the ansatz for the gluon fragmentation function.

The investigation of spectator fragmentation offers a method to detect contributions from qg→qg subprocesses, which does not depend on the knowledge of $D_g^h(z)$. We know that a forward pion at large $p_\perp$ contains a valence quark which is missing in the accompanying spectator. For the subprocess qg→qg ("quark-gluon compton scattering") the spectator at rapidities opposite to the trigger particle still contains all three valence quarks. As a consequence, the fragmentation functions into protons will differ for the two spectators - of course a three quark uud system is more likely to produce fast protons, than a spectator diquark.

In fig. 7.73 the ratio of densities of positive fragments in the two spectators is plotted as a function of $|x'|$. The particle density in the accompanying spectator is seen to drop faster in x', as compared to the "away spectator". This is expected for qg processes; for pure qq or gg interactions the ratio should be constant. Also shown is a QRM calculation for the ratio of proton production by two and three-quark spectators. Refering to this model, data are consistent with a strong contribution of qg→qg processes to forward large $p_\perp$ meson production.

Consider now the fragmentation function of the away spectator. Fig. 7.74 shows the distribution $x'd\sigma/dx'$ of positive fragments in the away spectator. In addition, fragmentation spectra of spectators in events with a central trigger particle at $x_\perp = 0.1$ are desplayed. The QCD model predicts that there as well the majority of the spectators consist of the three initial valence quarks.[326] In fact the two distributions agree very well.

To have a model independent reference spectrum, one can rely on the observation that the main features of longitudinal spectra in normal inelastic events are described by a model where a gluon is exchanged between the two incident hadrons which then fragment.[371] Hence the longitudinal distribution of fragments will be identical for such events and for away spectators in large $p_\perp$ events, provided that quark gluon scattering dominates.

Fig. 7.75 shows the ratio of the two distributions for both positive and negative secondaries. In order to exclude diffractive events in the "normal inelastic" sample, a charged particle at $|y|<0.5$ was requested. For each charge state, the ratio of densities is independent of x' and is close to 1. This result also points towards a dominant contribution of qg→qg graphs in large $p_\perp$ particle production.

The consistency of this conclusion can be checked using BFS-data on correlations between the yield of fast forward particles and the flavor of a central large $p_\perp$ hadron (fig. 7.76). Consider e.g. the ratio of densities of forward positive particles associated with a π^+ and a π^- trigger. Even if the correlation, measured by the deviation from unity is increased by a factor 2 to account for the fact that the accompanying (-correlated-) spectator and the away (-uncorrelated-) spectator are mixed up, the effect is smaller than reported for a forward trigger (figs. 7.63 and 7.68). One concludes that valence quark scattering is not the only source for central large $p_\perp$ production. In any non-fusion model however the contribution from sea quark scattering is expected to be small - what stays are the gluons.

Note that the correlation for k^-/π^- triggers shown in fig. 7.76 does not agree with the effect displayed in fig. 7.69. This indicates that the mechanism of strange particle production depends on the region of phase space under consideration.

Particle correlations in spectator jets.

The short range correlations observed between hadrons emitted in normal inelastic hadron reactions are usually described in terms of a cluster model,[90,372,373] assuming that in a first stage of the interaction hadronic clusters with masses of about 1-1.5 GeV are produced. There is some evidence that a "cluster" is a synonym for a sum over the known vector and tensor meson resonances.[374]

The mean decay multiplicity and the width of the correlation induced by cluster decay are characteristic and energy independent features of low $p_\perp$ interactions.

To investigate such short range rapidity correlations among spectator fragments, the perturbation by particles from the two jets at large $p_\perp$ has to be minimized. To achieve this goal the CCHK group[194,368] studied events were both the towards and the away jet are in the same rapidity hemisphere, at rapidities $y<-0.7$. The jet rapidities are taken as the rapidity of the trigger particle and as the rapidity of the fragment with largest $p_\perp$ in the away jet region.

Correlations were studied among spectator fragments at positive rapidities. Fig. 7.77 shows the two particle density correlation

$$C'(y_1|y_2) = \rho(y_1|y_2) - \rho(y_1)$$

for $y_2 = 2$ and $y_2 = 4$. The correlation function $C'(y_1|y_2)$ describes the change in particle density at y_1 for events which have a particle at y_2, as compared to the inclusive rapidity distribution. C' is closely related to the correlation function C defined by eqn. (4.47).[372] From fig. 7.77 a strong short range correlation is evident. Both size and width of the correlation essentially agree with the corresponding distributions obtained in ordinary nondiffractive proton-proton collisions at the same cms energy.[372]

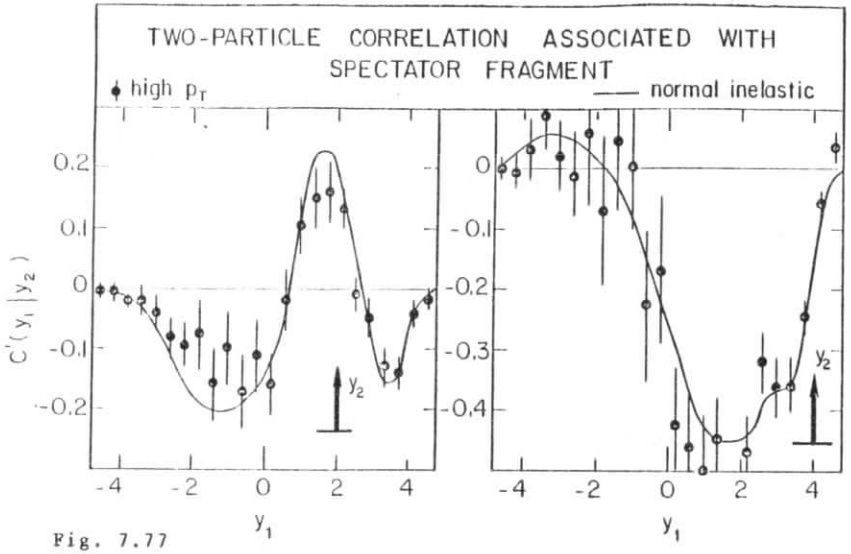

Fig. 7.77
Two particle density correlation $C'(y_1|y_2)$ for spectator fragments in large $p_\perp$ events, for two rapidities $y_2 = 2$ and $y_2 = 4$. The full lines show the corresponding distributions in normal inelastic events. From CCHK[368].

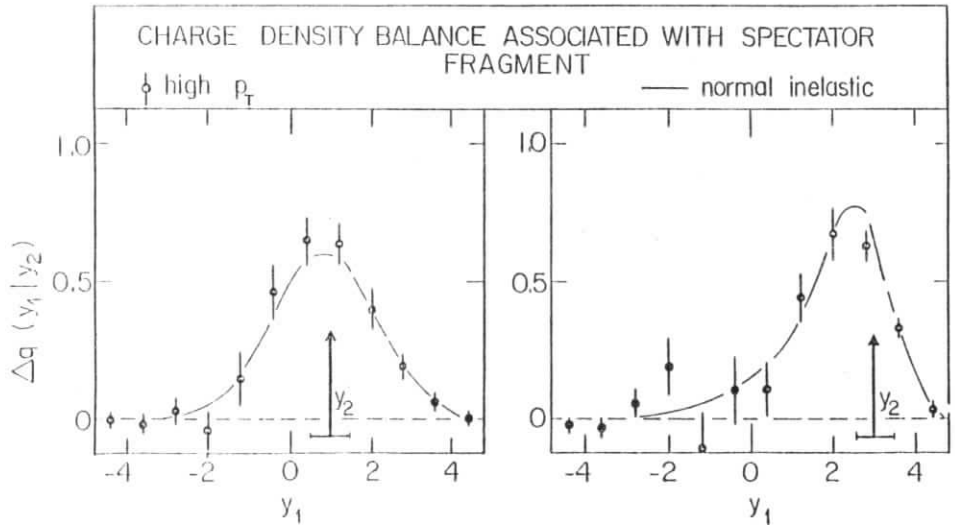

Fig. 7.78
Associated charge density balance $\Delta q(y_1|y_2)$ for spectator fragments as a function of y_1, for $y_2 = 2$ and $y_2 = 4$. Full lines show the corresponding distributions obtained in normal inelastic events. From CCHK.[368]

In fig. 7.78, the charge balance $\Delta q(y_1,y_2)$ is plotted as a function of the rapidity y_1. $\Delta q(y_1,y_2)$ (s. fig. 7.50) measures where in rapidity the charge of a particle selected at y_2 is balanced. Charge is seen to be conserved locally in phase space, like in normal nondiffractive hadron reactions.[372]

The similarity of correlations in inelastic events at low $p_\perp$ and in spectator fragmentation at large $p_\perp$ suggest that the same mechanism of fragmentation, or confinement acts, supporting the hypothesis of jet universality in its most general sense. Moreover, the observed correlations are in qualitative agreement with the preconfinement concept in QCD, which states that during the evolution of the rapidity plateau color singlet clusters with masses of the order 1 GeV are created. From parton diagrams describing jet formation via sucessive branching (fig. 5.6) one learns that these states tend to be flavor neutral. Assuming that such clusters decay without a large reshuffling of quark lines one immediately predicts both size and width of the observed correlations, and explains the observed local conservation of charge.

7.5 Summary

The distribution in phase space of secondaries in hadron-hadron interactions with large $p_\perp$ particles is consistent with the four jet structure characterizing a basic two body parton-parton scattering. The main features of both inclusive spectra and particle ratios at large $p_\perp$ are described in the QCD model, where quark-quark, quark-gluon and gluon-gluon subprocesses contribute. Especially at medium $p_\perp \approx 2\cdots5$ GeV/c, scale breaking effects and corrections due to parton $k_\perp$ have to be taken into account.

Significant contributions from constituent interchange processes, like $q\bar{q} \to M\bar{M}$, or $qM \to q'M'$ are excluded.

The properties of the jets at large $p_\perp$ agree with those of quark jets observed in e^+e^--annihilations, except for a possible

increase of the plateau height. There is no clear evidence for the presence of gluon jets with fragmentation functions markedly different from quark fragmentation. However, based on the experience gained from the study of T decays, such a difference is not expected to show up at jet momenta below 5···10 GeV.

In agreement with QCD predictions, the quantum numbers of partons at large $p_\perp$ are essentially uncorrelated, proving that no flavors are exchanged in the subprocess. Only for production of "exotic" particles which cannot result from favored fragmentation of a scattered valence quark, certain correlations are observed; however the experimental situation is still ambigious.

A further test of the QCD model was obtained by studying spectator fragmentation. It is shown, that in proton-proton reactions with a forward large $p_\perp$ π^+ and π^-, a u- and d-quark, respectivly, is scattered out of the proton moving in the same longitudinal direction as the pion, proving further that the underlying parton-parton cross section is strongly peaked forward.

There are strong indications that the spectator opposite in rapidity to the large $p_\perp$ particle still contains all three initial valence quarks.This observation fits into the QCD model, where forward large $p_\perp$ mesons are likely to be produced by scattering of a fast valence quark against a slow gluon.

A comparison of $p_\perp$ distributions and two particle correlations in the spectator region with those obtained in normal inelastic events proves, that similar mechanisms of fragmentation act in both cases.

8. Hadron-hadron interactions at low $p_\perp$

Motivated by the sucess of the quark-parton model in the description of deep inelastic processes, one is tempted to apply this picture to normal inelastic hadron interactions as well.

Many of the general aspects of low $p_\perp$ hadron interactions have been referenced already in chapters 2 and 7

- the secondaries form jets around the collision axis
- similar to the jets observed in lepton induced reactions, these jets consist of a fragmentation region carrying the quantum numbers of the incident particle, and of a plateau region. The retention of quantum numbers like charge is illustrated in fig. 8.1, where particle density and charge density distributions per event are shown as a function of the rapidity y, for pp reactions at $\sqrt{s}$ = 52 GeV[194].
- the s-dependence of particle spectra is described by the concept of limiting fragmentation [2,47]; inclusive spectra in the fragmentation region scale in Feynman x, resp. in $x_R = 2E/\sqrt{s}$. With increasing s, the length of the plateau increases, but its other characteristics essentially stay unchanged (fig. 8.2).
- inclusive fragmentation spectra factorize in a sense that at high energies beam and target fragmentation depend only on the type of beam and target particle, respectivly. This is visualized in fig. 8.3.
- transverse momenta with respect to the collision axis are limited; mean transverse momenta are of the same size as the nonperturbative component of $p_\perp$ in reactions at large momentum transfers.

All this is precisely what is expected in parton models where fragmentation spectra are related to the distribution of valence quarks in the incident particles.[13-15] In the

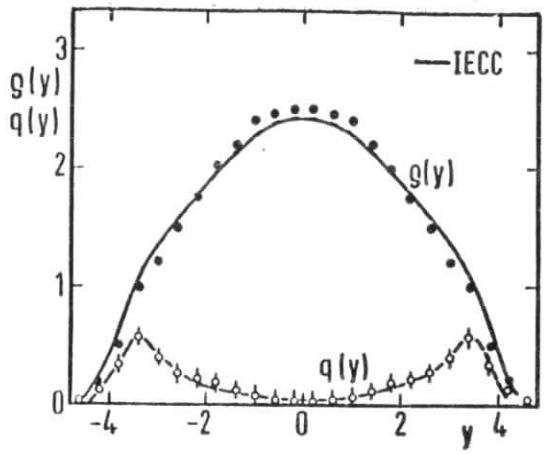

Fig. 8.1
Particle- and charge density in high multiplicity proton-proton reactions at $\sqrt{s}$ = 52 GeV, as a function of the rapidity y.
From CCHK[194].

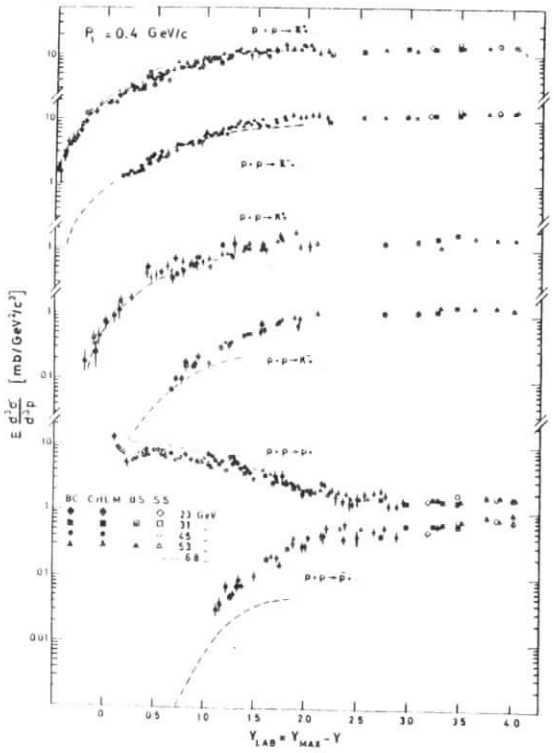

Fig. 8.2
Inclusive distributions of particles produced in proton-proton interactions at $\sqrt{s}$ = 6.8 to 53 GeV, plotted as a function of $y_{MAX} - y = -\ln x$ at fixed $p_\perp$.[74]

following section, we shall concentrate on the main characteristic of parton processes - the x distribution of fragments.

8.1 Longitudinal fragmentation spectra

To apply models like DCR or QRM to reactions at low $p_\perp$, one has to identify the basic interaction which gives rise to the fragmentation. In deep inelastic scattering the process initiating the fragmentation is well known: a large momentum transfer leads to a separation of color carriers in space.

The existence of a rapidity plateau connecting the fragmentation regions of low $p_\perp$ events indicates that in the initial interaction "something" is exchanged between the incident hadrons which gives rise to a long range force. The most natural candidate for this "something" is color. Within the general concept of QCD there are two mechanisms which could provide a color exchange

- color octet, vector gluon exchange (fig. 8.4a)[182,184,168]
- color triplet quark exchange, resp. quark-antiquark annihilation (fig. 8.4b)[4,100,15]

The gluon exchange mechanism was the starting point for the Pomeron model of Low [182] and Nussinov[184] and has the advantage of automatically generating a constant high energy cross section.

The quark exchange, or annihilation mechanism is the QCD equivalent of Feynmans wee parton exchange[4].

The quark exchange model yields total cross sections rising as ln S for sea-quark-sea-quark interactions, and constant cross sections for valence-quark-sea-quark reactions.[233] Processes like valence-quark-valence-quark fusion (e.g. in πN reactions) give a negligible contribution to the total high energy cross section, since the valence wave function of beam and target nearly don't overlap.

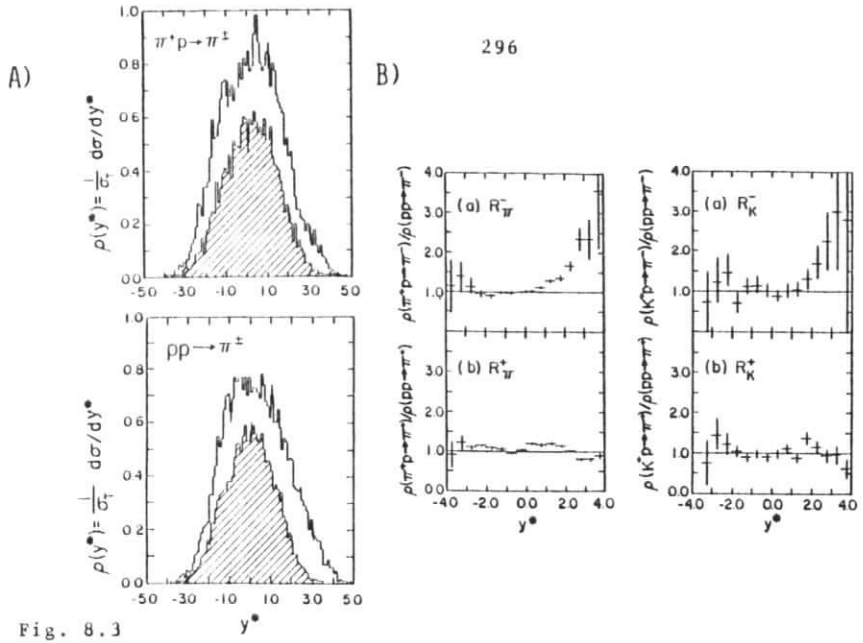

Fig. 8.3

a) Particle density per event $(1/\sigma)(d\sigma/dy)$ as a function of the cms rapidity y for $\pi^+p \to \pi^+, \pi^-$ (shaded) and $pp \to \pi^+, \pi^-$, at $\sqrt{s} = 14$ GeV.

b) Ratios of the positive and negative pion densities, respectivly, for $\pi^+p \to \pi+X/pp \to \pi+X$ ($R^\pm_\pi$) and for $K^+p \to \pi+X/pp \to \pi+X$ ($R^\pm_k$). Particle densities in the target fragmentation regions ($y < 0$) are independent of the type of the beam particle.

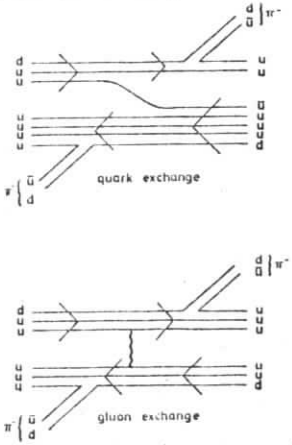

Fig. 8.4

Proton-proton interactions initiated by a) quark exchange
b) gluon exchange

The diagrams show the minimum graphs describing the production of two fast pions at opposite rapidities.[233]

A possibility to distinguish between the quark and gluon exchange mechanisms has been proposed by Brodsky and Gunion,[233] and is based on the ansatz that particle spectra at large x are determined by those quark diagrams containing the minimum number of quark lines; according to the DCR e.g. each additional spectator line damps the x distributions of fragments by at least (1-x) (see chapter 6.6). Consider now the reaction $pp \to \pi+\pi+X$, with two fast pions at opposite rapidities. The relevant minimal diagrams are displayed in fig. 8.4. One recognizes that for gluon exchange the production mechanisms are identical for both fragmentation regions; the pion momenta are not correlated. For a quark exchange to occur, one of the protons has to be in a higher Fock state containing sea quarks. In the framework of counting rules, the momentum sharing among at least five quarks results in a damping of quark structure functions and consequently of the pion spectra at large x; the production rates for fast mesons in opposite fragmentation regions are expected to show a pronounced anticorrelation.[233]

The corresponding predictions based on the recombination model are less evident, and depend on the choice of the multiquark wave function. Nevertheless it is evident that in a state a described by the upper half of fig. 8.4a), where one of the valence quarks is forced to be at low x, the mean momentum of the remaining valence quarks is larger than in a state as given by the lower part of fig. 8.4a).

Correlations between two fast pions have been studied at the ISR for $\pi^+\pi^+, \pi^+\pi^-$, and $\pi^-\pi^-$ combinations.[371] Fig. 8.5 shows the correlation function

$$R = (\sigma_{tot} \frac{d^6\sigma}{d^3\vec{p}_1 d^3\vec{p}_2}) / (\frac{d^3\sigma}{d^3\vec{p}_1} \frac{d^3\sigma}{d^3\vec{p}_2}) \qquad (8.1)$$

as a function of the Feynman x of the pion with momentum $\vec{p}_2$, for different momenta of pion 1. Full and dashed-dotted lines

indicate DCR and QRM predictions for quark exchange, respectivly. Dashed lines refer to uncorrelated emission after a gluon exchange. Obviously any subtantial contribution due to quark exchange is ruled out.

We are now prepared to predict single inclusive fragmentation spectra using the recombination model, or dimensional counting rules.

For a quantitative comparison, also collective excitation and dissociation of the incident hadrons has to be taken into account, besides the "quasiperturbative" processes given by the QRM, e.g.[233,237]. Conventionally, such processes are described in the triple Regge scheme. One obtains for A + B → C + X

$$E\frac{d^3\sigma}{dp^3} \simeq (1-x_c)^{1-2\alpha_{A\bar{C}}} (t_{AC}) \qquad \text{for } x_c \to 1 \qquad (8.2)$$

$\alpha_{A\bar{C}}(t)$ is the leading Regge trajectory identified in the exclusive reaction A + H → C + H'. The x - and $p_\perp$ - dependence of σ given by eqn. (8.2) allows to identify triple Regge - and parton contributions experimentally: for triple Regge terms, the slope in $p_\perp$ of $Ed^3\sigma/dp^3$ increases with increasing x, whereas for incoherent parton processes one expects factorisation of the type

$$E\frac{d^3\sigma}{dp_c^3} \sim (1-x_c)^n g(p_\perp) \qquad (8.3)$$

Triple Regge contributions turn out to be important[233,237] for reactions like

$$\begin{array}{lll} & A + B \to A' + X & \\ \text{e.g.} & p + p \to p + X & \\ & \pi + p \to \rho + X & \end{array} \qquad (8.4)$$

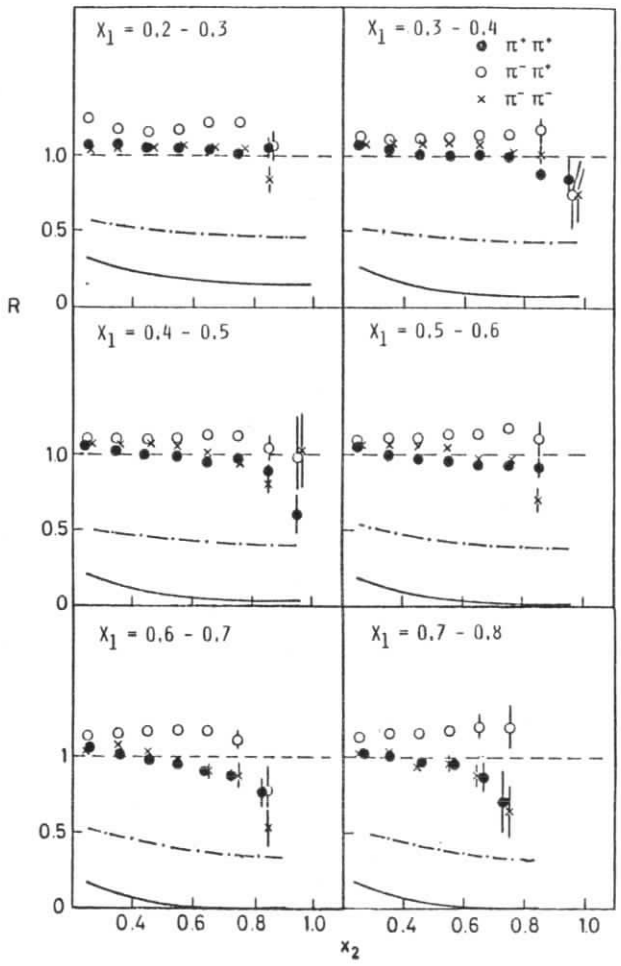

Fig. 8.5
Correlation coefficient R for emission of fast opposite pions, plotted vs x_2 at fixed x_1, for $\pi^+\pi^+$, $\pi^+\pi^-$, and $\pi^-\pi^-$, in pp interactions at $\sqrt{s}$ = 63 GeV.[371] The full line shows a prediction for quark exchange based on dimensional counting rules (s. 6.6), the dashed-dotted line refers to quark exchange and quark recombination, using a Kuti-Weisskopf matrix element (s. 6.5). The dashed line corresponds to gluon exchange.

where A and A' contain the same quarks. In quantum number exchange reactions, Regge terms are sizeable only at large $x \gtrsim 0.9$ [237]. Thus, reactions of the type (8.4) are omitted in the following discussion; the x range used is restricted to $0.3 \lesssim x \lesssim 0.8$. The lower x cut excludes central production mechanisms and reduces effects due to resonance decays.

The data quoted in the following discussion come from experiments performed at cms-energies between 14 and 63 GeV [264,296,297,299,369]. To compare with DCR predictions, n and g ($p_\perp$) is used as determined from fits of eqn. (8.3) to the data. At FNAL energies, it is preferable to use the scaling variable $x_R = 2E/\sqrt{s}$ instead of Feynman x, since the scaling limit was shown [263] to be approached faster in x_R. For the reactions considered, no significant deviations from factorisation in x and $p_\perp$ (eqn. 8.3) were seen [299,369].

The data available are summarized in figs. 8.6 a)-c). Since in most models the exponent n essentially depends only on the type - meson or baryon - of the beam particle, on the type of the beam fragment, and the number of common valence quarks, data e.g. on

$$\pi^+ N \to K^+ + X$$
$$\pi^- N \to K^- + X$$
$$K^+ N \to \pi^+ + X$$
$$K^- N \to \pi^- + X$$

are averaged over. The error bars given indicate the statistical error, resp. the rms. spread of n when averaged over several, theoretically identical processes, whatever is larger. The motivation for the second choice is that the spread in n measures the influence of finite mass effects, resonance decays and spill over from the target fragmentation region, and thus indicates the inherent limitations of such simplifying models.

The nomenclature is as follows:

$$H \underset{(m)}{\to} H'$$

H is an incident hadron, and H' is a particle out of the corresponding fragmentation region. m is the number of quarks common to H and H'.

Fig. 8.6a) presents values of n for meson production by meson and baryon beams, fig. 8.6 b) displays the corresponding values for baryon production. Finally, the results on spectator fragmentation in high $p_\perp$ reactions are shown in fig. 8.6 c).

Theoretical predictions are given for three different models.

a) Quark recombination (s. 6.5) enables very detailed predictions for processes where the fragment contains one or more valence quarks of the incident hadron; however the knowledge of the corresponding valence structure function is required. This condition restricts the predictive power of the model to processes where fast mesons are produced. QRM predictions are shown in more detail in fig. 8.7, for $pp \to \pi^\pm + X$ and $pp \to K^+ + X$. [237] Here the maximum amount of information is available both theoretically and experimentally. The shape of particle spectra is extremely well reproduced; questions concerning the absolute normalisation have been discussed in chapter 6.5. In fig. 8.6, definite predictions of the QRM are shown as black triangles, whereas values relying on the specific choice of the Kuti-Weisskopf structure function are given by open triangles.

b) Counting rules for pointlike emission (s. 6.6, eqn. 6.47). This version of counting rules is based on the same philosophy as the QRM: the distribution of fragments reflects the instantaneous distribution of quarks at the moment of the interaction. The predicted power n may be increased by one unit due to spin or isospin effects, e.g. for $pp \to \pi^- + X$ as compared to $pp \to \pi^+ + X$. The full bars shown in fig. 8.6 include this uncertainity.

c) "Standard" counting rules (s. 6.6), eqn (6.40). Here it is assumed the an equilibrium state containing all final state quarks preceeds particle emission. (open bars in fig. 8.6)

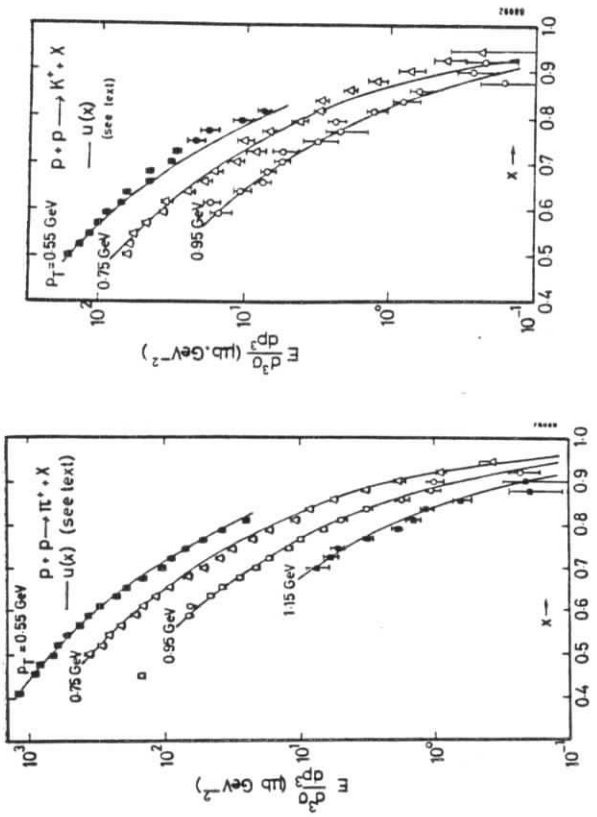

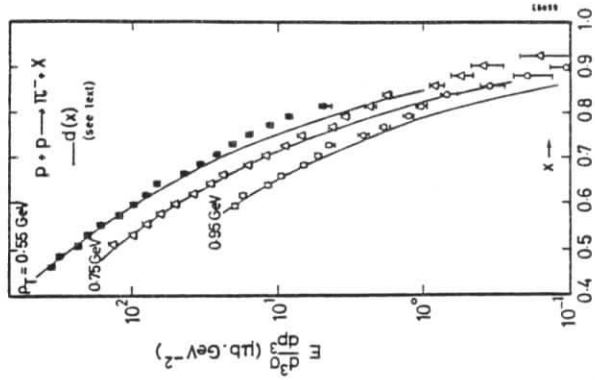

Fig. 8.7 Inclusive $\pi^{\pm}$ and K^{+} cross sections at ISR energies, compared to predictions based on the QRM. Deviations for $X \gtrsim 0.9$ result from triple Regge contributions.[237]

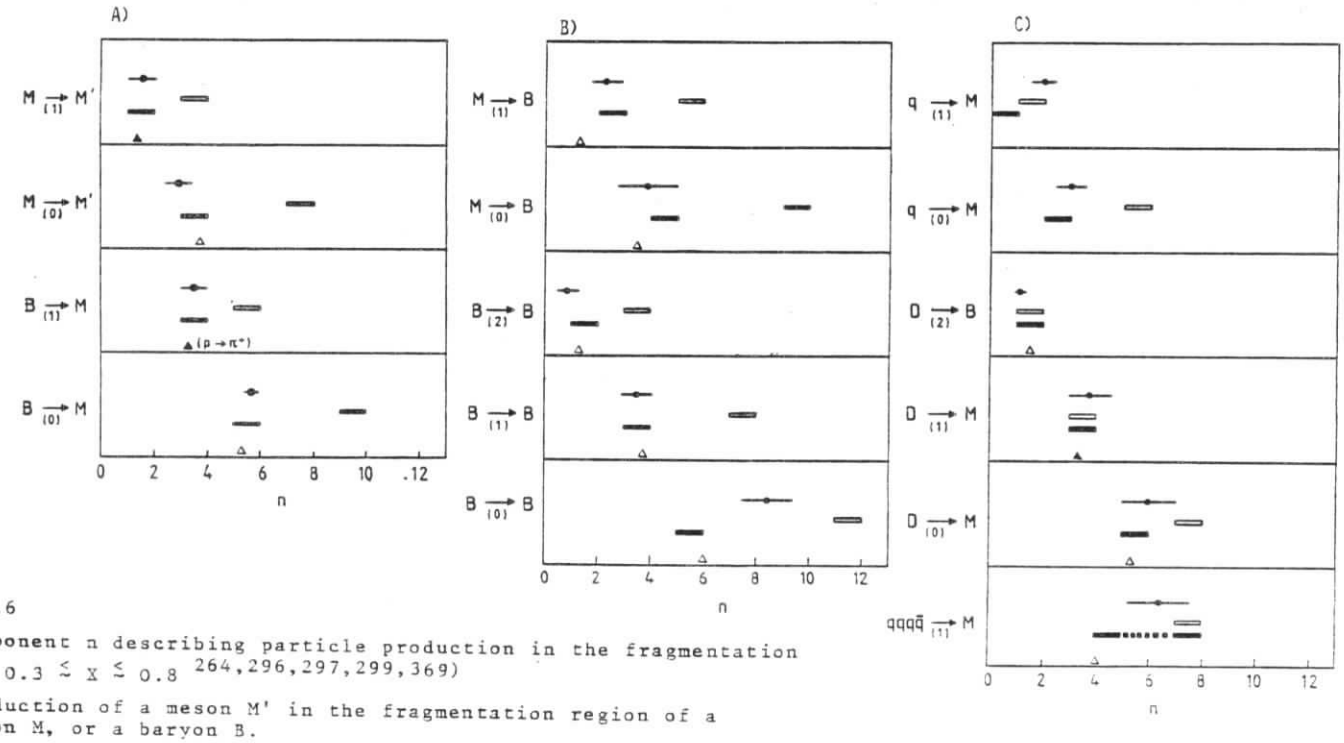

Fig. 8.6

The exponent n describing particle production in the fragmentation region $0.3 \lesssim X \lesssim 0.8$ [264,296,297,299,369]

a) production of a meson M' in the fragmentation region of a meson M, or a baryon B.

b) production of a baryon B

c) production of quark- and spectator fragments in reactions involving large momentum transfers ("D" denotes a diquark system)

m is the number of common valence quarks of initial hadron and fragment. Predictions of QRM, "standard" and "pointlike" DCR are shown as triangles, open and closed bars, respectivly.

Fig. 8.6 proves that these standard counting rules clearly disagree with data from low $p_\perp$ hadronic interactions. Both "pointlike" counting rules and the quark recombination model are in reasonable agreement with low $p_\perp$ data and with results on spectator fragmentation in events with large momentum transfers, with the following exceptions

- the distributions of antibaryons in hadronic collisions is predicted too flat.
- the QRM predicts $qqq\bar{q}$ $(\vec{1})$ M to be flatter than $D_{(\vec{8})}M$, in contradiction with the experiment (fig. 7.69)
- in events with a large $p_\perp$ proton the distribution of negative fragments is flatter than the distribution of d-quarks in the proton, as measured e.g. in events with a large $p_\perp$ π^+ trigger

Part of these discrepancies could be removed by choosing a more complicated wave function for the proton, which includes dynamical correlations between valence quarks. Especially the two last points however indicate that a certain redistribution of parton momenta occurs in between the hard scattering and the fragmentation; for definite conclusions more precise data are needed.

Do these models also describe the fragmentation of quark, or gluon jets at large Q^2?

Fig. 8.6 c) demonstrates that "pointlike" counting rules fail to predict the favored fragmentation function for quark jets; the prediction $(1-x)^0 \cdots (1-x)^1$ is flat in x compared to the measured spectra close to $(1-x)^2$ for $0.3 \lesssim x \lesssim 0.8$, which is the same range of x as used in the discussion of spectator fragments.

An explanation for this discrepancies is given by scale breaking effects: in the evolution of a quark jet, the formation of final state hadrons will occur at some scale $Q_o^2 \simeq 1\ \mathrm{GeV}^2 \ll Q^2$. The fact that hadron fragmentation is described by the QRM using the structure functions obtained in deep inelastic reactions indicates

$$Q^2 \gg Q_o^2 > \Lambda^2 \qquad (8.5)$$

where Λ is the QCD scale parameter. In the fragmentation from Q^2 to Q_o^2 partons are generated, which increase the number of spectator fields as compared to the minimum number: (see eqn 6.46)

$$zD(z) = (1-z)^{n_{eff}(Q^2)-1}$$

Recently it has been tried to quantify these ideas within the framework of the QRM[261]. QCD (eqn 5.30) is used to describe how a quark at Q^2 fragments into a "valence quark" and a number of "sea" partons of size Q_o^2. This evolution is usually characterized by the parameter ξ (see eqn. 5.35)

$$\xi \sim \ln\left(\frac{\alpha_s(Q_o^2)}{\alpha_s(Q^2)}\right) \sim \ln\left(\frac{\ln(Q_o^2/\Lambda^2)}{\ln(Q^2/\Lambda^2)}\right)$$

Fig. 8.8 shows how the parton density in a quark jet changes from $\delta(1-x)$ at $\xi = 0$ to a function decreasing with increasing x for large ξ.[121] Final state mesons are formed by recombination according to eqn 6.20

$$zD(z) = \int \frac{dz_q}{z_q} \frac{dz_{\bar{q}}}{z_{\bar{q}}} G(z_q, z_{\bar{q}}, Q_o^2) R(z_q, z_{\bar{q}}, z)$$

where $G(z_q, z_{\bar{q}}, Q_o^2)$ is the two parton density within the jet. To deal with gluons, one may e.g. [261] use the prescription "at Q_o^2 all gluons convert into quark-antiquark pairs".

Practical applications of this scheme suffer from the fact that the shape of $G(z_q, z_{\bar{q}}, Q_o^2)$ depends crucially on the unknown ratio Q_o/Λ, and that for the region of interest, $Q_o \sim 1$ GeV the perturbative expansion starts to become unreliable.

In ref. 261 $Q_o/\Lambda \simeq 1.1$ is used as extracted from deep inelastic lN scattering (in a model dependent way), and an "effective" Λ

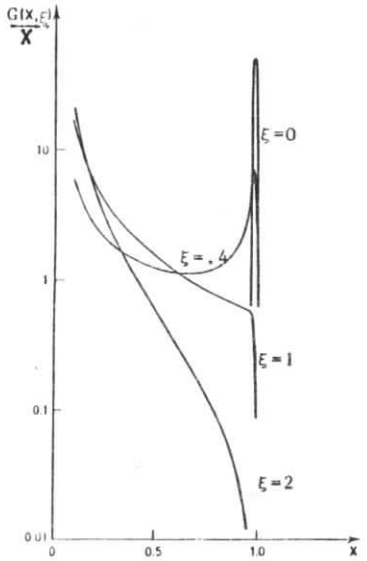

Fig. 8.8
Single parton (quark, antiquark, + gluon) inclusive distribution in a quark jet for different values of $\xi \sim \ln(\alpha_s(Q_o^2)/\alpha_s(Q))$. The curves are calculated using an approximation to the exact QCD matrix elements (eqn 5.23).[121]

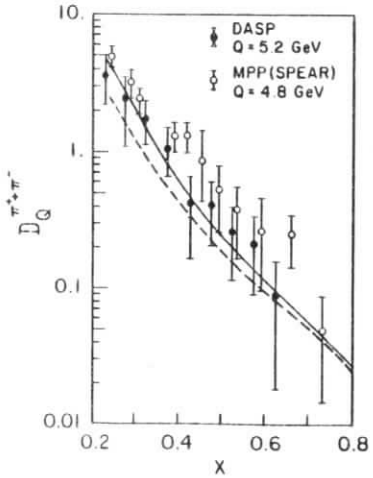

Fig. 8.9
Absolute QRM predictions for quark fragmentation functions with (—) and without (- - -) vector meson contributions.[261]

is chosen to account for higher order corrections.

Although this procedure is somewhat questionable, the results (fig. 8.9) look encouraging, especially if vector meson production is taken into account.

9. Summary

The existence of jet like structures is shown to be a general characteristic of hadronic final states in reactions of elementary particles at high energies. The quark parton model suggests that these jets result from the fragmentation of colored partons. Although the partons produced in various reactions may differ in their quark contents, in their color state, and in the momentum transfer Q^2 at which they are probed, the resulting jets are expected to exhibit many common features.

In the present work, properties of jets observed in
- e^+e^- annihilations into hadrons
- hadronic decays of the T meson
- deep inelastic lepton-nucleon scattering
- hadron-hadron reactions with large $p_\perp$ particles
- normal inelastic hadronic reactions

are compared, and phenomenological approaches to describe their properties are discussed.
In the parton model, the space-time evolution of a jet may be visualized as an "inside-outside" cascade: the color charge of the active parton induces a polarization cloud, which follows the parton and finally neutralizes its color.

It is shown that phenomenological models for jet fragmentation, like the Feynman-Field algorithm, can be derived from this concept.
The model of "inside-outside" cascades is further supported by QCD calculations, where parton fragmentation is treated as a successive branching into partons of smaller mass, yielding the same space-time structure of jets as the very naive parton model.

According to these concepts, a jet should consist of a fragmentation region, and a plateau region. Parton quantum numbers are essentially retained in the fragmentation region. Jets in different environments, and at different energies are related via scaling fragmentation functions, environmental independence of the fragmentation, and by the universality of the rapidity plateau.

Data on quark jets observed in e^+e^- annihilations and in lepton-nucleon interactions are consistent with these ideas. Small violations of the idealized concepts can be understood quantitativly as due to phase space effects at low energies, and due to QCD bremsstrahlung corrections at high energies.

In contradiction to QCD predictions, the investigation of gluon jets in T decays shows no evidence for a softening of fragmentation functions as compared to quark jets, and average multiplicities are very similar for both types of jets. However, parton fragmentation at these energies is governed by phase space effects rather than by asymptotical parton concepts.

In hadron-hadron interactions involving large momentum transfers, pairs of jets with opposite large transverse momenta are observed. Both longitudinal and transverse properties of these jets are essentially consistent with those of "standard" quark jets. This fact, as well as measurements of inclusive particle ratios at large $p_\perp$, favor QCD models, where quarks or gluons are scattered, as compared to constituent interchange mechanisms. The absence of correlations between the charge of a pion at large $p_\perp$, and the quantum numbers of the opposite recoiling parton proves further that parton scattering occurs through the exchange of flavor singlet fields, like gluons.

In such interactions, where a quark is scattered out of a hadron, or more general,where a current of large Q^2 interacts with a single parton, a colored spectator system is left over and fragments. In the present work, special emphasis is put on the investigation of spectator fragments, since only here the relation between the quark contents of a composed colored system and its fragmentation functions can be studied systematically.

Fragmentation spectra of diquark spectator systems produced in νN interactions are shown to be compatible with predictions based on counting rules (DCR) or the quark recombination model (QRM). Since the shape of fragmentation spectra characterizes the quark contents of the spectator, this provides a new method to determine the type of constituent subprocess occuring e.g.

in events with large $p_\perp$ particles.

This method has been applied to proton proton interactions; it is demonstrated that forward high $p_\perp$ pions are fragments of valence quarks scattered at small angles.

Similarly it is shown that forward large $p_\perp$ K^- and protons are likely to stem from scattered sea quarks, and diquarks, respectivly.

The investigation of the spectator opposite in rapidity to the high $p_\perp$ particle shows that this systems often contains all three initial valence quarks, indicating that one of the major subprocesses relevant for forward large $p_\perp$ particle production is the scattering of a fast valence quark against a slow gluon, as expected in QCD.

In an analogous way fragmentation models can be applied to hadron production at low $p_\perp$ in normal inelastic hadronic interactions, once the mechanism initiating the fragmentation is known. The absence of correlations between fast pions emitted in opposite rapidity hemispheres points towards a primary gluon exchange, as compared to flavor exchange mechanisms.

Fragmentation spectra of incident hadrons into mesons and baryons are consistent with the quark recombination picture, and with a "pointlike" version of counting rules.

There are indications that a combination of the perturbative evolution of parton densities in jets, as given by QCD, and of a recombination mechanism, provides a universal tool to understand parton fragmentation: the distribution of low "mass" partons within a jet of large Q^2 can be derived using QCD, resp. is given by the primordial parton distribution in reactions at moderate momentum transfers; the recombination principle tells how these quarks convert into hadrons.

1) J.D. Bjorken; Phys. Rev. 179 (1969) 1547
2) R.P. Feynman; Phys. Rev. Lett. 23 (1969) 1415
3) J.D. Bjorken; E.A. Paschos, Phys. Rev. 185 (1969) 1975
4) R.P. Feynman; Photon Hadron Interactions, Benjamin; New York (1972)
5) G.Hanson et.al.; Phys. Rev. Lett. 35 (1975) 196
6) P. Darriulat et.al.; Nucl. Phys. B 107 (1976) 429
7) CCHK Collab., M. Della Negra et.al.; Nucl. Phys. B 127 (1977) 1
8) B. Alper et.al.; Phys. Lett. 44B (1973) 521
9) M. Banner et.al.; Phys. Lett. 44B (1973) 537
10) F.W. Büsser et.al.; Phys. Lett. 46B (1973) 471
11) S.M. Berman, J.D. Bjorken, J. Kogut; Phys. Rev. D4 (1971) 3388
12) D. Amati, A. Stanghellini, S. Fubini; Nuovo Cimento 26 (1962) 896
13) W. Ochs; Nucl. Phys. B118 (1977) 397
14) K.P. Das, R.C. Hwa; Phys. Lett. 68B (1977) 459
15) S.J. Brodsky, J.F. Gunion; Phys. Rev. Lett. 37 (1976) 402
16) M. Gell-Mann; Acta Physica Austriaca, Suppl. IX (1972) 733
17) W.Bardeen, H. Fritzsch, M. Gell-Mann; Scale and Conformal Invariance in Hadron Physics, Wiley, New York (1973)
18) H.D. Politzer; Phys. Rep. 14 (1974) 129
19) T. Appelquist, H.D. Politzer; Phys. Rev. Lett. 34 (1975) 43
20) M. Dine, J. Sapirstein; Phys. Rev. Lett. 43 (1979) 668
21) G.P. Murtas; Proc. 19th Int. Conf. on High Energy Physics, Tokyo (1978)
22) G. Hanson; SLAC-PUB-2118 (1978) and Proc. Conf. on Gauge Theories and Leptons,Moriond (1978)
23) PLUTO Collab., Ch. Berger et.al.; Phys. Lett. 85B (1979) 413
24) TASSO Collab., R. Brandelik et. al.; DESY 79-61 (1979) and Phys. Lett. 89B (1980) 421
25) W. Chinowsky; Physica Scripta 19 (1979) 65
26) PLUTO Collab., Ch. Berger et.al.; Phys. Lett. 81B (1979) 410
27) TASSO Collab., R. Brandelik et.al.; Phys. Lett. 86B (1979) 243
28) S. Brand, Ch. Peyrou, R. Sosnowski, A. Wroblewski; Phys. Lett. 12 (1964) 57
29) H. Georgi, M. Machcek; Phys. Rev. Lett. 39 (1977) 1237
30) E. Farhi; Phys. Rev. Lett. 39 (1977) 1587

31) A. De Rújula et.al.; Nucl. Phys. B138 (1978) 387
32) J.D. Bjorken, S.J. Brodsky; Phys. Rev. D1 (1970) 1416
33) G. Hanson; Proc. 7th Int. Colloquium on Multiparticle Reactions, Tutzing (1976)
34) PLUTO Collab., Ch. Berger et.al.; presented at the 1979 Symp. on Lepton and Photon Interactions, Batavia
35) A. Raychaudhuri; Oxford 9/78 (1978)
36) G. Sterman, S. Weinberg; Phys. Rev. Lett. 39 (1977) 1436
37) H. Fesefeldt, W. Ochs, L. Stodolski; Phys. Lett. 74B (1978) 389
38) W. Ochs, L. Stodolski; Phys. Lett. 69B (1977) 225
39) G.C. Fox, S. Wolfram; Phys. Rev. Lett. 41 (1978) 1581
40) PLUTO Collab., Ch. Berger et.al.; Phys. Lett. 78B (1978) 176
41) H. Spitzer, Int. Report DESY PLUTO-79/03 (1979), unpublished and G. Flügge, DESY 79-26 (1979)
42) S.D. Drell, D.J. Levy, T.M. Yan; Phys. Rev. 187 (1969) 2159
43) S.D. Drell, D.J. Levy, T.M. Yan; Phys. Rev. D1 (1970) 1035, D1 (1970) 1616, D1 (1970) 2402
44) G. Hanson; SLAC-PUB 1814 (1976) and Proc. Conf. on High Energy Physics, Tblisi (1976)
45) DASP Collab., R. Brandelik et.al.; Nucl. Phys. B148 (1979) 189
46) Compiled by H. Wahl, CERN (private communication)
47) J. Benecke et.al.; Phys. Rev. 188 (1969) 2159
48) J. Whitmore; Phys. Rep. 10 (1974) 273
49) D.R.O. Morrison; Proc. 4th Int. Conf. on High Energy Collisions, Oxford (1972)
50) M. Bardadin, L, Michejda, S. Otwinowski, R. Sosnowski, Proc. Sienna Conf. on Elementary Particles, Vol. 1 (1963) 628 and
C. Bromberg et.al.; Nucl. Phys. B107 (1976) 82
51) R. Hagedorn; CERN 71-12 (1971)
52) B. Alper et.al.; Proc. 16th Int. Conf. on High Energy Physics, Batavia (1972)
53) D.L. Scharre et.al.; SLAC-PUB 2315 (1979), and Phys. Rev. Lett. 41 (1978) 1005
54) M. Piccolo et.al.; SLAC-PUB 2323 (1979)
55) P.A. Rapidis et.al.; Phys. Lett. 84B (1979) 507
56) V. Lüth et.al.; Phys. Lett. 70B (1977) 120

57) PLUTO Collab., J. Burmester et.al.; Phys. Lett. 67B (1977) 367
58) DASP Collab., R. Brandelik et.al.; Phys. Lett.80B (1979) 412
59) DASP Collab., R. Brandelik et.al.; Phys. Lett.70B (1977) 125, 70B (1977) 387, 70B (1978) 109, 76 B (1978) 361
60) A. Barbaro-Galtieri et.al.; Phys.Rev.Lett. 39 (1977) 1058
61) J.M. Feller et.al.; Phys. Rev. Lett. 40 (1978) 1677
62) W. Bacino et.al.; Phys. Rev. Lett. 41 (1978) 13, 42 (1979) 749
63) M. Piccolo et.al.; Phys. Rev. Lett. 39 (1977) 1503
64) T. Ferguson et.al.; Phys. Lett. 79B (1978) 161
65) PLUTO Collab., Ch. Berger et.al.; Phys. Lett. 86B (1979) 418
66) D.P. Barber et.al.; Phys. Rev. Lett. 43 (1979) 830
67) S.L. Wu, G. Zobernig; Z. Physic C2 (1979) 107
68) Y.L. Dokshitzer, D.I. Dyakonov; DESY L-Trans-234 (1979)
69) J. Kogut, L. Susskind; Phys. Rev. D9 (1974) 697
70) J. Ellis, M.K. Gaillard, G.G. Ross; Nucl. Phys. B111 (1976) 253, B130 (1976) 516
71) T.A. De Grand, Y.J. Ng, S.H.H. Tye; Phys. Rev. D16 (1977) 3251
72) G. Kramer, G. Schierholz, J. Willrodt; Phys. Lett. 79B (1978) 249, 80B (1979) 433
73) E. Laermann et.al.; PITHA 79/14 (1979)
74) P. Capiluppi et.al.; Nucl. Phys. B79 (1974) 189
75) L. Van Hove; Rev. Mod. Phys. 36 (1964) 655
76) A. Krzywicki; Nuovo Cimento 32 (1964) 1067
77) P.P. Srivastava, G. Sudarshan; Phys. Rev. 110 (1958) 765
78) R. Baier, J. Engels, H. Satz; Nuovo Cimento 28A (1975) 455
79) L. Foâ; Phys. Rep. 22 (1975) 1
80) K. Kajantie, V. Karimaki; Computer Phys. Comm. 2 (1971) 207
81) W. Kittel, L. Van Hove, W. Wojcik; Computer Phys. Comm. 1 (1970) 425
82) J. Engels, D. Satz; Phys. Rev. D17 (1977) 3015
83) H. Satz, Y. Zarmi; Nuovo Cimento Lett. 15 (1976) 421
84) W. Ernst, I. Schmitt; BI-TP-77/22
85) H. Satz; BI-TP-76/09
86) T. Atwood et.al.; Phys. Rev. Lett. 35 (1975) 704
87) M. Glück, E. Reya; Nucl. Phys. B130 (1977) 76 , B145 (1978)24
88) E.H. de Groot; Nucl. Phys. 48B (1972) 295
89) E.H. de Groot; thesis
90) F.W. Bopp; Riv. Nuovo Cimento 1 (1978) No.8, 1
91) K. Böckmann; BONN-HE-76-25 (1976)
92) A. Bialas, A. Kotanski; Acta Phys. Pol. B8 (1977) 779

93) R. Diebold; Proc. 19th Int. Conf. on High Energy Physics, Tokyo (1978)
94) E.H. De Groot, H. Satz; Nucl. Phys. B130 (1979) 257
95) A. Jabs; Nucl. Phys. B34 (1971) 177
96) K. Guettler et.al.; Phys. Lett. 64B (1976) 111
97) C. Kittel; Thermal Physics, John Wiley & Sons, New York (1969)
98) G. Cocconi; Phys. Lett. 49B (1974) 459
99) G.I. Kopylew, M.I. Podgoretzki; Sov. Nucl. Phys. 19 (1974) 434
100) R.P. Feynman; High Energy Collisions, edited by C.N. Yang et.al.; Gordon and Breach, New York (1969)
101) H. Fritzsch, M. Gell-Mann, H. Leutwyler; Phys. Lett. 47B (1973) 365
102) O.W. Greenberg; Phys. Rev. Lett. 13 (1964) 598
103) P. Hoyer et.al.; DESY 78-21 (1978)
104) P. Hasenfratz, J. Kuti; Phys. Rep. 40 (1978) 75
105) D.J. Gross; Proc. 19th Int. Conf. on High Energy Physics, Tokyo (1978) p. 486
106) J. Schwinger; Phys. Rev. 128 (1962) 2425 ; Theoretical Physics, Trieste Lectures (1962), I.A.E.A., Vienna
107) A. Casher, J. Kogut, L. Susskind; Phys. Rev. D10 (1974) 732
108) J.D. Bjorken; Current Induced Reactions, Springer Berlin (1976)
109) B. Andersson, G. Gustafson, C. Peterson; Z. Physik C1 (1979) 105
110) E. Eichten et.al.; Phys. Rev. Lett. 34 (1975) 369
111) B. Andersson, G. Gustafson, C. Peterson; Nucl. Phys. B136 (1978) 27
112) R.D. Field, R.P. Feynman; Nucl. Phys. B136 (1978) 1
113) A. Krzywicki, B. Petersson; Phys. Rev. D6 (1972) 924
114) J. Finkelnstein, R.D. Peccei; Phys. Rev. D6 (1972) 2606
115) L.M. Seghal; Proc. Int. Symp. on Lepton Photon Interactions at High Energies (1977)
116) G. Drews et.al.; Phys. Rev. Lett 41 (1978) 1433
117) S. Frautschi, A. Krzywicki; z. Physik C1 (1979) 43
118) S.J. Brodsky, J.F. Gunion; Phys. Rev. D19 (1979) 1005
119) R. Hartmann, BONN-HE-78-15 (1978)
120) P.C. Bosetti et.al.; Oxford 58/78 (1978)
121) P. Hoyer, NORDITA-79/33 (1979)
122) S.J. Brodsky, N. Weiss; Phys. Rev. D16 (1977) 2325
123) G.R. Farrar, J.L. Rosner; Phys. Rev. D7 (1973) 2747
124) R.N. Cahn, E.W. Colglazier; Phys. Rev. D9 (1974) 2658
125) J.L. Newmeyer, D. Sivers; Phys. Rev. D9 (1974) 2592

126) V. Barger, T. Gottschalk, R.J.N. Phillips; Phys. Rev. D14 (1976) 80, D16 (1977) 746
127) L.M. Seghal, P.M. Zerwas; Nucl. Phys. B108 (1976) 483
128) M. Suzuki; Phys. Lett. 68B (1977) 164
129) J.D. Bjorken; Phys. Rev. D17 (1978) 171
130) M. Suzuki; Phys. Lett. 71B (1977) 139
131) S. Pokorski; IFT/16/77 (1977)
132) R. Odorico, V. Roberto; Nucl. Phys. B136 (1978) 333
133) A. Ali et.al.; Phys. Lett. 83B (1979) 375, Z. Physik C2 (1979) 33
134) S.J. Brodsky, quoted in ref. 236)
135) G. Altarelli; Rivista Nuovo Cimento 4 (1974) 335
136) J. Kogut, L. Susskind; Phys. Rep. 8 (1973) 76
137) G. Altarelli, G. Parisi; Nucl. Phys. B126 (1977) 298
138) S.D. Drell; Phys. Rev. D1 (1972) 1716
139) R. Gatto; Phys. Rev. D7 (1973) 2524
140) G. Parisi; Phys. Lett. 43B (1973) 207, 50B (1974) 367
141) A. Ali et.al.; DESY 79-86 (1979)
142) J. Kogut, L. Susskind; Phys. Rev. D9 (1974) 3391
143) A. Casher, J. Kogut, L. Susskind; Phys. Rev. D9 (1974) 706
144) K.G. Wilson; Phys. Rev. Lett. 27 (1971) 690
145) K.G. Wilson; Phys. Rev. B4 (1971) 3174
146) A.M. Polyakov; Zh. Eksp. Teor.Fiz. 59 (1970) 542, 60 (1971) 1572
147) F.J. Yndurain; Phys. Lett. 74B (1978) 68
148) M. Glück, E. Reya; Nucl. Phys. B156 (1979) 456
149) J.G.H. de Groot et.al.; Z. Physik C1 (1979) 143
150) J.F. Owens; Phys. Lett. 76B (1978) 85
151) T.A. De Grand; Nucl. Phys. B151 (1979) 485
152) W. Furmanski et.al.; Nucl. Phys. B155 (1979) 253
153) K. Konishi, A. Ukawa, G. Veneziano; Phys. Lett. 78B (1978) 243
154) A. Kirschner; Phys. Lett. 84B (1979) 266
155) D. Amati, G. Veneziano; Phys. Lett. 83B (1979) 87
156) G. Veneziano; CERN TH-2691 (1979)
157) D. Amati; CERN TH-2650 (1979)
158) G.C. Fox, talk given at the Workshop on Quarks, Jets, and QCD, Hamburg, 1979
159) P. Cvitanović, P. Hoyer, K. Konishi; Phys. Lett. 85B (1979) 413
160) L. Caneschi, A. Schwimmer; Phys. Lett. 86B (1979) 179

161) H. Georgi, H.D. Politzer; Nucl.Phys. B136 (1978) 445
162) K. Konishi, A. Ukawa, G. Veneziano; Phys. Lett. 80B (1979) 259
163) R.K. Ellis, R. Petronzio; Phys. Lett. 80B (1979) 249
164) T. Kinoshita; J. Math. Phys. 3 (1962) 650
165) T.D. Lee, M. Nauenberg; Phys. Rev. 133 (1964) B 1549
166) B.G. Weeks; UM-HE 78-49 (1979)
167) K. Koller, T. Walsh; DESY 78/16 (1978)
168) J.F. Gunion, D.E. Soper; Phys. Rev. D15 (1977) 2617
169) S.J. Brodsky; Physica Scripta 19 (1979) 65
170) K. Shizuya, S.-H.H. Tye; Phys. Rev. Lett. 41 (1978) 787
171) M.B. Einhorn, B.G. Weeks; Nucl. Phys. B146 (1978) 445
172) H. Fritzsch; Phys. Lett. 74B (1975) 90
173) K. Koller, T. Walsh; Nucl. Phys. B140 (1978) 449
174) G. Eilam, M. Glück; Haifa Technion PH-79-20 (1979)
175) N.H. Fuchs; Phys. Rev. D14 (1976) 1912
176) A. De Rujula, H. Georgi, S.L. Glashow; Phys. Rev. D12 (1979) 147
177) P. Binétruy, G. Girardi; Phys. Lett. 83B (1979) 382
178) I.I.Y. Bigi; Phys. Lett. 86B (1979) 57
179) W. Furmanski; CERN TH-2664 (1979)
180) G.'t Hooft; Nucl. Phys. B72 (1974) 461
181) G. Veneziano; Nucl. Phys. B117 (1976) 519
182) F.E. Low; Phys. Rev. D12 (1975) 163
183) J.D. Bjorken; Phys. Rev. D7 (1972) 282
184) S. Nussinov; Phys. Rev. Lett. 34 (1975) 1286
185) M. Derrick et.al.; Phys. Lett. 88B (1979) 177
186) G.R. Farrar, J.L. Rosner; Phys. Rev. D10 (1974) 2226
187) D. Sivers; Phys. Rev. D15 (1977) 1306
188) S.J. Brodsky; SLAC-PUB-1937 (1977) and Proc. Symp. on Hadron Structure and Multiparticle Production, Kazimierz (1977
189) U. Ellwanger; Nucl. Phys. B154 (1979) 358
190) P.V. Landshoff; Phys. Lett. 66B (1977) 452
191) P.V. Landshoff, D.M. Scott; Nucl. Phys. B131 (1977) 172
192) J.F. Gunion, Phys. Lett. 88B (1979) 150
193) G. Veneziano, Proc. 19th Int. Conf. on High Energy Physics, Tokyo (1978)
194) W. Hofmann, Thesis, Karlsruhe 1977
195) G. Fontaine; Proc. GIF 78, Gif sur Yvette (1978)

196) J.H. Weis; Acta Phys. Pol. B9 (1979) 1051
197) D.F. Abbott, R.M. Barnett; SLAC-PUB-2325 (1979)
198) E.L. Berger; SLAC-PUB-2362 (1979)
199) R.K. Ellis et.al.; Phys. Lett. 78B (1978) 281 and CALT 68-684 (1978)
200) H.D. Politzer; Phys. Lett. 70B (1977) 430 and Nucl. Phys. B129 (1977) 301
201) D. Amati, R. Petronzio, G. Veneziano; CERN TH-2527 (1978)
202) N. Sakai; Phys. Lett. 85B (1979) 67
203) G. Altarelli et.al.; CTP 793 (1979)
204) R. Baier, K. Fey; BI-TP 79/11 (1979)
205) J. Bell et.al.; Phys. Rev. D19 (1979) 1
206) G. Drews et.al.; Phys. Rev. Lett. 41 (1978) 1433
207) I. Cohen et.al.; Phys. Rev. Lett. 40 (1978) 1614
208) N. Schmitz; MPI-PAE/Exp.El. 80 (1979)
209) W.G. Scott et.al.; CERN EP 79-65 (1979), CERN EP 79-91 (1979)
210) H. Saarikko et.al.; CERN EP 79-92 (1979)
211) J. Engels, J. Dabkowski, K. Schilling; Wu-B-79-17 (1979)
212) J.P. Berge et.al.; paper submitted to Neutrino '79 Conf. Bergen (1979)
213) W.G. Scott; Physica Scripta 19 (1979) 179
214) J.D. Bjorken, J. Kogut; Phys. Rev. D8 (1973) 1341
215) J. Ellis, talk given at the Int. Symp. on Lepton and Photon Interactions, Batavia, 1979, and CERN-TH 2744 (1979)
216) H.M. Chan, J.E. Paton, T. Sheung-Tsun; Nucl. Phys. B86 (1975) 479
217) H.M. Chan et.al.; Nucl. Phys. B92 (1975) 13
218) G. Veneziano; Phys. Lett. 52B (1974) 220, and Nucl. Phys. B74 (1974) 365
219) J. Dias de Deus, S. Jadach; Acta Phys. Pol. B9 (1978) 249
220) JADE-Collab., W. Bartel et.al., DESY 79/66, 79/80 (1979)
221) J.W. Chapmann et.al.; Phys. Rev. D14 (1976) 5 and Phys. Rev. Lett. 36 (1976) 124
222) C. del Papa et.al.; Phys. Rev. D13 (1976) 2934
223) K. Bunnel et.al.; Phys. Rev. D17 (1978) 2847
224) P.M. Stevenson; ICTP/78-79/1 (1979) and Nucl. Phys. B150 (1979) 357, B156 (1979) 43

225) T. Gottschalk, E. Monsay, D. Sivers;
ANL-HEP-PR-79-15 (1979)
226) T. Gottschalk, D. Sivers; ANL-HEP-PR-79-07 (1979)
227) P. Binétruy, G. Girardi; Nucl. Phys. B155 (1979) 150
228) W.M. Morse et.al.; Phys. Rev. D15 (1977) 66
229) D.R.O. Morrison; CERN/D.PhIII/Phys 73-46 (1973)
230) E.M. Ilgenfritz, J. Kripfganz, A. Schiller;
Acta Phys. Pol. B9 (1978) 881
231) K. Kinoshita, Y. Kinoshita; Phys. Lett. 66B (1976) 471
232) R. Blankenbecher, S.J. Brodsky; Phys. Rev. D10 (1974) 2973
233) S.J. Brodsky, J.F. Gunion; Phys. Rev. D17 (1978) 848
234) H. Goldberg; Nucl. Phys. B44 (1972) 149
235) M.J. Teper; RL-78-022 (1978)
236) F.E. Close; Proc. 19th Int. Conf. on High Energy Physics,
Tokyo, 1978
237) L. Van Hove; CERN TH-2628 (1979)
238) E. Takasugi et.al.; Phys. Rev. D20 (1979) 211
239) R.D. Field, R.P. Feynman; Phys. Rev. D15 (1977) 2590
240) D.W. Duke, F.E. Taylor; Phys. Rev. D17 (1977) 1788
241) T.A. De Grand; Phys. Rev. D19 (1979) 1398
242) W. Lockmann et.al.; Phys. Rev. Lett. 41 (1978) 680
243) R.G. Roberts, R.C. Hwa, S. Matsuda; RL-78-040 (1978)
244) L. Van Hove; Acta Phys. Pol. B7 (1976) 339 ;
Nucl. Phys. B86 (1975) 243
245) S. Pokorski, L. Van Hove; CERN-TH-2427 (1977)
246) J. Kalinowski, S. Pokorski, L. Van Hove; Z. Phys. C2
(1979) 85
247) T.A. De Grand, H.I. Miettinen; Phys. Rev. Lett. 40 (1978) 612
248) J. Kuti, V.F. Weisskopf; Phys. Rev. D4 (1971) 3418
249) M. Derrick et.al.; Phys. Rev. D17 (1978) 1
250) J.F. Gunion, S.J. Brodsky, R. Blankenbecler;
Phys. Lett. 39B (1972) 649
251) D. Sivers, Phys. Rep. 23C (1976) 1
252) V.A. Matveev, R.M. Muradyan, A.N. Tavkhelidze;
Nuovo Cimento Lett. 7 (1973) 719
253) S. J. Brodsky, G.R. Farrar; Phys. Rev. Lett. 31 (1973) 1153,
Phys. Rev. D11 (1975) 1309

254) R. Blankenbecler, S.J. Brodsky, J.F. Gunion; Phys.
Lett. 42B (1972) 461
255) J.F. Gunion, Phys. Rev. D10 (1974) 242
256) R. Blankenbecler, S.J. Brodsky; Phys. Rev. D10 (1974) 2973
257) G. Farrar; Nucl. Phys. B77 (1974) 429
258) R. Blankenbecler, S.J. Brodsky, J.F. Gunion;
Phys. Rev. D12 (1975) 3469
259) D.P. Barber et.al.; Phys. Lett. 89B (1979) 139
260) A.I. Vainshtein, V.I. Zakharov; Phys. Lett. 72B (1978) 368
261) V. Chang, R.C. Hwa; Phys. Rev. Lett. 44 (1980) 139
262) W.R. Frazer, J.F. Gunion; Phys. Rev. D19 (1979) 2447
263) F.E. Taylor et.al.; Phys. Rev. D14 (1976) 1217
264) M.M. Block; CERN-EP/79-82 (1979)
265) W.R. Innes et.al.; Phys. Rev. Lett. 66B (1978) 286
266) DASP II Collaboration, C.W. Darden et.al.;
Phys. Lett. 76B (1978) 246
267) Ch. Berger et.al.; Phys. Lett. 76B (1978) 243
268) DASP II Collaboration, C.W. Darden et.al.;
Phys. Lett. 78B (1978) 368
269) J.K. Bienlein et.al.; Phys. Lett. 78B (1978) 360
270) W. Bothe et.al.; DESY 79/08 (1979)
271) DASP II Collaboration, C.W. Darden et.al.;
Phys. Lett. 80B (1979) 419
272) DASP II, to be published
273) J.L. Rosner et.al.; Phys. Lett. 74B (1978) 350
274) T. Appelquist, H.D. Politzer; Phys. Rev. Lett. 34 (1975) 43
275) T. Appelquist, H.D. Politzer; Phys. Rev. D12 (1975) 1404
276) K. Koller, T. Walsh; Phys. Lett. B72 (1977) 227
B73 (1978) 504
277) K. Koller, T. Walsh; Nucl. Phys. B140 (1978) 449
278) T.A. De Grand et.al.; Phys. Rev. D16 (1977) 3251
279) S.J. Brodsky et.al.; Phys. Lett. B73 (1978) 203
280) H. Fritzsch, K.H. Streng, Phys. Lett. B74 (1978) 90
281) K. Hagiwara; Nucl. Phys. B137 (1978) 164
282) K. Johnson, C.B. Thorn; Phys. Rev. D13 (1976) 1934
283) A. De Rujulà; Proc. 19th Int. Conf. High Energy Physics,
Tokyo (1978)
284) I. Montvay; Phys. Lett. 84B (1979) 331

285) B. Andersson, G. Gustafson; LU-TP-79-2 (1979)
286) J. Randa; Phys. Rev. Lett. 43 (1979) 602
287) G. Knies; DESY 79-47 (1979)
288) F.H. Heimlich et.al.; Phys. Lett. 86B (1979) 399
289) K. Koller, H. Krasemann, T. Walsh; Z.Physik C1 (1979) 71
290) T. Appelquist, R.M. Barnett, K. Lane;
Ann.Rev. Nucl. Part. Sci. 28 (1978) 387
291) W. Schmidt-Parzefall; Proc. 19th Int. Conf. High Energy
Physics, Tokyo (1978)
292) H. Meyer; presented at the 1979 Symp. on Lepton and Photon
Interactions, Batavia, 1979; and DESY 79/81 (1979)
293) S. Brandt, H.D. Dahmen; Z. C. Physik C1 (1979) 61
294) A. Krzywicki et.al.; BI-TP 79/14 (1979)
295) N.N. Nikolaev, A.Y. Ostapchuck, V.R. Zoller, CERN-TH-2541
(1978)
296) D. Cutts et.al.; Phys. Rev. Lett. 43 (1979) 319
297) T. Edwards et.al.; Phys. Rev. D18 (1978) 79
298) D.A. Finley et.al.; Phys. Rev. Lett. 42 (1979) 1031
299) J.R. Johnson et.al.; Phys. Rev. D17 (1978) 1292
300) F.W. Büsser et.al.; Phys. Lett. 51B (1974) 306, 51B (1974) 311
301) B. Alper et.al.; Nucl. Phys. B100 (1975) 237
302) R. Kephart et.al.; Phys. Rev. D14 (1976) 2909
303) F.W. Büsser et.al.; Nucl. Phys. B106 (1976) 1
304) B. Alper et.al.; Nucl. Phys. B114 (1976) 1, B141 (1978) 149
305) K. Eggert et.al.; Nucl. Phys. B98 (1973) 49, B98 (1973) 73,
B 143 (1978) 40
306) CCHK-Collab., M. Della Negra et.al.; Nucl. Phys. B104 (1976) 365,
B127 (1977) 1
307) CCHK-Collab., D. Drijard et.al.; Nucl. Phys. B156 (1979) 309
308) P. Darriulat et.al.; Nucl. Phys. B107 (1976) 429,
B110 (1976) 365
309) M.G. Albrow et.al.; Nucl. Phys. B135 (1978) 461
310) M.G. Albrow et.al.; Nucl. Phys. B145 (1978) 305
311) M.G. Albrow et.al.; CERN-EP/79-56 (1979) and Nucl.Phys. B, in print
312) A.L.S. Angelis et.al.; Phys. Lett. 79B (1978) 505
313) A.G. Clark et.al.; Nucl. Phys. B142 (1978) 189;
Physica Scripta 19 (1979) 79; CERN-EP/79-74 (1979)

314) R. Kourkoumelis et.al.; Phys. Lett. 83B (1979) 257,
84B (1979) 271; 85B (1979) 39; Nucl. Phys. B158 (1979) 39;
CERN-EP/79-57 (1979)
315) J.W. Cronin et.al.; Phys. Rev. D11 (1975) 3105
316) D. Antreasyan et.al.; Phys. Rev. D19 (1979) 764
317) G. Donaldson et.al.; Phys. Rev. Lett. 36 (1976) 1110,
40 (1978) 917
318) C. Bromberg et.al.; Nucl. Phys. B134 (1978) 189;
Phys. Rev. Lett. 42 (1979) 1202, 43 (1979) 561
319) M.D. Corcoran et.al.; Phys. Rev. Lett. 41 (1978) 9
320) M. Dris et.al.; Phys. Rev. D19 (1979) 1361
321) M.D. Corcoran et.al.; Physica Scripta 19 (1979) 95
322) H. Jöstlein et.al.; Phys. Rev. D20 (1979) 53
323) C.W. Akerloff et.al.; Phys. Rev. Lett. 39 (1977) 861
324) D.A. Finley et.al.; Phys. Rev. Lett. 42 (1979) 1028,
42 (1979) 1031
325) S.D. Ellis, M. Kisslinger; Phys. Rev. D9 (1974) 2027
326) R.P. Feynman, R.D. Field, G.C. Fox; Phys. Rev. D18 (1978)
3320
327) J.F. Owens, E. Reya, M. Glück; Phys. Rev. D18 (1978) 1501
328) S.D. Ellis, R. Stroynowski; Rev. Mod. Phys. 49 (1977) 753
329) S.D. Ellis, M. Jacob, P.V. Landshoff; Nucl. Phys. B108
(1976) 93
330) M. Jacob, P.V. Landshoff; Nucl. Phys. B113 (1976) 395
331) R. Cutler, D. Sivers; Phys. Rev. D16 (1977) 679, D17
(1978) 196
332) B.L. Combridge, J. Kripfganz, H. Ranft; Phys. Lett. 70B
(1977) 234
333) R.R. Horgan, P. Scharbach; Phys. Lett. 81B (1979) 215
334) K. Hagiwara; Phys. Lett. 84B (1979) 241
335) R.D. Field; CALT-68-696 (1978)
336) R.P. Feynman, R.D. Field, G.C. Fox; Nucl. Phys. B128
(1977) 1
337) B.L. Combridge; Phys. Rev. D12 (1975) 2893
338) M.K. Chase, W.J. Stirling; Nucl. Phys. B133 (1979) 157
339) A.P. Contogouris, R. Gaskell, S. Papadopoulos;
Phys. Rev. D17 (1978) 2314

340) F. Halzen, G.A. Ringland, R.G. Roberts;
Phys. Rev. Lett. 40 (1978) 991
341) M.K. Chase; Nucl. Phys. B145 (1978) 189
342) R. Raitio, R. Sosnowski; HU-TFT-77-22 (1977)
343) F.E. Close, F. Halzen, D.M. Scott; Phys. Lett. 68B (1977) 447
344) J.B. Kogut; Phys. Lett. 65B (1977) 337
345) J.F. Gunion; Phys. Rev. D15 (1977) 3317
346) J.F. Owens; FSU-HEP-7907-12 (1979)
347) J.F. Gunion; "The Interrelationsship of the Constituent Interchange Model and QCD", presented at the Discussion Meeting on Large Transverse Momentum Phenomena, SLAC (1978)
348) W.E. Caswell, R.R. Horgan, S.J. Brodsky; Phys. Rev. D18 (1978) 2415
349) D. Jones, J.F. Gunion; Phys. Rev. D19 (1979) 867
350) R. Blankenbecler, S.J. Brodsky, J.F. Gunion;
Phys. Rev. D18 (1978) 900
351) W. Stirling; DAMTP 79/10 (1979)
352) W. Selove; UPR-70E (1979)
353) R. Stanek et.al.; quoted in ref. 351)
354) J. Rohlf; presented at Caltech Workshops on High Energy Physics (1979)
355) K.J. Anderson et.al.; Phys. Rev. Lett. 42 (1979) 951
J. Badier et.al.; submitted to '79 EPS Conference on High Energy Physics
R. Barate et.al.; Phys. Rev. Lett. 42 (1979) 1541
356) C. Michael; Proc. of Workshop on Large Transverse Momentum Phenomena, Bielefeld, 1977
357) R. Meinke; Proc. of Workshop on Large Transverse Momentum Phenomena, Bielefeld, 1977
358) CCHK-Collab., M. Della Negra et.al.; submitted to the Int. Conf. on High Energy Physics, Tblisi, 1976
359) H. Bøggild; NBI-HE-79-6 (1979)
360) Z. Kunszt, E. Pietarinen, E. Reya; DESY 79/28 (1979)
361) Z. Kunszt, E. Pietarinen; DESY 79/34 (1979)
362) A. Schiller; KMU-HEP-79-05 (1979)
363) G. Fox, quoted in CERN-TH 2700 (1979)

364) J.C. Van der Velde; Phys. Scripta 19 (1979) 173
365) CCHK-Collab., M. Della Negra et.al.; Phys. Lett. 59B (1975) 401
366) R. Baier, J. Engels, B. Petersson; BI-TP 79/10 (1979)
367) W.G. Scott; Proc. Int. Conf. on Neutrino Physics, Purdue, 1978
368) CCHK-Collab., D. Drijard et.al.; Nucl. Phys.B, in print
369) J. Singh et.al.; Nucl. Phys. B140 (1978) 189
370) R. Sosnowski, private communication
371) G.J. Bobbink et.al.; Phys. Rev. Lett. 44 (1980) 118
372) CCHK-Collab., D. Drijard et.al.; Nucl. Phys. B155 (1979) 269
373) A. Arnedo, G. Plaut; Nucl. Phys. B107 (1976) 262
374) G.H. Thomas, ANL-HEP-PR-77-01 (1977)
375) M.J. Tannenbaum, presented at the Annual Meeting of the Division of Particles and Fields, Montreal, 1979
376) K. Koller, T.F. Walsh, P.M. Zerwas;
Phys. Lett. 82B (1979) 263
377) M. Le Bellac; CERN 76-14 (1976)